Structure and dynamics of Soft Matter systems: bidisperse stackings, broken symmetries, gel networks

Inaugural-Dissertation

zur Erlangung des Doktorgrades
der Mathematisch-Naturwissenschaftlichen Fakultät
der Heinrich-Heine-Universität Düsseldorf

vorgelegt von

Matthias Kohl

aus Solingen

Düsseldorf, Oktober 2015

aus dem Institut für Theoretische Physik II: Weiche Materie
der Heinrich-Heine-Universität Düsseldorf

Gedruckt mit der Genehmigung der
Mathematisch-Naturwissenschaftlichen Fakultät der
Heinrich-Heine-Universität Düsseldorf

Referent: Dr. Michael Schmiedeberg
Korreferent: Prof. Dr. Hartmut Löwen

Tag der mündlichen Prüfung: 18. September 2015

Preface

This thesis is the product of my scientific studies [1–5], which I was allowed to carry out within the Emmy Noether Junior Research Group "*Structure and dynamics of colloidal particles on incommensurate substrates*" from May 2012 till today at the Institute of Theoretical Physics II: Soft Matter of the Heinrich-Heine-University in Düsseldorf. Under my supervisor Dr. Michael Schmiedeberg, whom I want to thank greatly with this statement for his support during my work and for giving me the chance to visit many interesting conferences, I was especially able to work within the highly competetive field of dynamically slowed-down processes.

The headstone of my scientific path probably started earlier in my academic studies, when I was a student under Prof. Dr. Hartmut Löwen. Within his Sonderforschungsbereich (SFB) TR6 I, he already gave me as a undergraduate student the opportunity to snuffle the tempting air of real science.

Since then, not only the accomplishments but also the inevitable failures and dead ends, which I had to deal with during my progress, gave rise for the evolution of personal attitudes. Getting the chance to work on physical matter, that is in a sense completely new for the community, is something that I would never want to miss.
I also want to thank my collaborators, Ronja Capellmann and Andreas Härtel, for the nice discussions and the fruitful cooperative advances, that are being presented within this work. Furthermore, my thanks go to my colleagues Tobias Glanz, Nicolas Höft, and Julian Bialké for proofreading this thesis.

Düsseldorf, October 9th, 2015

Abstract

The name *Soft Matter* refers to materials that are easily deformable. Famous representatives of such materials are for example suspensions that comprise of two components, one being the solvent and the other being the solute. The solute typically consists of micro-sized ($\sim$ 1nm – 1μm) constituents which are immersed in the solvent medium. The particles are exposed to the influence of thermal fluctuations and bear multifaceted application possibilities for material industry. In this thesis, we introduce theoretical model systems where the constituents are spherical particles. We slightly perturb the systems in order to obtain complex phenomena, such as segregation of distinct particle species, glassy dynamics in anisotropic environments, and network-like clusters of bonded particles. The respective perturbations are an external gravitational field, flat repulsive walls, or short-ranged interparticle attractions.
After drafting the technical fundament in Chapters 2 and 3, this thesis mainly discusses the microscopic structure and the relation to the accompanied dynamics for three setups that are obtained by the above-mentioned perturbations: *bidisperse stackings, broken symmetries, and gel-networks*. In Chapter 4, two species of ultra-soft but yet repulsive colloidal solvent particles under the influence of gravity are studied. The arising stackings remind of the so-called Brazil nut effect, that depicts the segregation of large and small nuts in a package of cereals after shaking. However, in our Soft Matter systems the observed states are even more manifold, e.g., as characterized by stackings of large particles at the top and the bottom of a basin and small colloids in between. Chapters 5 and 6 investigate the emergence of broken symmetries that occur for a system of hard spheres close to a flat wall. Besides the heterogeneous distribution of single particles in such a situation, we also acknowledge spatial correlations of a couple of particles by means of theory and computer simulations. Amorphous structures are obtained by polydisperse setups at high packing fractions. For such systems, the dynamics of individual tracers is supposed to slow down significantly due to the formation of local cages of neighboring particles. We explain this so-called glassy behavior in an anisotropic situation by the consideration of spatial correlations that are locally anisotropic and by employing a one-particle model that incorporates the history-dependent memory during a cage escape. In Chapters 7 and 8 we consider interactions, that are repulsive on long ranges and at contact, but attractive in between. The corresponding experiments with colloid-polymer mixtures, in which the polymers mediate an effective attraction, show the same intriguing finding as our simulations: even at low packing fractions heterogeneous bonded cluster-networks with different states occur. One is characterized by the possibility to draw a system spanning line through the interconnected network that may contain loops or backward steps; in the other state forward connections dominate the nature of the network. We identify only such so-called directed percolated gels with non-equilibrium arrested states. As we shear these gels a fracturing of the network into huge slab-like clusters occurs. The slabs only become teared apart at very large stresses. The presented results are mostly theoretical predictions. But due to the size of the particles our results can be experimentally verified with optical microscopy.

Zusammenfassung

Die Physik der *Weichen Materie* beschäftigt sich im Allgemeinen mit leicht deformierbaren Materialien. Diese Materialien bestehen häufig aus zwei Komponenten, nämlich einem flüssigen Lösungsmittel und der gelösten Substanz, die sich darin befindet. Dabei handelt es sich oft um kleine Teilchen in der Größenordnung von einigen Nanometern bis zu wenigen Mikrometern, die aufgrund ihrer Größe thermischen Fluktuationen ausgesetzt sind. Diese besondere Charakteristik Weicher Materie sorgt in vielen Anwendungen für interessante Phänomene. Im Verlauf dieser Arbeit werden einfache Kugel-Modelle so modifiziert, dass verschiedene komplexe Phänomene beobachtet werden können: Die Entmischung unterschiedlicher Teilchensorten auf verschiedenste Weisen, die glasartige Dynamik einzelner Teilchen in lokal anisotropen und dichten Umgebungen sowie netzwerkartige Strukturen, die wir mit Hilfe kolloidaler Gele untersuchen.
Nachdem in den einleitenden Kapiteln 2 und 3 das Fundament für theoretische Ansätze und Simulationsmethoden gelegt wird, beschäftigen sich die darauf folgenden Kapitel insbesondere mit den Ergebnissen zu den bereits angedeuteten Phänomenen. In Kapitel 4 widmen wir uns dem Effekt von Gravitation auf eine zwei-komponentige Mischung sehr weicher Teilchen. Hier beobachten wir, dass sich große und kleine Teilchen entmischen und übereinander stapeln, ähnlich dem "Paranusseffekt", bei dem sich während des Schüttelns größere und kleinere Bestandteile in einer Müslipackung trennen. Im Gegensatz zu diesem relativ einfachen Entmischungsvorgang (groß-klein) beobachten wir in unseren kolloidalen Systemen auch wechselnde Stapelung (z.B. groß-klein-groß) oder netzwerkartige Strukturen. In den Kapiteln 5 und 6 untersuchen wir einen Symmetriebruch, der durch die Anwesenheit einer flachen Wand hervorgerufen wird. Dieser Symmetriebruch äußert sich in der lokalen Struktur der Suspension sowie der damit einhergehende Dynamik. Die amorphen Strukturen, die wir mit Hilfe von kleinen Größenunterschieden der Teilchen erreichen, weisen in unseren dicht gepackten Mischungen vor der Wand ausgeprägte anisotrope Eigenschaften auf, welche wir mit der ebenfalls anisotropen glasartigen Dynamik in Verbindung bringen. Nachdem wir für diesen speziellen Fall auch den Zusammenhang von Dynamik und "Gedächtnis" eines Teilchens untersuchen, werden wir im Anschluss ein Ein-Teilchen-Modell benutzen, um das Entkommen des Teilchens aus seinem lokalen "Käfig" zu modellieren. Schließlich untersuchen wir in den Kapiteln 7 und 8 Gele, in denen Teilchen neben langreichweitigen repulsiven Wechselwirkungen auch eine kurzreichweitige Anziehungskraft besitzen. Hierbei bilden sich große Netzwerke, die das System durchspannen und dabei insbesondere in zwei Fälle unterschieden werden müssen: Entweder sind beim Verfolgen eines Verbindungsweges durch das Netzwerk Rückwärtsschritte erlaubt, oder es sind nur Vorwärtsschritte in eine spezielle Richtung erlaubt (gerichtete Perkolation). Wir legen dar, dass nur Letztere mit Nicht-Gleichgewichtsgelen in Verbindung gebracht werden können, die in große scheibenförmige Cluster aufbrechen, wenn sie von außen geschert werden.
Wenn auch diese Arbeit zu einem großen Teil aus theoretischen Vorhersagen besteht, so ist die experimentelle Validierung mit Hilfe von optischer Mikroskopie leicht möglich.

Contents

Chapter 1

Introduction

Our modern Physics comprises inexhaustible depths of questions that bother our daily life. A lot of different scientific fields have developed, among which especially *Soft Matter science* became a famous and competed area.
When talking about Soft Matter, skeptical people may ask two questions in the first place: What is the scope of this scientific field and how can we legitimate its significance for our world? Fortunately, they are rather easy to respond. In the prosperous and pulsating century of Soft Matter that we live in a lot of materials that are associated with it prevail in the most elementary situations of our life. Such particularly designed materials have not only become convenient for consumers, but also highly manifold for industrial applicants and especially incredibly interesting for us scientists. To name some of the most important candidates of Soft Matter: There are liquid crystals, whose studies have purportedly begun in the late 19th century and for which about 100 years later (in 1991) Pierre-Gilles de Gennes, who is sometimes referred to as the founding father of Soft Matter, was awarded with the Nobel prize[1]. Paints, inks, styling gels and toothpaste are also Soft Matter systems. They are pretty well understood and they become constantly improved in industrial fabrication. Furthermore, polymer physics play an important role as a subtopic of this field. Here, scientists investigate materials, such as, e.g., acrylic glass (Poly-methylmethacrylate/PMMA) or polystyrene (PS), which provide interesting applications as vitreous bodies in automotive industry, synthetic fibers in textile industry, or wrappers of perishable goods in the food industry.
There are many more technical applications, which make this field so important. However, one should also not forget about non-synthetic systems like cell membranes, vesicles, organelles and blood corpuscles, which consist of self-aggregating amphiphile lipid bilayers and which is equally worth to be studied due to its relevance in medicine. Such a broad spectrum of science is an optimal basis for interdisciplinary research. Nevertheless, as theorists explore models in order to describe the underlying physics, it turned out, that

[1] "*for discovering that methods developed for studying order phenomena in simple systems can be generalized to more complex forms of matter, in particular to liquid crystals and polymers.*"

the special kind of physics, which is in principle governed by the stochastic motion of its little compounds, is not only interesting for immediate applicable situations, but the inquired problems also led to the evolution of prominent model systems. Model systems are tremendously important for the understanding of universal problems, e.g., the drastic slow-down at the glass transition. The important role of the Soft Matter glasses became even more manifest due to handy realizations in experimental labs and the ability to track the behavior of (all) individual constituents. Although its particles are typically too small ($\sim$ 1nm – 1μm) for an observation with bare eyes, rather simple microscopy tools and and light scattering techniques give rise to the direct observation of the microscopic processes [6–8]. On the other hand, the underlying physics can often be described by means of simple statistical mechanics. In return, one is able to predict the accompanied macroscopic consequences, which can then for example be verified by mechanical studies.

In Ref. [9] it is proposed to arrange the huge variety of different investigation fields as well as the intricacy of given problems in a two-dimensional complexity plane, where the first axis would describe the complexity of the constituents and the second axis the complexity of the problem. For example, if one studies the polymer or dendrimer physics, the complexity along the first axis is increased from simple monomeric particles to chains or networks of successively docked particles. By manipulating the system from outside, e.g., by applying external fields, the complexity along the second axis is increased. The underlying problems become even more difficult to understand, when equilibrium or ergodicity assumptions are not fully valid anymore. In these cases the investigated systems are entitled with the tags *steady-state, metastability,* or *non-equilibrium*.

In this thesis, systems along the second (schematic) complexity axis, i.e., the complexity of problems, will be investigated, whereas the constituents are held rather simple. Thus, only spherically symmetric particles will be considered, where sizes, degree of repulsions, and also attraction potentials are varied. Additionally, external potentials will be used for the specific models, among which especially confining potentials are discussed. This way is chosen in order to obtain fundamental results out of mostly simplistic models. Nonetheless, we will see, that such simplistic particles still bear multi-particle cooperation, where huge aggregates are considered that are the predominant and determining factor for dynamical processes. As the title of this work already suggests, we study three different setups, which are shortly illuminated in the following.

Bidisperse stackings. The first setup, which will be introduced in Chapter 4, is given by stackings of spherical particles with two different sizes in a gravitational and with a wall at the bottom. Gravity is ubiquitous and it therefore plays a crucial role in many applications. It is important to understand the effects of gravity, because they may cause advantageous or disadvantageous features. Yet, the theoretical prediction is a challenging task. In our study of bidisperse stackings we will address the segregation of species according to their size [10]. Within this scope it is inevitable to ignore the famous topics of the *Brazil nut effect* or the *reverse Brazil nut effect* [11–14], whose names are associated with the demixing of larger and smaller pieces in a mixed cereals

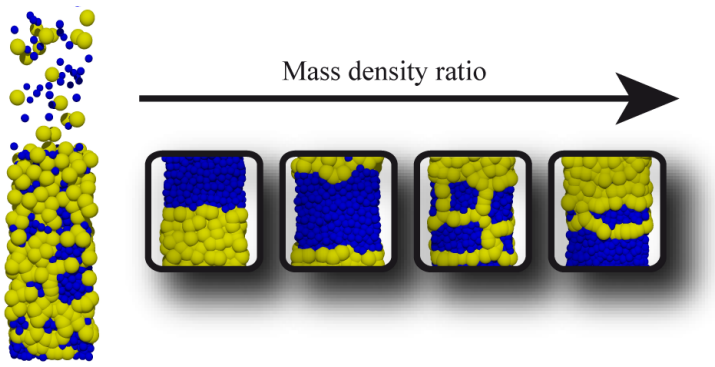

Figure 1.1: Binary soft spheres in the gravitational field sediment to the ground. The concurrent pressure gradient and the employed mass density ratio of the two species give rise to (from left to right) different stacking mechanisms as well as arrested network-like structures. The figure has been taken from Ref. [1].

package while shaking. Besides the research with macro-sized samples [15, 16] also for micro-sized systems elaborate experiments [17–19] as well as simulations and theoretical works [20–25] have been advanced. The major difference between macro-sized (granular) and micro-sized (Soft Matter) systems is, that the thermal energy can be neglected in the former one but not in the latter one. Furthermore, the effect has been discussed mostly for hard particles. Therefore, in this thesis a colloidal system of ultrasoft particles within the gravity field will be addressed. It typically differs from the granular one [26–31].
The addressed colloidal system shows very interesting phenomena, where a selection of the final states is in a simplified manner sketched in Fig. 1.1. With the help of theoretical predictions, that are based on buoyancy behavior of the colloids, we will show that by slightly changing the *mass density ratio* distinct stackings of species and even long-lasting network structures are obtained. Furthermore, we will give insight into the dynamical process of sedimentation and the evolution of a perturbation of already sedimented system. We will show, that restructuring processes are mainly dominated by multi-particle (cooperative) dynamics. We characterize this effect by adding a few particles at the top of already sedimented particles and trace the evolution of these additional particles. First, particles of the same species aggregate into a cluster, then this cluster consecutively sinks to the ground.

Broken symmetries. In this part of the thesis we study a system of hard spheres close to a wall. The ensemble consists of differently sized particles, such that no local crystallites can form, but rather *amorphous structures* arise at high densities [32]. Examples for amorphous materials are, e.g., plastics, window glasses, or gelatin. At high packing fractions (or low temperatures) the structure is similar to a liquid, but the dynamics becomes dramatically slow such that solid-like behavior is observed [33–38]. Often referred to as the *local cage* [39–41], the surrounding neighbors of an individual particle make sure that its motion is hindered for intermediate or even long times. Such local structural arrangements are fundamental for the understanding of relaxations [42, 43].

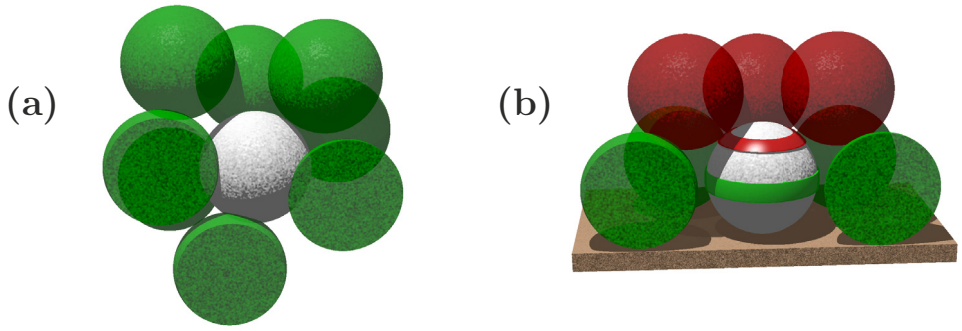

Figure 1.2: Sketch of cuttings in (a) bulk and (b) a system close to a wall. One particle (*white*) resides inside a typical configuration of neighboring particles (*green* and *red*). The colored rings around the white sphere in (b) mark regions of high contact probability and therefore increased local pressure.

As sketched in Fig. 1.2(a), the local cage (colored in green) of a particle in a homogeneous situation may look rather arbitrary such that often only average over all possible configurations can be calculated from theories. Contrarily, for a system that is perturbed by a flat wall, one will always observe a similar local arrangement, where some positions of neighboring particles are more probable than others. If not suppressed [44], layers of particles form in front of the wall [45–48], as represented by the differently colored particles in Fig. 1.2(b). In such a situation, *broken symmetries* appear not solely on the one-particle level [49, 50]. The tag also refers to broken symmetries of the two-particle structure (cf. Refs. [46, 51–53]), which becomes clear in Fig. 1.2(b) by the enhanced contact probabilities at the color-marked rings around the white sphere. But also the symmetries in the resulting diffusion process of individual particles are broken (cf. Refs. [45, 54, 55]). These closely related properties will be investigated in this thesis, where especially for questions concerning the structural, a very accurate theory (density functional theory) will be compared with computer simulations of extensively large multi-particle systems. Additionally, in the inspection of the dynamics, two mechanisms are important in glassy systems: the memory of a particle's history and a more detailed resolution of its local cage-structure. We will show, that these two ingredients are crucial by employing them in an effective one-particle model.

Gel networks. Finally, we probe the behavior of *gel networks* in a homogeneous environment (bulk) and in the case of pore confinement and shear. The label *gel* typically describes a whole class of different materials and solutions. However, in this thesis it will refer to colloidal spherical particles, which are able to form bonds and interconnect with each other. To facilitate such a bonding, particles not only repel each other but they also exhibit an attraction [56–64]. The interaction can be described within theoretical models, where smaller particles (polymers) induce an effective attraction between the larger colloids [65, 66]. For sufficiently strong attractions huge clusters of particles emerge (see Fig. 1.3).

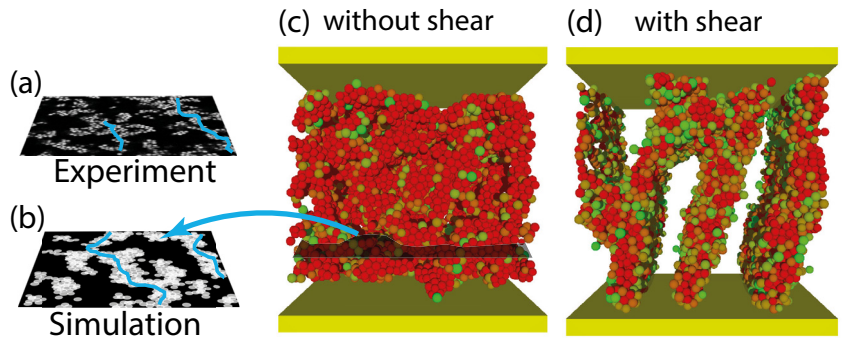

Figure 1.3: In the slice-cuts of (a) experimental and (b) simulation gels one can identify connected paths of particles (blue lines) through the network, which are directed (*directed percolation*). (c) Confinement of such gels between two plates gives rise to a local detachment from the plates. (d) If the gel is additionally sheared it may break into large vertical slabs.

We observe directed paths through clusters of bonded particles in experiments (Fig. 1.3(a)) and simulations (Fig. 1.3(b)). Systems with highly attractive particles show arrested dynamics [43,67–73] similar to the above-mentioned glasses. But the coherent structure is different and can contain huge empty (void) volumes [74]. Only few studies report about the interplay of dynamical slowdown and the local structure. For example, the dynamic arrest was associated with local arrangements of favored structures [57]. Also the rigidity percolation was linked to the dynamical arrest [75]. We will show, that especially the occurrence of directed percolated paths (blue lines in Fig. 1.3(a-b)) through the gel network can be related to the onset of dynamical slowdown and therefore non-equilibrium aging in the samples. As we start to shear these network structures in our simulations (Fig. 1.3(d)), we observe successive bond-breaking and the formation of larger slab-like domains. These structures may occur at intermediate shear rates. When the shear stress is increased even more, internal aggregates also fracture and homogeneous systems are regained.

This thesis is organized as follows: Chapters 2 and 3 are introductory chapters, where in particular the statistical description and the employed theories for our predictions as well as our Brownian dynamics simulations are explained. In Chapter 4, the binary system of ultrasoft particles in the gravitational field will be investigated by means of computer simulations and simple theoretical approximations for the dense and the dilute phases. Chapters 5 and 6 discuss the structure as well as the resulting dynamics of a binary hard-sphere system close to a flat wall. For the structural studies, computer simulations will be compared to calculations from density functional theory that is based on a very accurate fundamental measure theory, termed the *White Bear, mark II* [76]. Finally, Chapters 7 and 8 deal with the gel-networks. In the former one, structural properties are connected with observed dynamics by means of experiments and simulations. The latter chapter discusses the effect of confinement of such gels and the impact of shear.

Chapter 2

Colloidal suspensions

2.1 Thermodynamics of soft matter systems

Thermodynamics in general describes the interplay of so-called (natural) thermodynamic variables of a particular system with the heat or the mechanical work done by it. Its manifest is built on the so-called *laws of thermodynamics*, whose first member was written down in early works from the 19th century. They originated mainly as byproducts of considerations about power efficiency of steam engines from Rudolf Clausius [77] and works by Lord Kelvin (William Thomson) [78][1].

Following these laws, the equilibrium is, based on its constraints, defined by the so-called thermodynamic potentials. These potentials can be used to explain the change from one thermodynamic state to another. Within a particular thermodynamic potential it is possible to extract macroscopic quantities, e.g., such as compressibilities, expansion coefficients or heat capacities. Which potential has to be taken into account, depends on the choice of thermodynamic variables. For example, one choice of a parameter set is $(T, V, \{N_\nu\})$ for a system with a fixed number of particles $\{N_\nu\}$, where the subscript $\nu = 1, \ldots, m$ refers to the set of particle numbers of the different species. The number of particle species is m, the volume is V, and the temperature is T. A microscopic example of such a so-called *canonical ensemble* is shown in Fig. 2.1(a), where the confined particles can only move inside the constant volume, whilst the system is connected to a bath with constant temperature. One of the laws of thermodynamics states that, if such a system is connected with a heat reservoir of constant temperature, it adjusts its internal energy due to the exchange of heat with the thermal bath until the equilibrium is obtained. The thermodynamic potential, which describes this equilibrium state, is the *Helmholtz free energy* $F = F(T, V, \{N_\nu\})$. The differential form represents the change of this energy

[1] It should be noted, that in the very early 19th the physicists N.L.S. Carnot and J.P. Joule also had a huge contribution to the development of thermodynamics.

with respect to its thermodynamic variables

$$\mathrm{d}F = -S\mathrm{d}T - p\mathrm{d}V + \sum_{\nu} \mu_\nu \mathrm{d}N_\nu \,, \tag{2.1}$$

where p is the pressure and S is the total entropy of the system.

If the system is additionally allowed to exchange particles with the bath, as shown in Fig. 2.1(b), the natural variables $\{N_\nu\}$ are replaced by their conjugate variables, the so-called chemical potentials $\{\mu_\nu\}$. The set of parameters of such a *grand canonical ensemble* is then given by $(T, V, \{\mu_\nu\})$. The respective equilibrium potential is then the *grand canonical potential* $\Omega = \Omega(T, V, \{\mu_\nu\})$, which is related to the *Helmholtz free energy* via a Legendre transformation [79], i.e., $\Omega = F(T, V, \{N_\nu\}) - \sum_\nu \mu_\nu N_\nu$. The total differential reads

$$\mathrm{d}\Omega = -S\mathrm{d}T - p\mathrm{d}V - \sum_{\nu} N_\nu \mathrm{d}\mu_\nu \,. \tag{2.2}$$

Although these two presented potentials are fundamentally different, it is possible to make approximate comparisons. In the *thermodynamic limit*, where $N \to \infty$, both ensemble descriptions are equivalent. The chemical potential in a respective grand canonical system can be fixed in such a way that the average densities in the middle of both ensembles, e.g., far away from a perturbing wall, coincide. Consequently, both routes will lead to the same results, even in regions closer to the confining walls.

Coarse grained thermodynamic descriptions are nowadays due to their huge significance widely spread in teaching lectures of undergraduate students at almost every university. Thanks to the early studies of the Scottish physicist James Clerk Maxwell (1831-1879), who basically founded the *kinetic theory*, and Ludwig Boltzmann (1844-1906), who worked on the physical agreement of atomistic models with the accompanied macroscopics, low-level theories are able to verify these famous laws of thermodynamics. They start with individual particles and proceed with their microscopic interactions. Such theories give rise to investigations of the connection between materials and the atomistic matter they are made of. With the help of partly complicated and partly simple microscopic models of soft matter systems very important macroscopic properties can be predicted or even designed. Therefore, in this Chapter the focus will be laid on such microscopic approaches.

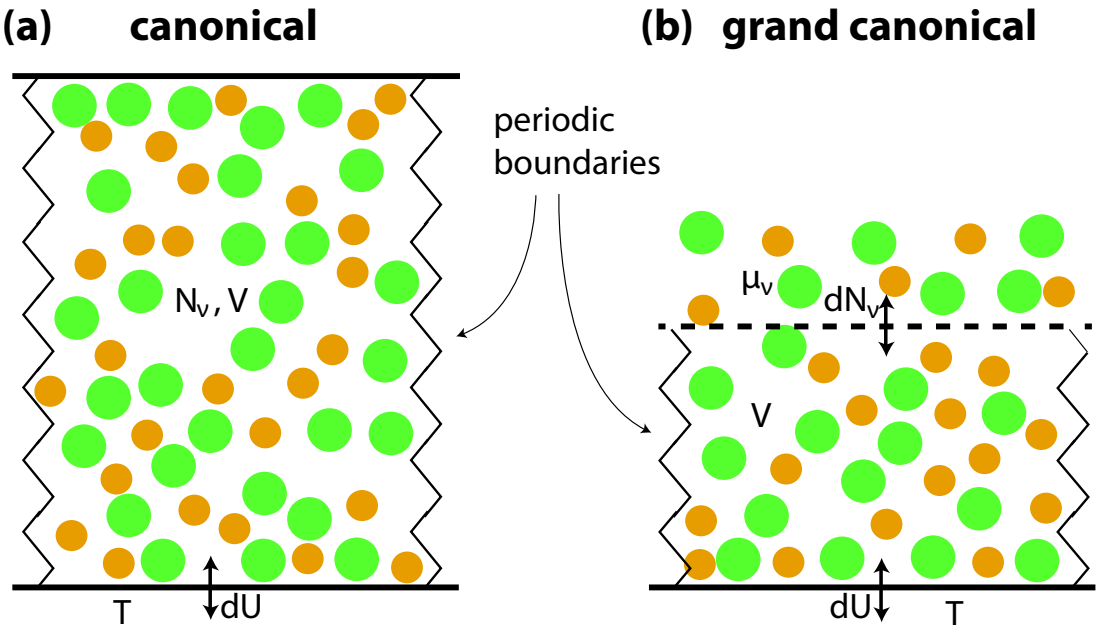

Figure 2.1: (a) Sketch of a *canonical* $(T, V, \{N_\nu\})$-ensemble, where the system is allowed to exchange heat with a surrounding bath and is confined by two walls (top and bottom). The left and right jagged lines are "periodic boundaries", as e.g. realized by a toroidal symmetry. (b) Example of a *grand canonical* $(T, V, \{\mu_\nu\})$-ensemble of half-confined microscopic particles. Instead of constant $\{N_\nu\}$, the system may also exchange particles with the bath, such that the chemical potentials $\{\mu_\nu\}$ equilibrate. Due to a proper choice of those chemical potentials the densities of both systems (a) and (b) may coincide in the middle of the system, i.e., far away from the perturbing wall.

2.2 Slowed-down dynamics in glasses and gels

In this thesis, the focus lays on the investigations of *glassy colloidal systems*, but the original tag is mostly associated with molecular glasses, where the single constituents are on the atomistic length-scale. In order to disclose the connection to colloidal glasses, there will first be a few words about molecular glasses.

Although most probably the first molecular glass has already been used in the ancient Egypt, the microscopic understanding of its behavior, which is the basis of all macroscopic properties, is still not overarching gathered. One of the most challenging debates runs around the dramatic slow-down of the dynamics of glasses. In today's industry the most common glass is made out of one fundamental material: Silica (chemical: SiO_2)[2]. Its applications range from simple windows, that must consist of a huge percentage of transparency for visible light, over extremely robust phone displays, to frequency-sensitive optical instruments, which are used in scientific as well as in industrial areas.

The transparency of a molecular glass stems from its microscopic structure, which differs from the structure of other solids. In metals, the behavior of the electrons are the main reason, why the macroscopic solid is not transparent for our visible light. In solid crystalline materials the electromagnetic waves are trapped by multiple intrinsic reflections with the underlying crystalline lattices. In contrast to that, glasses are typically fabricated by freezing a fluid-like structure very rapidly in such a way, that the microscopic structure, e.g., the relative position dependence of two particles, does not differ much from the fluid state. Contrarily, the dynamical properties slow down significantly by many orders of magnitude, which consequently makes the material to become solid-like. On the one hand this slow-down results in a macroscopic solid and its properties might be analyzed by rheology experiments such as shearing, where large dynamic viscosities of typically 10^{13}Poise occur [80], which is more than 15 magnitudes larger than for water at room temperature. Here, the viscosity might also be a function of the applied strain, such that materials may behave differently upon different load. On the other hand, the process of freezing into a glassy state can be quantified by the relaxation times of individual particles on microscopic lengths. From molecular considerations it is then also possible to derive the thermodynamic quantities, which have been mentioned before (compressibility, thermal expansion coefficients, specific heat).

About the definition of glasses. In contrast to the structure, which has no longer ranged order in a glass [81], at the transition from a fluid-like to a glassy state the above-mentioned specific thermodynamic *order parameters* (compressibility, etc.) exhibit abrupt changes at the (experimental) *glass transition temperature* T_g. This temperature typically depends on the fixation point of the corresponding experiments, as exemplary shown in Fig. 2.2. Here, the glass transition temperature is defined by the point, where

[2]Silica is mostly not used in its pure form, since it has a rather high transition (melting) temperature. Therefore one often adds impurities in order to simplify the processing in industrial operations.

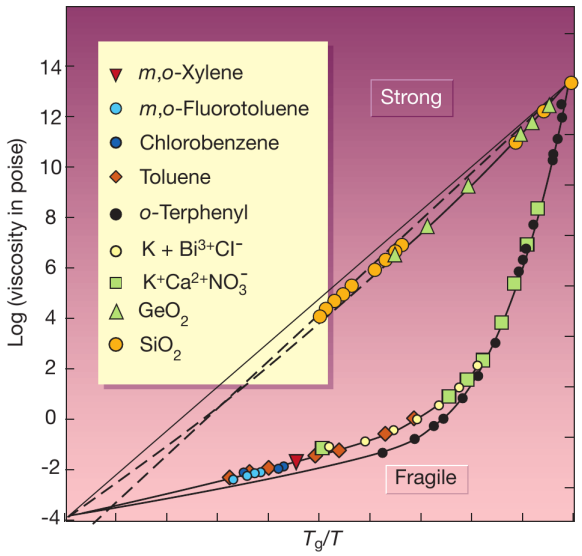

Figure 2.2: Angell-Plot (or Arrhenius plot) for different materials (from Ref. [35]). Semi-logarithmic presentation of the viscosities of different materials as a function of T_g/T, where T_g is the glass transition temperature, at which the viscosities of the different materials reach 10^{14}Poise. Linear dependencies in this representation are referred to as *strong glasses*, which obey the Arrhenius law (see Eq. (2.3)). Materials with curved data are referred to as *fragile glasses* with super Arrhenius behavior (see, e.g., Eq. (2.4)).

the dynamic viscosity η exceeds 10^{14}Poise. As the transition temperature is approached, the viscosity increases dramatically. Simultaneously a gradual drop in the specific heat and abrupt changes in other parameters can be observed (not shown in Fig. 2.2). The adapted plot is the well-known and hugely marveled *Angell plot* [82, 83], which is widely used to characterize the glassy character of substances. Furthermore, one can observe differences in the degree of the decrease of dynamics, i.e., some of the materials exhibit more curvature than others. While Silica (SiO_2) exhibits an exponential scaling, which is disclosed by a linear relation in a semi-logarithmic plot, some other materials seem so have a moderate viscosity increase at intermediate temperatures and an even more rapid increase very close to the transition. The former one is connected with *strong* glasses and sometimes called *Arrhenius-behavior*, i.e.,

$$\eta = \eta_0 \mathrm{e}^{-\alpha \frac{T}{T_\mathrm{g}}} . \tag{2.3}$$

This equation implies, that the viscosity stays finite for all finite temperatures. Here α is a dimensionless constant, which originates from the idea of a temperature-independent "activation energy" that can be formally described within the framework of the *Transition State Theory* (TST). The theory was applied for forward and reverse equilibrium chemical reactions by Pelzer, Wigner and Eyring [84, 85] as well as for more abstract systems, where general transition phenomena can be described by a particle which has to overcome an energy barrier. The latter one is referred to as the *Kramers transition state theory* (see, e.g., Refs. [86, 87]).

However, although the representation of data shown in Figure 2.2 incorporates many length-scales and shows nicely the slowdown of dynamics on approaching the transition, it lacks the fact that due to its definition the experimental glass transition does not necessarily coincide with a thermodynamic glass transition. The results typically depend on the duration of the experimental time windows. With ultrasound experiments it could be even argued, that the glass transition happens well above T_g [80]. Therefore one could conclude, that the glass transition is not well defined by experimental settings due to choice of measurement times and the fact, that systems already freeze into metastable states well above the actual glass transition temperature. Furthermore, by changing the reference values T_g in Fig. 2.2 the curvature in the shown viscosity range would also change. As a consequence, the difference between *strong* and *fragile glasses* could no longer be distinguished in a well-defined way. Another very important point is, that the glass transition also depends on the setup, e.g., the cooling rate of the system, and therefore the accompanied *aging*. The measured relaxation times depend on the history (=age) of the glass and would therefore lead to different reference points. Such effects must also be discussed in order to make results comparable with each other [88, 89].

Besides these problems, for the very basic assumptions there are also different theoretical approaches present in the scientific glass community. While on the one hand the glass transition could be thought as a steady slow down of dynamics [67], e.g. as represented by Eq. (2.3), there exist many other works which rely on the assumption of a finite glass transition temperature [90–92].

The former ones question, whether the slowdown is really connected with thermodynamic properties at all, or whether the jump in the corresponding order parameters is not a real equilibrium jump, but rather a jump induced by one frozen metastable and very long lasting configuration. This would mean that the glass transition is only a dynamic phenomenon. Contrarily, the latter ones postulate, that the transition is a thermodynamic one, where (several) order parameters change discontinuously. One of the most prominent examples is probably the Vogel-Fulcher-Tammann (VFT) ansatz, where the viscosity from Eq. (2.3) diverges at a finite glass transition temperature [90]

$$\eta = \eta_0 \exp\left(\frac{\alpha_\mathrm{T}}{T - T_\mathrm{VF}}\right) . \tag{2.4}$$

Here T_VF is the Vogel-Fulcher temperature, which lays below the experimental glass transition T_g and at which the dynamics becomes completely frozen. The prefactor α_T corresponds to a fitting parameter that equals the activation temperature for the given material. Moreover, it turned out that especially soft matter glasses serve as very valuable tools to study the mostly universal properties of glasses in general, since microscopy tools facilitate the *observation* of what is happening within such a system.

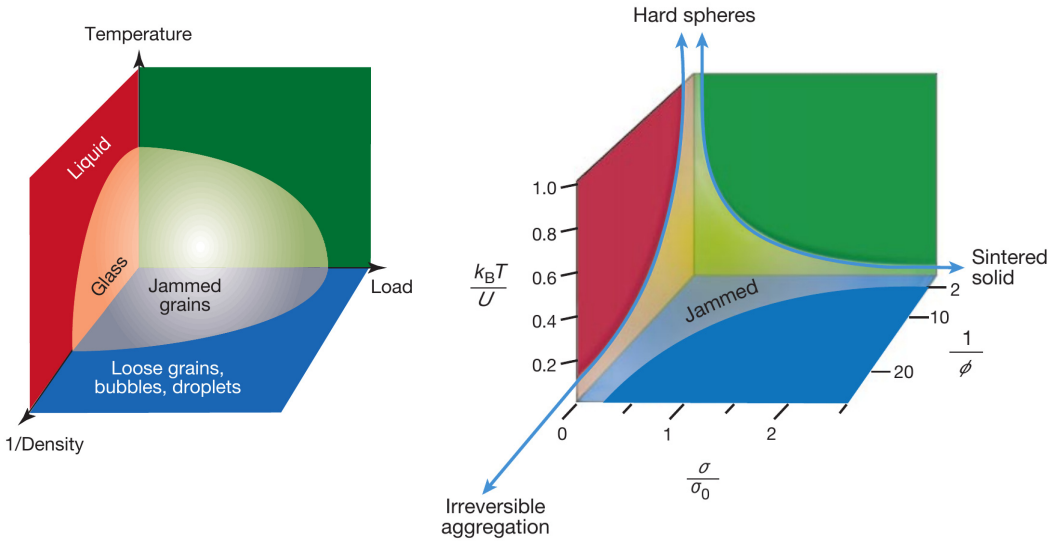

Figure 2.3: (a) Jamming phase diagram for repulsive particles by Liu et. al. [34]. The jammed state, which is represented by the transparent surface, can be reached by changing one of the three parameters while the other two are fixed. (b) Jamming phase diagram for particles with attractive interactions, by Trappe et. al. [93]. Here the inverse attraction energy U between a pair of particles replaces the temperature from (a). Systems can become jammed, when the attraction is sufficiently strong, and when the density (*here*: ϕ) or load (*here*: σ/σ_0) are varied.

Jamming. A real *transition point* is motivated by the experimental findings of glass transition temperatures. For this purpose the concept of the *jamming phase diagram* was proposed by A.J. Liu and S.R. Nagel [34] and other groups [94, 95]. The diagram is shown in Fig. 2.3(a) for three involved parameters: in this representation, for completely repulsive particles, jamming and the accompanied dynamical slowdown can be achieved, when either the density (ρ) is increased sufficiently, or the temperature (T) is lowered below a certain threshold, or an optional externally applied load (*here:* σ) is reduced. At the origin of the coordinate system, the density is at its maximum, whereas the temperature and stress vanish. Another representation of the jamming phase diagram can be found, when additionally attractive forces are incorporated between the particles, e.g., in colloid-polymer gels. If we measure the attraction strength between a pair of two particles by the binding energy U, again a jamming phase diagram can be constructed, where the temperature is now replaced by the inverse attraction energy, see Fig. 2.3(b). Such systems also show a slowdown of dynamics and similar jamming behavior at very low densities [68, 69, 71, 72].

In the athermal limit ($T \to 0$) the critical jamming packing fraction or jamming transition point is defined as the point where overlap cannot be prevented anymore. It probably cannot be connected directly with the glass transition, since recently it was found, that without shear "*the glass transition line does not extrapolate to the jamming point*" in this athermal limit [96]. It rather happens already at lower packing fractions.

The glassy regime. In the so-called *glassy regime* dynamical rearrangements are rare but still possible, in contrast to a thermodynamic glass. When considering the glassy dynamics, one can for example measure the probability distribution for finding a particle at a displacement vector $\mathbf{r}$ after a time t, i.e.,

$$G(\mathbf{r},t) = \frac{1}{N}\left\langle \sum_{i=1}^{N} \delta\big[\mathbf{r} - \big(\mathbf{r}_i(t) - \mathbf{r}_i(0)\big)\big] \right\rangle , \tag{2.5}$$

with the Dirac-δ function and the vectorial descriptors $\mathbf{r}_i(t)$ of the individual trajectories of all $i = 1, \ldots, N$ particles. Equation (2.5) is the density auto-correlation and is called *self part* of the *van-Hove correlation* function [97], where the brackets $\langle . \rangle$ denote an ensemble average.
The *intermediate scattering function* (ISF) $f(\mathbf{k},t)$ is defined as the Fourier transform of the van-Hove self-correlation. It can therefore be written as

$$f(\mathbf{k},t) = \int \mathrm{d}\mathbf{r}\, G(\mathbf{r},t)\mathrm{e}^{-i\mathbf{k}\mathbf{r}} . \tag{2.6}$$

A similar measure is given by the *mean square displacement* MSD, which is proportional to the second moment of the van-Hove function. It represents a more intuitive connection between length- and timescales and is defined over the *average squared displacement* of

the particles after a time t, i.e.,

$$\Delta\mathbf{r}^2(t) = \frac{1}{N}\left\langle \sum_{i=1}^{N} \left(\mathbf{r}_i(t) - \mathbf{r}_i(0)\right)^2 \right\rangle . \tag{2.7}$$

These equations are written as bulk-averages. Therefore, they do not depend on spatial coordinates. Of course, if one wants to investigate spatially resolved quantities around $\mathbf{r}'$ in inhomogeneous systems, it would be necessary to perform the average over an infinitesimal volume around $\mathbf{r}'$. The above presented well-defined measures allow us to quantify how glassy a system is. We will use them in this thesis to investigate dynamic properties of colloidal model systems. Such colloidal model systems are well suited to investigate the topic of glasses, since the visualization of its individual constituents is possible and the most interesting mechanisms are often universal, no matter whether the glass is a molecular glass or a colloidal one.

2.3 Statistical description

2.3.1 Classical many-body systems

A classical many-body system in general contains a certain number of particles N, where distinct particles are not necessarily of the same species. In this work, multi-component and polydisperse systems are studied that consist of m particle species[3]. For these systems summing over all numbers of particles of the individual species yields

$$N = \sum_{\nu=1}^{m} N_\nu \,. \tag{2.8}$$

We reduce the discussion on polydisperse many-body systems with isotropic interactions. Here, any individual particle, that resides at position $\mathbf{r}_{\nu,i}$ and is of species ν, may interact with any other particle (at $\mathbf{r}_{\nu',i'}$) via an interaction potential $v_{\nu\nu'}(|\mathbf{r}_{\nu,i} - \mathbf{r}_{\nu',i'}|)$. Additionally, all particles may have a kinetic energy and eventually be exposed to an external field. The many-body Hamiltonian for such a classical system reads

$$H_N = U_N + H_N^{\mathrm{kin}} + V_N^{\mathrm{ext}} \,, \tag{2.9}$$

where the right hand side represents the split-up of the Hamilton into the pair-interaction

$$U_N = \frac{1}{2} \sum_{\nu}^{m} \sum_{i}^{N_\nu} \sum_{\nu'}^{m} \sum_{\substack{i' \neq i \\ \text{for } \nu=\nu'}}^{N_{\nu'}} v_{\nu\nu'}(|\mathbf{r}_{\nu,i} - \mathbf{r}_{\nu',i'}|) \,, \tag{2.10}$$

where it has been assumed, that no explicit many-body interactions (between three or more particles) are present. The total kinetic energy reads

$$H_N^{\mathrm{kin}} = \sum_{\nu=1}^{m} \sum_{i=1}^{N_\nu} \frac{\mathbf{p}_{i,\nu}^2}{2m} \,, \tag{2.11}$$

where $\mathbf{p}_{\nu,i}$ are the momenta of the particles. The term V_N^{ext} origins from an external field and will be explained in Sec. 2.4.

2.3.2 Probability density and averages

In order to describe a problem within a statistical treatment, we need to introduce a *probability density* ω. It is a function of the current state of the system and depicts – in simple terms – whether the state is likely expected or not. Therefore, ω must depend on all particle positions and, in general, all particle momenta. Furthermore, if neither a

[3] In the following, the Greek letters ν and ν' will always account for the species of the particle.

steady state nor equilibrium is investigated, the function ω will additionally depend on the time t.
In a multi-component system it is tedious to always write down the exact dependencies on all positions $\mathbf{r}_{\nu,i}$ and momenta $\mathbf{p}_{\nu,i}$. Therefore, in the following abbreviations for the multidimensional phase space coordinates are introduced,

$$\mathbf{r}^N = (\mathbf{r}_{1,1}, \ldots, \mathbf{r}_{1,N_1}, \quad \ldots \quad, \mathbf{r}_{m,1}, \ldots, \mathbf{r}_{m,N_m}) \,, \tag{2.12}$$

$$\mathbf{p}^N = (\mathbf{p}_{1,1}, \ldots, \mathbf{p}_{1,N_1}, \quad \ldots \quad, \mathbf{p}_{m,1}, \ldots, \mathbf{p}_{m,N_m}) \,, \tag{2.13}$$

and for the infinitesimal elements

$$\mathrm{d}\mathbf{r}^N = (\mathrm{d}\mathbf{r}_{1,1}, \ldots, \mathrm{d}\mathbf{r}_{1,N_1}, \quad \ldots \quad, \mathrm{d}\mathbf{r}_{m,1}, \ldots, \mathrm{d}\mathbf{r}_{m,N_m}) \,, \tag{2.14}$$

$$\mathrm{d}\mathbf{p}^N = (\mathrm{d}\mathbf{p}_{1,1}, \ldots, \mathrm{d}\mathbf{p}_{1,N_1}, \quad \ldots \quad, \mathrm{d}\mathbf{p}_{m,1}, \ldots, \mathrm{d}\mathbf{p}_{m,N_m}) \,. \tag{2.15}$$

Assuming that the system is in a certain state around $(\mathbf{r}^N, \mathbf{p}^N)$, the function ω is defined in such a way, that the infinitesimal product $\omega(\mathbf{r}^N, \mathbf{p}^N, t)\mathrm{d}\mathbf{r}^N\mathrm{d}\mathbf{p}^N$ represents the configurational probability of finding the system in the phase space volume $\mathrm{d}\mathbf{r}^N\mathrm{d}\mathbf{p}^N$. The probability density must be a normalized function. Therefore, integrating the function $\omega(\mathbf{r}^N, \mathbf{p}^N)$ over the whole phase space (denoted by Γ) yields

$$\int_\Gamma \mathrm{d}\mathbf{r}^N\mathrm{d}\mathbf{p}^N \, \omega(\mathbf{r}^N, \mathbf{p}^N) = 1 \,. \tag{2.16}$$

As the name of the function suggests, the average value of a configuration-dependent observable $O(\mathbf{r}^N, \mathbf{p}^N)$ is calculated by evaluating its scalar product with respect to the probability density. The scalar product is defined as

$$\langle O \rangle = \langle \omega, O \rangle = \int_\Gamma \mathrm{d}\mathbf{r}^N\mathrm{d}\mathbf{p}^N \, \omega(\mathbf{r}^N, \mathbf{p}^N) O(\mathbf{r}^N, \mathbf{p}^N) \,. \tag{2.17}$$

2.3.3 Statistics of thermodynamic ensembles

Considering a problem in the framework of statistical mechanics, it is beneficial to treat it within the scope if a *thermodynamic ensemble*. Two of the most prominent examples have already shortly been mentioned in Sec. 2.1. In the *canonical ensemble* the thermodynamic variables were introduced as $(T, V, \{N_\nu\})$, where now the system's state is defined by the temperature T rather than by the internal energy.
If one would allow for the fact, that the number of particles may also fluctuate due to, e.g., a coupling to a reservoir of particles, it becomes necessary to fix for each particle species the chemical potentials $\{\mu_\nu\}$ such that they equal the chemical potentials of the reservoir $(T, V, \{\mu_\nu\})$. Any ensemble has a unique set of conjugate variables. The different state potentials can be formally connected to other state potentials via a Legendre transformation of one of the variables.

All simulations within this thesis are performed with a constant total number of particles and constant volume and temperature, which causes the system to be described within a canonical ensemble. For the application of density functional theory (DFT) the grand potential Ω, which is defined in the grand canonical ensemble, must be minimized. Therefore, we will shortly introduce these two ensembles within the preluded statistical manner of probability densities.

The canonical ensemble. The canonical ensemble describes closed systems, which have a fixed number of particles at fixed temperature and volume. In equilibrium the energy distribution is a Boltzmann distribution and therefore the probability density can be written as

$$\omega_{\mathrm{c}}(\mathbf{r}^N, \mathbf{p}^N) := \frac{\exp[-\beta H_N]}{Z(T, V, \{N_\nu\})}\,, \tag{2.18}$$

where H_N is the Hamiltonian, $\beta^{-1} = k_{\mathrm{B}}T$ is the inverse thermal energy and the so-called canonical partition function is [98]

$$Z(T, V, \{N_\nu\}) = \frac{1}{h^{3N}\prod\limits_{\nu'} N_{\nu'}!}\int\limits_{\Gamma} \mathrm{d}\mathbf{r}^N \mathrm{d}\mathbf{p}^N\, \exp[-H_N/k_{\mathrm{B}}T]\,, \tag{2.19}$$

with a prefactor that determines the smallest possible volume in phase space and therefore contains the Planck constant h. In the canonical ensemble the corresponding thermodynamic potential is the *Helmholtz free energy* F. By making use of the fundamental thermodynamic equations it can be shown, that the free energy is connected to the logarithm of the partition function (see, e.g., Refs. [98, 99])

$$F(T, V, \{N_\nu\}) = -k_{\mathrm{B}}T \ln\big(Z(T, V, \{N_\nu\})\big)\,. \tag{2.20}$$

Assuming, that the canonical partition function is known for the system, one is able to calculate all thermodynamic quantities and explain macroscopic physical properties of the system. For an *ideal gas*, consisting of N non-interacting and indistinguishable particles with mass m, the partition function can be calculated analytically. It reads [98]

$$Z^{\mathrm{id}} = \frac{q^N}{N!}\,, \tag{2.21}$$

where we have introduced the single-particle partition function $q = V/\Lambda^3$ with the thermal De Broglie wavelength $\Lambda = h/\sqrt{2\pi m k_{\mathrm{B}}T}$.
In the limit of large particle numbers Stirling's approximation for the factorial in Eq. (2.21) can be used (see, e.g., Ref. [100]). Combining Eq. (2.20) with Eq. (2.21) then yields

$$F^{\mathrm{id}} = N k_{\mathrm{B}}T\big(\ln(\Lambda^3\rho) - 1\big)\,, \tag{2.22}$$

with the bulk number density $\rho = N/V$. This equation determines the equilibrium free energy for an ideal gas (non-interacting, point-like particles without external field).

Unfortunately, as systems become more complex or particles start to interact with each other, the partition function is an unknown quantity, as well as the free energy. In this case it is usual to split the free energy into an *ideal* and a so-called *excess part*, which originates from interparticle interactions,

$$F = F^{\mathrm{id}} + F^{\mathrm{exc}} \,. \tag{2.23}$$

The latter part is unknown in the first place and requires assumptions or approximations.

The grand canonical ensemble. In the $(T, V, \{\mu_\nu\})$ ensemble the probability density needs to include the chemical potentials weighted by the number of particles in the current configuration, i.e.,

$$\omega_{\mathrm{g}}(\mathbf{r}^N, \mathbf{p}^N, \{N_\nu\}) := \frac{\exp\left[-\beta\left(H_N - \sum_{\nu'=1}^{m} \mu_{\nu'} N_{\nu'}\right)\right]}{\Xi(T, V, \{\mu_\nu\})} \,, \tag{2.24}$$

where the grand canonical partition function for a multi-component system with a given composition $\{N_\nu\}$ and with $N = \sum N_{\nu'}$ is given by

$$\Xi(T, V, \{\mu_\nu\}) = \sum_{\{N_\nu\}=0}^{\infty} \prod_{\nu'=1}^{m} \frac{z_{\nu'}^{N_{\nu'}}}{N_{\nu'}!} \int_\Gamma \mathrm{d}\mathbf{r}^N \mathrm{d}\mathbf{p}^N \exp[-H_N/k_{\mathrm{B}}T] \,. \tag{2.25}$$

Here we have made use of the abbreviations of the short-cut sum and the definition of the fugacity $z_{\nu'}$

$$\sum_{\{N_\nu\}=0}^{\infty} = \sum_{N_1=0}^{\infty} \dots \sum_{N_m=0}^{\infty} \qquad ; \qquad z_{\nu'} = \exp[\mu_{\nu'}/k_{\mathrm{B}}T]/\Lambda_{\nu'}^3 \tag{2.26}$$

In opposite to the one-component ideal gas case from before the thermal De Broglie wavelength is now also species-dependent ($\Lambda_{\nu'} = h/\sqrt{2\pi m_{\nu'} k_{\mathrm{B}} T}$). Again, the partition function is connected to the potential via a logarithm, i.e., the *grand canonical potential*,

$$\Omega(T, V, \{\mu_\nu\}) = -k_{\mathrm{B}}T \ln\left[\Xi(T, V, \{\mu_\nu\})\right] . \tag{2.27}$$

2.4 Particle correlations

The statistical description of microscopic properties of a soft matter system can be a great tool for the investigation of macroscopic quantities. If one is interested in the equilibrium value of some quantity, it is necessary to average over every possible configuration of the system weighted by the corresponding probability of that state. Many observables only depend on a reduced set of particle coordinates, e.g., such as the average distribution

of two individual particle positions relative to each other. In the thermodynamic limit the averages of such observables can be compared within different ensembles. For large systems we assume the approximate identity

$$\langle \mathcal{O} \rangle_{\mathrm{c}} \approx \langle \mathcal{O} \rangle_{\mathrm{g}} \tag{2.28}$$

where the indices refer to the two ensembles from the previous paragraphs. Without loss of generality, we introduce statistical quantities solely within the canonical description. Grand canonical averages can be made analogously.

2.4.1 One-particle quantities

In a multi-component system of m species a one-particle quantity is for example an external potential, which can be applied to an initially homogeneous liquid. The energetic contribution from the external potential in the Hamiltonian (see Eq.(2.9)), is given by the complete set of N particles. For a given configuration $\mathbf{r}^N = \mathbf{r}^{N_1}, \ldots, \mathbf{r}^{N_m}$ it is the sum of the external potential energies of all particles

$$V_N^{\mathrm{ext}}(\mathbf{r}^N) = \sum_{\nu=1}^{m} \sum_{i=1}^{N_\nu} V_\nu^{\mathrm{ext}}(\mathbf{r}_{\nu,i}) = \sum_{\nu=1}^{m} \int \mathrm{d}\mathbf{r}\, \rho_\nu^\star(\mathbf{r}; \mathbf{r}^{N_\nu}) V_\nu^{\mathrm{ext}}(\mathbf{r})\,. \tag{2.29}$$

Here the function $V_\nu^{\mathrm{ext}}(\mathbf{r})$ is the external potential for species ν at position $\mathbf{r}$. This function is a one-particle quantity since it only depends on the coordinates of a single particle. $\rho_\nu^\star(\mathbf{r}; \mathbf{r}^{N_\nu}) = \sum_i^N \delta(\mathbf{r} - \mathbf{r}_{\nu,i})$ is the instantaneous density at point $\mathbf{r}$ (in general a sum of δ-distributions). Of course, with respect to the chosen ensemble one can perform the statistical averages (see, Eq. (2.17)), where the probability density can be simplified to the number density in this case

$$V_N^{\mathrm{ext}} = \langle V_N^{\mathrm{ext}}(\mathbf{r}^N) \rangle = \sum_{\nu=1}^{m} \int_V \mathrm{d}\mathbf{r} \rho_\nu(\mathbf{r}) V_\nu^{\mathrm{ext}}(\mathbf{r})\,. \tag{2.30}$$

Here we have introduced the average *one-particle density*

$$\rho_\nu(\mathbf{r}) = \langle \rho_\nu^\star(\mathbf{r}; \mathbf{r}^{N_\nu}) \rangle = \left\langle \sum_i \delta(\mathbf{r} - \mathbf{r}_{\nu,i}) \right\rangle . \tag{2.31}$$

The one-particle density can be referred to as an one-particle correlation if the external field is present. For example, we will study the sedimentation of particles within a standard gravitational field. The average density as well as the external field will depend only on one coordinate. Therefore, the density measures the "correlation" of the particles with the bottom of the sediment in dependence of their height.

2.4.2 Two-particle correlations

Correlations of two particles of species ν and ν' are described by the total pair correlation functions $h^{(2)}_{\nu\nu'}(\mathbf{r},\mathbf{r}')$, with $\mathbf{r}$ corresponding to the position of the particle of species ν and $\mathbf{r}'$ corresponding to the position of the particle of species ν'. These functions are connected to the one- and two-particle densities. The two particle density is similarly to Eq. (2.31) defined as

$$\rho^{(2)}_{\nu\nu'}(\mathbf{r},\mathbf{r}') = \left\langle {\sum_{i,i'}}' \delta\left(\mathbf{r}-\mathbf{r}_{\nu,i}\right)\delta\left(\mathbf{r}'-\mathbf{r}_{\nu',i'}\right)\right\rangle . \tag{2.32}$$

It is therefore a statistic average of the product of the two number densities $\rho^{\star}_{\nu}(\mathbf{r};\mathbf{r}^{N_\nu})$ and $\rho^{\star}_{\nu'}(\mathbf{r}';\mathbf{r}^{N_{\nu'}})$ and has the dimension of $[V^{-2}]$. Inside the averages of Eqs. (2.31) and (2.32) both relevant indices have been printed for clarity. The primed sum $\sum'_{i,i'}$ runs over Dirac-δ distributions for all position indices $i = 1 \dots N_\nu$ and $i' = 1 \dots N_{\nu'}$ of the respective species ν and ν', while it avoids terms with $i = i'$ for $\nu = \nu'$ (in words: only pairs of distinct particles are considered).

The *pair-correlation* is obtained via the two-particle density by dividing by the respective densities:

$$g^{(2)}_{\nu\nu'}(\mathbf{r},\mathbf{r}') := \frac{\rho^{(2)}_{\nu\nu'}(\mathbf{r},\mathbf{r}')}{\rho_\nu(\mathbf{r})\rho_{\nu'}(\mathbf{r}')} \tag{2.33}$$

and the *total correlation* function is

$$h^{(2)}_{\nu\nu'}(\mathbf{r},\mathbf{r}') = g^{(2)}_{\nu\nu'}(\mathbf{r},\mathbf{r}') - 1\,. \tag{2.34}$$

2.5 Potential of mean force (PMF)

In Sec. 2.3.3 the thermodynamic potentials have been introduced, which depend only on their corresponding thermodynamic variables. In reality it is observed, that individual subsets of particles are able to evolve or reconstruct in such a way, that intermediate and metastable states with larger free energy might be obtained locally. One can deal with such local events by making use of similar statistical assumptions as before, but constraining the system on a so-called *reaction coordinate* R. This reaction coordinate can be defined as a scalar function $R\big(\mathbf{r}^N,\mathbf{p}^N\big)$ [101]. In practice this means, that mostly all parameters can be integrated out, despite those, which the reaction coordinate depends on. A typical example for the reaction coordinate is $R = z$, i.e., the z-position of an arbitrary particle. Another typical example is the distance $R = |\mathbf{r}_\mathrm{A} - \mathbf{r}_\mathrm{B}|$ between two particles A and B.
In more general examples the reaction coordinate could depend on even more particle positions or momenta.

The practical usage will become clear later on. Let us first define the constrained probability density of finding the system in a state, where its reaction coordinate has the value R'. Here, we can write such a density as the product [101]

$$\omega_{\mathrm{R}}(\mathbf{r}^N, \mathbf{p}^N, R') = \omega(\mathbf{r}^N, \mathbf{p}^N)\delta(R' - R(\mathbf{r}^N, \mathbf{p}^N))\,, \tag{2.35}$$

where $\omega(\mathbf{r}^N, \mathbf{p}^N)$ is the usual probability density given by Eq. (2.18). We now redefine the free energy for the system along the reaction coordinate R' (as in Eq. (2.20)). The whole set of coordinates is constrained in such a way, that they are always aligned with the particular path along R'. In the statistical sense, this means, that the partition function is not fully evaluated. It rather depends on a set of coordinates, aligned with the reaction coordinate, i.e.,

$$Z_{\mathrm{R}}(T, V, \{N_\nu\}; R') = \frac{1}{h^{3N}\prod\limits_{\nu'} N_{\nu'}!}\int\limits_{\Gamma} \mathrm{d}\mathbf{r}^N \mathrm{d}\mathbf{p}^N\, \exp[-\beta H_N]\delta\big(R(\mathbf{r}^N, \mathbf{p}^N) - R'\big)\,. \tag{2.36}$$

Assuming, that also along this path, the system is always in a local equilibrium, the definition of a potential makes sense. For the $(T, V, \{N_\nu\}; R')$ ensemble we can define the *reduced Helmholtz free energy*, which does then depend on the reaction coordinate R', i.e.,

$$F_{\mathrm{R}}(R') = -k_{\mathrm{B}}T\ln(Z_{\mathrm{R}})\,. \tag{2.37}$$

This result can be easier understood by introducing the reaction-coordinate probability

$$P_{\mathrm{R}}(R') = \frac{\int_\Gamma \mathrm{d}\mathbf{r}^N \mathrm{d}\mathbf{p}^N\, \omega_{\mathrm{R}}(\mathbf{r}^N, \mathbf{p}^N, R')}{Z}\,. \tag{2.38}$$

Putting Eqs. (2.36) and (2.38) together, one can rewrite the reduced free energy from Eq. (2.37)

$$F_{\mathrm{R}}(R') = -k_{\mathrm{B}}T\ln\big(P_{\mathrm{R}}(R')\big) - k_{\mathrm{B}}T\ln(Z)\,. \tag{2.39}$$

Now, $P_{\mathrm{R}}(R')$ represents the probability of finding the system in a state along the reaction coordinate at the specific position R'. The second term on the right hand side represents a constant offset of the reduced free energy. Eq. (2.39) is also referred to as the *potential of mean force* (PMF).

Mean force as a function of z. For the purposes of this thesis the distance between a wall and an arbitrary particle is used as the reaction coordinate, i.e., the z-component of its position ($R \equiv z$). One can then calculate the mean force on a particle of species ν from Eq. (2.39). By partial differentiation one obtains

$$\mathbf{f}_\nu(z) \equiv k_{\mathrm{B}}T\nabla\ln\big(P_{\nu,\mathrm{z}}(z)\big) = k_{\mathrm{B}}T\mathbf{e}_{\mathrm{z}}\frac{\partial\ln\big(\rho_\nu(z)\big)}{\partial z}\,, \tag{2.40}$$

where we have identified the probability of finding a particle of species ν at position z with the one-particle density $\rho_\nu(z)$ (cf. Eqs. (2.31) and (2.38) for $R = z$). We also used the notation $\nabla = \big(\partial/\partial x\,, \partial/\partial y,\, \partial/\partial z\big)$ for the Nabla operator.

2.6 Density functional theory (DFT)

Walter Kohn, who received the Nobel prize in chemistry "for his development of the density-functional theory" (DFT), brought out a new theory, which was capable to calculate density-profiles as well as direct correlation functions. DFT is based upon the Euler-Lagrange equation, which is associated with the minimization of the grand potential energy functional. An abbreviated pathway of the soft matter version of the DFT will be described in the following section. The general pathway of this chapter follows the paper by R. Evans [102] and accordingly the third edition of the book "*Simple Liquids*" by J.-P. Hansen and I. R. McDonald [98].

2.6.1 Functional derivatives

A functional is a mathematical function that can be used for variational calculus [103]. It is a mapping from a vector to scalar numbers. In practice, it assigns a whole function (or vector) $a(\mathbf{r})$, e.g., such as the density, a unique number $A[a(\mathbf{r})] \in \mathbb{R}$, which for example represents the energy of the respective density field.
The functional derivative defines the change of the functional with respect to a change in the vector that it depends on. Assuming, that $a(\mathbf{r})$ is changed by an infinitesimal $\epsilon b(\mathbf{r})$, where $a(\mathbf{r})$ and $b(\mathbf{r})$ are two particular functions out of the vector space of the functional, the *functional derivative* is defined as the integral [103]

$$\lim_{\epsilon \to 0} \frac{A[a(\mathbf{r}) + \epsilon b(\mathbf{r})] - A[a(\mathbf{r})]}{\epsilon} = \int \mathrm{d}\mathbf{r}' \, \frac{\delta A}{\delta a(\mathbf{r}')} b(\mathbf{r}') \,. \tag{2.41}$$

From this definition we can evaluate the limit on the left hand side and obtain the *functional differential*

$$\delta A[a(\mathbf{r}); b(\mathbf{r})] = \int \mathrm{d}\mathbf{r}' \, \frac{\delta A}{\delta a(\mathbf{r}')} b(\mathbf{r}') \,, \tag{2.42}$$

where formally, the first argument determines the derivative coordinate and the second argument is treated as the small change of the first argument, i.e., $b(\mathbf{r}) \equiv \delta a(\mathbf{r})$.
There exist some mathematical rules, which will be used within this work to derive final equations. The necessary tools (Eqs.(2.43), (2.44), (2.48)) are listed below.
Firstly, the chain rule reads [103]

$$\frac{\delta A}{\delta a(\mathbf{r})} = \int \mathrm{d}\mathbf{r}' \, \frac{\delta A}{\delta b(\mathbf{r}')} \frac{\delta b(\mathbf{r}')}{\delta a(\mathbf{r})} \,, \tag{2.43}$$

where for the special case $b(\mathbf{r}) = a(\mathbf{r})$ the functional derivative in the integral leads to a delta peak

$$\frac{\delta a(\mathbf{r})}{\delta a(\mathbf{r}')} = \delta(\mathbf{r} - \mathbf{r}') \,. \tag{2.44}$$

A second special case is given by the explicit functional definition

$$A[a(\mathbf{r})] = \int_V \mathrm{d}\mathbf{r}'\, a(\mathbf{r}')\, \ln\left[a(\mathbf{r}')\right] \,. \tag{2.45}$$

Its differential form can be written as

$$\delta A[a(\mathbf{r})] = \int_V \mathrm{d}\mathbf{r}'\, \left(\delta a(\mathbf{r}')\, \ln\left[a(\mathbf{r}')\right] + a(\mathbf{r}')\delta \ln\left[a(\mathbf{r}')\right]\right) \,. \tag{2.46}$$

The infinitesimal change in the term $\ln[a(\mathbf{r})]$ can be simplified,

$$\begin{aligned} \delta \ln[a(\mathbf{r})] &= \ln\left[a(\mathbf{r}) + \delta a(\mathbf{r})\right] - \ln[a(\mathbf{r})] = \ln\left[\frac{a(\mathbf{r}) + \delta a(\mathbf{r})}{a(\mathbf{r})}\right] \\ &\approx \frac{\delta a(\mathbf{r})}{a(\mathbf{r})} \,. \end{aligned} \tag{2.47}$$

A derivative of the functional in Eq. (2.45) follows by combining Eqs.(2.46) and (2.47):

$$\frac{\delta \int \mathrm{d}\mathbf{r}'\, a(\mathbf{r}')\, \ln\left[a(\mathbf{r}')\right]}{\delta a(\mathbf{r})} = \ln\left[a(\mathbf{r})\right] + 1 \,. \tag{2.48}$$

2.6.2 Functionals in classical systems

Although it is often convenient to first only describe bulk cases of the theories, it turns out, that in the derivation of DFT the general case can be discussed, including the assumption of an external field (e.g., such as confining walls). To separate the explicit impact of the external field from the equations two new quantities will be introduced: The first one is the *intrinsic free energy* $\mathcal{F}$, which is used in the canonical ensemble to measure the free energy with all *implicit* dependencies of the external field included, but all *explicit* dependencies being excluded. The second one is the *intrinsic chemical potential* ψ, where the explicit contribution of the external field is subtracted from the chemical potential.
In a situation, where the number of particles is preserved and the system is in equilibrium, the *Helmholtz free energy* is minimized, as discussed in Sec. 2.1. One can write the free energy as a unique functional of the density (with the other thermodynamic parameters $(T, V, \{N_\nu\})$ being fixed)[4],

$$F[\{\rho_\nu\}] \equiv F[\{\rho_\nu\}; T, V, \{N_\nu\}] \,. \tag{2.49}$$

Consequently, when the number of particles is not fixed, but the system is rather connected to a bath with constant chemical potentials $\{\mu_\nu\}$, the set of natural thermodynamic

[4]Please note, that this is not a trivial statement. For a complete and well-written proof of this assumption see Ref. [98].

variables changes from $(T, V, \{N_\nu\})$ to $(T, V, \{\mu_\nu\})$ and the minimizing thermodynamic potential is now determined by the *grand (canonical) potential*. Its functional form reads via Legendre transformation of Eq. (2.49)

$$\Omega[\{\rho_\nu\}] = F[\{\rho_\nu\}] - \sum_{\nu'} N_{\nu'}\mu_{\nu'} \tag{2.50}$$

$$= \mathcal{F}[\{\rho_\nu\}] + \sum_{\nu'} \int_V \mathrm{d}\mathbf{r}\, \rho_{\nu'}(\mathbf{r}) V_{\nu'}^{\mathrm{ext}}(\mathbf{r}) - \sum_{\nu'} N_{\nu'}\mu_{\nu'} \tag{2.51}$$

with

$$\mathcal{F}[\{\rho_\nu\}] = F[\{\rho_\nu\}] - \sum_{\nu'} \int_V \mathrm{d}\mathbf{r}\, \rho_{\nu'}(\mathbf{r}) V_{\nu'}^{\mathrm{ext}}(\mathbf{r}) \tag{2.52}$$

being the *intrinsic free energy*, where explicit impact from the external potential has been subtracted. Analogously, one can define the *intrinsic chemical potential*

$$\psi_{\nu'}\left(\mathbf{r}'; [\{\rho_\nu\}]\right) = \mu_{\nu'} - V_{\nu'}^{\mathrm{ext}}(\mathbf{r}')\,, \tag{2.53}$$

which has contrarily to the chemical potential (in equilibrium) an explicit dependency on the position and a functional dependence on the densities. Due to the particle interactions and the implicit effect of the external potential both intrinsic functions are in general unknown. Therefore, in analogy with Eq. (2.23), the intrinsic free energy can be split into two parts

$$\mathcal{F}[\{\rho_\nu\}] = \mathcal{F}^{\mathrm{id}}[\{\rho_\nu\}] + \mathcal{F}^{\mathrm{exc}}[\{\rho_\nu\}]\,, \tag{2.54}$$

where again $\mathcal{F}^{\mathrm{id}}$ is the *ideal gas* part and $\mathcal{F}^{\mathrm{exc}}$ is the over-ideal *excess* part. Assuming, that the considered system contains only ideal gas particles (without interactions), the second part vanishes. The first one (ideal part) is written in terms of a local representation of Eq. (2.22), where the constant prefactor N is rewritten as an integral over the in general inhomogeneous density, i.e.,

$$\mathcal{F}^{\mathrm{id}}[\{\rho_\nu\}] = k_{\mathrm{B}}T \sum_{\nu'} \int_V \mathrm{d}\mathbf{r}'\, \rho_{\nu'}(\mathbf{r}') \left(\ln(\Lambda_{\nu'}^3 \rho_{\nu'}(\mathbf{r}')) - 1\right)\,. \tag{2.55}$$

2.6.3 DFT iteration equation

As the second tag of the theory's name already suggests, the variational principle is used within the functional forms of the equilibrium potential in both ensembles (grand canonical, canonical). Originally DFT has been described in the grand canonical ensemble, where the natural variables are $(T, V, \{\mu_\nu\})$. In order to find the equilibrium state for these fixed parameters, one can write the grand potential as a functional of the density, or in general of the probability density ω. Note, that ω denotes a general probability density and not necessarily the equilibrium one. It shall be used to determine the equilibrium

state ω^{eq}. Following the work by N. D. Mermin [104], it is assumed, that for an arbitrary ω Eq. (2.24) holds. Although this is in general not the case, this pathway gives access to a variation procedure, where the equilibrium configuration ω^{eq} as an input yields the equilibrium grand potential, i.e., $\Omega^{\mathrm{eq}} = \Omega[\omega^{\mathrm{eq}}]$. For our purposes the functional should not be minimized with respect to the whole probability density ω but only on the densities ρ_ν, since otherwise it would lead to an unsolvable problem with a huge set of parameters.

Of course, the functional in Eq. (2.51) only coincides with the equilibrium grand potential of Eq. (2.27), when $\{\rho_\nu(\mathbf{r})\} = \{\rho_\nu^{\mathrm{eq}}(\mathbf{r})\}$ holds. All functional derivatives of the grand potential with respect to general density profiles ρ_ν, evaluated at equilibrium ρ_ν^{eq}, must be zero due to the minimization principle [104], i.e.,

$$0 = \left.\frac{\delta\Omega[\{\rho_\nu(\mathbf{r})\}]}{\delta\rho_{\nu'}(\mathbf{r}')}\right|_{\{\rho_\nu\}=\{\rho_\nu^{\mathrm{eq}}\}} \tag{2.56}$$

and also via Legendre transformation for the intrinsic free energy

$$0 = \left.\frac{\delta\mathcal{F}[\{\rho_\nu(\mathbf{r})\}]}{\delta\rho_{\nu'}(\mathbf{r}')}\right|_{\{\rho_\nu\}=\{\rho_\nu^{\mathrm{eq}}\}} - \mu_{\nu'} + V_{\nu'}^{\mathrm{ext}}(\mathbf{r}')\,. \tag{2.57}$$

The latter two equations are the fundamental DFT equations. In order to make them applicable for soft matter systems, one has to go back to previous results and plug in the split-up of the intrinsic free energy (Eq. (2.54)) into Eq. (2.57).
After using the differentiation rule from Eq. (2.48) for Eq. (2.55) we obtain the partial functional derivative of the ideal part,

$$\frac{\delta\mathcal{F}^{\mathrm{id}}[\{\rho_\nu(\mathbf{r})\}]}{\delta\rho_{\nu'}(\mathbf{r}')} = k_{\mathrm{B}}T\,\ln\left[\Lambda_{\nu'}^3\rho_{\nu'}(\mathbf{r}')\right] \tag{2.58}$$

and the partial functional derivatives of the yet unknown excess part of the intrinsic free energy, which are known as the so-called *direct correlation functions*. The first two members of these direct correlations read

$$c_{\nu'}^{(1)}(\mathbf{r}';[\{\rho_\nu\}]) = -\beta\frac{\delta\mathcal{F}^{\mathrm{exc}}[\{\rho_\nu\}]}{\delta\rho_{\nu'}(\mathbf{r}')}\,, \tag{2.59}$$

$$c_{\nu'\nu''}^{(2)}(\mathbf{r}',\mathbf{r}'';[\{\rho_\nu\}]) = -\beta\frac{\delta^2\mathcal{F}^{\mathrm{exc}}[\{\rho_\nu\}]}{\delta\rho_{\nu'}(\mathbf{r}')\delta\rho_{\nu''}(\mathbf{r}'')}\,. \tag{2.60}$$

Assuming, that the excess part of the functional (or the first member of the direct correlations) is known exactly, one can determine any higher order of particle correlations.

However, by putting Eqs. (2.57), (2.58) and (2.59) together, one can formally solve for the density profile by inverting the logarithm

$$\rho_{\nu'}^{(\mathrm{eq})}(\mathbf{r}') = z_{\nu'}\exp\left(-\beta V_{\nu'}^{\mathrm{ext}}(\mathbf{r}') + c_{\nu'}^{(1)}(\mathbf{r}';[\{\rho_\nu^{(\mathrm{eq})}\}])\right)\,, \tag{2.61}$$

with the same definition of the fugacity as before (Eq. (2.26)). This result is an implicit equation for ρ^{eq}, since the direct correlation functions themselves depend on equilibrium density profiles.

What remains, is to find an approximation for the free energy functional. There exist many different approaches for this. For example, one approach was proposed by T.V. Ramakrishnan and M. Yussouff [105] or by the *mean field approximated density functional* (MFA DF) in which it is assumed, that the particles are very soft, such that entropic contributions can be fully neglected [106]. In this case the excess part of the functional is given only by the respective mean field, i.e., the integration over the pair-interaction weighted with the respective densities,

$$\mathcal{F}^{\mathrm{exc}}\big[\{\rho_\nu\}\big] \overset{\text{MFA DF}}{\approx} \frac{1}{2}\sum_{\nu',\nu''}\int \mathrm{d}\mathbf{r}' \int \mathrm{d}\mathbf{r}''\rho_{\nu'}(\mathbf{r}')\rho_{\nu''}(\mathbf{r}'')v_{\nu'\nu''}(|\mathbf{r}'-\mathbf{r}''|)\,, \tag{2.62}$$

where $v_{\nu'\nu''}$ is the pair interaction potential between species ν' and ν''. This is of course a very poor approximation and mostly only applicable for dilute systems or soft particles, which is undesired for our purposes.
Probably one of the most promising approaches for hard bodies is the so-called *fundamental measure theory* (FMT), which relies upon the deconvolution of the particle interactions into their "fundamental measures", such as their position, their surface and their volume. In the next section, the FMT will be introduced and other possible approximations for the excess free energy are mentioned. Later, in section 5.3, the DFT with FMT will be applied for a special anisotropic case, where correlations are neither homogeneous nor isotropic.

However, let us for a moment assume, that the excess free energy is known (at least approximately). A one-step calculation of the right hand side of Eq. (2.61) cannot be carried out straight forward. The mechanism to solve this formal DFT-equation or other transcendental equations is based on an iteration scheme. Such an iteration scheme will now shortly be sketched, before returning to the approximations for the unknown excess part.

2.6.4 Fixed point iterations

The iterative solution of non-linear equalities as in Eq. (2.61) can be regarded as a so-called *fixed point problem*

$$\{\mathbf{a}_n\} \mapsto \mathbf{T}(\{\mathbf{a}_n\})\,, \tag{2.63}$$

where the right-hand-side is iteratively evaluated and the result is successively used as a new input for the next iteration step. Here, $\{\mathbf{a}_n\}$ is the series of vectors, that have been iterated and $\mathbf{T}(\ldots)$ is the function, which provides the next iteration step. The key idea behind this is, that the newly mapped vector is a better approximation of the actual solution of the equation. Such mapping techniques can sometimes be implemented by

direct *Picard iteration*, or more likely *Krasnoselskij iteration* [107]. In these two methods, the function $\mathbf{T}$ does only depend on the last iteration vector, i.e.,

$$\mathbf{a}_{n+1} = \lambda \mathbf{T}(\mathbf{a}_n) + (1-\lambda) a_n \,, \tag{2.64}$$

where $\lambda \in [0,1]$ and $\lambda = 1$ in the case of Picard iteration.

Sometimes it is needed due to stability and performance problems, to implement more complicated techniques. In any case, the sequence of vectors

$$\mathbf{a}_0,\, \mathbf{a}_1 = \mathbf{T}(\mathbf{a}_0),\, \ldots,\, \mathbf{a}_{n+1} = \mathbf{T}(\{\mathbf{a}_n\}),\, \ldots$$

may converge or not. A powerful mathematical theorem states, that, if $\mathbf{T} : A \to A$ is a *contraction self-mapping*[5] in the sense of

$$\lim_{n\to\infty} \|\mathbf{a}_{n+1} - \mathbf{a}_n\| = 0 \,, \tag{2.65}$$

any such sequence converges to a unique solution. This statement is called *Banach's fixed-point theorem*. Although the requirements are a priori not provable for a certain problem, the theorem nevertheless provides the possibility to measure by the norm in Eq. (2.65) the convergence of the iterative scheme in DFT-like equations or even more complicated integral equations [108], e.g., such as the Ornstein Zernike (OZ) relation that will be introduced later. We will see, that the OZ relation can be used to transform the direct correlation functions $c^{(n)}$ into the more illustrative total correlation functions $h^{(n)}$.

Besides the very easy linear fixed point iteration, which was presented above, there are also other types of iteration schemes, which for example use the history of the last few iteration steps in order to improve the convergence for the next iteration step. One very important method it the *direct inversion in the iterative subspace* (DIIS), in which the norm between the actual and the last step shall be minimized with respect to the iteration history. A short description of the algorithm is given in Appendix A.1. It increases the degree of convergence and the overall stability of the algorithm. Such special procedures are not always needed for the DFT iterations. Only at high densities DIIS might be inevitable to apply them. It is also suitable for the fix point iterations in our integral equation theory (the OZ relation), which will be introduced in Sec. 2.8.

2.7 Fundamental Measure Theory (FMT)

DFT is a great tool to inspect classical many-body systems and calculate thermodynamic quantities. But the remaining challenge is to find an appropriate expression for the excess free energy.

[5] For further details please see Refs [107] or [108].

In 1989 the Fundamental Measure Theory (FMT) has been published for hard-sphere mixtures in a famous paper by Y. Rosenfeld [109]. Since then a lot of development has been made. In a review paper by R. Roth [110] from 2010 the major milestones are nicely itemized. Although in this thesis, only a special version of the excess free energy functional is used, namely the *White Bear mark II* version [76], the most basic points of the origin and foundation of FMT will shortly be sketched in this section along with other possible approximations. The steps that are presented within this section are the following:

First, the virial expansion of the excess free energy is identified with integrals over distinct pairs of so-called Mayer-f correlation functions. This expansion is truncated after the third order, such that it only represents a good solution for low densities and becomes only exact in the low-density limit. Next, the decomposition of the integrands of the above-mentioned functional is presented, namely the decomposition of the Mayer-f functions into so-called *weight functions* $\omega_\nu^{(\alpha)}$. Consequently, it is shown, how the weight functions are used to generate the so-called *weighted densities* n_ν by simple integration with the local densities ρ_ν. These weighted densities can then be inserted into the expression for the excess free energy in order to obtain the functional expression in the low-density limit. Finally, using the excess free energy for the low density limit as a motivation, it will be shown, how the weighted densities can be used as a set of basis functions to extrapolate towards higher densities. We will see, that for this step the famous Caranahan-Starling equation of state [111] and its extended versions [112–114] can be used as approximations for higher densities.

The fundamental measures are defined in three spatial dimensions by all sub-spaces with an Euler-characteristic being equal or lower than three. They are therefore given by *volume terms* (3D), *surface terms* (2D), *distances* (1D), and *curvatures* (0D). FMT stems from the idea, that the so-called Mayer-f function [115, 116] can be expressed in terms of fundamental measures. The Mayer-f-function is for an isotropic pair potential of interacting particles given by

$$f_{\nu\nu'}(r) = \exp[-\beta v_{\nu\nu'}(r)] - 1\,, \tag{2.66}$$

where for hard spheres $v_{\nu\nu'} = \infty$, if the particles are overlapping, and zero otherwise. The reason, why the Mayer-f function has been introduced, is, because J.E. Mayer and E. Montroll found out that it can be used to expand the intrinsic excess free energy in terms of the density [115]. The expansion reads [110, 115]

$$\begin{aligned}\beta\mathcal{F}^{\mathrm{exc}}\big[\{\rho_\nu\}\big] = &-\frac{1}{2}\sum_{\nu',\nu''}\int \mathrm{d}\mathbf{r}'\int \mathrm{d}\mathbf{r}''\rho_{\nu'}(\mathbf{r}')\rho_{\nu''}(\mathbf{r}'')f_{\nu'\nu''}(|\mathbf{r}'-\mathbf{r}''|) \\ &-\frac{1}{6}\sum_{\nu'\nu''\nu'''}\int \mathrm{d}\mathbf{r}'\int \mathrm{d}\mathbf{r}''\int \mathrm{d}\mathbf{r}'''\rho_{\nu'}(\mathbf{r}')\rho_{\nu''}(\mathbf{r}'')\rho_{\nu'''}(\mathbf{r}''') \\ &\qquad\times f_{\nu'\nu''}(|\mathbf{r}'-\mathbf{r}''|)f_{\nu'\nu'''}(|\mathbf{r}'-\mathbf{r}'''|)f_{\nu''\nu'''}(|\mathbf{r}''-\mathbf{r}'''|) \\ &+\mathcal{O}(\rho^4)\end{aligned} \tag{2.67}$$

The expansion truncated after the second order is an approximation that is suitable for low densities or high densities and soft potentials. We can identify the connection to the MFA DF (Eq. (2.62)) by inserting the approximate Mayer-f function

$$f_{\nu\nu'} = \exp(-\beta v_{\nu\nu'}) - 1 \approx -\beta v_{\nu\nu'} \tag{2.68}$$

into the expansion (Eq.(2.67)) and truncating it after the first term.

Virial series. For better approximations one has to acknowledge more terms from the series of Eq. (2.67). First, it provides a general formulation[6] that is in principle valid for any interaction potential. Second, the series is applicable to any externally perturbed system, where the external field is only incorporated implicitly. But for the special case, when there is truly no external field acting on the system, one can assume that the densities are homogeneous and therefore constant. Consequently, they can be pulled out of the integrals from Eq. (2.67). The remaining terms can then be identified with the virial coefficients, where the first coefficient equals zero and the next coefficients read

$$B^{(2)}_{\nu\nu'} = -\frac{1}{2V}\int \mathrm{d}\mathbf{r}\int \mathrm{d}\mathbf{r}' f_{\nu\nu'}(|\mathbf{r}-\mathbf{r}'|) \tag{2.69}$$

$$B^{(3)}_{\nu\nu'\nu''} = -\frac{1}{3V}\int \mathrm{d}\mathbf{r}\int \mathrm{d}\mathbf{r}'\int \mathrm{d}\mathbf{r}'' f_{\nu\nu'}(|\mathbf{r}-\mathbf{r}'|) f_{\nu\nu''}(|\mathbf{r}-\mathbf{r}''|) f_{\nu'\nu''}(|\mathbf{r}'-\mathbf{r}''|) \tag{2.70}$$

$$B^{(4)}_{\nu\nu'\nu''\nu'''} = \cdots \tag{2.71}$$

From the coefficients $B^{(i)}$ one can already see the reason, why the previous expansion from Eq. (2.67) becomes accurate in the low-density limit: correlations between three (as regarded by Eq. (2.70)) or more particles are negligible in this limit and the expansion can be truncated.

Homogeneous case – virial series. By means of the series expansion of the excess free energy functional, it is possible to obtain the common *virial series*. In the case of a bulk monodisperse hard-sphere mixture with density $\bar{\rho} = N/V$ and the particle diameter σ, one can use the thermodynamic relation $p = \partial F/\partial V|_{T,N}$[7] to write down such a series, multiply it by β and divide by the density, such that the dimensionless so-called *equation of state* (EOS) is obtained. It reads

$$z_{\mathrm{EOS}} = \frac{\beta p}{\bar{\rho}} = \frac{\beta}{\bar{\rho}}\left.\frac{\partial F^{\mathrm{exc}}}{\partial V}\right|_{T,N} = 1 + \sum_{i=2}^{\infty}\left(\frac{6}{\pi\sigma^3}\right)^{i-1} B^{(i)}\phi^i \tag{2.72}$$

$$= 1 + 4\phi + 10\phi^2 + 18.365\phi^3 + 28.225\phi^4 + \dots\,, \tag{2.73}$$

with the packing fraction $\phi = \pi\sigma^3/6$. In the above equation the first few virial coefficients have been evaluated approximately by E.J Janse van Rensburg [117].

[6] For further reading see sections 3.4-3.9 from Ref. [98] about the *cluster expansion*.

[7] Note, that the excess free energy equals the intrinsic excess free energy for the bulk.

General case – FMT for low densities. In the general case Eq. (2.67) represents a virial expansion, where the densities cannot be pulled out of the integrals. Additionally, the number of considered orders in the density will increase the accuracy with increasing density.

The remarkable notice by Rosenfeld was, that the Mayer-f function of spherical hard bodies could be decomposed in odd dimensions into the above-mentioned weight functions[8]. If one defines the convolution $y_1 \circ y_2$ of two functions as

$$(y_1 \circ y_2)(\mathbf{r} - \mathbf{r}') = \int \mathrm{d}\mathbf{r}''\, y_1(\mathbf{r}'' - \mathbf{r}) y_2(\mathbf{r}'' - \mathbf{r}')\,, \tag{2.74}$$

then the deconvolution of the Mayer-f function in three spatial dimensions reads

$$\begin{aligned} -f_{\nu\nu'}(r) = \quad & \omega_\nu^{(3)} \circ \omega_{\nu'}^{(0)} + \omega_\nu^{(0)} \circ \omega_{\nu'}^{(3)} \\ & + \omega_\nu^{(2)} \circ \omega_{\nu'}^{(1)} + \omega_\nu^{(1)} \circ \omega_{\nu'}^{(2)} \\ & + \omega_{\nu'}^{(2)} \circ \omega_{\nu'}^{(1)} + \omega_{\nu'}^{(1)} \circ \omega_{\nu'}^{(2)}\,, \end{aligned} \tag{2.75}$$

where now the *weight functions* have been introduced. They are given by [109]

$$w_\nu^{(3)}(\mathbf{r}) = \Theta(R_\nu - |\mathbf{r}|) \tag{2.76}$$

$$w_\nu^{(2)}(\mathbf{r}) = \delta(R_\nu - |\mathbf{r}|) \tag{2.77}$$

$$w_\nu^{(1)}(\mathbf{r}) = \frac{1}{4\pi R_\nu}\delta(R_\nu - |\mathbf{r}|) \tag{2.78}$$

$$w_\nu^{(0)}(\mathbf{r}) = \frac{1}{4\pi R_\nu^2}\delta(R_\nu - |\mathbf{r}|) \tag{2.79}$$

$$\mathbf{w}_\nu^{(2)}(\mathbf{r}) = \frac{\mathbf{r}}{|\mathbf{r}|}\delta(R_\nu - |\mathbf{r}|) \tag{2.80}$$

$$\mathbf{w}_\nu^{(1)}(\mathbf{r}) = \frac{\mathbf{r}}{|\mathbf{r}|}\frac{1}{4\pi R_\nu}\delta(R_\nu - |\mathbf{r}|) \tag{2.81}$$

with the particle radius $R_\nu = \sigma_\nu/2$ and the Heaviside step function

$$\Theta(x) = \begin{cases} 0 & , \quad x < 0 \\ 1 & , \quad x \geq 0 \end{cases}\,. \tag{2.82}$$

It should be noted, that this deconvolution is not a unique one. One year after Rosenfeld, in 1990, the authors E. Kierlik and M.L. Rosinberg found another deconvolution, which does not incorporate any vectorial components at all [119]. Both approaches are equivalent.

[8] The original paper by Rosenfeld [109] had a inconsistency in the actual definition of the convolution, which would cause a sign change in the equation of the deconvolution. This mistake has been corrected later [118].

Now, going back to the low density functional of Eq. (2.67), one can define the weighted densities[9]

$$n_\alpha(\mathbf{r}) = \sum_{\nu=1}^{n} \int_V \rho_\nu(\mathbf{r}') w_\nu^{(\alpha)}(\mathbf{r}-\mathbf{r}') d\mathbf{r}' \,, \tag{2.83}$$

that "weight" the actual microscopic densities ρ_ν with the above introduced weight functions. Via the presented deconvolution the weighted densities can be identified in the low-density expansion, i.e., the truncation of Eq. (2.67) after the first term. It is given by

$$\beta\mathcal{F}^{\text{exc}}\left[\{\rho_\nu\}\right] = \int \mathrm{d}\mathbf{r}\left(n_0(\mathbf{r})n_3(\mathbf{r}) + n_1(\mathbf{r})n_2(\mathbf{r}) - \mathbf{n}_1(\mathbf{r})\cdot\mathbf{n}_2(\mathbf{r})\right) . \tag{2.84}$$

General case – FMT for higher densities. Equation 2.84 was a very important milestone in the history of FMT, since it gave rise to the idea, what an actual approximate expression for the intrinsic free energy should be built of. Although it is strictly mathematically derived, it cannot be applied for higher densities, contrarily to heuristic or empirical findings, e.g., such as the *Caranahan-Starling* (CS) virial equation of state [111] or its improved version, the Boublík-Mansoori-Carnahan-Starling-Leland (BMCSL) equation of state [112, 113].

These equations turned out to be well-suited for the prediction of compressibilities of HS mixtures, even in the regime of high densities. The hour of birth of the CS equation was in 1969, when N.F. Carnahan and K.E. Starling had recognized that one could approximately replace the series of virial coefficients $B^{(i)}$ of a hard-sphere (HS) system by an infinite series of integers, such that a simple formula would come out. The virial coefficients, on which the final formula is based on, is obtained by using a mixture of 2/3 of the solution of the so-called Percus-Yevick (PY) integral equation [120] via the compressibility route and 1/3 of the solution via the pressure route[10]. The formula is until today a very accurate and well accepted approximation for the HS fluid. It reads for the homogeneous and one-component case [111]

$$z_{\text{CS}}(\phi) := \frac{\beta p}{\bar{\rho}} = \frac{1+\phi+\phi^2-\phi^3}{(1-\phi)^3} \,. \tag{2.85}$$

For the two-component case the *extended* BMCSL-equation [112, 113] is used. It depends on the particle diameters σ_ν, the dimensionless concentrations $x_\nu = \rho_\nu/(\rho_1+\rho_2)$, and on the total packing fraction $\phi = \phi_1 + \phi_2$ and reads [114]

$$z_{\text{eCS}} := \frac{1}{1-\phi} + \frac{3\phi}{(1-\phi)^2}\frac{\xi_1\xi_2}{\xi_3} + \frac{\phi^2(3-\phi)}{(1-\phi)^3}\frac{\xi_2^3}{\xi_3^2} + \frac{\phi^3}{(1-\phi)^3}\frac{\xi_2}{\xi_3^2}(\xi_1\xi_3-\xi_2^2) \,, \tag{2.86}$$

[9] Note, that this definition of the weighted densities also holds for the vectorial weights, e.g. $\mathbf{n}_1(\mathbf{r}) = \sum_{\nu'} \int \mathrm{d}\mathbf{r}' \rho_{\nu'}(\mathbf{r}') \omega_{\nu'}^{(1)}(\mathbf{r}-\mathbf{r}')$.

[10] The original PY solution was proposed by J.K. Percus and G.J. Yevick [120]. Their proposition of the HS solution was later used by other authors [121, 122] to evaluate the virial coefficients.

with the abbreviations $\xi_i = x_1\sigma_1^i + x_2\sigma_2^i$.

Coming back to the actual problem, the inconvenience of FMT as presented so far is, that it can only be applied for very low densities. On the other hand, the above presented heuristic equations of state hold up to higher densities. Therefore, it is an excellent step to extrapolate the low-density limit from Eq. (2.84) in such a way that the extrapolation towards higher densities goes along with the heuristic equations.

In each FMT the basic approach is always the same [109,110]. One expresses the intrinsic excess free energy as an integral over the local excess free energy density $\Phi\left[\{n_\nu\}\right]$, which itself is a functional of the weighted densities, as defined in Eq. (2.83). The relation reads

$$\beta\mathcal{F}^{\text{exc}}[\{\rho_\nu\}] = \int_V \Phi\left[\{n_\nu(\mathbf{r})\}\right] \mathrm{d}\mathbf{r}. \tag{2.87}$$

Using the low-density ansatz as a starting point and extrapolating towards higher densities leads to different versions of the FMT. In Rosenfeld's paper from 1989, he presents the course of doing this [109]:

> "*Note that* n_0, $n_1 n_2$, n_2^3, $\mathbf{n}_1 \cdot \mathbf{n}_2$, *and* $n_2(\mathbf{r}_2 \cdot \mathbf{n}_2)$ *are the only five positive power (to yield a virial expansion) combinations of* $\{n_\alpha\}$ $[\ldots]$ *providing the basis for expressing* Φ $[\ldots]$ *with dimensionless,* n_3*-dependent, coefficients.*"

This perception was the result of combining the mathematical formalism of FMT (deconvolution of the Mayer-f function) with thermodynamic equations (for the pressure). Rosenfeld managed to put both together, which led to a system of five differential equations, that will not be discussed in detail[11]. However, with the solution of the set of equations, he could state, that any FMT-functional density $\Phi[\{n_\nu\}]$ must therefore be a representation in the basis functions n_ν, that are listed in the quotation. The coefficients must only be dependent on n_3.

There were slight problems within the first version of Rosenfelds functional, which for example led to a divergence of the functional in the exact zero- or one-dimensional limit [123]. These so-called "*lost cases*" were fixed by later propositions: one should especially mention the extended deconvolution FMT (edFMT) for anisotropic convex shaped hard particles [124] and the White Bear [125] and White Bear mark II [76] versions for hard spheres, which typically include tensorial corrections to recover the exact zero-dimensional limit of extremely confined systems. These tensorial corrections must of course be formulated on the lowest level of the FMT, namely the weight functions. Following Refs. [123,126], the correction to get the desired approximation of the functional is given by the additional tensorial weight

$$\overset{\leftrightarrow}{w}_\nu^{(2)}(\mathbf{r}) = \left(\frac{\mathbf{r}\cdot\mathbf{r}^T}{|\mathbf{r}|^2} - \frac{\overset{\leftrightarrow}{\mathrm{I}}}{3}\right)\delta(R_\nu - |\mathbf{r}|), \tag{2.88}$$

[11] For the actual solutions of the differential equations, see Eqs.(5) et seq. from Ref. [109].

where $\overset{\leftrightarrow}{\mathrm{I}}$ is the 3D unity matrix and $\mathbf{r}^T$ is the transposed of $\mathbf{r}$.

For this thesis the White Bear mark II (WBII) version with the tensorial correction has been chosen, because it has accurately predicted not only the freezing transition in hard spheres [127] but also phase coexistence and the involved crystal-fluid interface [128]. Its excess free energy density reads

$$\begin{aligned}\Phi^{\mathrm{WBII}}[\{n_\nu\}] = &-\log(1-n_3)n_0 \\ &+\left(1+\frac{1}{9}n_3^2\phi_2^{\mathrm{WBII}}(n_3)\right)\frac{n_1n_2-\mathbf{n}_1\cdot\mathbf{n}_2}{1-n_3} \\ &+\left(1-\frac{4}{9}n_3\phi_3^{\mathrm{WBII}}(n_3)\right) \\ &\times\frac{n_2^3-3n_2\mathbf{n}_2\cdot\mathbf{n}_2+\frac{9}{2}\left(\mathbf{n}_2^t\cdot\overset{\leftrightarrow}{n}_2\cdot\mathbf{n}_2-\mathrm{tr}(\overset{\leftrightarrow}{n}_2^3)\right)}{24\pi(1-n_3)^2},\end{aligned} \tag{2.89}$$

with $\mathrm{tr}(\overset{\leftrightarrow}{A})$ denoting the trace of the argument $\overset{\leftrightarrow}{A}$ and the two functions $\phi_2^{\mathrm{WBII}}(n_3)$ and $\phi_3^{\mathrm{WBII}}(n_3)$ are defined by

$$\phi_2^{\mathrm{WBII}}(n_3) = \frac{6n_3-3n_3^2+6(1-n_3)\log(1-n_3)}{n_3^3}, \tag{2.90}$$

$$\phi_3^{\mathrm{WBII}}(n_3) = \frac{6n_3-9n_3^2+6n_3^3+6(1-n_3)^2\log(1-n_3)}{4n_3^3}\,. \tag{2.91}$$

In Eqs. (2.89) one can nicely distinguish between the basis system of functions, that have been postulated by Rosenfeld (including the tensorial correction), and the coefficients of these functions.

As we state in the submitted paper [2], for all FMT functionals with an excess free energy density that only depends on the weighted densities n_α, the direct pair correlation functions from Eq. (2.60) can be written as

$$-c^{(2)}_{\nu\nu'}(\mathbf{r},\mathbf{r}\,') = \sum_{\alpha,\beta}\int_V \mathrm{d}\mathbf{r}\,''\,\frac{\partial^2\Phi}{\partial n_\alpha\partial n_\beta}(\mathbf{r}\,'')w_\nu^{(\alpha)}(\mathbf{r}\,''-\mathbf{r})w_{\nu'}^{(\beta)}(\mathbf{r}\,''-\mathbf{r}\,'). \tag{2.92}$$

In bulk, the derivative with respect to the weighted densities becomes independent of the spatial coordinate and the direct correlation function can be calculated analytically [109, 125, 129]. For an anisotropic system with only cylindrical symmetry we report in Sec. 5.3 a semi-analytical form for general multi-component mixtures in the framework of the FMT.

2.8 Ornstein Zernike (OZ) integral equation

In physics, integral equation theory is a very powerful tool to deal with multi-particle problems, where the correlation of observables, e.g., the positions of two distinct particles, can be predicted. Such microscopic arrangements can then be investigated by solving integral equations up to the first or second [47, 49, 52, 130–133] and even up to the third order [134]. It is noteworthy, that once a solution of a certain order has been achieved, the lower orders immediately follow by integrating out the respective degrees of freedom. A nice overview over integral equations that are relevant in physics is given in Ref. [98], which we use as a reference for this section.

One of the most prominent representatives of integral equations in statistical soft matter physics is the Ornstein-Zernike (OZ) relation[12]

$$h^{(2)}_{\nu\nu'}(\mathbf{r},\mathbf{r}') = c^{(2)}_{\nu\nu'}(\mathbf{r},\mathbf{r}') + \sum_{\nu''}\int_V \mathrm{d}\mathbf{r}''\, h^{(2)}_{\nu\nu''}(\mathbf{r},\mathbf{r}'')\rho_{\nu''}(\mathbf{r}'')c^{(2)}_{\nu''\nu'}(\mathbf{r}'',\mathbf{r}')\,. \tag{2.93}$$

It relates the *two-particle total correlation* $h^{(2)}$ with the *two-particle direct correlation* $c^{(2)}$. How the two functions are connected with each other becomes obvious, when we write down the OZ relation up to the zeroth order approximation, where the integral is neglected, i.e.,

$$h^{(2)}_{\nu\nu'}(\mathbf{r},\mathbf{r}') \approx c^{(2)}_{\nu\nu'}(\mathbf{r},\mathbf{r}')\,. \tag{2.94}$$

Up to the first order one would replace the total correlation $h^{(2)}_{\nu\nu'}$ in the integral by Eq. (2.94), such that on the right hand side and inside the integral only direct correlations appear. Recursively the integral can be written as an infinite series of couplings over $c^{(2)}_{\nu\nu'}$-functions. Thus, the meaning of the OZ relation (2.93) is the following: The total correlation is the sum over direct correlations between two particles for all possible amounts of intermediate particles.

In the following we derive the OZ relation from the statistical equations, that have already been introduced in the previous sections.
The differential forms of the free energy (2.1) and the grand potential (2.2) provide starting points for the derivation of the OZ relation. First, let us have a look at the canonical case: If we assume an infinitesimal change in the intrinsic part of the free energy, this causes in the case of the intrinsic free energy a change in the term $p\mathrm{d}V$, which can be expressed as an infinitesimal change in density. Therefore, the differential

[12] The name is a credit to L.S Ornstein and F. Zernike (1910s). Sometimes it is called OZ equation. Within this thesis the term "relation" will be used predominantly due to the fact that it will be applied to relate two different correlation functions with each other.

form of the intrinsic free energy can be written in functional nomenclature as [98]

$$\delta\mathcal{F}[\{\rho_\nu\}] = -S\delta T - \sum_{\nu'}\int_V \mathrm{d}\mathbf{r}'\,\delta\rho_{\nu'}(\mathbf{r}')V^{\mathrm{ext}}_{\nu'}(\mathbf{r}') + \sum_{\nu'}\mu_{\nu'}\delta N_{\nu'} \tag{2.95}$$

$$\overset{\text{Eq.(2.53)}}{=} -S\delta T + \sum_{\nu'}\int_V \mathrm{d}\mathbf{r}'\,\delta\rho_{\nu'}(\mathbf{r}')\psi_{\nu'}(\mathbf{r}')\,. \tag{2.96}$$

The intrinsic chemical potential then follows as the functional derivative of the intrinsic free energy (Eq. (2.96))

$$\psi_{\nu'}\left(\mathbf{r}';[\{\rho_\nu\}]\right) = \frac{\delta\mathcal{F}[\{\rho_\nu\}]}{\delta\rho_\nu(\mathbf{r}')}\,. \tag{2.97}$$

Second, in the case of the grand potential, the change in volume V can be written as the external work against the hydrostatic pressure p, i.e., $\delta V^{\mathrm{ext}} = p\delta V$. This infinitesimal change in the external potential is used in Eq. (2.2) rather than the volume change. The accompanied differential reads [98]

$$\begin{aligned}\delta\Omega[\{\rho_\nu\}] &= -S\delta T + \sum_{\nu'}\int_V \mathrm{d}\mathbf{r}'\,\rho_{\nu'}(\mathbf{r}')\delta V^{\mathrm{ext}}_{\nu'}(\mathbf{r}') - \sum_{\nu'}N_{\nu'}\delta\mu_{\nu'}\\ &= -S\delta T - \sum_{\nu'}\int_V \mathrm{d}\mathbf{r}'\,\rho_{\nu'}(\mathbf{r}')\delta\psi_{\nu'}(\mathbf{r}')\,.\end{aligned} \tag{2.98}$$

The first derivative of Eq. (2.98) with respect to the intrinsic chemical potential can be made with the functional differentiation rules from Eqs. (2.43) and (2.44). It follows

$$\begin{aligned}\frac{\delta\Omega}{\delta\psi_\nu(\mathbf{r})} &= -\sum_{\nu'}\int_V \mathrm{d}\mathbf{r}'\,\rho_{\nu'}(\mathbf{r}')\int_V \mathrm{d}\mathbf{r}''\,\frac{\delta\psi_{\nu'}(\mathbf{r}')}{\delta\psi_{\nu''}(\mathbf{r}'')}\frac{\delta\psi_{\nu''}(\mathbf{r}'')}{\delta\psi_\nu(\mathbf{r})}\\ &= \int_V \mathrm{d}\mathbf{r}'\int_V \mathrm{d}\mathbf{r}''\,\rho_\nu(\mathbf{r}')\delta(\mathbf{r}'-\mathbf{r}'')\delta(\mathbf{r}-\mathbf{r}'')\\ &= -\rho_\nu(\mathbf{r})\,,\end{aligned} \tag{2.99}$$

where all terms in the sum are zero for $\nu \neq \nu'$.

With the grand partition function from Eq. (2.25) it is a straight forward procedure to show that the second order partial functional derivatives with respect to the intrinsic chemical potential can be connected to partial functional derivatives with respect to the so-called *local activities*

$$z^*_\nu(\mathbf{r}) = z_\nu e^{-\beta V^{\mathrm{ext}}_\nu(\mathbf{r})}\,, \tag{2.100}$$

such that

$$\frac{\delta\Omega}{\delta\psi_\nu(\mathbf{r})\delta\psi_{\nu'}(\mathbf{r}')} = -\beta z^*_\nu(\mathbf{r}')\frac{\delta}{\delta z^*_\nu(\mathbf{r}')}\left(\frac{1}{\Xi}z^*_\nu(\mathbf{r})\frac{\delta\Xi}{\delta z^*_\nu(\mathbf{r})}\right). \tag{2.101}$$

By plugging in the grand potential partition sum and evaluating the expression on the right hand side, one can see that most of the integrals cancel out. Only a few expressions survive, which can be reduced into terms of the one- and two-particle densities from Eqs. (2.31) and (2.32) such that the resulting so-called *density-density correlation function* comes out

$$\begin{aligned} H_{\nu\nu'}(\mathbf{r},\mathbf{r}') &:= k_\mathrm{B}T\frac{\delta\Omega}{\delta\psi_\nu(\mathbf{r})\delta\psi_{\nu'}(\mathbf{r}')} \\ &= \rho_\nu(\mathbf{r})\rho_{\nu'}(\mathbf{r}') - \rho_\nu(\mathbf{r})\delta(\mathbf{r}-\mathbf{r}')\delta_{\nu\nu'} - \rho^{(2)}_{\nu\nu'}(\mathbf{r},\mathbf{r}')\,. \end{aligned} \tag{2.102}$$

This result can be rewritten in terms of the total correlation functions from Eq. (2.34), i.e.

$$H_{\nu\nu'}(\mathbf{r},\mathbf{r}') = \rho_\nu(\mathbf{r})\rho_{\nu'}(\mathbf{r}')h^{(2)}_{\nu\nu'}(\mathbf{r},\mathbf{r}') + \rho_\nu(\mathbf{r})\delta(\mathbf{r}-\mathbf{r}')\delta_{\nu\nu'}\,. \tag{2.103}$$

The tag "density-density correlation" comes from the fact that this function measures the fluctuations of local (equal or distinct species) density profiles about their average values, i.e., $H_{\nu\nu'}(\mathbf{r},\mathbf{r}') = \langle[\rho_\nu(\mathbf{r}) - \langle\rho_\nu(\mathbf{r})\rangle][\rho_{\nu'}(\mathbf{r}') - \langle\rho_{\nu'}(\mathbf{r}')\rangle]\rangle$. Together with Eq. (2.99) one can write the density-density correlation also as

$$H_{\nu\nu'}(\mathbf{r},\mathbf{r}') = k_\mathrm{B}T\frac{\delta\rho_\nu(\mathbf{r})}{\delta\psi_{\nu'}}\,, \tag{2.104}$$

which says that the density profile of every species ν is mediated not only by their own intrinsic chemical potential, but also by each other specie's intrinsic chemical potential $\psi_{\nu'}$. The inverse function $H^{-1}_{\nu\nu'}(\mathbf{r},\mathbf{r}')$ of the density-density correlator $H_{\nu\nu'}(\mathbf{r},\mathbf{r}')$ is defined through the identity [98]

$$\sum_{\nu''}\int_V \mathrm{d}\mathbf{r}''\, H_{\nu\nu''}(\mathbf{r},\mathbf{r}'')H^{-1}_{\nu''\nu'}(\mathbf{r}'',\mathbf{r}') = \delta(\mathbf{r}-\mathbf{r}')\delta_{\nu\nu'}\,. \tag{2.105}$$

With the differentiation rules for functionals (Eqs. 2.43 and 2.44) the inverse must be equal to

$$H^{-1}_{\nu\nu'}(\mathbf{r},\mathbf{r}') = \beta\frac{\delta\psi_\nu(\mathbf{r})}{\delta\rho_{\nu'}(\mathbf{r}')}\,, \tag{2.106}$$

which corresponds exactly to the intuitive perception of an inverse of Eq. (2.104).

We can now systematically deduce the (OZ) relation, especially by using the orthogonality property (Eq. (2.105)). For this purpose, we take the identity relation (2.105) and replace $H_{\nu\nu''}$ with Eq. (2.103) and $H^{-1}_{\nu''\nu'}$ with Eq. (2.106). This yields

$$\begin{aligned} \delta(\mathbf{r}-\mathbf{r}')\delta_{\nu\nu'} = \sum_{\nu''}\int_V \mathrm{d}\mathbf{r}''\, &\Big[\rho_\nu(\mathbf{r})\rho_{\nu''}(\mathbf{r}'')h^{(2)}_{\nu\nu''}(\mathbf{r},\mathbf{r}'') + \rho_\nu(\mathbf{r})\delta(\mathbf{r}-\mathbf{r}'')\delta_{\nu\nu''}\Big] \\ &\times\beta\frac{\delta\psi_{\nu''}(\mathbf{r}'')}{\delta\rho_{\nu'}(\mathbf{r}')}\,. \end{aligned} \tag{2.107}$$

If now the intrinsic chemical potential is replaced by the derivative of the intrinsic free energy according to Eq. (2.97), the second factor in the integrand will become a second order functional derivative of the total intrinsic free energy $\mathcal{F} = \mathcal{F}^{\mathrm{id}} + \mathcal{F}^{\mathrm{exc}}$, where the ideal part is defined by the derivative of Eq. (2.58) and the excess part is defined over the direct correlation function (2.60) from the DFT:

$$\delta(\mathbf{r}-\mathbf{r}')\delta_{\nu\nu'} = \sum_{\nu''}\int_V \mathrm{d}\mathbf{r}'' \left[\rho_\nu(\mathbf{r})\rho_{\nu''}(\mathbf{r}'')h^{(2)}_{\nu\nu''}(\mathbf{r},\mathbf{r}'') + \rho_\nu(\mathbf{r})\delta(\mathbf{r}-\mathbf{r}'')\delta_{\nu\nu''}\right] \times k_{\mathrm{B}}T\left[\frac{1}{\rho_{\nu''}(\mathbf{r}'')}\delta(\mathbf{r}''-\mathbf{r}')\delta_{\nu''\nu'} - c^{(2)}_{\nu''\nu'}(\mathbf{r}'',\mathbf{r}')\right]. \tag{2.108}$$

Simplification then yields the OZ relation

$$h^{(2)}_{\nu\nu'}(\mathbf{r},\mathbf{r}') = c^{(2)}_{\nu\nu'}(\mathbf{r},\mathbf{r}') + \sum_{\nu''}\int_V \mathrm{d}\mathbf{r}''\, h^{(2)}_{\nu\nu''}(\mathbf{r},\mathbf{r}'')\rho_{\nu''}(\mathbf{r}'')c^{(2)}_{\nu''\nu'}(\mathbf{r}'',\mathbf{r}')\,. \tag{2.109}$$

One realization from this relation is, that one has to know the complete $(V\times V')$-resolution of, e.g., the direct correlations, in order to obtain the total correlations for two specific particle positions and species. Since also the opposite statement is true ($c^{(2)} \leftrightarrow h^{(2)}$), the mapping between the two functions is a bijection.

Closure relations Because the OZ relation is not directly applicable in the first place, since usually both two-particle correlation functions are unknown, there exist many approximations [135], that relate $h^{(2)}$ and $c^{(2)}$ with each other. These relations are called *closure relations*. They provide at least an approximate solution for one of the two functions. One of the most famous approximations is the already mentioned Percus-Yevick (PY) approximation [120,136], which is good for hard spheres. The hypernetted-chain closure (HNC) [137] is also nicely applicable for softer particle. The Zerah-Hansen (ZH) closure [138] combines PY and HNC by interpolating between them. Furthermore, one should also mention the often applied Rogers-Young (RY) closure [139], the Mean Spherical Approximation [98] that connects the direct correlations with the interaction potential, and the Generalized Mean Spherical Approximation (GMDA) [140]. On the one hand, by only knowing particle interactions and applying a closure relation, the OZ yields both, the one- and two-body correlations. On the other hand, the OZ relation is also an useful tool for the transformation of the correlation functions $h^{(2)}$ and $c^{(2)}$ into one another. This will be used in Sec. 5.3 and Sec. 5.4 to translate the information from direct correlations, which are produced via our DFT/FMT route, into the total correlations that are comparable to simulation results.

Chapter 3

Computer simulations

3.1 Overview over different simulation methods

For the numerical investigation of soft matter systems different approaches exist. Besides the integral equation approaches, e.g., those which are based upon iterative [108] solution of the Ornstein-Zernike relation [131, 135, 136, 138], there are computational methods, which *simulate* the multi-particle dynamics by using rather simple individual equations. With increasing computational power such computer simulations[1] have become more and more relevant for scientific applications. They are able to predict accurately experimental structures and especially dynamics, whereas simultaneously the absolute run times, which are more advantageous in integral equation theories, decrease due to our modern processor techniques[2]. Here the three most popular techniques are pictured with their accompanied advantages and disadvantages as well as their application idea.

Monte Carlo (MC) method. The term *Monte Carlo* coins to the massive use of random numbers, which the founders[3] associated with the *Monte Carlo Casino* in Monacco. The algorithmic Monte Carlo integration scheme uses random numbers, to integrate over a high-dimensional space, e.g., such as a many particle ensemble. The basic idea is to generate a lot of numbers randomly, associate them with parameters or coordinates of the underlying problem and decide from a physical or mathematical point of view, whether the rolled random numbers can be accepted, since they reflect e.g. energetic constraints, or not. The sampling of a soft matter system is in this framework connected with random

[1] For comprehensive overviews over the most common computer simulation techniques see the textbooks by M.P. Allen and D. Tildesley [141] or G. Gompper et al. [142].

[2] The ability of performing algorithms in parallel gives rise to a modern and very powerful tool: graphics processing units (GPU).

[3] First principles with applications have been developed by Stanislaw Ulam and Nicholas Metropolis in cooperation with John von Neumann in 1946 at the Scientific Laboratory of Los Alamos

displacement of particles about very small distances according to the so-called Metropolis algorithm [141]. After such a step the energy is evaluated and by means of this energy the step is either rejected or accepted. A very intuitive picture is given by the distance relation between two hard spheres. As one of them is displaced randomly, such a step can always be accepted when particles do not overlap, but the step must be rejected as soon as particles exhibit an overlap. In the Monte Carlo algorithm no real time evolution is involved. One is rather interested into the statistics of a final equilibrium state than into dynamical aspects, which could possibly also reveal pathways through different metastable states.

Molecular dynamics (MD). One of the most widely used and fundamental models to study the evolution of a soft matter system is Molecular Dynamics (MD). In this scheme, the Newton's equations of motion for a system of interacting particles are used to describe the individual behavior of all particles at the same time. This means, that the total internal energy, which is composed of a kinetic and an interaction part, must be a constant. Numerically this procedure needs the effort to calculate pair interactions at a certain time and integrate the system over a short time interval Δt. A symplectic integrator, e.g., such as *Leap frog* or *Verlet algorithm* [141], is needed in order to guarantee stability. Additionally, computational errors lead to a heating or cooling of the system, i.e., the increase or decrease of internal energy. Therefore, standard procedures exist for holding the temperature at a constant value[4]. This makes the integration scheme more time consumable than those, which go along without the implementation of a thermostat. Furthermore, when interaction potentials become steep and densities become high, a lot of computational effort must be spent for the *rattling* of particles in their local cages. Although the MD algorithm can for short ranged interparticle potentials nicely be scheduled in parallel, the above disadvantages make MD less popular, when only the solute particles are interesting.

Brownian dynamics (BD). In Brownian Dynamics, the motion of particles in a solvent medium is described via stochastic differential equations. The name is a credit to the Scottish Botanist Robert Brown, who purportedly discovered the jittering motion of small particles under his microscope. Although the motion of particles is caused by the random kicks with the surrounding solvent molecules, within BD these molecules are – contrarily to MD simulations – described as a continuum [145]. This leads to a set of differential equations, where only the larger solute particles are described explicitly and the smaller solvent molecules are only mimicked by a random force, acting on the larger particles in a well-defined statistical manner. BD simulations are often applied for soft matter systems with a viscous background medium. In these systems, due to the high friction between solute and solvent, one can often even neglect the momentum term in the underlying differential equations. Such systems are called *overdamped*. In addition,

[4] A constant temperature can be guaranteed by a thermostat, e.g., the Nosé-Hoover thermostat [143,144].

due to the thermalizing random forces the overdamped BD simulations do not need an external thermostat.

Throughout the whole thesis BD simulations have been applied, since the underlying problems were either motivated by experimental studies where the systems are overdamped, or motivated by very fundamental questions regarding universal observations, for which it is more profitable to investigate effects by means of the most simple model. In Sec. 3.3 the BD simulation will be explained in more detail. It is the implementation of the so-called Langevin equation [146], which will be introduced in the next section.

Hydrodynamics interactions (HI). As particles are moving, they typically induce long-ranged flows in the surrounding medium. The induced motion of the background can for example be explained by the viscous friction of the particles and with the accompanied energy and momentum conservation. On the one hand, by means of these flows a particle responds to its own motion through a re-coupling with the relative velocity of the background fluid. On the other hand, all particles are coupled to the flow fields of other particles.
Incorporating HI, even if it is implemented only implicitly into an algorithm, often means, that a lot of additional computational power is needed. There are possibilities to deal with effects from hydrodynamics on an approximate level, e.g., such as with the Oseen tensor that is the Green's function of the linear Navier-Stokes equation [147] or the Rotne-Prager tensor [148]. Other Methods, such as the full MD simulations or *Lattice Boltzmann* simulation [149], often lead to more accurate results with respect to the experiments. Although the HI are ubiquitous in all soft matter systems, its relevance does strongly depend on the application and the quantitative concern of detailed peculiarities, in which we are not interested. Thus, we will not employ HI in this thesis.

3.2 Langevin dynamics

Mesoscopic particles, which are suspended in a medium of much smaller particles, undergo Brownian motion. The smaller solvent molecules are treated to be in equilibrium at a constant temperature. This means, that they are moving with their thermal velocity, which is Maxwellian distributed. In Brownian dynamics they are treated as a continuum, which acts on the one hand as a damping medium for the solute particles and on the other hand as the source of a stochastic force due to the stochastic collisions with the much larger particles. Typically, the damping is characterized by a damping constant γ_ν, which is a function of the shape and size of the particle species ν as well as of the macroscopic viscosity of the solvent medium. Particularly, for spherically symmetric particles in viscous fluids (low Reynolds numbers) the damping constant is known by the Stokes' law

$$\gamma_\nu = 6\pi\eta R_\nu \,, \tag{3.1}$$

where η is the macroscopic viscosity of the medium and R_ν is the radius of the particle of species ν. In 1905, A. Einstein developed the prominent relation, which connects the friction of such a particle with its self-diffusion coefficient [145]

$$D_\nu = \frac{k_\mathrm{B}T}{\gamma_\nu}\,, \tag{3.2}$$

where $k_\mathrm{B}T$ is the thermal energy. Eq. (3.2) is the so-called Stokes-Einstein-relation that characterizes the magnitude of the free diffusion of a particle due to the random forces acting on it. The random forces are given by a stochastic function $\mathbf{f}_{\nu,i}(t)$. It is referred to as the thermal white noise and must obey the *fluctuation-dissipation theorem*. The theorem states, that in terms of a noise average $\langle . \rangle$ the first two moments of the function $\mathbf{f}_{\nu,i}(t)$ have to fulfill the constraints [98, 145]

$$\langle \mathbf{f}_{\nu,i}(t) \rangle = 0\,, \tag{3.3}$$

$$\langle \mathbf{f}_{\nu,i}(t) \mathbf{f}^\mathrm{T}_{\nu' i'}(t') \rangle = 2D_\nu \delta_{ii'} \delta_{\nu\nu'} \delta(t-t') \overset{\leftrightarrow}{I}\,, \tag{3.4}$$

where the superscript T on the left-hand side of Eq. (3.4) denotes the transposed of the vector $\mathbf{f}_{\nu',i'}(t')$, $\overset{\leftrightarrow}{I}$ is the unity matrix with rank equal to the number of spatial dimensions, and $\delta_{\nu\nu'}$ and $\delta(t-t')$ are the Kronecker-Delta and the Dirac-delta function, respectively. Eq. (3.3) ensures, that there is no spatially preferred direction. Although the second moment in Eq. (3.4) looks rather complicated, the carrying information is simple: any component of any stochastic force acting on a particle is completely uncorrelated with any other component of a stochastic force except with itself. The above definitions of the first and second moment are enough to describe the *random walk* of the particles. The *Langevin equation* for each particle i of species ν reads [146]

$$m_\nu \ddot{\mathbf{r}}_{\nu,i}(t) + \frac{1}{\gamma_\nu} \dot{\mathbf{r}}_{\nu,i}(t) + \nabla_{r_{\nu,i}} U_{\nu,i}\big(\mathbf{r}^N(t)\big) = \mathbf{f}_{\nu,i}(t)\,, \tag{3.5}$$

where m_ν is its mass and $-\nabla_{r_{\nu,i}} U_{\nu,i}(\mathbf{r}^N)$ the systematic force acting on particle i of species ν. It is composed of interaction with other particles and the external force.

One can neglect the inertia term at very low Reynolds numbers, i.e., $m_\nu \ddot{\mathbf{r}}_{\nu,i} \ll \gamma_\nu^{-1} \dot{\mathbf{r}}_{\nu,i}$. Then the Langevin equation simplifies to

$$\frac{1}{\gamma_\nu} \dot{\mathbf{r}}_{\nu,i}(t) = -\nabla_{r_{\nu,i}} U_{\nu,i}\big(\mathbf{r}^N(t)\big) + \mathbf{f}_{\nu,i}(t)\,. \tag{3.6}$$

3.3 Implementation of algorithms

A suitable numerical solver for Eq. (3.6) is provided by a first order integration scheme. Such a scheme is stable [141, 150] and already well tested for different kinds of problems

[151–153]. Oppositely to MD simulations, where energy must be conserved explicitly, the BD dynamics of overdamped systems does not need for such an artificial conservation and can therefore be handled with a linear expansion in time. If Δt denotes a small timestep, one can write a simple forward time differentiation scheme as

$$\dot{\mathbf{r}}(t) = \frac{\mathbf{r}(t+\Delta t) - \mathbf{r}(t)}{\Delta t}\,, \tag{3.7}$$

which yields with Eq. (3.6) the evolution equation

$$\mathbf{r}_{\nu,i}(t+\Delta t) = \mathbf{r}_{\nu,i}(t) - \gamma_\nu \nabla_{\mathbf{r}_{\nu,i}} U_{i\nu}\big(\mathbf{r}^N(t)\big) + \Delta\mathbf{r}\,, \tag{3.8}$$

where $\Delta\mathbf{r}$ is a random displacement vector due to the random force. Its first two moments must satisfy the fluctuation dissipation theorem of Eqs. (3.3) and (3.4). Following the principle of maximizing the ignorance with respect to these two constraints, one can draw the components of $\Delta\mathbf{r}$ from a Gaussian distributed random number generator with zero mean and the second moment (variance) being $2D_\nu\Delta t$.[5]
The random number generator RAN3 from Ref. [154] has been used as an input of a Box-Muller transform [155], in order to generate Gaussian distributed random numbers. A very striking positive side effect of the simple first order algorithm from Eq. (3.8) is its low computational cost, where in principle only pair interactions and random displacements have to be evaluated.

Cell-linked list. Whereas the computational time to produce random numbers for the above algorithm scales linearly with the number of particles in the system ($\mathcal{O}(N)$), the most effort is typically spent on calculating pair interactions, that are hidden in the $\nabla_{\mathbf{r}_{\nu,i}} U_{\nu,i}(\mathbf{r}^N)$ term of Eq. (3.8). Because in principle every particle could interact with every other particle, the computational power scales as $\mathcal{O}(N^2)$. Nevertheless, in many situations, e.g., when the pair interaction potential has a finite range, it is not necessary to calculate interactions between all pairs of particles. When the interaction potential has a finite range, the algorithm has been designed in such a way, that prior to a calculation of pair interactions all particles are collated to *cells*, where the size of these cells just exceeds the maximum interaction range of the interaction potential (see Fig. 3.1). In the next step, all pair interactions of particles that are sitting in the same cell or in a neighboring cell (*cell-linked list*) are evaluated. Since the range of the potential is constant for a certain simulation and the intermediate number of particles per cell is also constant in the most cases, this algorithm only scales as $\mathcal{O}(N)$ and should be used whenever possible, especially when system sizes become large.

[5] Note, that the random numbers could in principle also be drawn from other random number distributions with the same first and second moment, e.g., from a uniform distribution. In the central limit theorem, such a distribution will converge against a uniform Gaussian.

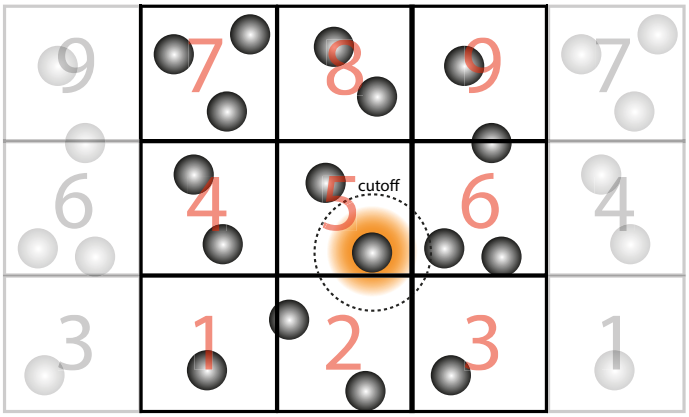

Figure 3.1: Sketch of a simulation box with periodic boundary conditions at the left and right borders and with a *Cell-linked list* structure, demonstrated by a two-dimensional representation. Each individual particle is interacting with any other particle only if the distance is below a certain threshold (cutoff). This fact allows for a previous sorting of particles into cells (1-9) and a subsequent calculation of pair interactions only with particles, which are sitting in the same cell or in a neighboring one (cell-linked).

Chapter 4

Particle segregation in binary soft systems with gravity

Preface. The present chapter is based on the original paper "*Particle segregation in a sedimenting bidisperse soft sphere system*" [1] by the author of this thesis and contains literal adoptions of the text and figures. Little modifications of the original paper have been made in order to obtain a consistent nomenclature.

4.1 Introduction

We study the sedimentation of a binary particle system by means of Brownian dynamics. In our model system particles are very soft and are therefore able to reduce their effective diameter. With given masses of large and small particles, we can predict the phase separation and complicated stackings in the gravitational field by making use of low density and high density approximations of the equation of state (EOS). Whereas in the low density regime the EOS can be approximated up to the second order virial coefficient, the very dense systems can be quantified in the framework of the so-called Mean Spherical Approximation (MSA). One species has twice the diameter of the other species and both species have a completely penetrable core. We show, that soft spheres show a richer behavior than hard ones and that the final states not only depend on the mass densities of the involved particle species, but also on the temperature. We present a theoretical ansatz for calculating final sedimentation states qualitatively. By making use of approximate solutions of the EOS for soft particles in the two limiting cases of very dilute and very dense packings separately for both of the particle species, we are able to make conclusions for the resulting sedimentation profile. This chapter is organized as follows: Firstly, the EOS of soft particles is discussed for bulk systems without any external field. Secondly, we predict the influence of a linear external field by assuming different buoyant forces to be responsible for the phase separation. Theoretical predictions are compared to

results from Brownian dynamics computer simulations. Finally, metastable states and the dynamics of yielding towards the final state are investigated by computer simulations.

4.2 Model

We consider a binary mixture consisting of N_s small particles with diameter σ_s and mass m_s and N_l large particles with diameter σ_l and mass m_l. Throughout the whole chapter we fix $\sigma_\mathrm{l} = 2\sigma_\mathrm{s}$ but vary the masses. As a control parameter, we employ the ratio of the mass densities, i.e.,

$$\xi = \frac{m_\mathrm{s}/\sigma_\mathrm{s}^3}{m_\mathrm{l}/\sigma_\mathrm{l}^3}. \tag{4.1}$$

The particles interact according to a finite-ranged purely repulsive harmonic pair potential

$$v_{\nu\nu'}(r) = \begin{cases} \frac{\varepsilon}{2}\left(1 - \frac{r}{\sigma_{\nu\nu'}}\right)^2 & r < \sigma_{\nu\nu'} \\ 0 & r \geq \sigma_{\nu\nu'} \end{cases}, \tag{4.2}$$

where r is the distance between the centers of two spheres, $\sigma_{\nu\nu'} = (\sigma_\nu + \sigma_{\nu'})/2$ is their average diameter and the prefactor ε defines the energy scale.

We study particles in a gravitational field in z-direction. Moreover, there is a plane wall at the bottom of the simulation box. This corresponds to an additional external field acting on every sphere

$$V_\nu^\mathrm{ext}(\mathbf{r}) = m_\nu g z + V_\nu^\mathrm{w}(z)\,, \tag{4.3}$$

with $m_\nu = m_\mathrm{s}$ or m_l depending on the type of the particle and

$$V_\nu^\mathrm{w}(z) = \begin{cases} \frac{\varepsilon_\mathrm{w}}{2}\left(1 - \frac{z}{\sigma_\nu/2}\right)^2 & z < \frac{\sigma_\nu}{2} \\ 0 & z \geq \frac{\sigma_\nu}{2} \end{cases}. \tag{4.4}$$

The stiffness of the wall is given by a dimensionless constant $\varepsilon_\mathrm{w}^* = \varepsilon_\mathrm{w}/\varepsilon$ and the strength of the gravitational field by $g^* = m_\mathrm{s} g \sigma_\mathrm{s}/(\xi k_\mathrm{B} T)$.

In the following we use the particle diameter σ_s of the smaller particles as a suitable length scale and the prefactor ε of the interaction potential as an energy scale. Throughout this chapter we employ the Brownian time $\tau_\mathrm{B} = \sigma_\mathrm{s}^2/D_s$ as a time scale, with $D_s = k_\mathrm{B}T/\gamma_\mathrm{s}$ denoting the short-time self-diffusion coefficient of small particles and where γ_s is the friction coefficient of a small sphere. We also introduce the dimensionless temperature $T^* = k_\mathrm{B}T/\varepsilon$ and the dimensionless pressure $P^* = p\sigma_\mathrm{s}^3/\varepsilon$. The total bulk number density of the system is given by $\rho = N/V$, where $N = N_s + N_l$ is the total number of particles and V denotes the volume of the system.

4.3 Simulation details

We perform Brownian dynamics simulations, i.e., we simulate the particle trajectories according to the overdamped Langevin equation (3.6), where depending on the species γ_ν is either the friction constant of a small sphere $\gamma_\nu = \gamma_\mathrm{s}$ or the friction constant of a large sphere $\gamma_\nu = \gamma_\mathrm{l} = \gamma_\mathrm{s}\sigma_\mathrm{l}/\sigma_\mathrm{s}$. The force $-\nabla_{r_{\nu,i}} U_{\nu,i}(\mathbf{r}^N)$ from Eq. (3.6) is given by the pair interactions, the external wall potential, and the gravitational force.

In our simulation we consider $N_\mathrm{s} = 2000$ small and $N_\mathrm{l} = 2000$ large particles. We employ periodic boundary conditions perpendicular to the gravitational force. The length of the simulation box in x and y-direction is $L_\mathrm{x} = L_\mathrm{y} = 10\sigma_\mathrm{s}$. We use finite time steps with $\Delta t = 10^{-4}\tau_\mathrm{B}$ or below. In the beginning we place all the particles randomly into the simulation box at a low packing fraction of $\phi = \phi_\mathrm{s} + \phi_\mathrm{l} = 0.1$, with $\phi_\nu = \pi\sigma_\nu^3\rho_\nu/6$. After an initial relaxation time without gravity of $200\tau_\mathrm{B}$, the external field is instantaneously switched on.

We choose an almost hard wall with a stiffness $\varepsilon_\mathrm{w}^* = 100$ that makes it rather impenetrable for the particles. The strength of the gravitational field throughout this chapter is held constant at $g^* = 1.5$.

4.4 Results

4.4.1 Bulk equation of state: limiting cases

In the gravity field we observe a segregation of the two particle species. In order to predict which species is forced to the top and which one to the bottom, we first consider the low and high number density limits of the bulk EOS of separate phases that consist either of small particles or large particles only.

For low densities, the EOS for species ν can be estimated by truncating the virial expansion (2.72), that is expressed by the series of virial coefficients (2.69) et seq., after the second term, i.e.,

$$z_{\mathrm{EOS},\nu} = \frac{\beta p}{\rho_\nu} = 1 + B_{\nu\nu}^{(2)}\rho_\nu \,, \tag{4.5}$$

where again $\beta = (k_\mathrm{B}T)^{-1}$. For sufficiently fast decaying interaction potentials the second virial coefficient is equal to the integral over the Mayer-f function with the given pair-potential

$$B_{\nu\nu}^{(2)} = 2\pi \int_0^\infty \mathrm{d}r \, \left[1 - \exp\left(-\beta v_{\nu\nu}(r)\right)\right] r^2 \,. \tag{4.6}$$

For large densities, we employ the so-called Mean Spherical Approximation (MSA) [98]. The MSA is a well-established approximation for soft particle systems at large densities

[156–159]. Note that sometimes the MSA is also called random phase approximation (RPA) [156, 159]. For soft penetrable spheres the hard core within the MSA framework becomes infinitely small and the overall approximate closure relation [158][1]

$$c_{\nu\nu}(r) = -\beta v_{\nu\nu}(r)\,. \tag{4.7}$$

The EOS of a monodisperse system of species ν is determined by integrating over the compressibility factor [98]

$$z_{\mathrm{EOS},\nu} = \frac{\beta p}{\rho_\nu} = \frac{\beta}{\rho_\nu}\int_0^{\rho_\nu} \mathrm{d}\rho'_\nu \frac{\partial p(\rho'_\nu)}{\partial \rho'_\nu} = \frac{1}{\rho_\nu}\int_0^{\rho_\nu} \mathrm{d}\rho'_\nu \left[1 - \rho'_\nu \hat{c}_{\nu\nu}(k \to 0)\right]\,, \tag{4.8}$$

where $\hat{c}_{\nu\nu}(k)$ is the Fourier transform of the direct correlation function $c_{\nu\nu}(r)$. Since $\hat{c}_{\nu\nu}(k)$ according to Eq. (4.7) does not depend on the density, one finds for the high density regime

$$z_{\mathrm{EOS},\nu} = 1 - \frac{1}{2}\hat{c}_{\nu\nu}(0)\rho_\nu\,. \tag{4.9}$$

In summary, for our soft sphere systems we can use the limiting approximations

$$z_{\mathrm{EOS},\nu} = \begin{cases} 1 + B^{(2)}_{\nu\nu}\rho_\nu & , \quad \rho_\nu \le \rho^{\mathrm{low}} \\ 1 - \frac{1}{2}\hat{c}_{\nu\nu}(0)\rho_\nu & , \quad \rho_\nu \ge \rho^{\mathrm{high}} \end{cases} \tag{4.10}$$

The prefactor in the low number density case is calculated by Eq. (4.6). For the high number density regime an analytical estimate for the prefactor is given by the MSA (see Eq. (4.7)). For our system, we use the dimensionless packing fraction $\phi = \rho\pi\sigma_\nu^3/6$ and fix the boundaries ρ^{low} and ρ^{high} deep in the limiting cases according to the packing fractions $\phi^{\mathrm{low}} = 2^{-3}$ and $\phi^{\mathrm{high}} = 2$, respectively.

In Fig. 4.1 the bulk equations of state for monodisperse soft spheres at different temperatures are presented theoretically for the limiting cases of high and low densities together with data from Brownian dynamics simulations. Note that the packing fraction can be larger than one [160–162]. In order to prevent crystallization effects at very high densities in our simulations, we have introduced a small bidispersity for the diameters, which is equivalent to a variance of 0.04. The approximations for small and large packing fraction describe our simulation results very well. Apparently, at low packing fractions the pressure increases for increasing temperature. However, at large packing fractions, the pressure is approximately independent of the temperature. Therefore, the slopes in the intermediate regime must also become larger. Since the EOS is typically not analytically known in an intermediate number density regime, we will later approximate the intermediate regime by a polynomial interpolation of the two limiting cases, with the respective cutoff-values of the two regimes chosen according to ϕ^{low} and ϕ^{high}.

[1] The equation can formally be derived by inserting the approximate expression of the Mayer-f function (Eq. (2.68)) into the second order truncation of Eq.(2.67) and applying a subsequent double functional differentiation.

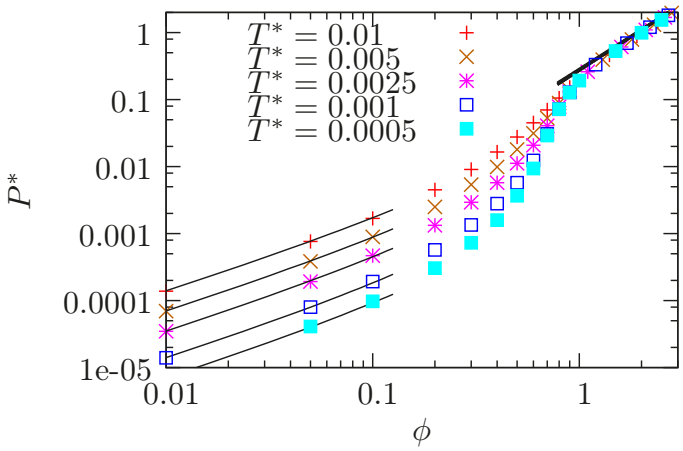

Figure 4.1: Double logarithmic plot of the equation of state of a system consisting of one particle species with only a small amount of bidispersity in order to avoid crystallization. The different colors denote cases with different temperatures. The points show the simulation data. Additionally, the limiting cases of the analytical approximations from Eq. (4.10) are plotted (solid lines). All curves converge against a limiting line at large packing fractions.

4.4.2 Sedimentation profiles

To introduce gravity it is necessary to also incorporate the masses m_s and m_l into the discussion. As mentioned before, we investigate the particular case, where small and large particles have a size ratio $\sigma_\mathrm{l}/\sigma_\mathrm{s} = 2$. The masses are set by the dimensionless mass density ratio ξ defined in Eq. (4.1). The sedimentation profiles will strongly depend on this mass density ratio.

For hard particles with a ratio $\xi = 1$ no phase separation due to buoyant forces is expected. Inertia effects that are important for the Brazil nut effect in granular systems [163, 164] can be neglected because the dynamics is overdamped.

However, in our case particles are very soft and as a consequence their thermodynamic properties strongly depend on the temperature and pressure (see Fig. 4.1). As we will show in the following, especially the compressibility will determine the buoyant forces, which for soft particles also depend on temperature and pressure. We will use estimates of the buoyancy in order to predict the segregation of sedimenting soft colloids. The buoyancy of the large particles for a given temperature T^* and pressure P^* depends on the ratio of the mass densities, i.e., the ratio of the number densities $\rho_\mathrm{l}(P^*, T^*)/\rho_\mathrm{s}(P^*, T^*)$ weighted by the corresponding masses m_l and m_s. We introduce a buoyancy function

$$b_\mathrm{l}(P^*, T^*, \xi) := 1 - \frac{\rho_\mathrm{l}(P^*, T^*) m_\mathrm{l}}{\rho_\mathrm{s}(P^*, T^*) m_\mathrm{s}} = 1 - \frac{\phi_\mathrm{l}(P^*, T^*)}{\phi_\mathrm{s}(P^*, T^*)\xi}. \tag{4.11}$$

If $b_\mathrm{l}(P^*, T^*, \xi)$ is positive, the larger particles will be lifted up with respect to the smaller ones. On the other hand they sink to the ground as soon as $b_\mathrm{l}(P^*, T^*, \xi)$ becomes negative.

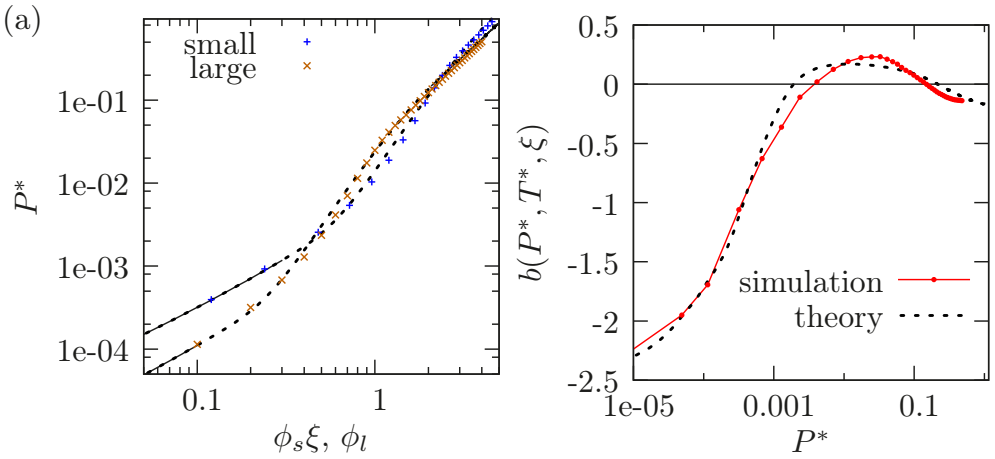

Figure 4.2: (a) Equations of state of large and small particles with a mass density ratio of $\xi = 2.4$ and at temperature $T^* = 0.005$. Note that the packing fraction of the larger particles is not weighted, whereas for the small particles it is multiplied by ξ for the visualization of the corresponding impact of gravity. Points indicate simulation data, the solid lines are the limiting approximations of equation (4.10). In order to obtain the dashed lines, the limiting cases are interpolated by a polynomial function. The curves have two intersection points. (b) The buoyancy function $b_l(P^*, T^*, \xi)$ denoting the buoyancy of the larger particles. For small and large pressures the function is negative indicating that large particles sink while for intermediate pressure $b_l(P^*, T^*, \xi)$ is positive and therefore large particle rise. The red points and line denote the simulation results, the black dashed line corresponds to a theoretical prediction obtained by the interpolation of the analytical limiting cases of the EOS (cf. dashed line in (a)).

In Fig. 4.2(a) we show the normalized pressures P^*, which are the product of the EOS with the density, for small and large particles with $\xi = 2.4$ and $T^* = 0.005$. Note, that we have weighted the packing fraction of the small particles with the mass density ratio ξ. In Fig. 4.2(b) we plot the buoyancy function as a function of P^*. As it turns out, for $\xi = 2.4$ the buoyancy function has two zeros corresponding to the two intersecting points of the weighted equations of state in Fig. 4.2(a). The zeros denote the pressures for which the direction of the buoyant forces on large particles reverse. Consequently, for intermediate pressures the larger particles are lifted up in a bath of smaller particles, whereas for small and large pressures they sink. In the further discussion we will focus on the second zero, because in our simulations the pressure due to gravity is usually larger than the one at the first zero of b_l. In the next section, we will discuss the final states that we expect from considering the buoyancy function and compare these predictions to the final states we find in the simulations.

4.4.3 Final states

In this section we discuss the final states of the sedimentation process for different values of the mass density ratio ξ defined in Eq. (4.1). For hard particles from considerations of buoyancy one expects that large particles reside on top of the small ones for $\xi > 1$ or the other way around for $\xi < 1$. In our case of soft particles, buoyancy also depends on the pressure. Gravity induces a monotonic increasing pressure from the top to the bottom of the system and therefore the pressure depends on the height. As a consequence, we find equilibrium phases, where large particles gather both on the top and at the bottom of the system.

In Fig. 4.3 the buoyancy function $b_\mathrm{l}(P^*, T^*, \xi)$ together with final states of simulations are shown for a constant temperature $T^* = 0.005$. For $\xi = 1.3$ the function $b_\mathrm{l}(P^*, T^*, \xi)$ is negative at any pressure. Therefore, smaller particles are always expected to lay above the larger ones. The corresponding simulated final state is shown in Fig. 4.3(a). For $\xi \approx 1.8$ there is one zero, for $\xi > 1.8$ even two zeros are possible. In case of two zeros, i.e., $1.8 < \xi < 2.76$, an intermediate pressure regime exists, where the large particles move upwards. As a consequence, for a simple sedimentation with a randomly distributed mixture at the beginning, one will always obtain a 3-phase-stacking. These states are mainly governed by large particles that are lifted up for the intermediate pressure in the upper part of the system and large particles that sink due to sufficiently high pressure in the lower part of the system. The small particles gather in the center part of the system. It is important to note, that the thickness of the top slice of larger particles is limited. If one adds more particles at the top of the box, the pressure at the upper interface will increase and therefore the threshold for the uplift of larger particles will be exceeded. Then, some of the larger particles aggregate into a cluster and sediment cooperatively to the bottom basin. This procedure may appear several times until the condition of positive buoyancy is recovered. We will describe the dynamics of this process in more detail in the next section.

For $\xi \approx 2.76$ the buoyancy function is only negative for very low pressures, then it becomes positive and converges roughly towards zero for very high pressures. For this value no preferred stacking is expected at high pressures. In the simulations (cf. Fig. 4.3(d)), particles segregate into a network structure at high pressure regions at the bottom of the simulation box. Despite the network-like segregation no net flow of one of two species can be observed over the whole time of the simulation and we can not discriminate from our simulation times whether a further segregation process takes place only very slowly or whether the networks depict some kind of a metastable state. For intermediate pressures towards the top of the system the uplift of the larger particles becomes significant. A further increase of the mass density ratio, i.e., $\xi > 2.76$, again leads to segregation into two phases with an oppositely stacking than for small ξ. Except for the small pressures in the top layer, for all other pressures within the sedimentation profile $b_\mathrm{l}(P^*, T^*, \xi) > 0$ and therefore the large particles move to the top. In principle, this behavior is confirmed by

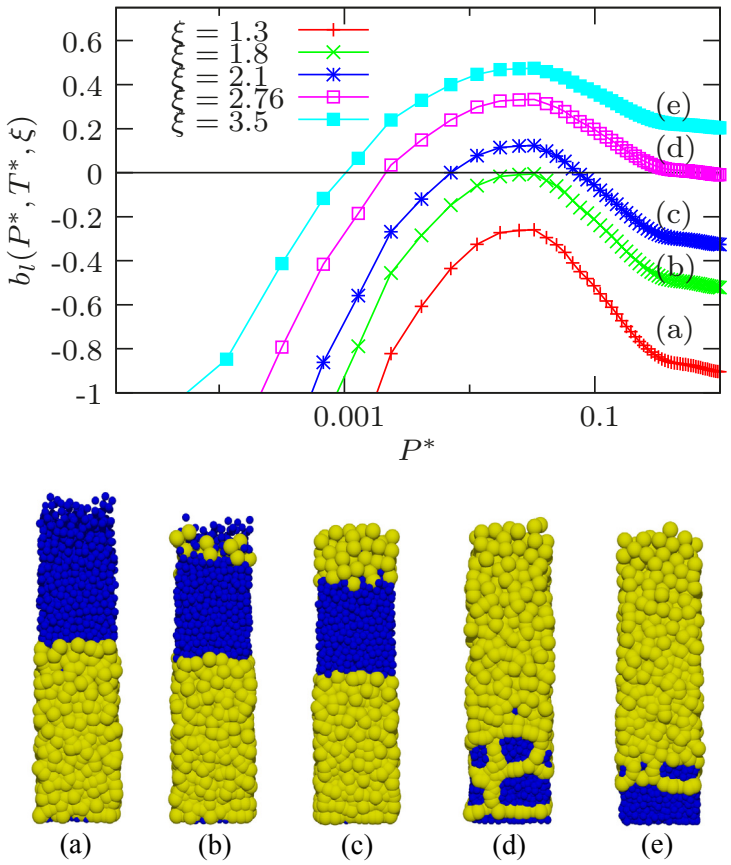

Figure 4.3: (*Top panel*) Dependency of the buoyancy function $b_l(P^*, T^*, \xi)$ on the pressure P^* for different mass density ratios ξ. (a-e) Corresponding final sedimentation profiles obtained from Brownian dynamics simulations after $500\tau_B$ simulation time for a temperature $T^* = 0.005$. Large particles are colored yellow, small particles are depicted blue. The mass density ratios are (a) $\xi = 1.3$, (b) $\xi = 1.8$, (c) $\xi = 2.1$, (d) $\xi = 2.76$ and (e) $\xi = 3.5$ (cf. corresponding buoyancy functions in the upper plot). Note that the first zero of $b_l(P^*, T^*, \xi)$ corresponds to small pressures that usually only occur in a small slice at the top layer of the system and therefore is not to be considered here. The stacking of the rest of the system depends on whether the second zero of $b_l(P^*, T^*, \xi)$ exists. (a) For small ξ, the buoyancy function is always negative and therefore all large particles move to the bottom. (c) $b_l(P^*, T^*, \xi)$ possesses two zeros and therefore large particles rise to the top in the upper part of the system and sink to the bottom in the lower part. (e) If $b_l(P^*, T^*, \xi)$ possesses only one zero at small pressures, the large particles gather at the top of the system. (b) and (d) show the limiting cases where the relaxation into a stationary final state takes a very long time and therefore clusters and network-like structures occur.

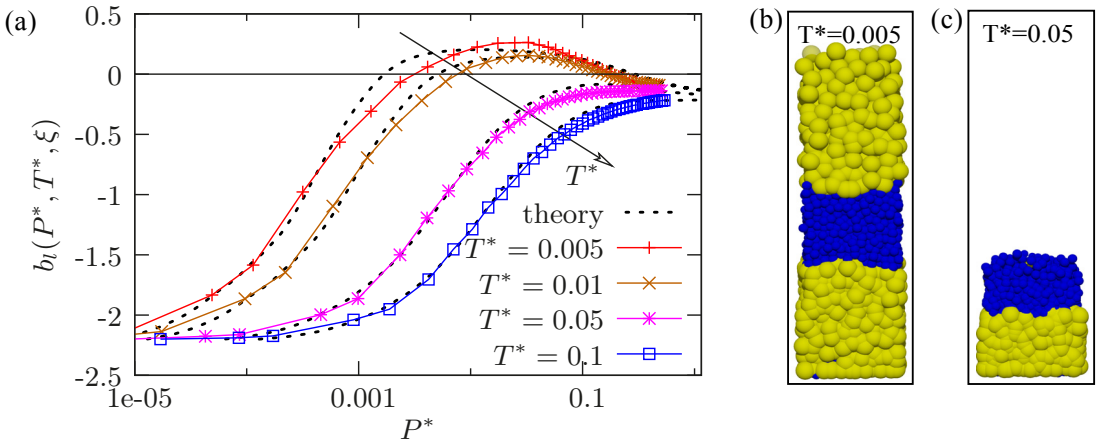

Figure 4.4: Buoyancy functions b_l as function of the pressure for $\xi = 2.5$ and (a) for different temperatures, computed from simulations (colored linepoints) and from calculated theoretically (dashed curves). The uppermost curve ($T^* = 0.005$) corresponds to a final 3-phase-stacking displayed in (b), whereas the simulation snapshot displayed in (c) belongs to $T^* = 0.05$ and shows only a 2-phase-stacking in the final state. This is expected from the corresponding buoyancy functions.

our simulations (see Fig 4.3(e)). However, we also observe an unexpected non-equilibrium behavior at the interface of the two phases. Particles at the interface are arranged in bubble-like objects, where the shell consists of large and the core of small particles. Though these structures are very stable over the whole simulation run of $500\tau_B$, the behavior probably does not denote the equilibrium case. We suppose that the occurrence of these bubbles stems from the different effective softnesses of the particle species. Due to the fact that all particles have the same maximum potential, larger particles can easily have more absolute overlap with each other. Therefore, a shell of larger particles that forms during the sedimentation process is stable and hardly penetrable for a cluster of smaller particles. A shell of large particles forms when a cluster of small particles moves through the bath of large particles until the basin of small spheres is attained. However, the shell of large particles does not break up in order to release the small particles. Instead a protuberance is formed at the interface.

In Fig. 4.3 we have considered the final states for constant temperature, constant relative softness of the particles, and varying relative mass densities. In order to investigate how the buoyancy function and therefore the final states depend on the temperature or on the relative softness of the particles, we also consider systems with a fixed mass density ratio of $\xi = 2.5$ but with varying temperature (cf. Fig. 4.4(a)). While at a small temperature the buoyancy function possesses two zeros and therefore we observe a 3-phase-stacking (see also Fig 4.4(b)), for a larger temperature the buoyancy function is negative for all pressures and as a consequence for a large temperature the small particles always end up on top of the large particles (see final state shown in Fig. 4.4(c)).

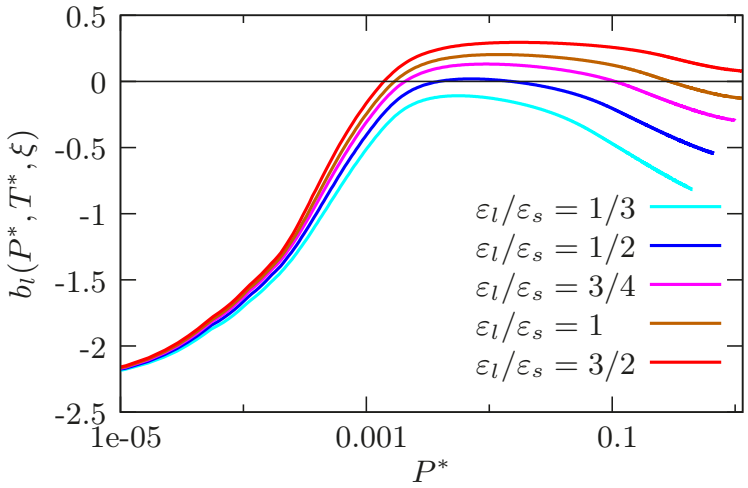

Figure 4.5: Buoyancy functions b_l calculated from the theoretical approximations in case of different softnesses of the two particle species. The relative softness is measured by the aspect ration $\varepsilon_\mathrm{l}/\varepsilon_\mathrm{s}$ of the respective potential prefactors ε_s and ε_l in case of overlaps between two small or two large particles, respectively.

Particles of distinct species may not have the same softness. Therefore, for the buoyancy functions shown in Fig. 4.5 we again fixed the temperature at $T^* = 0.005$, where the 3-phase-stacking has been found, but now vary the relative softness of the particles. The relative softness is given by the fraction $\varepsilon_\mathrm{l}/\varepsilon_\mathrm{s}$, where ε_ν denotes the prefactors of the interaction potentials of small and large particles in Eq. (4.2). Here, the temperature has been normalized with respect to the energy scale of the small particles. Our theoretical approximations predict a 3-phase-stacking in case of $\varepsilon_\mathrm{l} \approx \varepsilon_\mathrm{s}$ or $\varepsilon_\mathrm{l} > \varepsilon_\mathrm{s}$. However, for $\varepsilon_\mathrm{l} < \varepsilon_\mathrm{s}/2$, the buoyancy functions are negative for all pressures and therefore, we only expect 2-phase stackings with the softer large particles at the bottom and the small particles on top. Note, that the theoretical formalism for the prediction of buoyancy functions does not depend on the softness prefactor ε_ls for the interaction between a small sphere and a large sphere. Thus, our considerations should only be valid if mixing of the particles is not artificially supported, e.g., by a prefactor ε_ls that is much smaller than ε_l or ε_s.

4.4.4 Dynamics

In the following we discuss the dynamics of the sedimentation processes. Fig. 4.6 shows the evolution of the sedimentation for a mass density ratio $\xi = 2.5$. At time zero the particles are randomly mixed. While they sink to the ground the pressure is increased at any point within the already sedimented particles. High densities cause a segregation of large and small particles, where the larger particles either sink at high pressures or raise at low pressure regions. The final state after $500\tau_\mathrm{B}$ is shown in the last snapshot and consists of a clear 3-phase-stacking.

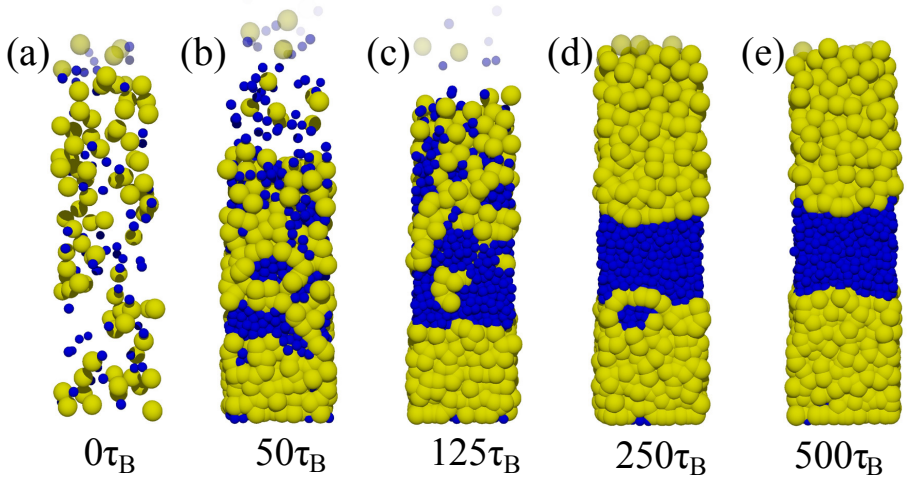

Figure 4.6: Sedimentation of small and large particles with $\xi = 2.5$ from an initial system with randomly distributed spheres with $\phi = 0.3$. The snapshots only show the bottom of the simulation box. In the final state large particles can be found below and above the smaller ones. A fully time resolved visualization of this exemplary sedimentation process is included in the supplementary video material of Ref. [1].

The segregation process consists of different steps. First the particles locally segregate. This is due to the fact that the gain in volume fraction for overlaps between particles of the same species is larger than the volume gain of overlaps between small and large particles.

In order to quantify this effect, we plot the relative gain in free volume $\Delta V_{\nu\nu'}/(V_\nu + V_{\nu'})$ due to an overlap of spheres of species ν and ν' as a function of the overlap energy $E_{\nu\nu'}$ in Fig. 4.7. The overlap energy $E_{\nu\nu'}$ is given by the respective pair interaction potentials as in Eq. (4.2). The relative gain in volume for overlaps of spheres of the same kind is energetically preferred in comparison to the volume gained by overlaps of two spheres of distinct species. The effect becomes even larger at higher energies, i.e., large overlaps. Therefore, the segregation of particle species will occur faster if the overlaps become large. For this reason the segregation in colder systems is slowed down mainly because of two influences, one being the dynamical slow-down due to the low temperature and the other being the less significant volume gain due to smaller overlaps. Indeed, in some of our simulations we could observe that at lower temperatures segregation does not take place within the whole simulation time. Unfortunately, from finite simulation time one can not discriminate between real asederotrope phases (as in the experiments by Serrano et al. [19]) and a very slow separation process. Nevertheless, one can conclude that particles in cold systems with less overlaps stay mixed at least for very long times.

At the temperatures that we usually consider in most of our simulations, in the first step

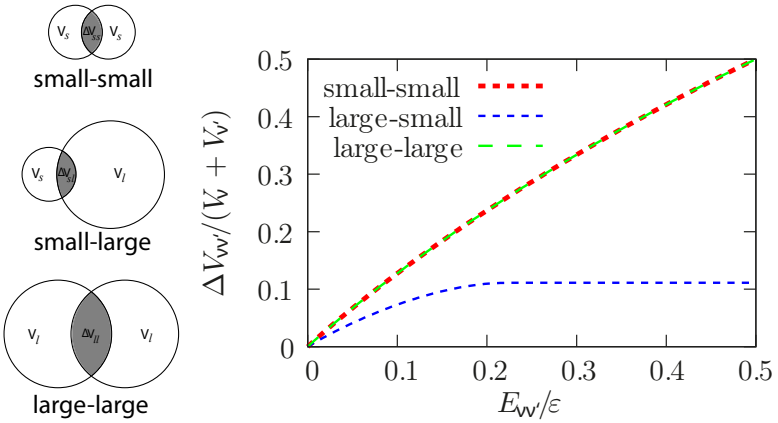

Figure 4.7: Schematic picture of the three different cases of possible particle overlaps. The plot shows the relative gain of volume $\Delta V_{\nu\nu'}$ between two particles of species ν and ν' as a function of their overlap energy $E_{\nu\nu'}$.

the particles locally segregate and we observe the formation of clusters of the particles that are unstable in the region they are located. In the next step these clusters raise or sink. Finally the clusters merge with the phase consisting of the same particles at the top or bottom of the system. Note that the merging process can take a long time and might include the formation of protuberances as we have already mentioned at the end of the previous section.

In order to study the cluster formation and movements, we perturb final states by adding additional small or large particles such that we can observe the relaxation process of the additional particles in detail. We begin with the state that for granular systems is referred to as the reverse Brazil nut effect. Here, small particles lay on top of the larger ones. We choose $\xi = 1.8$, which is the threshold value for such a stacking (cf. Fig. 4.3(b)). Now we add a small amount of large particles and let them sediment on top of the small particles. In Fig. 4.8 the resulting relaxation process is shown. First, larger particles stay segregated from the small ones on the top. Then they form a cluster, which subsequently is able to pass through the barrier formed by the small particles. The cluster sinks downwards and finally merges with the lower phase of large particles. The process repeats several times with other clusters until a stable final state is recovered.

If the initial state is the other way around, i.e., large particles are on top of the small ones (as in Brazil nut systems), we observe how additional small particles also pass the central zone of large spheres by forming clusters. In Fig. 4.9 we show the dynamics of such a relaxation process for $\xi = 3.5$ (see also Fig. 4.3(e) for the corresponding final state). Interestingly, the cluster formation of small particles only occurs at sufficiently high pressures and densities. While in the diluted regions close to the top of the system the small particles slip through voids between the large particles and therefore penetrate the central zone of large particles one by one, this is no longer possible if the particles are further away from the top region, i.e., when the pressure becomes larger and overlaps

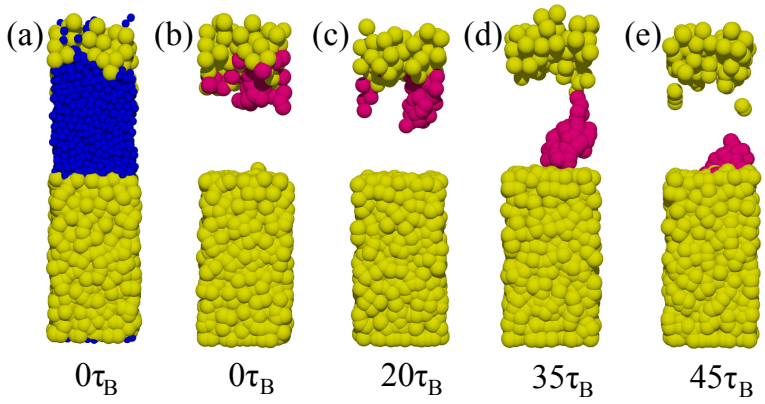

Figure 4.8: Snapshots of a system with small particles (blue) sitting on large particles (yellow) at a mass density ratio of $\xi = 1.8$ (cf. Fig. 4.3(b)). The system is perturbed by additional large particles that are placed on top of the final state. The snapshots (b)-(e) shows the resulting relaxation process. The small particles have been faded out for better insight on the large spheres. First, a cluster of large particles (for better visibility colored magenta) emerges from the unstable top layers of larger particles, then the cluster sinks through the basin of small particles until it merges again with the stable ensemble of the larger particles. A movie of this cluster sedimentation can be found in the supplementary material of Ref. [1].

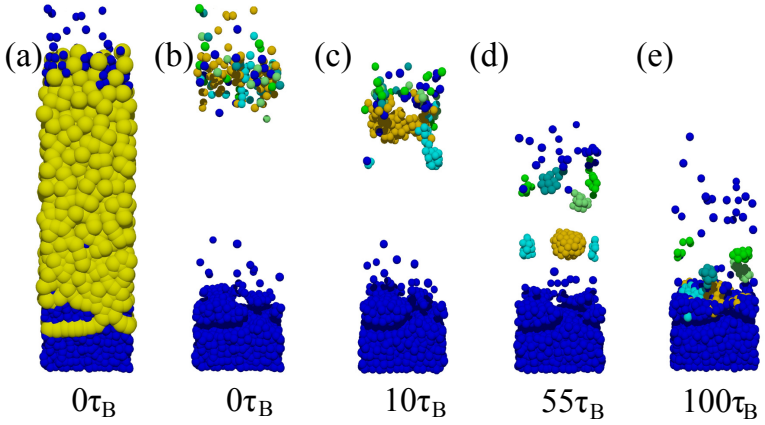

Figure 4.9: Snapshots of a system with large particles on top of small particles at $\xi = 3.5$ (cf. Fig. 4.3(e)). Additional small particles are added on the top. The relaxation process is displayed in (b)-(e) where the larger particles are faded out and clusters of small particles are marked by different colors. The newly added small particles first penetrate the zone of large particles where they form clusters. The clusters then sink to the interface, where they may remain in bubbles or form protuberances that are meta-stable and stay for a long time.

between large particles become more pronounced. At the depth, where the motion of single small colloids through the voids of large particles is no longer efficient, formation of clusters of small particles sets in. Subsequently these clusters pass through the zone of large particles. When the clusters reach the interface, they usually remain stable for a long time while they are still surrounded by a shell of the opposite species (cf. description in the previous section and Fig. 4.3(e)).

4.5 Conclusions

We have presented approximative theoretical predictions for the final states of a sedimentation process within a binary colloidal soft sphere system and confirmed them by Brownian dynamics simulations. The results turned out to differ significantly from the behavior of sedimenting hard spheres. For example, we observe 3-phase-stackings as well as metastable or long-lasting network-like structures. Furthermore, the sedimentation process is even more comprehensive. In order to demonstrate the relaxation process, we have perturbed sedimented states by adding particles on top of already finished sedimentation profiles. We observe that particles do not sediment homogeneously through the zone of the other species in order to re-establish the equilibrium state, but they rather aggregate into clusters and sink to the ground cooperatively.

We want to mention that, if the buoyancy function b_l that we introduced in Section 4.4.2 possesses two zeros, our theory will even allow for a 4-phase-stacking with small particles on top followed by large particles, then small particles again, and finally large particles at the bottom. The reason, why we did not observe such a stacking, is that the first zero occurs at very small pressures such that for our gravitational strength the uppermost small particle phase is only stable within a small layer. However, further investigations with other pair interactions or other parameters might lead to situations where the 4-phase-stacking is stable.

For our analysis we employed a harmonic model pair potential. However, we expect that our method and the reported mechanisms of separation are also valid for other soft particle systems whenever significant overlaps between the particles occur. Furthermore it would be interesting to study the particle separation process in a system of a soft granular material, where in addition to the buoyancy effects studied here also inertia effects might be important.

Chapter 5

Structure and particle correlations close to a wall

Preface. The present chapter is based on the paper "*Anisotropic pair correlations in binary and multi-component hard-sphere mixtures in the vicinity of a hard wall: a combined density functional theory and simulation study*" [2], which has been submitted to the journal *Physical Review E*. It contains literal adoptions of text and figures. Whereas the introductory section of this chapter is not fully regarded in the paper, the subsequent sections contain only minor modifications of the original manuscript.

5.1 Introduction and the hard-sphere (HS) limit

In theory, the interaction between two particles is often described analytically by using approximations or assumptions for the actual physical system. For example, soft colloids are often treated in the fashion of soft model-potentials. Typical models describe the interaction between star-polymers [165–167], polymer coils [168] or microgel particles [169]. For such model potentials a limiting case occurs in BD simulations at very low temperatures, as long as the potential drops to zero at a finite distance [91]. In this special case the interaction potential between particles becomes very steep compared to the thermal energy. Due to this fact particles are no longer able to notice the softness and the underlying system becomes *hard sphere* (HS) like, as the temperature is lowered sufficiently [91, 170, 171]. The HS system is a purely theoretical model system. Still, its outstanding importance as a universal model for the explanation of a variety of experimental setups is prevailing. As a matter of fact, the monodisperse version of a HS system crystallizes already at a packing fraction closely below 0.5 [172]. For this reason, polydispersity is studied in theories and simulations [46, 173]. It has a major influence on the solidification and the formation of amorphous glassy materials. In the early days of research on simple liquids, systems were assumed to be as simple as possible, in other

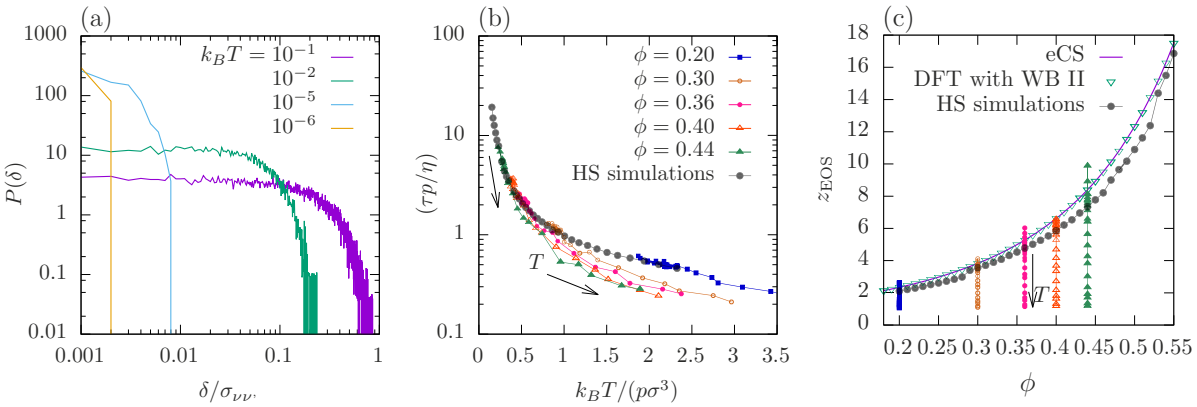

Figure 5.1: The HS limit of binary (50:50) mixtures with diameters σ_1 and $1.4\sigma_1$, represented in different diagrams: (a) The probability $P(\delta)$ for finding a pair of particles with an overlap of δ is plotted for different temperatures in a double logarithmic representation and for constant a packing fraction of $\phi = 0.3$. (b) Typical relaxation times against $k_{\mathrm{B}}T/(p\sigma^3)$ for systems with different temperatures and packing fractions. The black dotted curve corresponds to the HS limit simulation. Arrows indicate increasing temperature. (c) The equation of state z_{EOS} as a function of the total packing fraction ϕ. The black dotted curve is HS limit data, the purple solid line is the analytic prediction from Ref. [114] (cf. Eq.(2.86)). The green triangles are calculated from our DFT, as explained in the text.

words monodisperse and homogeneous. For these and advanced studies, like for example binary systems, typically integral equations and bridge functions were formulated [135] to describe the second order (pair) correlations between particles [174–177].

Throughout the whole thesis soft model-potentials are used. In Chapter 4 a binary mixture of ultra-soft particles was employed, since the main feature, which gave rise to the various results, is the ability of the particles to penetrate each other up to a certain degree. In this chapter the feature of the *hard sphere limit* will be used. One could ask, why no hard core interaction between the particles with momentum conserving hard collisions has been implemented in the first place. The answer to that question stems from the nature of the simulation method. In BD simulations, the thermal input is modelled statistically, although it originated from the bath of smaller surrounding molecules. At a constant timestep the stepwidth of a particle is drawn from a Gaussian. This means in return, that the particle will very probably make only a small random jump in a random direction. But there is also a very low probability for the particle to make a larger jump. Unfortunately, when simulation times and the number of particles become large, the *event driven* technique, which would be able to solve this problem, causes a rather poor computational performance. It is more efficient to allow for small overlaps between particles and simulate them close to being hard spheres.

The pair potential again reads

$$v_{\nu\nu'}(r) = \begin{cases} \frac{\varepsilon}{2}\left(1 - \frac{r}{\sigma_{\nu\nu'}}\right)^2 & r \leq \sigma_{\nu\nu'} \\ 0 & \text{else} \end{cases} , \tag{5.1}$$

where r is the distance beween the two particles centers and where ν and $\nu^{'}$ are their species. $\sigma_{\nu\nu'}$ again is the intermediate diameter of the two particle species. The prefactor ε in Eq. (5.1) fixes the energy scale of the potential and is therefore the only parameter being changed during a cooldown to the HS regime. However, if $\varepsilon/k_{\mathrm{B}}T$ is around one, the potential is very soft and particles at high densities are even overlapping, which can lead to multiple reentrant transitions for the jammed state [161] or also multiple rheological changes [178]. However, for such soft particles the assumption of a fixed diameter as in Eq. (5.1) does not hold. In these systems it is possible to calculate an effective particle width via an approximation that has been elaborated by Andersen et al. [179].

At sufficiently low temperatures, when the prefactor is dominating over the thermal energy, i.e., that $\varepsilon/k_{\mathrm{B}}T \gg 1$ holds, the particle overlaps become very small and the definition of an intermediate diameter σ_ν as used in the model potential makes sense. To illustrate the transition from soft to hard interactions, we have investigated a structural, a dynamic and a thermodynamic property of a binary system under the aspect of decreasing temperature. Fig. 5.1 shows the corresponding plots for bulk situations. For the bulk-plots we have studied small systems with only 1000 particles. In the later considerations, where we study the impact of a wall, we employ a cubic simulation box with side length l, periodic boundary conditions in x- and y-direction, and walls at $z = 0$ and $z = l$, where the same harmonic overlap potential as in Eq. (5.1) is used for the walls. In these simulations $N = 32000$ particles are used, such that the box is large enough to avoid confinement effects such as non-trivial correlations of particles with both walls.

First, in Fig. 5.1(a) it is shown how the convergence against the well defined and universal HS limit arises in structure. This is nicely represented by a vanishing width of the distribution of particle overlaps with decreasing temperature. As the temperature is still of the order of the particle interactions (*purple curve*), large overlaps are possible and the effective diameter of particles is significantly below the model parameter $\sigma_{\nu\nu'}$. As temperature decreases, a sharp distribution around 0 emerges. The limit distribution for hard particles would be a δ-peak.
Second, in Fig. 5.1(b) the dynamical behavior is shown in dependence of the average relaxation times of the particles. Here, τ corresponds to the typical time that the intermediate scattering function needs to drop below a certain threshold. In the presented data this threshold has arbitrarily been set to $f(k = 2\pi\rho^{1/3}, t = \tau) = 1/e$. The (normalized) relaxation time is plotted against $k_{\mathrm{B}}T/(p\sigma^3)$, which is a uniform measure for systems with different temperatures and pressures [91]. As one can see, the colored curves of different packing fractions converge against the black dotted mastercurve, which represents the HS limit. The datapoints first approach this curve when a certain temperature is undershooted. Consequently, the datapoints simply follow the mastercurve.
Finally, in Fig. 5.1(c) the equation of state is shown for the same data. While the packing

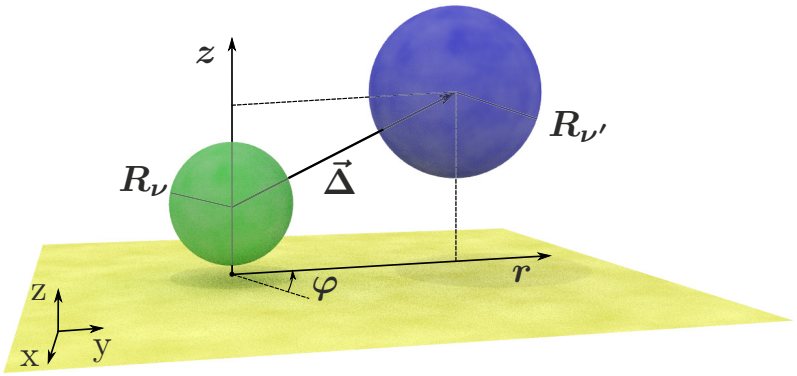

Figure 5.2: Sketch of two hard spheres of different species ν and ν' close to a hard wall. Their respective positions $\mathbf{r}$ and $\mathbf{r}'$ (not shown) define their relative distance $\mathbf{\Delta} = \mathbf{r}' - \mathbf{r}$. Particle diameters are $\sigma_\nu = 2R_\nu$ and $\sigma_{\nu'} = 2R_{\nu'}$. We employ cylindrical coordinates z, r, φ around the green (left) sphere.

fraction of the soft particles is held constant, z_{EOS} converges against the prediction of Eq. (2.86). In order to obtain HS like results for denser systems the temperature had to be significantly lower than in the diluted systems. Therefore temperature adjustments in the HS simulations have been made while increasing the density. These adjustments result in little "jumps" of the mastercurve at $\phi = 0.29, 0.47$ and 0.53[1]. Via the framework of DFT the equation of state with pressure $p = -\Omega/V$ [98] can be determined by the minimization of the grand potential Ω. The calculated values are shown by the green triangles and coincide with the eCS from Eq. (2.86). In summary, it can be observed, that all major properties of the underlying model become universal in the corresponding low temperature simulations.

5.2 Model

We investigate monodisperse, binary, and six-component mixtures in front of a wall, which we access with both classical density functional theory (DFT) and Brownian dynamics (BD) computer simulations in the HS limit. For the latter, the number of particles of each species ν is fixed, i.e., at a 50:50 mixture in case of a binary system. In the grand canonical framework of DFT all species are assumed to have the same averaged number densities in a reference bulk system. In case of the binary system, the spheres have diameters σ_1 and $\sigma_2 = 1.4\sigma_1$ in order to avoid crystallization effects [32].

The wall is located in the $xy-$plane at position $z = 0$ (see Fig. 5.2). To express two-particle correlations, we consider one sphere at position (x', y', z') as reference particle such that the positions (x, y, z) of all other particles can be expressed in cylindrical

[1]Note, that some values slightly overshoot the theoretical prediction. This is not a real effect, but it is rather due to the statistical noise.

coordinates relatively to the reference sphere. As a consequence, two-particle correlations depend on the distance z' of the reference sphere to the wall, the distances z of the other particles to the wall, and the distance $r = [(x-x')^2 + (y-y')^2]^{1/2}$ between the particles and the reference sphere measured parallel to the wall. All other coordinates are integrated out due to symmetry. As a consequence, no crystallization or other symmetry breaking ordering parallel to the wall is resolved.

5.3 FMT and OZ calculations restricted in half space

As a flat wall is introduced to the system due to the symmetry of the structure close to that wall, all density profiles ρ_ν as well as all derivatives $\partial^2\Phi/(\partial n_\alpha \partial n_\beta)$ in Eq. (2.92) solely depend on the spatial coordinate z, perpendicular to the wall. Furthermore, the direct correlation functions only depend on three coordinates, i.e., $c^{(2)}_{\nu\nu'} \equiv c^{(2)}_{\nu\nu'}(r, z, z')$.

For numerical reasons, we sample our functions on a distance L between the wall and the bulk fluid and on equidistant discrete points $z_i = i d_\mathrm{z}$ with $d_\mathrm{z} = L/M$ for $i = 0, \dots, M-1$. When we consider intervals $I_i = [z_i - \frac{1}{2}d_\mathrm{z}, z_i + \frac{1}{2}d_\mathrm{z}]$, we can split the integration volume $V = \mathcal{R}^3$ on the right-hand side of Eq. (2.92) into slices $V_i = \mathcal{R}^2 \times I_i$ and rewrite the direct correlation functions as

$$-c^{(2)}_{\nu\nu'}(\mathbf{r}, \mathbf{r}\,') \approx \sum_{i=0}^{M-1} \sum_\alpha \sum_\beta \frac{\partial^2\Phi(z_i)}{\partial n_\alpha \partial n_\beta} \times \int_{V_i} \mathrm{d}\mathbf{r}\,'' \, w^{(\alpha)}_\nu(\mathbf{r}\,'' - \mathbf{r}) w^{(\beta)}_{\nu'}(\mathbf{r}\,'' - \mathbf{r}\,'). \tag{5.2}$$

In order to calculate the direct correlation functions, it is necessary to compute the integral in Eq. (5.2), which for given combinations of particle species and weight functions solely depends on the interval I and the distance $\mathbf{\Delta} = \mathbf{r}\,' - \mathbf{r}$. Thus, we define auxiliary functions

$$W^{(\alpha\beta)}_{\nu\nu'}(I, \mathbf{\Delta}) := \int_{\mathcal{R}^2 \times I} \mathrm{d}\mathbf{r}\,'' \, w^{(\alpha)}_\nu(\mathbf{r}\,'') w^{(\beta)}_{\nu'}(\mathbf{r}\,'' - \mathbf{\Delta}) \,, \tag{5.3}$$

which we pre-compute analytically whenever possible. This reduces the computational cost significantly. For further details about the calculations we refer to Appendix A.4.

Finally, the knowledge of the density profiles ρ_ν and of the direct correlations $c^{(2)}_{\nu\nu'}$ enables us to determine the total correlations $h^{(2)}_{\nu\nu'}$ via the OZ relation from Eq. (2.93). It is useful to solve this relation partially in Fourier space to exploit the symmetries of our system. For this purpose, we define an in-plane Fourier or Hankel transform (see Appendix A.3) by

$$\begin{aligned} \mathrm{H_r}\big\{h^{(2)}_{\nu\nu'}(\cdot, z, z')\big\}(K) &\equiv h^{(2)}_{\nu\nu'}(K, z, z') \\ &= \frac{1}{2\pi} \int_0^\infty \mathrm{d}r \int_0^{2\pi} \mathrm{d}\vartheta \, r h^{(2)}_{\nu\nu'}(r, z, z') e^{-\imath K r \cos(\vartheta)} \,, \end{aligned} \tag{5.4}$$

which only assigns the radial components of a function and usually is employed to obtain structure factors of layers parallel to a symmetry-breaking wall (cf. [180]). With such a transform, the OZ relation from Eq. (2.93) can be re-written in the form

$$\mathrm{H_r}\big\{h^{(2)}_{\nu\nu'}(\cdot,z,z')\big\}(K) = \mathrm{H_r}\big\{c^{(2)}_{\nu\nu'}(\cdot,z,z')\big\}(K) + 2\pi \sum_{\nu''=1}^{n} \int_{-\infty}^{\infty} \mathrm{d}z''\, \rho_{\nu''}(z'') \times \Big[\mathrm{H_r}\big\{h^{(2)}_{\nu\nu''}(\cdot,z,z'')\big\}\mathrm{H_r}\big\{c^{(2)}_{\nu''\nu'}(\cdot,z'',z')\big\}\Big](K). \tag{5.5}$$

For several values K, we determined the total correlations from this equation using an iterative numerical scheme (see Sec. 2.6.4 or, for a more sophisticated approach, Appendix A.1). In order to cope with numerical circumstances, we define our discrete lattice for the radial coordinate r in a way that the value $r = 0$ is avoided in real space. For this reason, we solely provide data, where the radial component is very close but not equal to zero.

5.4 Results

In this section we quantitatively compare the results that we obtain from our multi-component DFT and the (BD) simulations. First, we focus on one-particle densities. Second, we bear in mind the anisotropy in our system and consider the two-particle correlations. Consequently, all these results are employed in order to quantitatively analyze the contact properties of particles. These contact values are directly related to the anisotropic force distribution acting on a particle. As a result, the net force for a particle can be determined (cf. [51]). The nonuniform distribution of forces leads to the differences between effective diffusion coefficients in different directions and therefore to anisotropic diffusion paths as we will discuss in the next chapter.
Finally, we demonstrate the impact of polydispersity by a comparison between our findings for a binary and a six-component mixture. In this context we discover a significant improvement of the agreement between the predictions of DFT calculations and the results of BD simulations for an increasing number of particle species.

5.4.1 One-particle density profiles

In Fig. 5.3 we show density profiles of both DFT calculations and BD simulations for small and large particles in our binary (50:50) mixture of hard spheres. The bulk densities have been fixed such that the corresponding total packing fractions are deep in the liquid phase ($\phi = 0.3$), close to the fluid-crystal transition in monodisperse systems ($\phi = 0.48$), and in the regime where glassy dynamics sets in ($\phi = 0.54$). The most obvious differences between DFT calculations and BD simulation results occur in the second-layer peak of the density profiles. Especially in the profiles of higher bulk densities, the second-layer

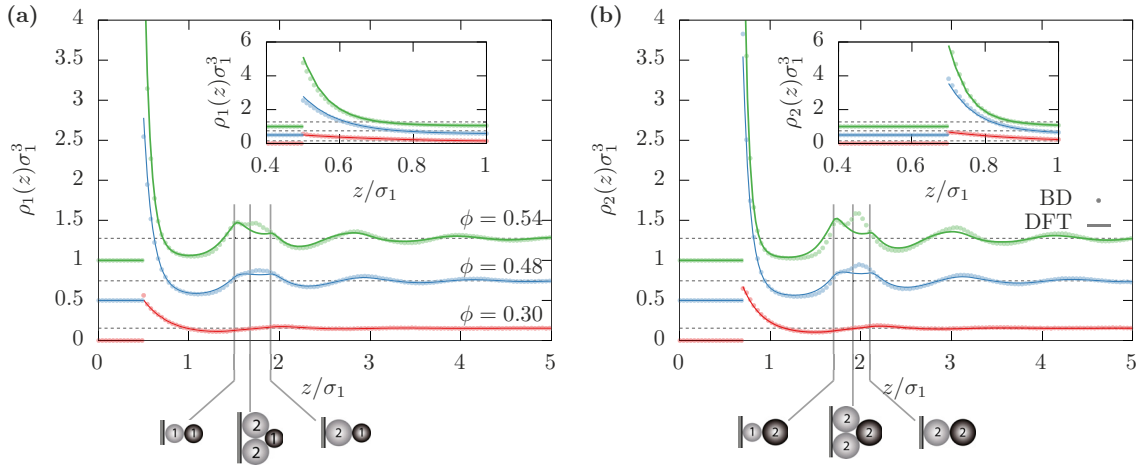

Figure 5.3: Density profiles of (a) small and (b) large particles in binary (50:50) mixtures of hard spheres with diameters σ_1 and $\sigma_2 = 1.4\sigma_1$ in the vicinity of a flat hard wall (at $z = 0$). Circles represent simulation data, whereas results of DFT calculations are given by solid lines. To enhance readability, density profiles are shifted for different packing fractions by 0.5 ($\phi = 0.48$) and 1.0 ($\phi = 0.54$) upwards and the dashed lines denote the bulk values. The small sketches at the bottom of the figures mark distinct packings of spheres.

peak splits up into two peaks in case of the simulation results (circles in Fig. 5.3) or they just contain shoulders in case of the DFT predictions (solid lines). Each local peak or shoulder can be connected with a particular stacking of particles belonging to different species, as illustrated by some exemplary sketches at the bottom of Fig. 5.3. Note that local crystal-like ordering is not precisely captured in our DFT approach because we assume translational invariance along the wall. As a consequence, as soon as such locally ordered structures are preferred by the system, our DFT predictions become less accurate, even though the overall structure is not yet a crystal. Accordingly, the overall agreement between simulations and theory is very good for low packing fractions.

5.4.2 Two-particle correlations

In DFT, the two-particle or pair correlations can be obtained via the test-particle or the compressibility route. For the first, density profiles are determined around a fixed test particle which results in an effective two-particle density. We follow the compressibility route, where the direct correlation functions $c^{(2)}_{\nu\nu'}$ from DFT are used to close the OZ relation (Eq. (2.93), or more precisely, Eq. (5.5)). Using the WBII functional, we obtain the density profiles ρ_ν and direct correlation functions $c^{(2)}_{\nu\nu'}$, where we calculate the latter directly via Eqs. (5.2) and (5.3) for our inhomogeneous system.

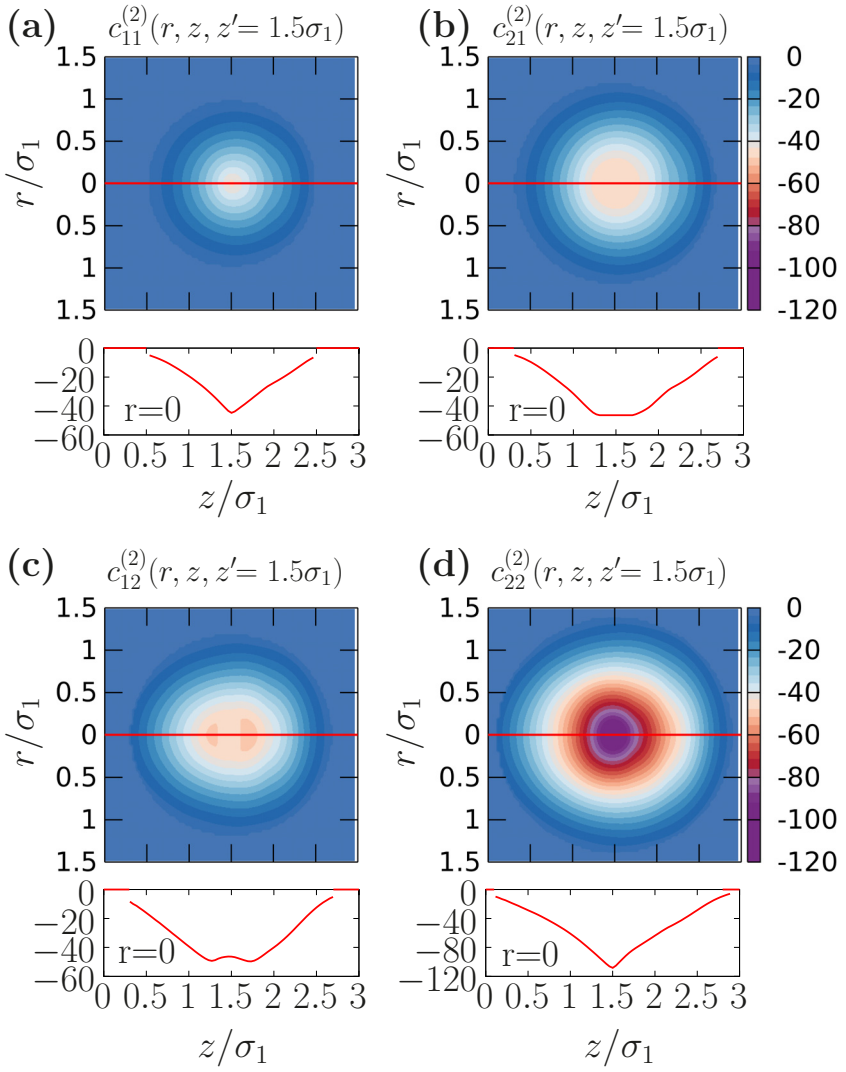

Figure 5.4: Direct correlation functions obtained from DFT using Eqs. (5.2) and (5.3) for the binary HS mixture as explained in the text. The reference particle is fixed at $z' = 1.5\sigma_1$. For a second particle at position r, z we show the direct correlations (a) $c_{11}^{(2)}$ between small and small, (b) $c_{21}^{(2)}$ between large and small, (c) $c_{12}^{(2)}$ between small and large, and (d) $c_{22}^{(2)}$ between large and large particles. Note that the second index always denotes the fixed reference particle. The total volume fraction is $\phi = 0.5$. Below the contour plots the profile along the z-axis with $r = 0$ are shown (marked by red lines in the contour plots).

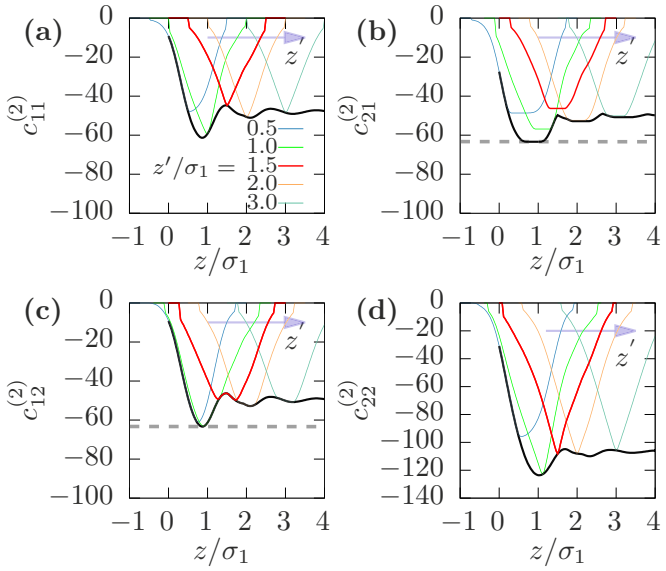

Figure 5.5: Direct correlation profiles along the z-axis as shown in Fig. 5.4, but for various positions z' of the reference particle. The profiles from Fig. 5.4 with $z' = 1.5\sigma_1$ are shown in solid bold red. Again, the correlations are between (a) small and small, (b) large and small, (c) small and large, and (d) large and large particles. In addition, the envelopes of all profiles are shown. The horizontal stroked lines mark the depths of the minima in (b) and (c), which are equal.

Direct correlations. The direct correlations are shown exemplarily in Figs. 5.4-5.6 for the binary mixture of hard spheres. First, in Fig. 5.4, we compare $c_{\nu\nu'}^{(2)}$ for the four combinations between the two species with each other (small-small, large-small, small-large, and large-large). The position of the reference particle is fixed at $z' = 1.5\sigma_1$ and the direct correlations are plotted as functions of the position of the other particle, where the position can be expressed in the natural cylindrical coordinates (r, z). In addition, we show the profile along the z-axis together with each plot. While the correlations between two large or two small particles only differ by a constant factor and by the length scale, the correlations between a small and a large particle depend on which particle is used as reference particle. In both cases the direct correlation functions do not have one clear minimum. While in case of a small reference particle there is a plateau with an extent of $0.4\sigma_1$ in z-direction, in case of a large reference particle there are two distinct minima at $z \approx 1.3\sigma_1$ and $z \approx 1.7\sigma_1$.

Note that in bulk, both correlation functions between large and small particles are identical (see Appendix A.2) and possess a plateau for $r < 0.2\sigma_1$ where the direct correlation function is constant. The plateau is due to the fact, that in the FMT for the 3D-fundamental measures the intersection volume of two spheres does not change as long as the smaller one is located completely inside the large one (for an illustrative sketch see Fig. A.1(a) in Appendix A.2). Therefore, the value of the integral in Eq. (2.92) does not change and the observed plateau develops.

Back to the anisotropic case of Fig. 5.4, a similar explanation holds: when the position

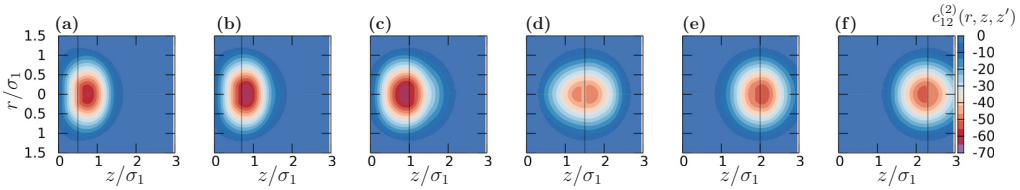

Figure 5.6: Direct correlation functions $c_{12}^{(2)}(r, z, z')$ as shown in Fig. 5.4(c) for a large reference particle at different positions z', which are marked by vertical lines at (a) 0.5, (b) 0.7, (c) 1.0, (d) 1.5, (e) 2.0, and (f) 2.3.

of a small particle is fixed, as in Fig. 5.4(b), the integration volume V in Eq. (2.92) is restricted to the shape of this particle as long as the small particle is completely contained inside the larger one. In contrast, when a large particle is fixed, as in Fig. 5.4(c), the previously mentioned integration volume depends on the position of the small particle. Thus, the result of the integral in Eq. (2.92) depends also on the relative positions of the particles[2]. The resulting direct correlation function is similar to the self correlations between two small particles, because the relevant combinations of weight functions $w^{(\alpha)}$ that enter Eq. (2.92) give the same results in this case (for further details see Appendix A.4, Case 3).

In Fig. 5.5 we compare slice cuts of the direct correlation profiles along the z-axis for various positions z' of the reference particle. Additionally, we draw the envelope to all shown profiles. Figures 5.5(a) and (c) demonstrate the similarity between small-small and small-large correlations, which was mentioned in the previous paragraph.

In Figs. 5.4(c) and 5.5(c), we observe a splitting of the minimum of the direct correlation function into two minima. The splitting occurs for the parameters where the direct correlation functions reach local maxima in the corresponding envelope of the profiles as can be seen in Fig. 5.5(c). This suggests that there exists a z-dependent maximum correlation for a particular combination of species. In Fig. 5.6 we show a series of direct correlation functions with varying position z' of the reference particle.

These positions are marked by vertical lines and, obviously, the absolute minima of the direct correlations are located in the vicinity of these positions. Specifically, the global minima of the direct correlation functions shown in Fig. 5.6 can be found at $z > z'$ in (a), (b), and (e), but at $z < z'$ in (c) and (f). In (d) the minimum is split into two local minima on both sides of the center of the reference particle. This behavior can again been understood from studying the corresponding profiles in Fig. 5.5(c), where the shape of the region around the minimum of each profile always follows the maximum possible correlation, given by the envelope.
The anisotropic arrangement of the direct correlation around the center of the reference particle will lead to the emergence of an anisotropic force, as we will show in the later sections.

[2]The position dependence enters via the derivative of the excess free energy density Φ.

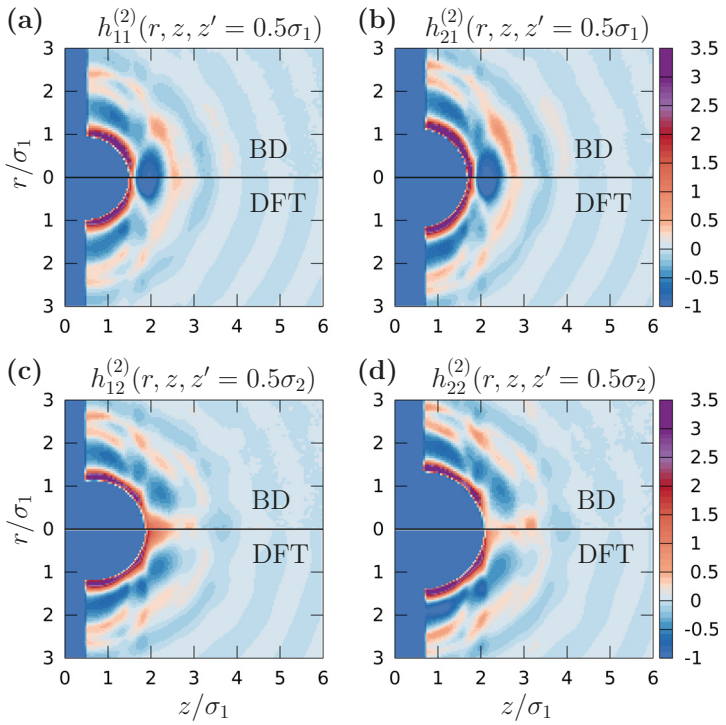

Figure 5.7: Total correlation functions $h_{\nu\nu'}^{(2)}(r, z, z')$ for a reference particle at position $z' = 0.5\sigma_{\nu'}$ between (a) small and small, (b) large and small, (c) small and large, and (d) large and large particles, where the second particle denotes the reference particle. The packing fraction is $\phi = 0.5$ in the bulk limit and each plot is split up into data from BD simulations (upper half) and DFT results (lower half), where the total correlation functions were determined via the OZ equation. Note that in case of the DFT calculations all numerical artifacts at forbidden positions (inside the wall and inside the reference particle) have been reset to -1.

Total correlations. Starting from the direct correlations and one-particle densities determined with DFT, we calculate the total correlations between two particles using the OZ relation from Eq. (5.5). As mentioned in Sec. 5.3, this equation is exact, but we have to deal with numerics in order to perform this transformation. Especially the finite number of Fourier modes in our discretization gives rise to artifacts. We illuminate the impact of the artifacts by means of bulk calculations in Appendix A.2. There we show, that basically the resulting total correlation functions show unphysical values differing from -1 inside the core. Note that this behavior not only originates from numerical inconveniences during solving the OZ relation but also depends on the inconsistency of the approximate excess free energy functional we have used. Such inconsistencies are common for all approximate functionals and could only be resolved by the exact functional, which in general is not known [104].
In our case the specific artifacts in the forbidden regions could be avoided by employing the earlier mentioned test-particle route, where one particle is fixed at a position in

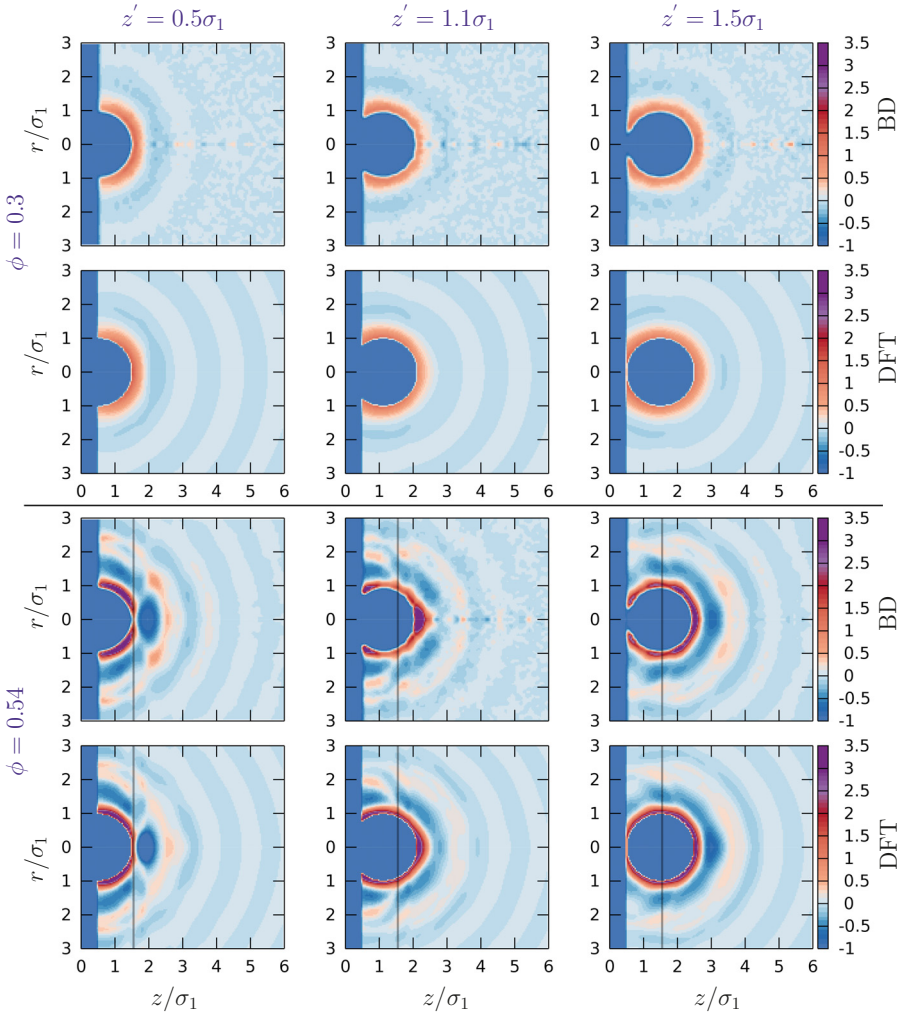

Figure 5.8: Total correlations $h_{11}^{(2)}(r, z, z')$ between small and small particles with diameter σ_1. The reference particle is fixed at a position z' and the position of the other particle is given in cylindrical coordinates (r, z). The hard wall is located at $z = 0$. BD data is shown in the first and third row, DFT results in the second and forth row. In the two rows at top a low packing fraction $\phi = 0.3$ is employed, while a high density case with $\phi = 0.54$ is shown in the two bottom rows. Each column denotes a different position z' of the reference particle ($z'/\sigma_1 = 0.5$, 1.1, or 1.5). All numerical artifacts at forbidden positions have been removed and reset to -1 in case of DFT results. The speckled pattern in the lower density simulation data arises from poorer statistics at the location of local minima in the density close to the z-axis with $r = 0$. The vertical lines in the bottom panel indicate the position of the profiles shown in Fig. 5.9.

front of the wall whilst the number density around it is calculated with the help of DFT. However, this route is expected to show deviations in other regions of the profiles where the compressibility route might work more precisely. Furthermore, solving for the two-particle correlations via the compressibility route provides a better computational performance. Deviations between both routes could provide a measure for the consistency of functionals.

Similar to Fig. 5.4, we show the total correlation functions for all possible pairs of particles in Fig. 5.7. In addition to our results determined with DFT and the OZ relation, we plot the total correlations obtained from BD simulations. Simulation results are presented in the upper half of each plot, in the lower half the immediate comparison to the DFT results is shown. In general, both DFT calculations and BD simulations show good agreement for all total particle correlations. However, as we have already noted in case of the direct correlation function in the previous subsection, the corresponding local structures are usually underestimated by DFT predictions whenever local ordering occurs. For example, deviations can be seen in Figs. 5.7(a) and (b), where simulations lead to stronger correlations between the fixed reference particle and a second particle at ($r \approx 1\sigma_1$, $z \approx 2.2\sigma_1$). At this position, particles in the second layer of a local fcc or bcc structure are located. Such orderings occur more often for higher packing fractions and they are not incorporated in our DFT approach.

In Fig. 5.8 a small reference particle is fixed at different positions z' and the total correlation with another small particle at position (r, z) is shown. Besides the previously discussed small deviations, the comparison between DFT calculations and BD simulations in general reveals a good quantitative agreement.

In order to study possible deviations in more detail, we show the profiles along the vertical lines in the bottom panel of Fig. 5.8 separately in Fig. 5.9. Note that this data is taken at the rather high packing fraction $\phi = 0.54$ where glassy dynamics sets in. Nevertheless, the overall agreement is still good. The most pronounced differences occur close to particle contact. In the simulation data this behavior is affected by two effects: on one side, the slight softness of the repulsive interactions, and on the other side, the uncertainty of the actual position of the reference particle due to the discretization of the z-axis. In the next subsection, we study contact values and resulting forces on the test particle in more detail.

5.4.3 Contact values and anisotropic forces

Anisotropy in structure results in an anisotropic distribution of forces acting on a particle. Obviously, such an anisotropic distribution can result in a non-vanishing net force. The force distribution and the net force depend on the total pair correlations at particle-particle contact. For this reason, we explored the value of the total pair correlation functions $h_{\nu\nu'}^{\mathrm{cont}} = g_{\nu\nu'}^{\mathrm{cont}} - 1$ at particle-particle contact. Note that the condition of contact effectively reduces the amount of independent parameters by one, i.e., $(r, z, z') \to (z, z')$.

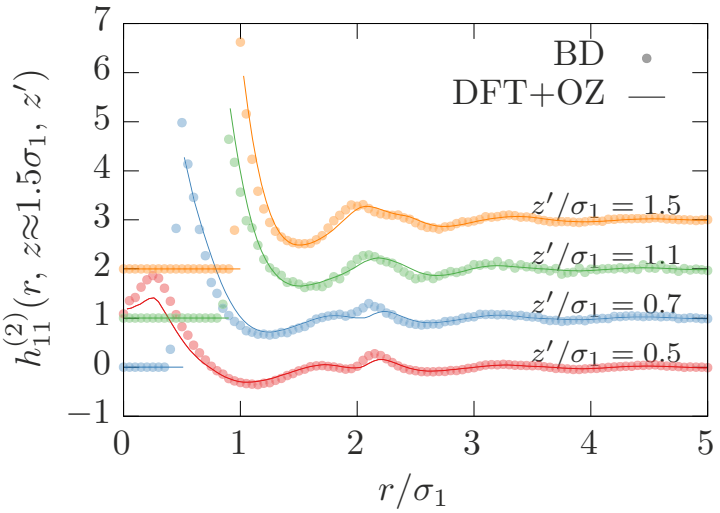

Figure 5.9: Profiles of the total correlation function $h_{11}^{(2)}$ along the vertical lines drawn in Fig. 5.8 and located at the second layer of particles ($z = 1.55\sigma_1$). The packing fraction of the system is $\phi = 0.54$ and the slice cuts are shown for three positions z' of the fixed reference particle. The solid lines denote DFT data and circles represent results from the respective BD simulations. For DFT all total correlations at forbidden positions have been reset to -1 and the curves have been shifted by 0.0, 1.0, 2.0, 3.0 (from bottom to top).

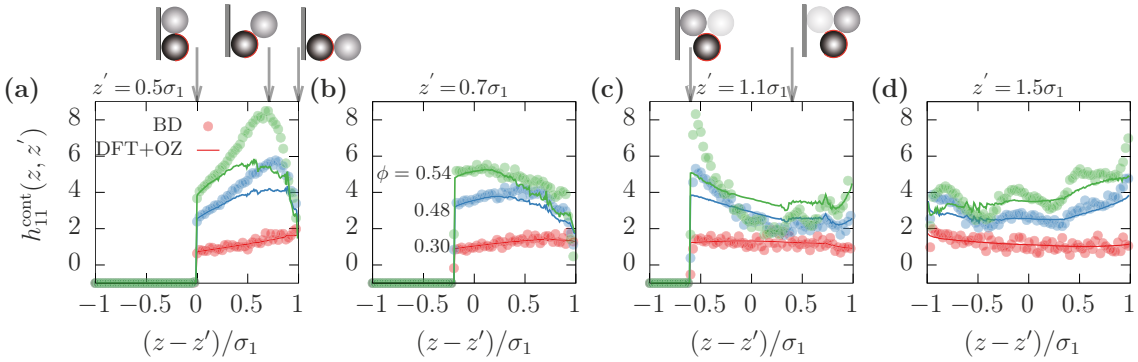

Figure 5.10: The total correlation function $h_{11}^{\mathrm{cont}}(z, z')$ at contact of a small reference particle at position z' with a small neighbor particle at wall distance z. The position of the reference particle z' is (a) $0.5\sigma_1$, (b) $0.7\sigma_1$, (c) $1.1\sigma_1$, and (d) $1.5\sigma_1$. Data from BD simulations (circles) and DFT results (lines) are shown for packing fractions $\phi = 0.30$ (bottom curves), 0.48 (center curves), and 0.54 (upper curves), as marked in plot (b). The sketches above the figures illustrate certain arrangements of neighbor particles with the respective $(z - z')$ positions.

In Fig. 5.10 we present the contact values along the surface of a small reference particle in a binary mixture, which is located at several distances from the wall. Starting in Fig. 5.10(a) with wall contact, the reference particle is slowly detached from the first layer at the wall in Figs. 5.10(b) and (c) until it reaches the second layer in Fig. 5.10(d). For these different positions, we compare results obtained from our BD simulations with the results calculated from DFT and the OZ relation. We find reasonable overall agreement. However, aside of statistical noise, some details of the data reveal significant differences: First, in Fig. 5.10(a) the total correlations $h_{\nu\nu'}^{\mathrm{cont}}(z, z')$ obtained from the simulations exhibit a very pronounced maximum at around $(z - z')/\sigma_1 \approx 0.71$ in case of the two systems with higher densities. The contact values obtained from DFT also possess maxima at these positions, but they are less pronounced. Probably, this is again due to the neglect of the local structure parallel to the wall in our theory. Indeed, the simulation data show some entropically favored contact correlations which are most obvious by the stronger oscillations in Fig. 5.10(d).

As mentioned before, anisotropies in structure also cause anisotropic force distributions. For such a situation we have introduced the PMF (Eq. (2.39)) and the accompanied mean force (Eq. (2.40)) as a function of the reaction coordinate that is z in our case. Recalling the derivation from the introductory chapter (Sec. 2.5), it reads

$$f_{\nu,\mathrm{z}}(z) = k_{\mathrm{B}}T \frac{\partial \ln\big(\rho_\nu(z)\big)}{\partial z}\,. \tag{5.6}$$

Now, the Lovett-Mou-Buff-Wertheim equations [181, 182] can be used to connect the gradient of the density profile, and therefore the resulting mean force, with the two-particle direct correlations by

$$f_{\nu',\mathrm{z}}(z') = 2\pi k_{\mathrm{B}}T \sum_{\nu=1}^{n} \int \mathrm{d}z\, \mathrm{d}r\, r c_{\nu\nu'}^{(2)}(r, z, z') \frac{\partial \rho_\nu(z)}{\partial z} \tag{5.7}$$

and via an orthogonality relation for the density-density correlations (cf. Eq. (2.105)), which was introduced within the derivation of the OZ relation (see Sec. 2.8), the mean force can also be connected with the pair correlation functions leading to [181]

$$f_{\nu',\mathrm{z}}(z') = 2\pi k_{\mathrm{B}}T \sum_{\nu=1}^{n} \sigma_{\nu\nu'} \int \mathrm{d}z\, \rho_\nu(z) g_{\nu\nu'}^{\mathrm{cont}}(z, z') \frac{z' - z}{\sigma_{\nu\nu'}}\,. \tag{5.8}$$

Note that Eqs. (5.6) and (5.8) provide an exact relation between a one- and a two-particle correlation, because Eq. (5.8) corresponds to the first member of the Born-Green-Yvon hierarchy [51, 52].

In Fig. 5.11, we plot the net forces obtained from our theoretical calculations via Eqs. (5.6), (5.7), and (5.8); in comparison, we additionally plot the forces directly obtained from our BD simulations. Clearly, the net forces that are theoretically obtained via the density profiles as in Eq. (5.6) match the simulation results very well. However, at high densities we observe a significant deviation between the curves at around $z = 1.9\sigma_1$, where the small

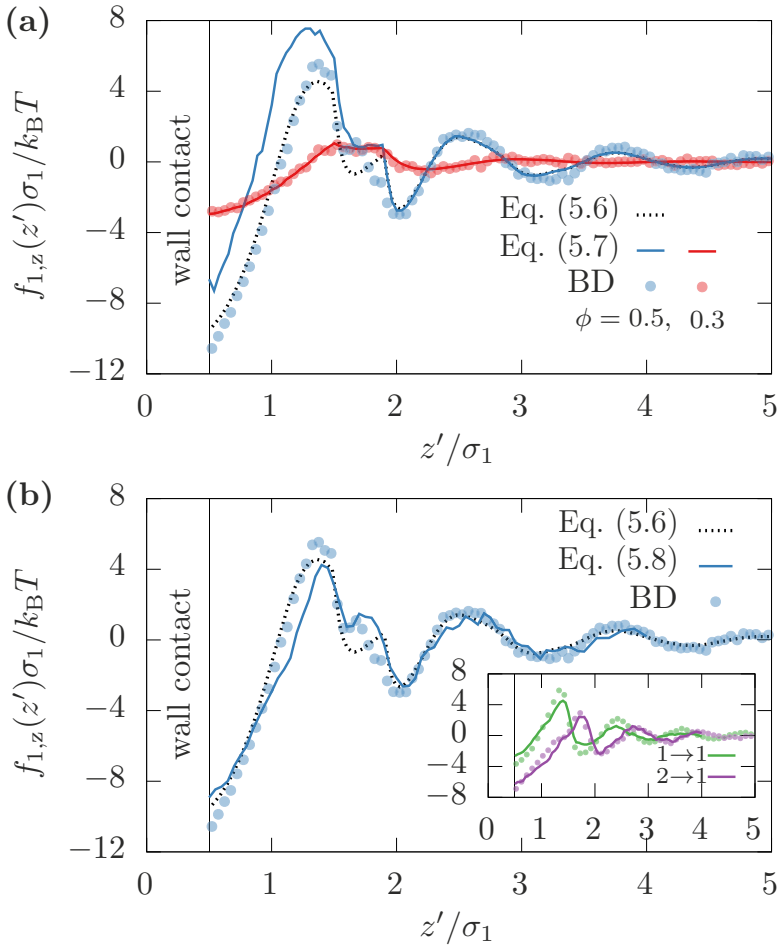

Figure 5.11: Normalized force $f_{1,z}$ on a small test particle at position z' in z-direction, which originates from the surrounding particles in a binary mixture at packing fractions $\phi = 0.5$ (blue) or 0.3 (red). Data from BD simulations is plotted with circles. For comparison, different methods to predict the force distribution from DFT are shown: Employing the potential of mean force as in Eq. (5.6) leads to the dotted lines, the solid lines in (a) denote the force distribution calculated from the direct correlations as in Eq. (5.7) for both packing fractions ($\phi = 0.5$ and 0.3), while the solid line in (b) corresponds to the distribution determined via the pair correlations as in Eq. (5.8) for the larger packing fraction ($\phi = 0.5$) only. The inset in (b) shows the separated contributions from small ($1 \to 1$) and large ($2 \to 1$) particles to the mean force at $\phi = 0.5$.

test particle can stack exactly on top of one large particle that is in contact with the wall and where local ordering might have a pronounced influence on the particles structure. Employing Eqs. (5.7) and (5.8) lead to forces that deviate from the simulation results for $z < 1.9\sigma_1$. These differences are probably due to the thermodynamic inconsistency of the functional, which for example manifests in the differences between the compressibility and the test-particle route. Note that Eq. (5.6) corresponds to the test-particle route, because it solely involves the density profiles, while Eqs. (5.7) and (5.8) involve the direct correlations. The latter seem to capture the behavior around $z = 1.9\sigma_1$ better, while the results from Eq. (5.6) have a better agreement close to the wall.

In the inset of Fig. 5.11(b) we finally separate the contributions from small and large particles to the net force on the small test particle. Close to the wall, the large particles push the small test particle stronger to the wall than the small particles do. If the test particle is moved away from the wall, first the contribution from the small particles reverses its direction such that they start pushing the particle away from the wall. For the larger particles the reversal of force direction occurs at a larger distance. Between the positions of these two reversals of directions, the resulting net force is small.

Differences between Eqs. (5.7) and (5.8). Even if Eqs. (5.7) and (5.8) are equivalent, only Eq. (5.8) allows directly to decode which directions contribute most to the net force and which species of neighboring particles has most impact on the average force of a certain particle. The contributions to the net force which result from different species are shown in the inset of Fig. 5.11(b). Contrarily, this information is contained only indirectly in Eq. (5.7). Thus, splitting up the sum in Eq. (5.7) leads to force contributions, which on the one hand add up to the overall force but on the other hand only represent forces with respect to direct correlations, whose impact must be integrated (via the OZ relation) over all possible amounts of intermediate particles in order to yield the actual interaction between a combination of two particular species.

5.4.4 Comparison between one-, two- and six-component mixtures

For an increasing amount of components in a mixture, local ordering is suppressed even at high densities. As we will show in the following the signatures of local structures in one- or two-particle correlations are smeared out with an increasing number of components. As a consequence, DFT calculations that neglect some types of local ordering become more accurate in such a type of polydispersity.

In Fig. 5.12 we demonstrate this effect for a packing fraction of $\phi = 0.5$, where (a) a one-component, (b) a two-component, and (c) a six-component system have been used. The binary mixture is the same as discussed throughout this work with particle diameters σ_1 and $\sigma_2 = 1.4\sigma_1$, whilst the more polydisperse system contains an equimolar mixture with particles of six discrete sizes σ_1, $1.1\sigma_1$, $1.2\sigma_1$, $1.3\sigma_1$, $1.4\sigma_1$, and $1.5\sigma_1$. In the left panel of Fig. 5.12 we show the total self-correlation function $h_{11}^{(2)}(r, z, z')$ of the smallest

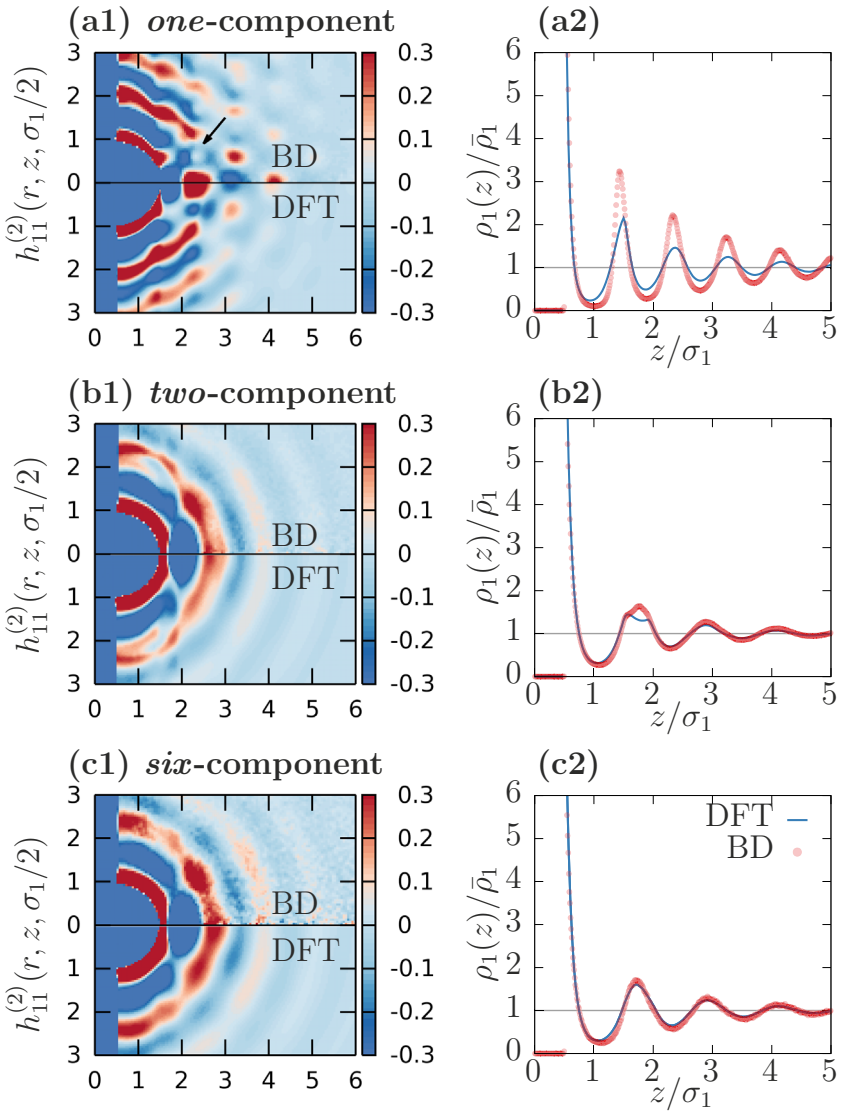

Figure 5.12: Two- and one-particle correlations at a packing fraction of $\phi = 0.5$ for (a) a *one*-component, (b) a *two*-component, and (c) a *six*-component mixture, where the distribution of particle diameters is explained in the text. All plots compare data from our BD simulations and DFT. The left panel (a1),(b1),(c1) shows the total self-correlation functions $h_{11}^{(2)}(r, z, \sigma_1/2)$, whilst the right panel (a2),(b2),(c2) illustrates the accompanied density profiles $\rho_1(z)$. The latter are shown normalized with the respective bulk density $\bar{\rho}_1$.

particles, where one particle is in contact with the wall. Obviously, for the monodisperse case the peaks are very pronounced and, due to the high packing fraction of $\phi = 0.5$ and the induced anisotropy, crystal-like structures are visible already on the two-particle level. As expected, major differences occur between DFT calculations and simulations in this case, e.g. at the position indicated by the arrow in Fig. 5.12(a1). However, the peaks due to local orderings are less pronounced if more components are added. Therefore, Figs. 5.12(b1) and (c1) show a much better agreement between simulations and theory. This result is confirmed by the right panel of Fig. 5.12, where we compare the density profiles obtained from simulations and DFT. The smoothing of these profiles, while increasing the number of components, is the result of the increasing number of possible configurations of different stackings next to the wall. As a consequence, the peaks are smeared out for an increasing number of components and the splitting of a peak can no longer be observed in case of a more homogeneous spectrum in the polydispersity distribution. Nevertheless, Figs. 5.12(b1) and (c1) already show the trend that prominent peaks in the pair correlations still occur in the polydisperse situation even for the second shell of surrounding particles. These peaks are retained even if the averaged correlation functions $h_1(r, z, z') = \frac{1}{n} \sum_{\nu=1}^{n} h_{\nu 1}^{(2)}(r, z, z')$ (not shown here) would be plotted instead of the self-correlations between solely the smallest ones. Obviously, these peaks represent the most probable positions of next-neighboring particles, no matter what size they have.

5.5 Conclusions

Using comparisons to BD simulations, we have quantitatively explored the strengths and weaknesses of the WBII FMT approach within DFT in predicting one- and two-particle correlations in hard sphere systems. In order to study anisotropic situations, we broke the symmetry and explored the behavior in the vicinity of a hard wall. Especially in case of our six-component systems, DFT led to excellent predictions even at high packing fractions. However, in case of mono- or bidisperse systems, DFT not necessarily resolved the formation of local order. We demonstrated that the compressibility route of DFT can be employed to calculate two-particle correlations, contact values, and forces acting on a particle, even in the investigated strongly anisotropic situations.

Our finding, that particularly at packing fractions above $\phi = 0.5$ two-particle correlations can be well-predicted, might turn out to be important to understand the relation of structure and dynamics of such systems. For these large packing fractions the dynamics tends to become very slow. Such a dramatic slowdown of dynamics usually is termed as glassy dynamics and its relation to structure is the subject of intensive research in experiments [43, 50, 183, 184] as well as in simulations or theory [43, 45, 51, 185]. Advanced theories that deal with glassy dynamics, e.g., mode coupling theory [186, 187] or similar approaches [39, 185, 188–190], rely on the knowledge of the structure of the system.
Our work demonstrates that FMT is a suitable approach to obtain a reliable input for these theories even in the case of anisotropic geometries, e.g., in the vicinity of a wall.

Chapter 6

Dynamics close to a wall

6.1 Introduction

In search of explanations for the dramatic slowdown of dynamics in glassy systems many different approaches and also a huge variety of theories exist, cf. Refs. [67, 191] with [90–92]. One of the most promising theories that copes with the matter of glassy systems is the so-called mode coupling theory (MCT) [191–193]. Within MCT particles are assumed to have a memory about their past. This fact results in an adaption of time-dependent transport-coefficients, which can be handled by approximations of so-called memory kernels. Whereas these theories are mostly and most easily applied for bulk-situations, the incorporation of, e.g., the external potential of a flat wall, is less studied. In this chapter, rather than with MCT, we will focus on a more simplistic and intuitive picture for the dramatic slowdown of dynamics with the help of a symmetry-breaking flat wall. Rather than as an inconvenience, we will use the wall as a feature, that enables us to study a pre-designed cage for a particle that resides in a dense environment.

We use the same model as in the previous chapter and apply the identical pair potential (Eq. (5.1)). Furthermore, we employ $\tau_B = \sigma_1^2/(3\pi D_1)$ as a suitable Brownian time throughout the whole chapter, where D_1 is the self-diffusion coefficient (cf. Eq. (3.2)). We will start with the presentation of anisotropic diffusion paths close to a wall and from this starting point step-wise deduce characteristics of the dynamics, that will in the end be used to probe a *one-particle* random-walk model. We will show, that even at high densities the main features of the dynamical process close to a wall can be described with the help of single-tracer memory and without the involvement of multi-particle dynamics. We use measured bulk history-dependent forces, apply them for our random-walk model close to the wall, and finally show, that the simulation short-time (or short-distance) dynamics can nicely be allegorized by our modified one-particle random walk.

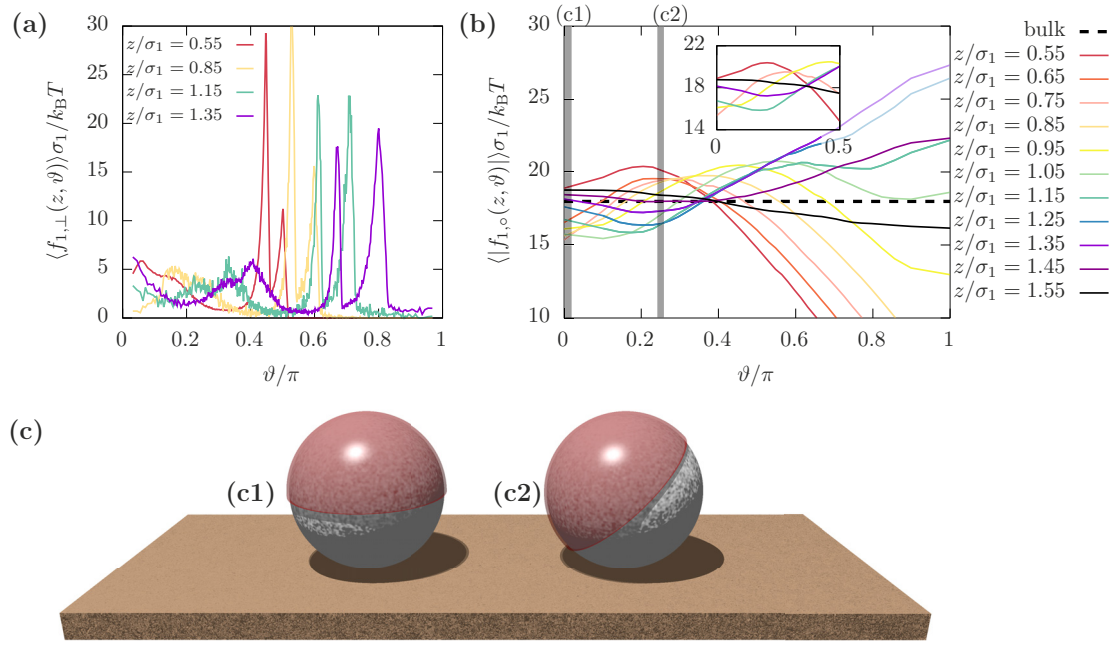

Figure 6.1: (a) Distribution of the mean normal forces that act on a small particle from different directions in a system with $\phi = 0.58$. Here, ϑ is the polar angle that determines the direction of the force (0 = top, 1 = bottom) and z is the position of the particle. (b) Cross section forces as a function of the polar angle ϑ and the position z of a small particle, compared to the bulk value (dashed line). The inset highlights the behavior on the upper hemisphere of the particles, with respect to the z-axis. The forces are results from an average over a half-spherical cross section as explained in the main text. The direction for different cross sections is determined by the angle ϑ. Two particular examples for such cross sections are indicated in the main plot, i.e., the gray lines at (c1) $\vartheta = 0$ and at (c1) $\vartheta = \pi/4$. The corresponding surfaces of these gray lines are sketched in (c) for a particle with wall contact.

6.2 Results

6.2.1 Diffusion paths of a binary mixture

In bulk it is not possible by means of two-particle correlations to identify a preferred path for the tracer out of its cage. The only thing one can do is taking into account averaged quantities and design a cage from them. It is possible to model the "*activated hopping*" [190] of particles due to fluctuations of the surrounding neighborhood in order to design a more sophisticated cage [185,189]. Since in this chapter we want to investigate the particular process, that describes the cage escape of a tracer particle through a given path (namely the z-direction), we first have to be sure, that the path is a probable route for an escape.

We use computer simulations to calculate the average normal force $\langle f_{1,\perp}(z,\vartheta)\rangle$[1] acting on a small particle's surface with respect to its position z and from a certain direction denoted by the polar angle ϑ. Fig. 6.1(a) shows these forces in a dense system with $\phi = 0.58$. The two very prominent peaks in all the distributions stem from the pair correlations with small and large particles of the first layer, respectively. As the particle detaches from the wall, the peaks shift towards the bottom hemisphere of its surface (with respect to the z-axis). However, from atop ($\vartheta = 0$) the forces become smaller. This is due to the unfavored position of a neighboring particle on top of it, which must necessarily buckle from the second density layer in order to stack with the upcoming particle. This already suggests, that the perpendicular direction is a more probable direction than the tilted one.

The above argument becomes even more manifest, when we consider total forces acting on a cross section of a particle. One can integrate over the component of the force distribution which is parallel to a certain vector $\mathbf{a}$ that points into the middle of the (half-spherical) cross section cap. We define this normalized *pointing vector*

$$\mathbf{a}(\vartheta,\varphi) = \sin(\vartheta)\cos(\varphi)\mathbf{e}_\mathrm{x} + \sin(\vartheta)\sin(\varphi)\mathbf{e}_\mathrm{y} + \cos(\vartheta)\mathbf{e}_\mathrm{z} \tag{6.1}$$

in spherical coordinates, with the additional (azimuthal) angle φ. In Fig. 6.1(c) two such cross sections are sketched, the first defined by the vector $\mathbf{a}(0,0) \equiv \mathbf{e}_\mathrm{z}$ (cf. Fig. 6.1(c1)) and the second by $\mathbf{a}(\pi/4,0) \equiv (\mathbf{e}_\mathrm{z} + \mathbf{e}_\mathrm{x})/\sqrt{2}$ (cf. Fig. 6.1(c2)). We call the resulting force $\langle f_{1,\circ}(z,\vartheta)\rangle$ the *cross section force* (marked by $\circ$). It is determined by the average

$$\langle f_{1,\circ}(z,\vartheta)\rangle = \langle f_{1,\perp}(z,\vartheta')\mathbf{a}(\vartheta',\varphi')\cdot\mathbf{a}(\vartheta,0)\rangle_{\vartheta',\varphi'}\,, \tag{6.2}$$

where the right-hand-side averages the projection of the normal force $\langle f_{1,\perp}(z,\vartheta')\rangle$ onto the direction of the pointing vector $\mathbf{a}(\vartheta)$, evaluated for a particle at a certain position z. The average is taken with the coordinates ϑ' and φ' over the whole cross section cap, where its alignment is set by the angle ϑ.
Results of the angle-dependent cross section forces are shown in Fig. 6.1(b) for different particle positions z. The curves represent forces that a particle has to countervail in order to move into that direction. However, one can nicely see the change of the forces with the angle and the particle detachment. When a particle is at contact, the cross section force exhibits a subtle local minimum perpendicular to the wall (red line, $\vartheta = 0$) and a maximum into the tilted direction (red line, $\vartheta \approx \pi/4$). The total minimum exists for the direction parallel to the plane ($\vartheta = \pi/2$)[2]. As the particle moves farther away from the wall towards the middle of the first two density layers, the minimum in the perpendicular direction becomes even more pronounced, whilst the maximum shifts towards the parallel direction, e.g., as represented by the yellow/green lines. This gives information about the fact that the "channel", which the particle has to pass in order to arrive at the second layer, becomes stabilized from the lateral sides, such that a motion in the xy-plane

[1] This force is proportional to the anisotropic distributed pressure around the surface of a particle.
[2] Note, that although the forces for larger angles are even lower, these regions cannot be entered due to the repulsive wall, which is not incorporated in the description via $\langle f_{1,\circ}(z,\vartheta)\rangle$.

is more improbable. Note, that the cross section force can be calculated from theory only within a two-body description as presented in the previous chapter, because the anisotropy of the force distribution is crucial. Thus, the prediction of drags due to, e.g., the cross section force, needs a theory, that is at least based on two-particle correlations.

In cylindrical coordinates the van Hove self correlation function $G_\nu(r, z; t)$ (cf. Eq. (2.5)) is the probability density for a particle of species ν at the point $(r, z; t)$ after it initially started at $(0, 0, 0)$. It represents in principle the fully resolved information about the diffusion pathways or preferred particle trajectories. For example the mean square displacement (MSD), which is proportional to the second moment of the self-part of the van Hove correlation function, only connects one distance with the time, where all other information is integrated out. In dilute bulk systems, the van Hove self correlation function starts as a δ-peak, that smears out as an isotropic Gaussian, where the width at long times is proportional to t.

In dense systems and close to a wall, the situation is different, as shown in Fig. 6.2. The upper panel (Fig.6.2(a)) displays $G_1(r, z; t)$ for small particles (first row) and $G_2(r, z; t)$ for large particles (second row) at $\phi = 0.50$ and for different evolution times, as indicated. The dynamics is already slowed down significantly for shorter times (Fig. 6.2, (a1-a3) and (a6-a8)), the diffusion is prohibited inside the wall, but the overall diffusion process still looks rather homogeneous. On the other hand, for a density close to the glass transition (Fig.6.2(b), $\phi = 0.58$), $G_\nu(r, z; t)$ displays a much slower diffusion process (note the different timescales). Furthermore, it becomes more anisotropic. Whereas the diffusion parallel to the wall is barely affected, smaller particles tend to use on average a perpendicular path to swap into the second layer (Fig. 6.2, (b2-b3)) before spreading into the parallel plane (Fig. 6.2, (b4-b5)). This fortifies the predictive conclusion of our calculated cross section force, where we concluded, that paths more likely are perpendicular and not tilted. However, for the large particles, the typical diffusion paths look different. First, when approaching the second layer, they remain normal to the wall (Fig. 6.2, (b6-b8)). Subsequently, when arriving at a distance of approximately $1.7\sigma_1$, trajectories branch away from the z-axis. This can be explained by a preferred stacking of large particles above small particles. If a large particle was initially located next to a small one, it raises towards the second layer until it is possible to stack with its smaller neighbor. In order to do so, it leaves the actual perpendicular path. The last plot of the time series of the large particle's van Hove function (Fig. 6.2, (a10 and b10)) suggests, that first such isolated peaks evolve before the probability density washes out in the second layer. These two mechanisms, namely the perpendicular diffusion of small and the tilted diffusion of large particles, account for local rearrangement processes. Such rearrangements also occur in the bulk case, just that in our situation the probability densities $G_\nu(r, z; t)$ are anisotropic and therefore bear pre-defined more probable diffusion paths due to the local structural neighborhood.

One might state, that preferred paths are a result of local structures. This is for sure not only the case at a symmetry-breaking wall, but also in bulk. Unfortunately, for an individual particle that resides inside its cage in bulk, there is on average no information

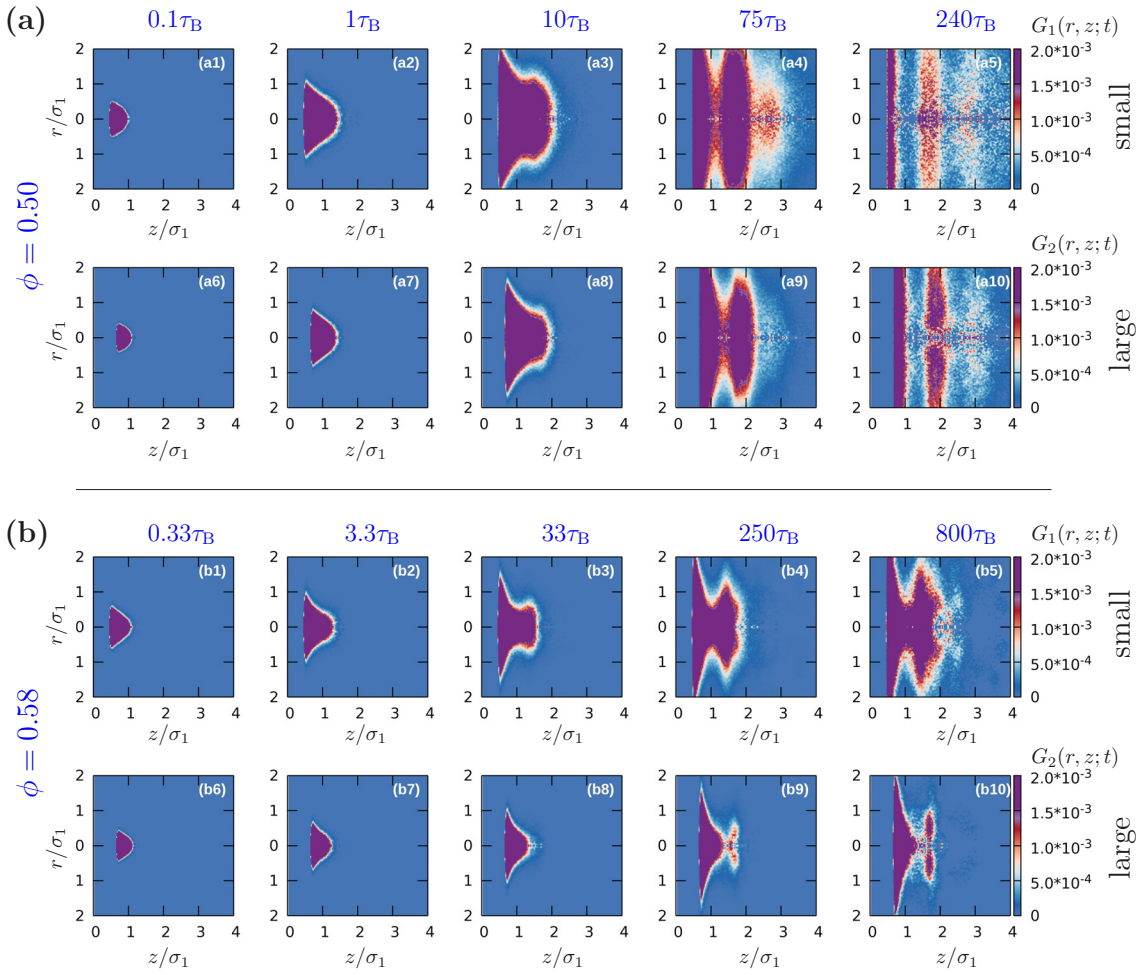

Figure 6.2: Self parts of the van Hove correlation function (cf. Eq. (2.5)) for (a) $\phi = 0.50$ and (b) $\phi = 0.58$. Plots from left to right show the functions $G_\nu(r, z; t)$ after different times, as indicated over the plots (a1-a5) and (b1-b5). The upper row of each panel (a1-a5 or b1-b5) represents data of small particles whereas the lower row of both panels (a6-a10 or b6-b10) are plots of the large particles self correlation functions. Note, that the timespan in (a) is by a factor of 1/3 smaller than in (b). The color code is unchanged for all plots and given on the right hand side of the array.

about spatially modulated two-particle correlations and therefore no direction-dependent diffusion probabilities. This is, because in bulk the cage usually is just known on average (over all possible configurations and alignments). We want to take the advantage of the knowledge of the alignment and the shape of such a cage in front of a wall in order to describe one local rearrangement process in more detail.

Let us first have a closer look at the motion of one small particle from the wall into the second layer, by means of our BD simulations. We have learned, that this process is obviously rather well described by the diffusion just along the z-axis. We now show, that the diffusion process and the accompanied escape of the cage into that direction is similar to other spatial directions, only that it is weighted with a probability to chose such a path in the first place. If we introduce $\Delta\mathbf{r}(t) = \mathbf{r}(t) - \mathbf{r}(0)$ (with the respective components (x, y, z)) we can plot in Fig. 6.3 the normalized MSDs of small particles in different directions, i.e., in z-direction,[3]

$$\left\langle \Delta z(t)^2 \right\rangle = \frac{1}{N_1} \sum_{i=1}^{N_1} \big(z_i(t) - z_i(0) \big)^2 \tag{6.3}$$

parallel to the wall,

$$\left\langle \Delta r(t)^2 \right\rangle = \left\langle \Delta x(t)^2 \right\rangle + \left\langle \Delta y(t)^2 \right\rangle \,, \tag{6.4}$$

and the radial MSD into certain solid angle $[\vartheta_\mathrm{I}, \vartheta_\mathrm{II}]$,

$$\left\langle \Delta\mathbf{r}(t)^2 \right\rangle_{[\vartheta_\mathrm{I},\vartheta_\mathrm{II}]} = \frac{1}{N_1'} \sum_{i=1}^{N_1} \theta\big(\vartheta_i(t) - \vartheta_\mathrm{I}\big)\theta\big(\vartheta_\mathrm{II} - \vartheta_i(t)\big) \big(\mathbf{r}_i(t) - \mathbf{r}_i(0) \big)^2 \,, \tag{6.5}$$

where in the formulas we have used the Heaviside step function $\theta(.)$ and the number of considered particles N_1', i.e., the number of non-zero addends. The last equation represents the diffusion process of selected particles, that move only into the desired direction. Their final positions after time t are restricted to $\vartheta_\mathrm{I} \leq \vartheta_i(t) \leq \vartheta_\mathrm{II}$.

The MSDs from Fig. 6.3(a) are calculated with respect to different starting positions, i.e., $z(t=0)/\sigma_1 = 0.55, 0.95, 1.55$, where in Fig. 6.3(b-d) the particles always start at wall contact. As it is clearly visible in Fig. 6.3(a), the effect of different starting positions has major impact on the shape of the vertical MSD for intermediate or high packing fractions. If the test particle starts inside a layer, i.e., the maximum of the density profile ($z_1/\sigma_1 = 0.55$, 1.55), it immediately feels the impact of the confining cage at that position. This fact makes it to become trapped at short and intermediate times and only jump after larger waiting times. Furthermore, if a particle starts in the second layer, it is able to jump forward or backward. Therefore, especially at shorter times the diffusion is enhanced by a factor of approximately 2 with respect to a particle that starts in front of the wall. Contrarily, if the starting position is in between the first two layers ($z_1/\sigma_1 = 0.95$), the diffusion in z-direction is larger for short times and smaller for

[3]Note, that for reasons of simplicity the index 1 for the smaller particle species has been omitted.

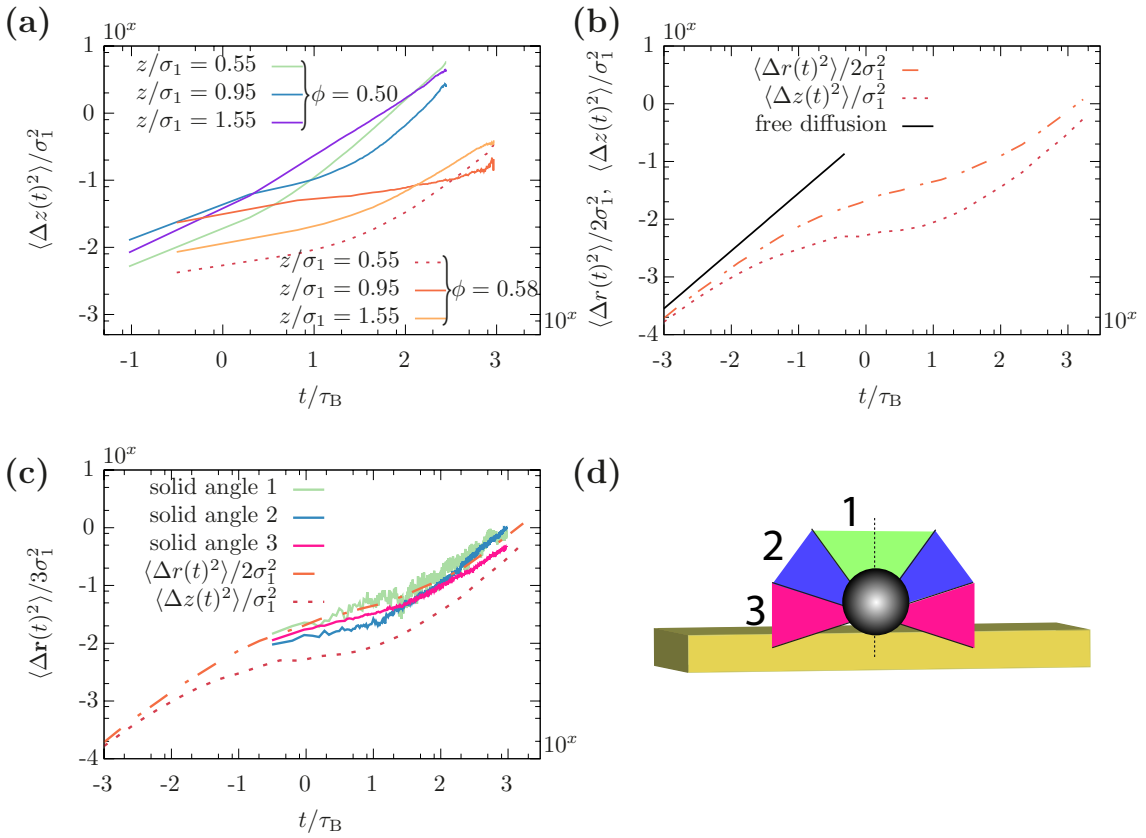

Figure 6.3: Double logarithmic plots of the mean squared displacements (MSD) of small particles (species 1). (a) The MSDs in z-direction for two packing fractions and three different starting positions of the respective trajectories. (b) The dashed curves show the normalized MSD parallel ($\langle \Delta r^2 \rangle$) and perpendicular ($\langle \Delta z^2 \rangle$) to the wall, compared with the analytic expression of the free diffusion (solid black). The packing fraction for the dashed lines in this plot and the following is $\phi = 0.58$. (c) The dashed curves are the same as in (b), whereas the solid lines represent normalized radial MSD ($\langle \Delta \mathbf{r}^2 \rangle_{[\vartheta_I, \vartheta_{II}]}$), for which the average has only been performed over a subset of particles, that have moved into the given solid angle (see Eq. (6.5)). The considered ranges of angles describing these directions (1,2,3) are sketched in (d): the intervals in the standard representation of the polar angle ϑ are (1)=$[0, \pi/5]$, (2)=$[\pi/5, 2\pi/5]$, and (3)=$[2\pi/5, 3\pi/5]$.

long times. This is due to the fact, that the starting position for such a particle is less stable, because it is unfavorable to stay in between two layers. Successively, when the particle relocates along the z-axis, it inevitably reaches one of the neighboring layers, where it will stay stable for a typical period. However, as we want to investigate the local rearrangement from one stable position to another, in the following, we will always consider particles, that start at the wall.

In Fig. 6.3(b) we plot the MSD for the higher packing fraction ($\phi = 0.58$) parallel and perpendicular to the wall in comparison with the free diffusion. The averaged curves suggest, that the diffusion process in the z-direction is stronger alleviated than parallel to the wall. This is of course the case, when we take the average over all particles. However, as anticipated in Fig. 6.3(c), the MSD with pre-selected directions (see Eq. (6.5) together with the demonstrative sketch in Fig. 6.3(d)) look all rather akin and fall approximately onto the curve of the parallel wall diffusion from Fig. 6.3(b). This intriguing finding motivates for the following conclusion: The diffusion behaves similar in all spatial directions. Since in the usual representation of the MSD the displacement is weighted by the probability of the accompanied sampling in a certain direction, a more pronounced plateau emerges when inspecting less probable directions, e.g., as in Fig. 6.3(b).

One has to be careful with the interpretation of the above presented averages, since a particle could for example escape in a tilted direction due to the lack of a neighboring particle at that position by chance. Furthermore, a cooperative motion with its neighbors might be possible. Such cooperativity cannot be resolved by means of simple equilibrium two-body correlations. Still, the above described perceptions motivate for the fact, that the escape in other directions can probably be treated in a similar way as the perpendicular escape, just with the difference, that some directions are more probable than others. Concerning the importance for the bulk, the completely averaged diffusion process is probably the result of the weighted composition of the separate diffusion mechanisms in all possible directions. In the following sections we will illuminate the cage escape in z-direction for our setup.

6.2.2 History dependence in dense systems

On the way to deduce atomistic descriptions of potential barriers that a particle needs to overcome in order to leave its cage into a given direction, we found out that for a small particle the escape from the cage along the z-axis is a probable process. The intermediate and restoring forces along this reaction coordinate are given by the mean force (Eq. (2.40)) that have been investigated for the same model in the previous chapter (cf. Fig. 5.11). As it will turn out, it is not sufficient to simply apply the PMF as an external field describing the confinement by a local cage. The reason is, that the PMF is the statistical average over all particles at the desired position, no matter what history they comprise. Since the particles have different histories and therefore also completely different memories, one has to reduce the description to only those particles, whose

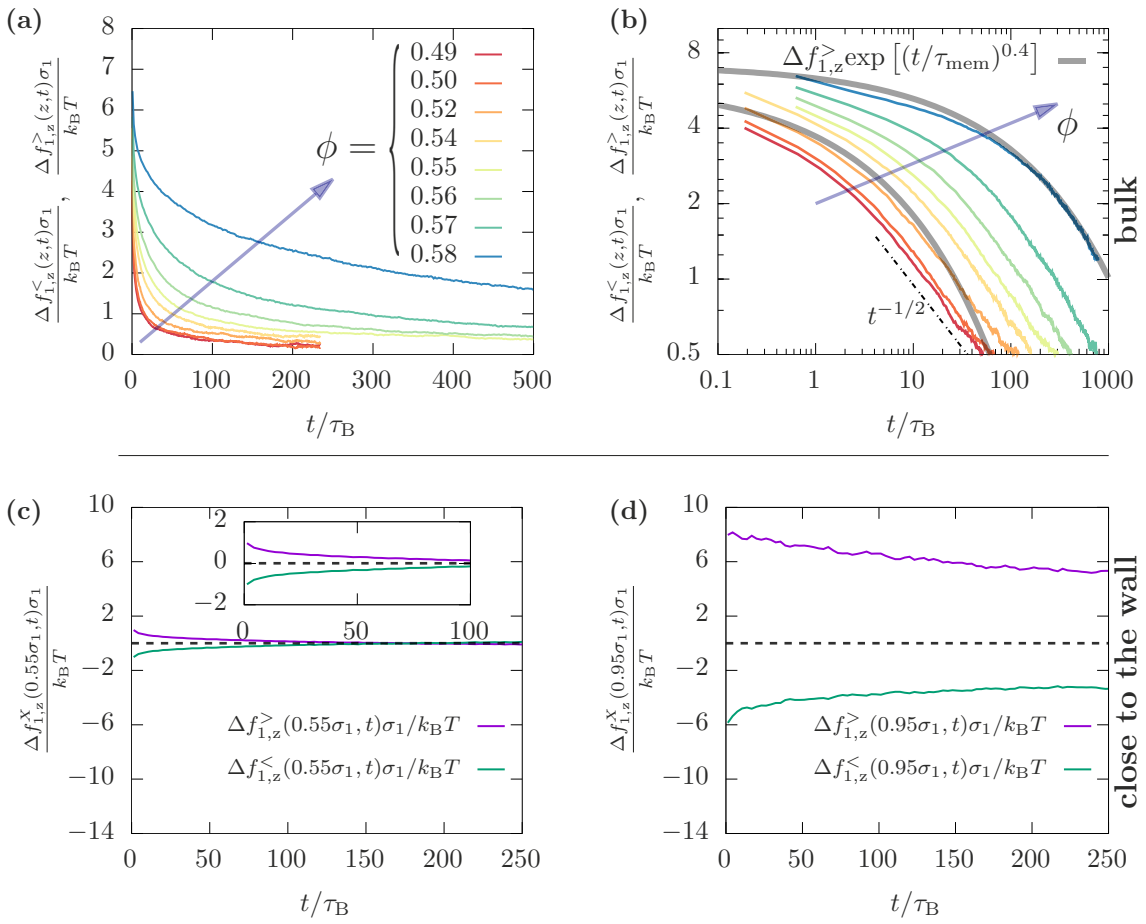

Figure 6.4: The upper panel shows the bulk force memories $\Delta f^{<}_{1,z}(z,t)$ and $\Delta f^{>}_{1,z}(z,t)$, as defined in Eq. (6.8) for different packing fractions and arbitrary z. Note, that the different force memories ($<$ or $>$) coincide in a bulk situation. In (a) a linear and (b) a double-logarithmic representation are shown, respectively. The black dashed line (b) is a power-law with exponent $-1/2$ and the thick gray lines are fits according to $\Delta f^{>}_{1,z}\exp\left[(t/\tau_{\rm mem})^{0.4}\right]$, with $\tau_{\rm mem} \approx 187.5\tau_B$ (for $\phi = 0.58$) or $\tau_{\rm mem} \approx 6.3\tau_B$ (for $\phi = 0.52$). In the lower panel the force memory is evaluated close to the wall in the case of the largest packing fraction ($\phi = 0.58$) for small particles at (c) $z = 0.55\sigma_1$ and (d) $z = 0.95\sigma_1$. The dashed black lines indicate zero.

history starts with wall contact. We elaborate a model that relies on forces acting on individual particles containing also information about their history.

In order to acknowledge the history dependence, we separately determine the forces for the following two groups of particles: Firstly, particles that at a previous time $-t$ were at a position $z(-t) > z(0)$, i.e., *above* the current position. Secondly, particles that were at a previous time $-t$ *below* the current position ($z(-t) < z(0)$). The average force on a particle, if it was *above*, is then

$$f^{>}_{1,\mathrm{z}}(z,t) = \frac{1}{N_1'} \sum_{i=1} f_{1,\mathrm{z}}\big(z_i(0)\big)\theta\big(z_i(-t) - z_i(0)\big)\,. \tag{6.6}$$

Here, $N_1^{'}$ is again the number of the considered particles only. Similarly, if in the past the particle was *below*, it is exposed to the force

$$f^{<}_{1,\mathrm{z}}(z,t) = \frac{1}{N_1'} \sum_{i=1} f_{1,\mathrm{z}}\big(z_i(0)\big)\theta\big(z_i(0) - z_i(-t)\big)\,. \tag{6.7}$$

Furthermore, we introduce the deviations from the average value $\langle f_{1,\mathrm{z}}(z)\rangle$ and call those functions the *force memories*, i.e.,

$$\Delta f^{X}_{1,\mathrm{z}}(z,t) = f^{X}_{1,\mathrm{z}}(z,t) - \langle f_{1,\mathrm{z}}(z)\rangle\,, \tag{6.8}$$

with the placeholder $X \in \{<,>\}$. In Fig. 6.4(a-b) we plot the history dependent *force memories* for bulk systems with different packing fractions in (left) linear as well as (right) double logarithmic representation. As the packing fraction is increased, two major characteristics determine the curves. The first is the starting point of the memory curve, i.e. $\Delta f^{>}_{1,\mathrm{z}}(z) := \Delta f^{>}_{1,\mathrm{z}}(z, t \to 0)$, which sets the magnitude of the force memory. The second is the timescale, on which the memory approximately decays. For the bulk, we pick out two systems, one being at intermediate packing fraction ($\phi = 0.52$) and the other one being close to the glass transition density ($\phi = 0.58$) and fit the force memories via stretched exponentials[4] [194]

$$\Delta f^{>}_{1,\mathrm{z}}(z,t) = \Delta f^{>}_{1,\mathrm{z}}(z)\exp\left[-(t/\tau_{\mathrm{mem}})^{\alpha}\right]\,, \tag{6.9}$$

where we fixed the exponent $\alpha = 0.4$, in order to obtain reasonably comparable fits. For the two shallow dark lines in Fig. 6.4(b) the characteristic memory times are $\tau_{\mathrm{mem}} = 187.5\tau_{\mathrm{B}}$ (for $\phi = 0.58$) and $\tau_{\mathrm{mem}} = 6.3\tau_{\mathrm{B}}$ (for $\phi = 0.52$).
Whilst the simulation curves seem to follow such a stretched exponential for short to intermediate times, for very old histories the memories behave like a power-law with an exponent $-1/2$. This is expected, since in an overdamped system our definition of the instantaneous force deviations are supposed to behave similar to the velocity-autocorrelation function (see, e.g., Ref. [195, 196]) that is expected to decay with an

[4]Stretched exponentials are often referred to as Kohlrausch-Williams-Watts [194] functions, which account for the approximate descriptor of a spectrum of distinct (ordinary) exponential decays and are often used to picture the relaxation of disordered systems with more than one typical timescale.

exponent of $-3/2$ in 3D [197]. Since we restrict the diffusion direction to 1D, our curves should be comparable with the 1D velocity-autocorrelation functions with a decay exponent of $-1/2$ [196].

The meaning of the force memory can be interpreted in the following way: as a particle leaves its initial location, in the case of dense systems it has to overcome an effective energy barrier that is induced by its cage. During a short-distance movement the particle already deforms its cage in such a way, that the probability of finding a neighboring particle in the direction of its movement increases. At the same time, the probability to lack a neighbor in the opposite direction also increases. This causes the particle to feel an average opposing force, the *force memory*. Such an effect is more pronounced for denser systems than for dilute suspension.

Whereas in bulk the force memory does not depend on the position z, close to the wall it does. Thus, in Fig. 6.4(c-d) we show the $\Delta f^X_{1,\mathrm{z}}(z,t)$ for the densest system ($\phi = 0.58$) at wall contact and in between the first two layers. One can nicely see the quantitative difference between the memories at the two investigated positions. For a particle, which is in the first layer and therefore very close to the wall, the force memory has only very subtle impact (Fig. 6.4(c)). Contrarily, the memory for a particle in between two layers seems to be crucial (Fig. 6.4(d)). This finding suggests that the magnitude of the force memories is position-dependent in an inhomogeneous system.
To study this further, we plot in Fig. 6.5(a) the average forces as functions of the position, with the short-time history for the particle, i.e. $f^X_{1,\mathrm{z}}(z, t \ll \tau)$, and in Fig. 6.5(b) the respective force memories $\Delta f^X_{1,\mathrm{z}}(z) = \Delta f^X_{1,\mathrm{z}}(z, t \ll \tau)$. Here, τ is the rearrangement time and in the figures we use $t = \tau_\mathrm{B}/3$, because for dense suspensions the typical rearrangement time τ is much larger than τ_B. By this choice we approximately sample the zero-time limit.

Intriguingly, as marked by the vertical lines in Fig. 6.5(b) a connection between maxima of the local density (red line) and the magnitude of the force history (green and blue lines) becomes visible. Always, when a local density peak emerges, the magnitude of the memory becomes decreased. The opposite is true for local density minima, where the magnitude of the corresponding force memories is increased. This connection makes intuitively sense: on the one hand, when particles reside inside a local density layer, they are supposed to be more stable at this position for longer times and individually occurring forces are similar. In return, this would precipitate in the average of the force memory and therefore result in a less pronounced deviation from the total average. On the other hand, when a particle is on its way from one density maximum to another, it necessarily crosses a local minimum. On this crossing, its history has major influence on the average forces. For example, when the particle is moving in positive z-direction, it possibly leaves void space behind it, whereas in front of it a barrier of neighboring particles is blocking its path. Therefore, it is very likely that at such a position the memory has a large effect on the consecutive motion.

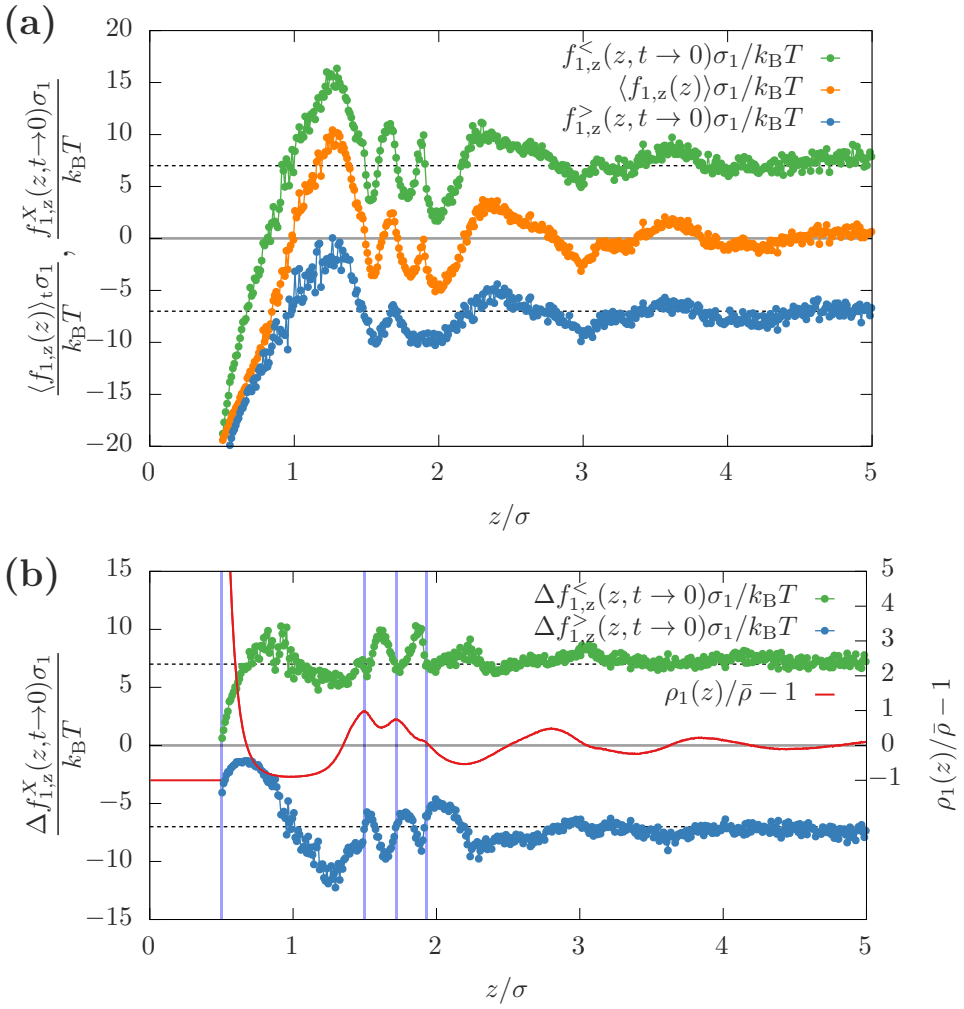

Figure 6.5: (a) History-dependent forces (green and blue lines) for small particles in a binary 50:50-mixture as defined in Eqs. (6.6) and (6.7), at $\phi = 0.58$ and as a function of their height z above the wall. The forces are calculated for $t = 1/3\tau_B$. The central orange line corresponds to the average force profile $\langle f_{1,z}(z)\rangle$. (b) Force memories (green and blue line, left axis) of the same data as in (a), in conjunction with the local density profile of the smaller particle species (red line, right axis). The vertical shallow blue lines mark local density maxima (or enhancements) in $\rho_1(z)$ and correspond to local drops of the absolute values of $\Delta f^X_{1,z}(z)$.

6.2.3 Force distribution in the hard-sphere limit

In this section we study another ingredient of Brownian systems at low temperatures. As presented in Sec. 5.1, we employ a soft model potential that is truncated. We perform BD simulations in the HS limit, where by a decrease of temperature the average forces between particles also decrease due to the constant prefactor (energy scale ε) of the potential from Eq. (5.1). However, this is not only due to smaller overlaps between the particles, but also due to the fact, that the fraction of contacts becomes significantly decreased. We will now deduce a way to estimate the probability to observe contacts in the HS limit.
The Boltzmann-factor for two particles of the species ν and ν' with the interaction potential $v_{\nu\nu'}(d)$ is proportional to the probability of finding those two particles with an overlap d. It is given by

$$P_{\nu\nu'}(d) \propto \exp\left[-\frac{v_{\nu\nu'}(d)}{k_\mathrm{B}T}\right] . \tag{6.10}$$

Since the force $|f|$ is in our harmonic model potential proportional to the overlap d (Eq. (5.1)), we can immediately rewrite the Boltzmann-factor, such that it resembles the distribution of instantaneous forces $|f|$, i.e.,

$$P_{\nu\nu'}(|f|) \propto \exp\left[-\frac{|f|^2\sigma_{\nu\nu'}^2}{2\varepsilon k_\mathrm{B}T}\right] , \tag{6.11}$$

where $\sigma_{\nu\nu'}$ is again the intermediate diameter. In Fig. 6.6(a) we plot the force distribution of our (50:50) binary systems at different temperatures, where the lowermost temperatures have been fitted according to an uniform intermediate Boltzmann-factor of such a mixture, yielding the force density (distribution of instantaneous forces)

$$P(|f|) = \frac{A\sigma_1}{4\varepsilon}\sum_{\nu,\nu'=1,2}\exp\left[-\frac{|f|^2\sigma_{\nu\nu'}^2}{2\varepsilon k_\mathrm{B}T}\right] , \tag{6.12}$$

where A is a dimensionless fitting parameter. For temperatures below $10^{-4}k_\mathrm{B}T$, the fits in Fig. 6.6(a) become sufficiently good and the prefactor of the distribution stays constant. Therefore, if we calculate the first moment of the distribution, $\langle|f|\rangle \equiv \langle|f|, P(|f|)\rangle$, the result (Fig. 6.6(b)) is inversely proportional to the temperature, as it should be. Since the force distributions follow a Gaussian, the expectancy value of a modified normalization only over non-zero forces must be proportional to $A\sqrt{k_\mathrm{B}T}$. The simulation results are shown in Fig. 6.6(c) together with a square root power-law, $P_{1,\mathrm{coll}} \propto \sqrt{k_\mathrm{B}T}$, which can be applied as a prediction of the fraction of interacting (or colliding) particles at low temperatures, where sufficiently below jamming particles exhibit only one or zero overlaps.

However, if one used the HS equation of state (Eq. 2.86) in bulk or the integration over a pre-calculated force distribution around a particle in an anisotropic situation to estimate the intermediate force (or pressure) on a particle, it would be possible to calculate the

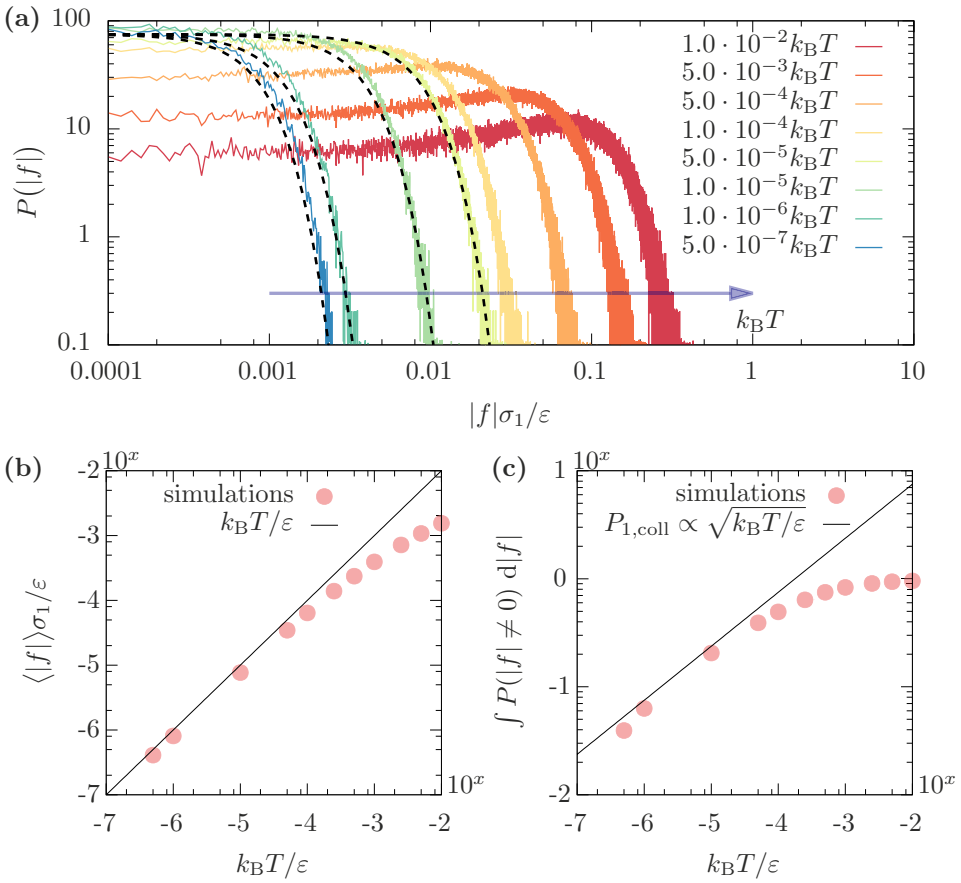

Figure 6.6: (a) Force distributions $P(|f|)$ of absolute instantaneous forces $|f|$ in a binary (50:50) mixture for the soft model-potential from Eq. (5.1), at a packing fraction of $\phi = 0.54$ and for different temperatures. The black dashed lines are fits according to Eq. (6.12). The prefactor according to Eq. (6.12) is constant, $A = 75$. (b) Average value of the instantaneous force as a function of temperature, measured in the simulations. The black line is proportional to $k_\mathrm{B}T/\varepsilon$. (c) Fraction of non-zero forces, i.e., the normalization of the distributions from (a), where the integral runs only over all non-zero forces. Points are from simulations and the line is proportional to $\sqrt{k_\mathrm{B}T/\varepsilon}$.

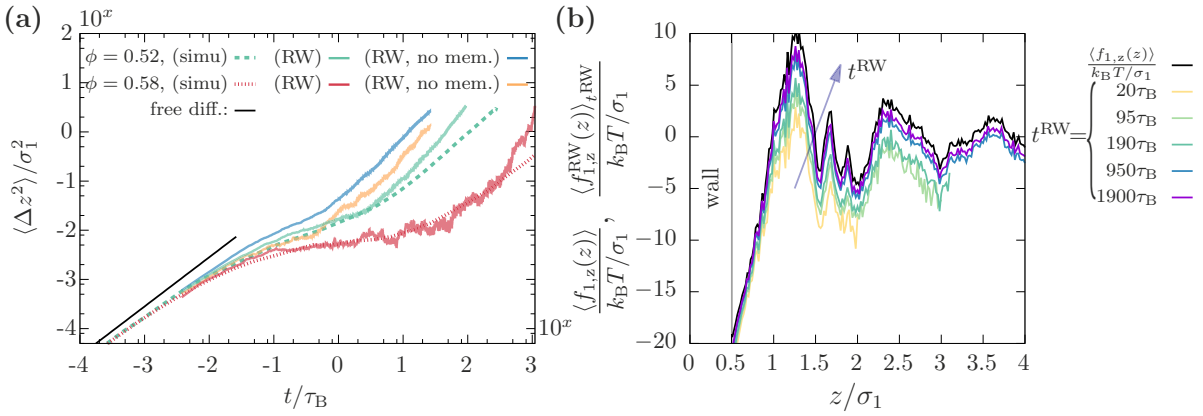

Figure 6.7: (a) MSDs in z-direction for small particles starting at the wall. The plot shows two different packing fractions ($\phi = 0.52, 0.58$), compared to a free particle (black solid line). The dashed lines are measured in our multi-particle simulations, whereas the colored shallow lines are data from our random-walk model, (RW) with and (RW, no mem.) without history-dependent memory. (b) Measured (average) position-dependent force in the random-walk model with incorporation of memory and for different runtimes. As the runtime goes to infinity, the random-walk model approaches the average force from our multi-particle simulation (black solid line).

prefactor A in Eq. (6.12). Applying this prefactor A for our binary system, one can then deduce the collision probability

$$P_{1,\mathrm{coll}} = \frac{A}{8}\sqrt{\frac{2\pi k_B T}{\varepsilon}} \sum_{\nu,\nu'=1,2} \frac{\sigma_1}{\sigma_{\nu\nu'}} \,. \tag{6.13}$$

This ingredient will be used in the next section of this chapter to develop a random walk model for a single tracer particle in front of the wall, that is not in every step interacting with its environment, but rather only with a probability equal to $P_{1,\mathrm{coll}}$.

6.2.4 Random-walk model for a particle at the wall

In this section a random-walk (RW) model will be applied for the motion of a single small particle starting at the wall, moving towards the second layer in a perpendicular straight path. For the most simplistic model, we use the average force profiles in order to calculate the typical paths along the z-axis, where the diffusion coefficient is set by the temperature and the probability for a collision is input from simulation data. Nevertheless, it can in principle be calculated via the Boltzmann force-distribution as explained above[5]. We use

[5]For the results presented in this chapter we rather use the measured collision probability from the simulations. Nevertheless, as Fig. 6.6 suggests, in the HS limit via the functional form of the fits the respective values can also be calculated using a known equation of state.

two RW models to mimic the diffusion of single tracer particles that are starting in front of the wall.

Model 1: RW, no mem. Our first model does not incorporate any memory but rather only employs the average force $\langle f_{1,\mathrm{z}}(z)\rangle$ acting on a particle. It consists of the steps:

1. Calculate a three-dimensional diffusion step $\Delta\mathbf{r}^{\mathrm{step}}$ within Δt^{step} and with a diffusion coefficient according to the Stokes-Einstein relation (Eq. 3.2) and an optional external force.

2. Decide from an equally distributed random number, if the particle collides with another particle, according to the z-dependent collision probability $P_{1,\mathrm{coll}}(z)$:

   2(a). **no collision**: go to 1.

   2(b). **collision**: apply the force $\mathbf{f}^{\mathrm{step}}$ to the particle and go to 1.

The force $\mathbf{f}^{\mathrm{step}} = \mathbf{f}^{\mathrm{step},1} + \mathbf{f}^{\mathrm{step},2}$ consists of two contributions, the first being the kickback with respect to the movement direction, i.e.,

$$\mathbf{f}^{\mathrm{step},1} = -\frac{\Delta\mathbf{r}^{\mathrm{step}}}{|\Delta\mathbf{r}^{\mathrm{step}}|}\frac{\langle|\mathbf{f}_{1,\perp}(z)|\rangle}{P_{1,\mathrm{coll}}(z)}\,, \tag{6.14}$$

where $\langle|\mathbf{f}_{1,\perp}(z)|\rangle$ is the average of the absolute (normal) forces acting on the particles surface at a position z. It is proportional to the local average pressure and can be calculated from the one-particle density together with the anisotropic pair correlations. The second force is the mean force, exerted by the structure of the neighboring particles,

$$\mathbf{f}^{\mathrm{step},2} = \mathbf{e}_{\mathrm{z}}\frac{\langle f_{1,\mathrm{z}}(z)\rangle}{P_{1,\mathrm{coll}}(z)}\,, \tag{6.15}$$

where in both cases the normalization with the collision probability $P_{1,\mathrm{coll}}(z)$ guarantees, that the average force profile $\langle f_{1,\mathrm{z}}(z)\rangle$ is recovered over time.

Model 2: RW. Our second RW model incorporates the memory of the particles history, namely the fact that it has started at the wall and therefore is supposed to recognize the impact of the force memory $\Delta f^{<}_{1,\mathrm{z}}(z,t)$. In this model the second force is slightly modified, such that

$$\mathbf{f}^{\mathrm{step},2} = \mathbf{e}_{\mathrm{z}}\frac{\langle f_{1,\mathrm{z}}(z)\rangle + \Delta f^{<}_{1,\mathrm{z}}(z)\exp\big[-(t/\tau_{\mathrm{mem}})^{0.4}\big]}{P_{1,\mathrm{coll}}(z)}\,, \tag{6.16}$$

where we use the fits of the force memories from Eq. (6.9) as an input and the respective parameters as indicated in Fig. 6.4(b).

In Fig. 6.7(a) we plot the MSD of small particles in z-direction for simulation data, compared with results from our RW models for the two different densities[6]. In case of the improved model the discrepancies between the RW and the simulation are small, at least for a typical rearrangement. For the simple RW model without memory, the curves deviate from the measured ones already very early. This deviation is less pronounced for the dilute system, where memory is supposed to play a smaller role than for systems close to the glass transition.

One can conclude, that the memory improves the details of the RW model. Its impact is illustrated in Fig. 6.7(b), where we plot the average measured forces on a particle in dependence on the particle position z and the runtime τ_{RW}. For short runtimes, the particles do not manage to hop over the first few particle layers. This results in truncated lines. However, as the runtime increases, the time-averaged forces from our RW model converge, as expected, against $\langle f_{1,\mathrm{z}}(z)\rangle$. This mimics the loss of memory.

6.3 Conclusion

Whereas studies about the structural aspects of dense and polydisperse systems seem to be allegeable and even accessible with theoretical tools (as demonstrated in the previous chapter), the multifaceted behavior of slowed-down dynamics in glassy systems remains hardly comprehensive. In this chapter we studied dense systems of binary suspensions in front of a wall and connected the predominant structure with the dynamics.
We considered a small test particle and used the symmetry breaking of its two-body particle correlations to explain qualitatively the anisotropic nature of its surrounding potential landscape. It turned out, that the neighboring particles form a cage that is more fragile for some particular escape directions. Specifically, we identified a cage-weakness in the normal direction with respect to the wall.

Subsequently, this direction was further studied and the dynamics compared to predictions of an one-particle RW model. The first model (**RW, no mem.**) was designed without any memory. It applied the instantaneous force acting on a configuration-averaged particle with respect to its distance from the wall, no matter what history the particle went through in its past. In the second model (**RW**), the force history was determined from bulk simulations and used as an input for the memory in the modified random walk. This memory acknowledged the initial starting position of the particle with wall contact. We found out, that the obtained results of the RW without memory deviated very early from BD simulations, whereas in the case of the memory-dependent RW the obtained dynamics in the z-direction resembled those of the multi-particle simulations. This intriguing finding lets us adumbrate, that the anisotropic and locally non-equilibrium nature of the cage are both two very important ingredients for the explanation of single-particle dynamics.

[6] In case of the improved model the respective memory times are $t_{\mathrm{mem}} = 187.5\tau_{\mathrm{B}}$ for $\phi = 0.58$ and $t_{\mathrm{mem}} = 6.3\tau_{\mathrm{B}}$ for $\phi = 0.52$.

In the case of bulk one should split up the problem such that first the averaged cage-structure, as represented by radial symmetric pair correlations must be modified such that it contains correlation maxima (cage fortifications) and minima (cage flaws). This could for example be introduced by the employment of three-body correlations. Successively, one needs to determine the memory-dependent diffusion through the modulated potential landscapes and in the end an average over all possible paths must be made.

Chapter 7

Colloid-polymer mixtures

Preface The present chapter is based on the paper "*Directed percolation identified as equilibrium pre-transition towards non-equilibrium arrested gel states*" [3], which has been submitted to the journal *Nature Communications*. It contains literal adoptions of text and figures. Whereas the first two introductory sections of this chapter are not fully regarded in the paper, the subsequent sections contain only minor modifications of the original manuscript.

7.1 Introduction

Colloid-polymer mixtures are widely investigated and also used in many useful industrial applications. The more common appellation for a special phase that these mixtures are able to form is *gel*. A gel can consist mostly of the solvent with only very little packing fraction of the gel-forming solute. It is a flabby and solid-like material, which consists of network-like connections of its microscopic components. Induced by the microscopic structure the macroscopic properties of such gels can have a very diverse exposure. When changing a suitable parameter, e.g., such as the concentration of the polymers in the mixture or the temperature, the viscosity can be tuned from very small to very large values.

In gel-forming colloid-polymer mixtures, the colloids are typically larger than the polymers. Nevertheless, the polymers also play a crucial role. Assuming that the interaction between two polymers is negligible compared to the colloid-colloid or colloid-polymer interactions, one can derive effective interactions between the larger colloidal particles, which are due to entropically favored void-spaces at close distances. As sketched in Fig. 7.1(a) there are depleted shells around the colloids, which cannot be entered by the polymers due to repulsive interactions. As soon as two colloids come close to each other they feel an effective attraction that is mediated by the following picture: The space that can be

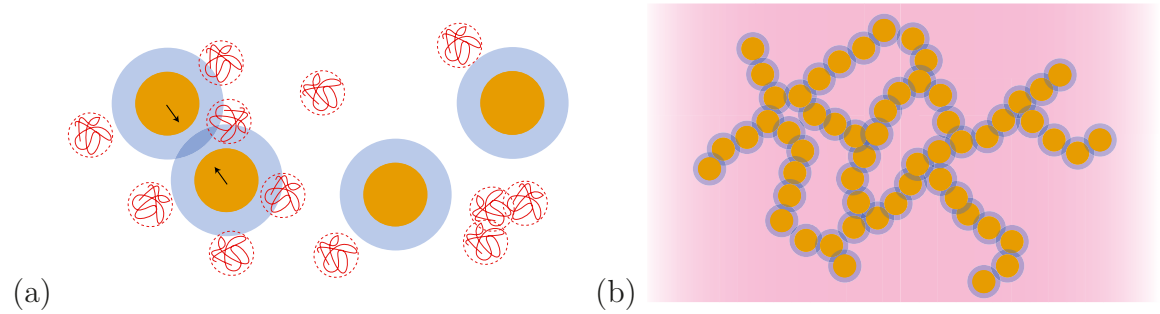

(a) (b)

Figure 7.1: Sketch of the *depletion mechanism* in a colloid-polymer mixture. (a) The depleted shells (blue) of the colloids (orange) cannot be entered by the centers of the polymer coils (red). Therefore the pair of colloids on the very left, which has overlapping depletion shells, "feels" an effective interaction due to the higher osmotic pressure from polymer coils, which are still present at the averted hemispheres. (b) At sufficiently large polymer concentrations, the colloids bond with each other and form network-like structures.

occupied by the centers of the polymer coils is limited to the free volume in the whole solution minus the shell volumes around the colloids. This configurational space can be increased by partial overlap of several of these shells. It will result in an increase of the overall entropy and therefore in an accompanied decrease of the free energy. Another intuitive picture, which incorporates the osmotic pressure, is represented by the fraction of polymer coils which are colliding with the involved colloids from the outer hemispheres over those, which are colliding with the inner hemispheres. By the underpopulation due to the shell overlap an overbalance of pressure from outside arises, resulting in an attractive force. If the attraction strength is large enough, the colloids become bonded with each other, such that large and even system spanning networks can form, as sketched in Fig. 7.1b.

In 1954 S. Asakura and F. Oosawa captured the entropic mediated imbalance of pressure around approaching colloids. They extracted the effective force on spherical and plate-like objects, which are immersed in a bath of macromolecules [65]. Today this procedure is still well known as the Asakura-Oosawa (AO) model, which assumes that the force is proportional to the overlap volume of the depleted shells of colloidal particles.

7.2 Model

The attractive force can be quantified in a mathematical manner. If one assumes hard core repulsions for colloid-colloid and colloid-polymer interactions and negligible interactions between polymers, one is able to integrate out the polymers. In a simplified setup, we consider only two spheres whose depletion shells are overlapping (see Fig. 7.2(a)). The diameters of the spheres are σ and those of the polymers are given indirectly by the

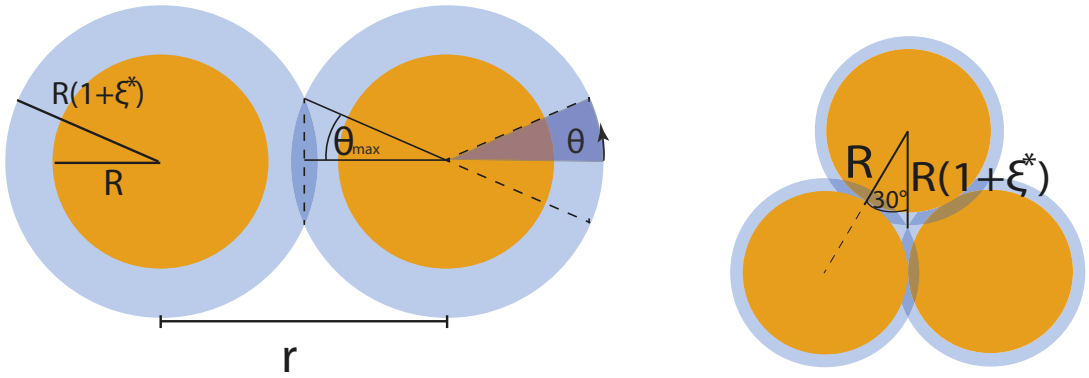

(a) (b)

Figure 7.2: (a) Sketch of the depletion mechanism in colloid-polymer mixtures. The blue shells around the larger colloids cannot be entered by the centers of the smaller polymers. Due to this fact the overlap region (depletion volume) in between the two particles causes a lack of osmotic pressure exerted by these polymers. This results in an effective attractive force as explained in the text. (b) Limit for negligible three-body interactions: the depletion model becomes exact for $\xi^* \lesssim 0.155$, when there is no possibility for three blue shells to overlap at the same point.

aspect size ratio $\xi^* = \sigma_\mathrm{P}/\sigma$, where σ_P is the radius of gyration of the polymers [147].

A normal and uniform pressure p on the colloids surfaces is exerted by the polymers from all directions. Due to the depleted region around the spheres and the intersecting volumes, there is a leak of pressure on the two inner caps of the spheres. The attractive force is obtained by integrating over the parallel component of the force density (pressure), $p_\parallel = p \sin\theta$, with respect to the connecting axis. θ is the polar angle and sketched in Fig. 7.2(a). The surface element at θ is given by $\mathrm{d}A = \pi/2\big(\sigma(1+\xi^*)\big)^2 \sin\theta \,\mathrm{d}\theta$. An upper boundary angle for the integration can be calculated by the separation r of the two spheres, i.e.

$$\theta_\mathrm{max} = \mathrm{arc\ cos}\left(\frac{r}{\sigma(1+\xi^*)}\right) . \tag{7.1}$$

Now, one can calculate the depletion force

$$f_\mathrm{D}(r) = \begin{cases} f_\mathrm{D,overlap}(r) & , \quad r \le \sigma(1+\xi^*) \\ 0 & , \quad \text{else} \end{cases} , \tag{7.2}$$

where $f_\mathrm{D,overlap}(r)$ is given by the integration of $p_\parallel$ over the surface A_D of the intersecting

spherical cap, i.e.,

$$\begin{aligned} f_{\mathrm{D,overlap}}(r) &= \int_{A_\mathrm{D}} \mathrm{d}A\, p_\parallel \\ &= \int_0^{\theta_\mathrm{max}} \mathrm{d}\theta\ (p\cos\theta)\left(\frac{\pi}{2}\big(\sigma(1+\xi^*)\big)^2\sin\theta\right) \\ &= \frac{\pi p}{2}\big(\sigma(1+\xi^*)\big)^2 \int_0^{\theta_\mathrm{max}} \mathrm{d}\theta\ \cos\theta\sin\theta \\ &= -\frac{\pi p}{2}\big(\sigma(1+\xi^*)\big)^2\left[1-\frac{r^2}{\sigma^2(1+\xi^*)^2}\right]. \end{aligned} \tag{7.3}$$

By inserting Eq. (7.3) into Eq. (7.2) and integrating over it under the condition of a steady potential, the standard AO depletion part of the potential is obtained. Together with the hard-core interaction, represented by a function $V_\mathrm{H}(r)$, one gets the overall potential

$$V_\mathrm{D}(r) = \begin{cases} -D_0\left[1-\frac{3(r/\sigma)}{2(1+\xi^*)}+\frac{(r/\sigma)^3}{2(1+\xi^*)^3}\right]+V_\mathrm{H}(r) & , \quad r\le\sigma(1+\xi^*) \\ 0 & , \quad \text{else} \end{cases}. \tag{7.4}$$

In Eq. (7.4) we have abbreviated the constants by a prefactor D_0, which sets the energy scale of the system, typically with respect to the thermal energy $k_\mathrm{B}T$.
Although in the above discussion no constraints on the polymer sizes have been made, in a multi-particle ensemble it is important to note, that the polymers radius of gyration must be smaller than a certain fraction of the colloids radius. This is due to the fact, that only two-body interactions have been discussed in the model, although three particles could possibly interact at the same time. The three-body interactions mediated by the polymers can be neglected and reduce to two-body interactions as soon as one can fit exactly one polymer coil in the middle of three triangular aligned colloids (see Fig. 7.2(b)). The threshold value for this situations can be calculated and is equal to $\xi^* = 1.0/\cos(30°) - 1 \approx 0.155$.

In order to prevent flocculation in experiments colloidal particles are often charged. The charge, which is – without screening – well described by a r^{-1} Coulomb potential, is long ranged and makes the suspension stable against strong and short ranged van-der-Waals attractions. Nevertheless, in the experiments the range of the repulsion can be manipulated by imposing salt to the solution. Salt is composed of anoins and cations, such that the chemical compound is neutral, e.g., sodium chloride $\mathrm{Na^+Cl^-}$ (common salt). Immersed into water, it splits up due to the dipolar character of the water molecules. Successively, one species of ions will tend to accumulate in a layer at the surface of the charged colloids, whereas the counterions will arrange in the subsequent region (*double layer*). The inhomogeneous distribution of oppositely charged ions makes sure, that the

Coulombic potential is screened with an exponential, such that it can be written as [198]

$$V_{\mathrm{C}}(r) = C_0 \left(\frac{2}{2+\kappa\sigma} \right)^2 \frac{\sigma}{r} \exp\left[-\kappa(r-\sigma)\right] . \tag{7.5}$$

Here the prefactor C_0 is an energy scale of the electrostatic coupling between the colloids and is in principle set by the charge of the particles [98]. The parameter κ is the inverse screening length and can be varied by the salt concentration [98]. Lastly, the colloids must be modeled with a finite diameter, which introduces the prefactor $4/(2+\kappa\sigma)^2$ and a shift by σ in the exponential [198].

7.3 Simulation details

We simulate a system consisting of N particles with mean model diameter σ and a polydispersity of about 7%. The polydispersity is realized through 17 different particle diameters σ_ν, where their numbers N_ν are normally distributed with a standard deviation of the diameter of $0.07\,\sigma$ and $N = \sum_\nu N_\nu$. In the calculation of pair interactions the above introduced model potentials are being shifted according to the deviation from intermediate diameter (for further information, see Appendix A.5). If not stated otherwise, $N = 9856$.

Motivated by the experiments, we fix $\xi^* = 0.03$ for Eq. (7.4) although in our model this does not necessarily imply that the position of the potential minimum is fixed. The hard interaction of particles with diameter σ is approximated by $V_{\mathrm{H}}(r) = H_0(r/\sigma)^{-32}$ [199]. The prefactor H_0 defines the energy scale of the potential and is kept constant at $H_0 = 0.25\,k_{\mathrm{B}}T$. For different particle sizes the potential is also shifted according to Appendix A.5. Note, that due to the softness of the hard core potential the model parameter σ not necessarily coincides with the position of the potential minimum, but it is typically slightly smaller. We cut the potential and the corresponding force at 4σ and shift them to zero at the cut-off distance. In our model, the range of the attractive part in the potential may vary while other parameters are changed. The interaction potential exhibits a minimum $V_{\min} = V(\sigma^{\mathrm{eff}})$ with the effective diameter σ^{eff} slightly smaller than σ. The effective packing fraction $\phi^{\mathrm{eff}} = (\pi/6V) \sum_\nu N_\nu (\sigma_\nu^{\mathrm{eff}})^3 = 0.2$, with V the volume of the system, is kept constant. For our bulk simulations we employ periodic boundary conditions to the cubic simulation boxes and simulate the particle trajectories according to the Langevin equation (3.6).

The Brownian time $\tau_{\mathrm{B}} = \sigma^2/(3\pi D)$, with the short-time self-diffusion coefficient $D = k_{\mathrm{B}}T/\gamma$ and the friction coefficient γ of a particle with diameter σ, is used as time scale. The time steps are $10^{-4}\tau_{\mathrm{B}}$ or less. Starting from an initial randomly-distributed ensemble, the systems were equilibrated for $300\,\tau_{\mathrm{B}}$ before statistics are gathered.

7.4 Experiment

The experimental realization was performed by Ronja Capellmann from the Soft Condensed Matter Institute at the Heinrich-Heine-Universität Düsseldorf.

Samples. The samples, which have been set up in the corresponding experiments, consist of spherical Poly-Methylmethacrylate (PMMA) colloids, which is mostly referred to as *acrylic glass*. In order to prevent flocculation, the colloids are synthesized in such a way, that their surface is coated with very small polymeric chains. This procedure is well established in colloid synthetization and is called steric stabilization. In the case of our experiments, polyhydroxystearic acid (PHSA) polymers have been attached to the colloids. The colloids have been fluorescently labeled with 7-nitrobenzo-2-oxa-1,3-diazole-methylmethacrylate (NBD-MMA) in order to make them visible in the experimental setups. The reason for this label is, that solvent and solute have the same refractive index. This adjustment makes the solvent transmittable for the laser light[1], but on the same time it makes the colloidal particles visible under the microscope.

Additionally, linear Polystyrene (PS) polymers have been added to the solution. These polymers form coils and induce the depletion attraction. All components are dispersed in a chemical mixture of cis-decalin and cycloheptylbromide (CHB). These chemical compounds have different mass densities (CHB has a higher mass density) and their proportions are successively adjusted in such a way, that the overall mass density matches that of the particles (*density matching*). This calibration of the mass density of the solvent with respect to the solute is needed in order to remove sedimentation effects from the samples, which are otherwise always present in gravitational fields.

The colloids have an average (hydrodynamic) radius of $R = 0.5\,\sigma = 0.86\ \mu$m and a polydispersity of 7%. Rather than the real radius of the particles, only the hydrodynamic radius can be determined by static and dynamic light scattering of a very dilute suspension (volume fraction $\phi = 0.005$). In such experiments, one can fit with the self-diffusion law (eq. 3.1 and 3.2) an effective radius to the measured density fluctuations, where the radius is their hydrodynamic one (see, e.g. Refs. [200, 201]). Of course the real radius of the particles should only slightly differ from the obtained value.

For the PS with a mass average molar mass of $M_\mathrm{w} = 10^6$ kg/mol and polydispersity $M_\mathrm{w}/M_\mathrm{n} = 1.17$, where M_n is the number average molar mass, the radius of gyration was calculated following Berry's work [202]. Here a value of $r_\mathrm{g} = 65$ nm has been obtained. This leads to a polymer-colloid size ratio of $\xi = 0.076$ for a dilute solution. As the size of a polymer coil changes with the concentration of polymers and the polymers start to overlap at a concentration higher than the overlap concentration – which will be labeled c_p^* in the following – an effective polymer-colloid size ratio was estimated from

[1] The laser excites the NBD-MMA and is not scattered at the interface between the particles and the solvent.

Sample	ϕ	c/c^*	c^{free}/c^*	ξ^*	c_{salt} $[mM]$
B1	0.19	1.46 ± 0.01	1.95 ± 0.01	0.031 ± 0.001	3.5 ± 0.5
B2	0.23	1.54 ± 0.01	2.06 ± 0.01	0.030 ± 0.001	9.4 ± 0.5
B3	0.21	1.55 ± 0.01	2.01 ± 0.01	0.030 ± 0.001	20.1 ± 0.5
C1	0.20	2.25 ± 0.01	2.87 ± 0.01	0.025 ± 0.001	0.0 ± 0.5
C2	0.23	2.24 ± 0.01	2.98 ± 0.01	0.024 ± 0.001	3.2 ± 0.5
C3	0.20	2.25 ± 0.01	2.87 ± 0.01	0.025 ± 0.001	4.0 ± 0.5
C4	0.20	2.24 ± 0.01	2.86 ± 0.01	0.025 ± 0.001	7.8 ± 0.5
C5	0.24	2.24 ± 0.01	3.02 ± 0.01	0.024 ± 0.001	8.4 ± 0.5
D1	0.19	0.76 ± 0.01	0.97 ± 0.01	0.045 ± 0.001	2.8 ± 0.5

Table 7.1: Experimental samples with their corresponding parameters calculated after GFVT [203, 204]. The first column corresponds to the tag of the different paths through the bond-phase-diagram, that is discussed in the results section.

the Generalized Free Volume Theory (GFVT) [203–205]. This effective size ratio ξ^* for our samples is shown in table 7.1, where $c_{\text{p}}^{\text{free}}$ is the polymer concentration in the volume which is not occupied by colloids, estimated according to GFVT. The overlap concentration was calculated using $c_{\text{p}}^* = 3M_{\text{w}}/4\pi N_{\text{A}} r_{\text{g}}^3$.

PMMA colloids become charged when they are dispersed in the used solvent mixture of CHB and cis-decalin [206]. As discussed above, these charges can be screened. In such a solvent the screening can be realized by the addition of the salt tetrabutylammonium-chloride[2] (TBAC) [207, 208]. We use samples with different amounts of salt (see table 7.1) to vary the Debye length (κ^{-1}) of the particles.

Sample preparation. In order to obtain colloid-polymer mixtures, separate colloid and polymer stock solutions were prepared and successively mixed together. For the colloid stock solution, the colloids were sedimented in a centrifuge. The sediment was assumed to be random close packed with a volume fraction $\phi_{\text{RCP},1} = 0.65$, as found in simulations [209]. After diluting the sediment to a nominal volume fraction of $\phi = 0.4$, the sample was imaged with a confocal microscope and the actual volume fraction was determined to be $\phi = 0.43$. This actual volume fraction was calculated by the mean volume fraction per particle from a Voronoi construction. With this value, the before measured random close packed volume fraction needed to be adjusted at $\phi_{\text{RCP},2} = 0.68$. This calibration gave rise for a starting value in the dilution process of further samples.

Restarting with $\phi_{\text{RCP},2}$, the sediment was diluted to a colloid stock solution with $\phi_{\text{CS}} = 0.4$. For the polymer stock solutions, dry polymers were dispersed in the bare solvent mixture. The corresponding polymer concentrations of the polymer stock solutions $c_{\text{P}} = m_{\text{P}}/V_{\text{solvent}}$ were calculated with the mass of the dry polymers m_{P} and the density and mass of the

[2]For further studies with more insight into the behavior of such suspension, which are loaded with TBAC, see also the thesis in Ref. [206].

added solvent mixture. By mixing the two stock solutions with a ratio 50:50, we obtained colloid-polymer mixtures with an average volume fraction of $\phi = 0.2$[3]. The exact values for all relevant samples, which are being discussed within this thesis, are reported in table 7.1. These mixtures were intensively mixed in a vortex mixer for some minutes and then left in a flask shaker for homogenization for at least one day. After this, different amounts of TBAC were added to the colloid-polymer mixtures. Then they were gently moved in the flask shaker for three days to ensure that as much salt as possible was dissolved.

Confocal microscopy. The finished solutions were imaged in a self-built sample cell [210] with a VT-Eye confocal microscope (Visitech International) mounted on a Nikon Ti-U inverted microscope. The measurements were performed with a Nikon Plan Apo VC 100 oil immersion objective[4]. For each sample, 25 to 30 image stacks were recorded, consisting of 151 single images (512 x 512 pixels) with z-steps of 200 nm in between. Each slice was calculated as an average over three snapshots. With an imaging rate of 30 fps, a sampling time of at most 20 s per stack could be achieved. Each measured image stack corresponds to a volume of 54 x 54 x 20 μm^3 and contains usually around 7000 particles. We extracted the particle coordinates with standard routines, originally written by J. Crocker and D. Grier [211]. The measurements with confocal microscopy were performed within three hours after mixing the sample to avoid aging.

7.5 Results

7.5.1 States of the system

In charged colloid-polymer mixtures, two particle-particle interactions compete on different length scales: First, screened electrostatic interactions, which are long ranged for low salt concentrations and become shorter ranged upon addition of salt; second, depletion interactions, which are short ranged, typically at most one tenth of the colloidal particle diameter, and controlled through the radius of gyration of the polymers.

In experiments and simulations, we have consistently observed four different states that show distinct structural arrangements of the colloidal particles (Fig. 7.3, left). A transition between these states can be induced by varying, e.g., the salt concentration c_{salt}, and therefore the screening length κ^{-1}, at fixed polymer concentration c_{p}, i.e. attraction strength. This path will be referred to as path B. In the absence of salt, a fluid state

[3] To obtain colloid-polymer mixtures with $\phi \approx 0.20$, for samples B1–B3, C1, C3 and D1 colloid and polymer stock solutions were mixed with a volume ratio 50 : 50, while dry polymers were added to the diluted colloid stock solution in the case of samples C2, C4 and C5.

[4] Oil can – due to its refraction properties – be used to improve the numerical aperture, which represents a measure for the resolution quality in optics.

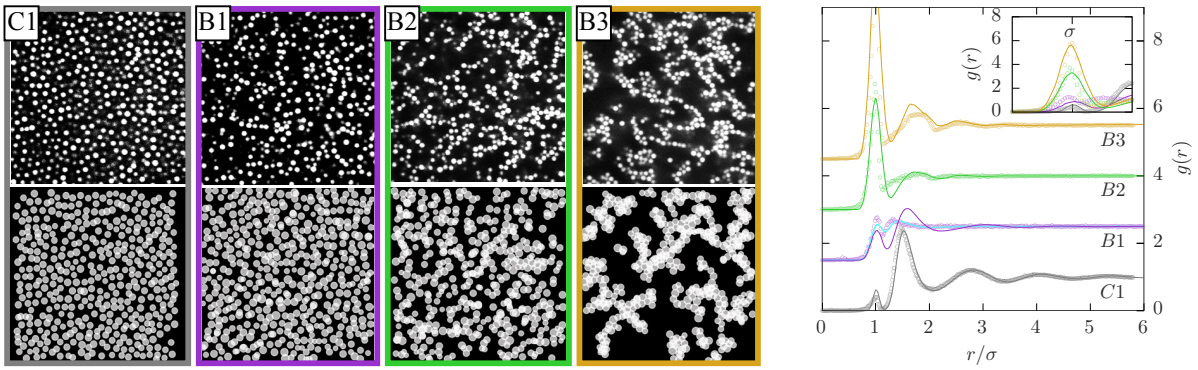

Figure 7.3: (left) Two-dimensional slices of the thee-dimensional systems. The upper row shows confocal microscopy data, where the polymer concentrations are $3c^*$ (C1) and $2c^*$ (B1-B3) with the overlap concentration c^*. The salt concentration increases from left to right (Tab. 7.1). The lower row represents the corresponding states as observed in the simulations. (C1) Fluid state with only very few small aggregates, (B1) non-percolated chain-like clusters of particles having on average at most two bonds, (B2) percolated network and (B3) directed percolated network. (right) Corresponding pair correlation functions $g(r)$ as a function of the particle distance r in units of the particle diameter σ, which, for the simulation data, is taken to be the effective particle diameter, i.e. $\sigma \equiv \sigma_{\text{eff}}$ that denotes the position of the potential minimum and is typically slightly deviating from the actual model parameter σ. Symbols represent experimental data, solid lines simulation data and (only for B1) the light blue solid line simulation data with parameters obtained by a multi-parameter fit (for details see Appendix A.6). Data have been shifted for clarity. The inset shows the (unshifted) first peaks.

is observed (sample C1; note that c_p of this sample is higher than the one of the other samples, see Tab. 7.1). Adding salt, particles aggregate into isolated small clusters (sample B1). At large salt concentrations, larger clusters are observed and the particles form a continuously percolated network (sample B2), while at the largest salt concentration studied, a heterogeneous network structure of even larger, dense clusters with thick strands is formed (sample B3). As will be shown later, directed percolation characterizes this network.

The different states show distinct pair correlation functions $g(r)$ (Fig. 7.3, right). In the fluid (C1), $g(r)$ is dominated by a peak located at the mean particle distance $\rho^{-1/3}$. Furthermore, a small peak at particle contact reflects the presence of a small number of aggregated particles. For small amounts of added salt (B1), the presence of doublets, triplets or small string-like clusters is indicated in $g(r)$ by an increase in the contact peak and a corresponding decrease of the second peak. The size of the clusters is limited by the repulsive contribution to the potential [212–214]. For sample B2 the large peak at contact is consistent with the large fraction of particles forming clusters that connect to a space-spanning network, i.e., a percolated gel-like structure. Finally, the radial distribution function of sample B3 with its very high first peak at contact reflects the presence of a large number of bonded particles and a local increase of order. Furthermore, its deep first minimum and pronounced split second peak arise from triplet structures and local close packed arrangements. These features are observed in the experiments as well as in the simulations. (The mapping of the simulation and experimental parameters is described in Appendix A.6.)

7.5.2 Bond number diagram

The different structures are distinguished by the degree of particle aggregation. This is linked to the mean number of bonds per particle, $\langle N_\mathrm{b} \rangle$. Individual particle-particle bonds cannot be determined unambiguously because the first peak in $g(r)$ is broadened due to polydispersity (about 7 %). Hence two particles are defined to be bonded if they are closer than the position of the first minimum in $g(r)$, which is located between 1.10 and $1.22\,\sigma_\mathrm{eff}$ (Fig. 7.3, right), where σ_eff denotes the position of the minimum of the interaction potential and is for the simulations typically slightly smaller that the actual model parameter σ.

The mean number of bonds per particle, $\langle N_\mathrm{b} \rangle$, is determined as a function of the interactions, namely the salt concentration c_salt, controlling the screening lengths κ^{-1}, and the polymer concentration c_p, represented by the depletion part of the potential $V_\mathrm{D,min} = V_\mathrm{D}(\sigma_\mathrm{eff})$ that is evaluated at the overall potential minimum $V_\mathrm{min} = V(\sigma_\mathrm{eff})$ (Fig. 7.4). A transition from a fluid, indicated by the absence of a significant number of bonds (white to purple), to a bonded state (red) can be achieved by increasing the polymer, c_p, and/or salt, c_salt, concentrations. In contrast to previous results [56], $\langle N_\mathrm{b} \rangle$ monotonically grows without a reentrant transition. The highly-bonded gels are not in equilibrium and therefore, even for large screening and strong attraction, $\langle N_\mathrm{b} \rangle$ hardly

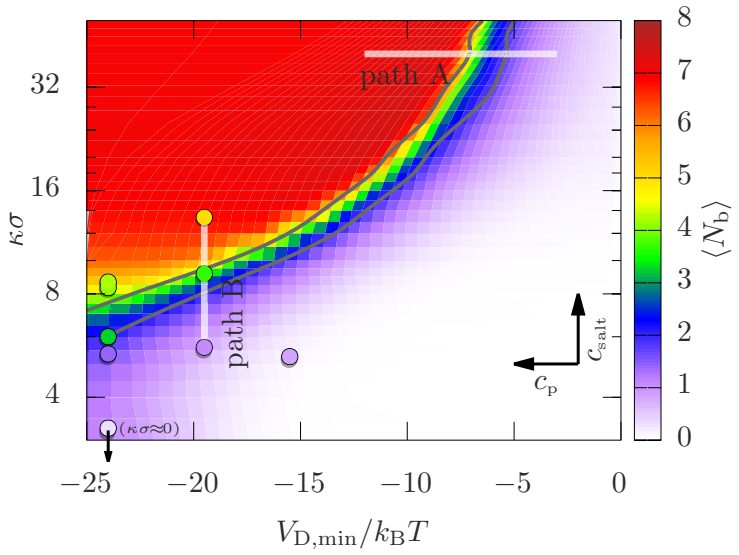

Figure 7.4: Mean number of bonds per particle, $\langle N_{\mathrm{b}}\rangle$, as a function of the minimum of the attractive part of the potential, evaluated at the global minimum, $V_{\mathrm{D,min}}$ in units of the thermal energy $k_{\mathrm{B}}T$, and the inverse screening length κ in units of the particle diameter σ, which, for the simulation data, is taken to be the mean model diameter, i.e. σ, in a semi-logarithmic representation. The background color represents $\langle N_{\mathrm{b}}\rangle$ as obtained by simulations, the circles and their colors denote the positions and $\langle N_{\mathrm{b}}\rangle$ of the experimental systems, respectively. The two white lines indicate paths from fluid systems via continuous percolation networks to directed percolation networks, during which either the polymer concentration ('path A') or the salt concentration ('path B') are increased. The upper dark solid line indicates the directed percolation transition, the lower one denotes the continuous percolation transition.

exceeds seven. As will be discussed later, the systems do not reach equilibrium and aging sets in beyond a threshold mean number of bonds per particle. For a purely repulsive interaction such a transition is expected once the system becomes isostatic, i.e., globally stable with six bonds per particle [32, 215].

The observed structures along two paths are now analyzed in more detail (Fig. 7.5). Along path A, the salt concentration c_{salt} and hence the screening length κ^{-1} is kept constant while the polymer concentration c_{p} and hence the depth of the potential minimum $V_{\mathrm{D,min}}$ is decreased. Instead, along path B the screening length κ^{-1} is reduced at constant attraction. For path A, i.e. upon increasing attraction, $\langle N_{\mathrm{b}}\rangle$ increases and the distribution of the number of bonds per particle, $p(N_{\mathrm{b}})$, first broadens, indicating a more heterogeneous structure, but then narrows again once a gel state is observed (Fig. 7.5(a)). While $p(N_{\mathrm{b}})$ sharpens, the probability to find monomers is reduced to zero. Along path B, i.e. increasing c_{salt} (inset), the distributions also shift to larger N_{b} and broaden, again indicating the coarsening of the structure. Compared to path A, the $p(N_{\mathrm{b}})$ are sharper, indicating that monomers are suppressed by the strong repulsion.

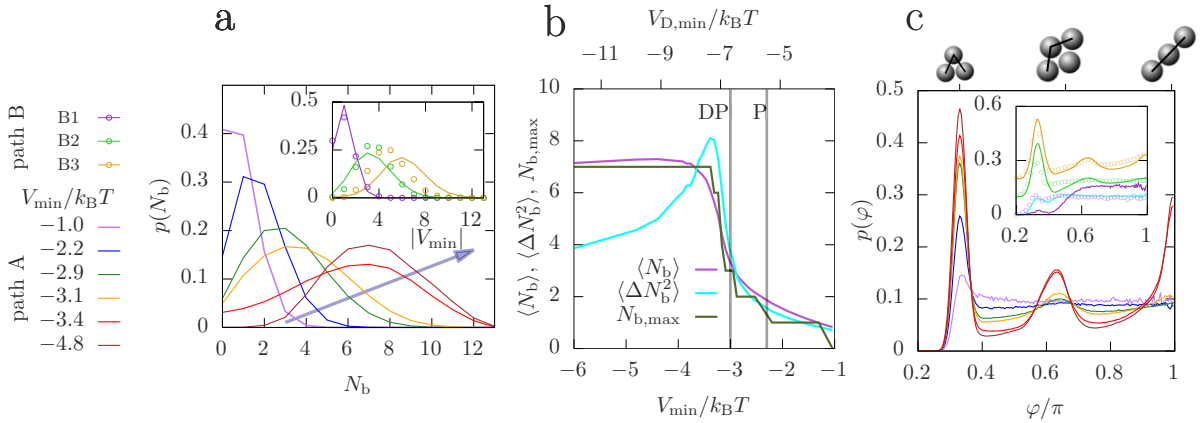

Figure 7.5: (a) Distribution of the number of bonds per particle, $p(N_b)$, as obtained by simulations for constant screening length $\kappa\sigma = 40$ and varying attraction (as indicated on the left), i.e. path A in Fig. 7.4. In the inset simulation (lines) and experimental (circles) results for varying $\kappa\sigma$ and constant attraction, i.e. path B, are compared. (b) Mean $\langle N_b\rangle$, variance $\langle \Delta N_b^2\rangle$ and the most probable value $N_{b,\max}$ of $p(N_b)$ as a function of the attraction strength, $V_{\min}$. The gray vertical lines denote the percolation (P) and the directed percolation (DP) transition. (c) Distribution of the angle between two successive bonds, $p(\varphi)$, along path A. The inset shows $p(\varphi)$ obtained in simulations and experiments along path B. The light blue line represents simulation data with parameters obtained by a multi-parameter fit (for details see Appendix A.6). Colors of the lines are same as in (a) and indicated on the left.

We characterize $p(N_b)$ by its mean $\langle N_b\rangle$, variance $\langle \Delta N_b^2\rangle$ and maximum $N_{b,\max}$. With increasing attraction, that is $|V_{D,\min}|$, they all sharply increase at $V_{\min} \approx -3.0\,k_BT$ (Fig. 7.5(b)). Furthermore, we consider the distribution $p(\varphi)$ of angles between two successive bonds, φ, which is normalized by the solid angle covered by the angle φ, i.e. such that $2\pi \int p(\varphi) \sin\varphi \, d\varphi = 1$. It reveals a qualitative change that also occurs at $V_{\min} \approx -3.0\,k_BT$ (Fig. 7.5(c)). While the peak at $\varphi = \pi/3$, which is related to locally dense tetrahedral packings, grows monotonically with $|V_{\min}|$, a second peak at $\varphi = 2\pi/3$ develops and becomes pronounced for $|V_{\min}| > 3.0\,k_BT$. Furthermore, for these large potential depths, a peak at $\varphi = \pi$ emerges, which indicates the formation of straight strings of connected particles.

7.5.3 Directed percolation

The data presented above indicate two percolation transitions from the fluid to the gel: first, a continuous percolation transition, second, a directed percolation transition. Both networks span the whole system. In continuous percolation, a walk along a percolating cluster may contain steps in all directions, including backward steps (Fig. 7.6(a), P).

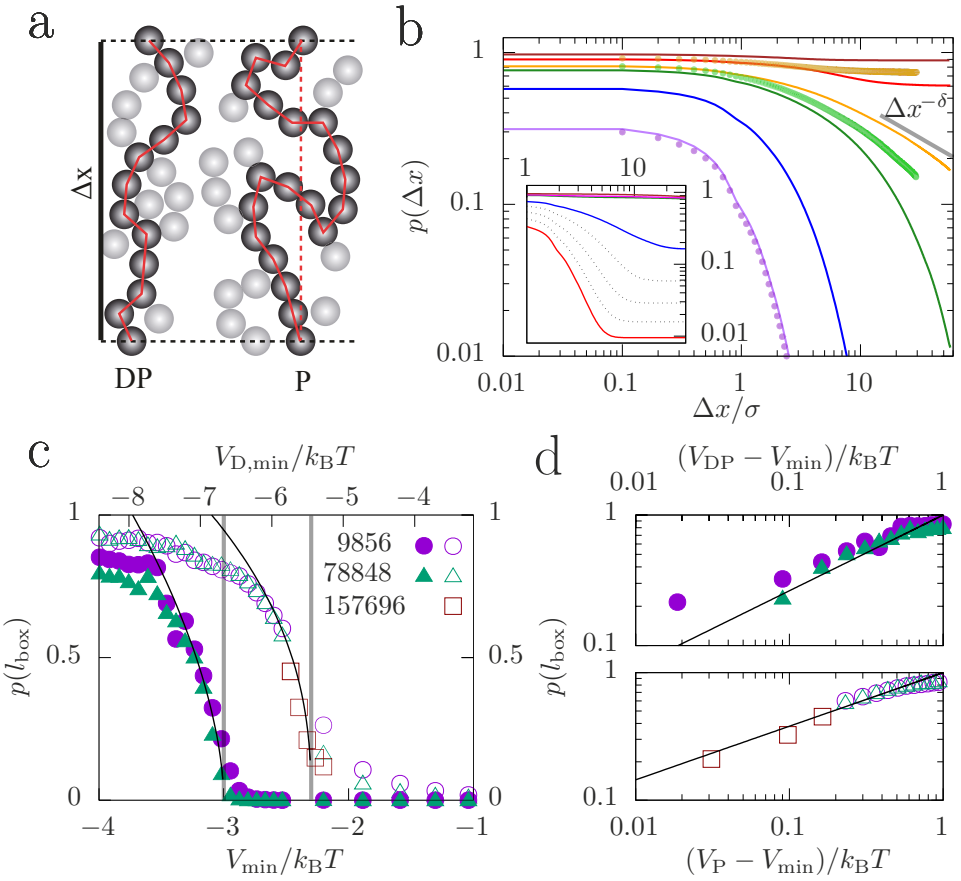

Figure 7.6: (a) Sketch of (DP) a directed and (P) an undirected cluster of length Δx. (b) Probability $p(\Delta x)$ for a particle to reside in a (main figure) directed and (inset) undirected cluster with a length smaller than the maximum length Δx. Solid lines represent simulation data along path A and symbols experimental data along path B. Colors of the lines are defined in the legend of Fig. 7.5. The gray solid line indicates the DP critical point, where the percolation probability is expected to be proportional to Δx^{δ} with $\delta = 0.451$ [216]. (c) Probability $p(l_{\mathrm{box}})$ for a particle to reside in a (solid symbols) directed and (open symbols) undirected cluster with the maximum possible length, i.e. the box size l_{box}, and hence system-spanning, for different system sizes, quantified by the number of particles N (as indicated). Vertical lines indicate the (left) directed and (right) continuous percolation transitions. Solid black lines represent critical power law fits with (left) $p(l_{\mathrm{box}}) \sim (V_{\mathrm{DP}} - V_{\mathrm{min}})^{0.58}$ and (right) $p(l_{\mathrm{box}}) \sim (V_{\mathrm{P}} - V_{\mathrm{min}})^{0.42}$. (d) Same data as in (c) but in double-logarithmic representations and relative to the (top) directed and (bottom) continuous percolation transitions.

Instead, in the case of directed percolation, a walk along a percolating cluster must always be directed along the main direction of the cluster (Fig. 7.6(a), DP). In our simulations following path A, the continuous percolation transition occurs at $V_{\mathrm{min}} \approx -2.3\,k_{\mathrm{B}}T$ and the directed percolation transition at $V_{\mathrm{min}} \approx -3.0\,k_{\mathrm{B}}T$. The latter coincides with the significant changes observed in $p(N_{\mathrm{b}})$ and $p(\varphi)$ (Fig. 7.5). Furthermore, this indicates that continuous percolation occurs for $\langle N_{\mathrm{b}} \rangle \lesssim 2$ and directed percolation for $\langle N_{\mathrm{b}} \rangle \gtrsim 3$. This suggests a connection between the percolation transitions with $\langle N_{\mathrm{b}} \rangle$.

The (cumulative) probability $p(\Delta x)$ to observe continuous and directed percolation up to a length Δx is shown in the inset and main part of Fig. 7.6(b), respectively, where the solid lines represent simulation data along path A and symbols results from experiments along path B. For both percolation transitions, the probabilities decay to zero in the case of weak attractions (small $|V_{\mathrm{min}}|$). In contrast, for strong attractions plateaus develop, indicating large clusters that span the whole system. The height of the plateau corresponds to the fraction $p(l_{\mathrm{box}})$ of particles that are part of a cluster with the maximum possible length, i.e. the box size l_{box} (Fig. 7.6(c)). The system size determines l_{box} and also affects the simulations. Nevertheless, within the investigated system sizes only a weak dependence on system size, quantified by the total number of particles N, is observed and, in particular, no significant effect on the percolation transitions and their positions is observed. We determined the continuous percolation and directed percolation transitions in simulations for the complete parameter space of Fig. 7.4. The locations of these transitions are indicated by dark solid lines in the figure. The threshold for these curves is chosen according to the percolation probability for system spanning clusters, i.e., $p(N_{\mathrm{b}}) \geq 0.2$ for systems with $N = 9856$ particles[5].

Along path A, the probability for space-spanning clusters becomes non-zero at $V_{\mathrm{P}} = -2.3\,k_{\mathrm{B}}T$ for continuous percolation and at $V_{\mathrm{DP}} = -3.0\,k_{\mathrm{B}}T$ for directed percolation, consistent with our other findings. Furthermore, the values of $p(l_{\mathrm{box}})$ obey critical power law scaling close to the transitions (Fig. 7.6(c,d)). Our data are consistent with theoretical predictions for the critical exponents of the power law scalings, i.e., $\beta_{\mathrm{P}} = 0.42$ for continuous percolation [217, 218] and $\beta_{\mathrm{DP}} = 0.58$ for directed percolation [216] (black lines in Figs. 7.6(c,d)).

7.5.4 Slowdown of dynamics and onset of aging

The dynamics of the different network structures are quantified by the self-intermediate scattering function (Fig. 7.7), i.e., Eq. (2.6). Along path A, a dramatic slowdown of the dynamics is observed beyond the DP transition. Directed percolation is characterized by dense clusters with thick strands (Fig. 7.3, B3) and thus rearrangements are expected to involve long-range, global motions and/or the breaking of several bonds. Correspondingly, they require long times. In contrast, in continuous percolation more open structures (B2)

[5] The threshold value stems from the observation, that systems with 9856 particles exhibit an enhanced percolation probability of $p(N_{\mathrm{b}}) \approx 0.2$ along the actual transition line, due to finite size effects.

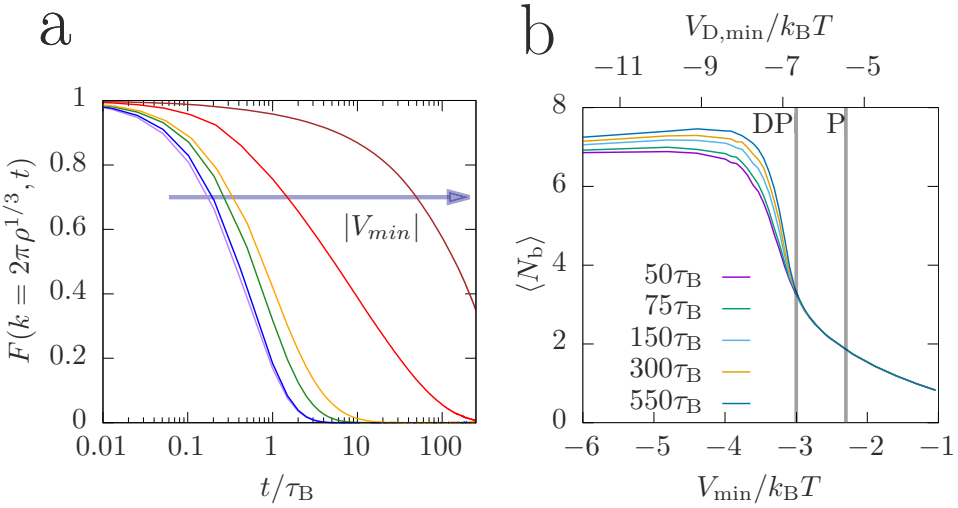

Figure 7.7: (a) Self-intermediate scattering function F at the scattering vector $k = 2\pi\rho^{-1/3}$ as a function of delay time t, normalized by the Brownian time τ_B, along paths A from simulations. Colors of the lines are defined in the legend of Fig. 7.5. (b) Mean number of bonds per particle, $\langle N_b\rangle$, as a function of the attraction strength for different waiting times after the initial quench (as indicated). Vertical lines indicate the (DP) directed and (P) continuous percolation transitions.

are formed that can be rearranged by local motions requiring less time, of the order of the Brownian time τ_B. This is consistent with our observations.

The dependence of the mean number of bonds per particle, $\langle N_b\rangle$, on the potential depth V_{min} has been linked to the continuous and directed percolation transitions (Fig. 7.5(b)). It (as well as all other parameters) has been determined a waiting time $300\,\tau_B$ after the initial quench. Now its dependence on waiting time is considered (Fig. 7.7(b)). For small attraction strengths, $|V_{min}| \leq 3.0\,k_BT$, $\langle N_b\rangle$ is independent of the waiting time within the examined time range. However, for $|V_{min}| > 3.0\,k_BT$ and thus directed percolation, $\langle N_b\rangle$ is found to increase with waiting time. This indicates that aging effects are important in directed percolated systems. In contrast, in continuous percolation equilibrium is attained quickly. These findings support the importance of the above-mentioned local and global rearrangement processes in continuous and directed percolation, respectively. Furthermore, in continuous percolation equilibrium is reached quickly, while in directed percolation it is reached only very slowly.

7.6 Conclusions

We have investigated gel formation in a system with competing attractive and repulsive interactions. Confocal microscopy experiments on charged colloid-polymer mixtures

were combined with Brownian dynamics simulations of particles interacting via the Asakura-Oosawa and Coloumb potentials. Depending on the overall potential minimum V_{min}, which can be varied through the attractive and/or repulsive component of the interactions, different states have been identified; a fluid and continuous as well as directed percolated networks. The transitions between these states are associated with changes in structural parameters, in particular the number of bonds per particle with significant increases in the mean, variance and most probable value of the distribution of the number of bonds.

The effect of continuous percolation on the dynamics is small. However, directed percolation leads to a significant dynamic slowdown. This is attributed to the large number of bonds and concomitant strong confinement of the particles in the attractive potentials of their neighbors. This is also reflected in significant aging observed in directed percolated systems. It suggests that equilibration is very slow in directed percolated systems, but occurs quickly in continuous percolated systems. Our results hence contribute to an improved understanding of the relation between structural and dynamic features of gel forming systems and hint at their importance for their rheological properties.

Chapter 8

Colloid-polymer mixtures: confinement and shear

8.1 Introduction

This chapter is directly tied to the last one, but now the influence of pore confinement, i.e., the incorporation of two parallel flat walls, as well as the influence of shear on the gel model system from the previous chapter are explained. Especially at low shear strengths for gels beyond the DP transition a selective yielding of the network structures can be observed, which typically results in the formation of larger clusters, that will be referred to as *gel-slabs*.

8.2 Model

Repulsive flat walls. A very crucial ingredient for the discussions is the influence of walls, which turn out to mediate a local microscopic synersis, i.e., the detachment of the short-ranged but purely repulsive wall. The walls in our simulations are realized via completely repulsive potentials, which we define via the repulsive force on species ν

$$\mathbf{f}_{\nu}^{\mathrm{ext}}(z) = \mathbf{e}_{\mathrm{z}} \begin{cases} f^{\mathrm{wall}} \operatorname{atan}\left(-\frac{z-(\sigma_\nu/2)}{10\sigma}\right) & , \quad z < \sigma_\nu/2 \\ 0 & , \quad \text{else} \end{cases} , \tag{8.1}$$

for the bottom wall. For the top wall, we apply the same repulsive force. The energy scale of the wall potential has been set to $f^{\mathrm{wall}}\sigma = 10^4 k_{\mathrm{B}}T$ in order to obtain a steep wall potential without softness effects.

Couette shear flow. A second external field is applied on our systems: a linear *Couette shear flow*. The shear flow is induced in the y-direction of the simulation box, whereas the gradient is imposed in the z-direction. The corresponding solvent velocity in the dependence of the spatial coordinates is defined as

$$\mathbf{u}^{\infty}(z) = \mathbf{e}_{\mathrm{y}} u(z) = \mathbf{e}_{\mathrm{y}}(-u_{\max} + z\dot{\gamma})\,, \tag{8.2}$$

where the shear rate $\dot{\gamma}$ and the maximum velocity $u_{\max} = \dot{\gamma} l_{\mathrm{z}}/2$ (with l_{z} being the box size in z-direction) have been introduced. The shear rate has the dimension of a frequency and determines the strength of the gradient of the applied flow.

The magnitude of the external field is expressed by the dimensionless number, that is referred to as the *Peclét number*, i.e. Pe. For a monodisperse system with a self-diffusion coefficient D and particle radius $R = \sigma/2$ it is defined by

$$Pe = \frac{\dot{\gamma} R^2}{D}\,. \tag{8.3}$$

We are dealing with a slightly polydisperse system. Therefore, particles of different sizes have also different Peclét numbers. Since larger particles have a larger contribution to the overall packing fraction, we define our applied shear rate in terms of the Peclét number Pe as

$$\langle\dot{\gamma}\rangle = \frac{1}{m}\sum_{\nu=1}^{m} Pe\frac{D_\nu}{R_\nu^2}\,, \tag{8.4}$$

with D_ν the diffusion coefficient of species ν is (Eqs. (3.1) and (3.2)). The externally applied shear flow imposes a linear force field in the system. The fact that the shear can easily be represented as a force with linear dependence comes from the assumption of neglected hydrodynamic interactions. Although for low Pe the effect should not be too large, at this point it is important to note, that in general hydrodynamic interactions play an important role for non-equilibrium setups. In some cases can lead to fundamentally different results, as shown, e.g., by J. Vermant and M.J Solomon [219].

We neglect hydrodynamic interactions and assume no-slip boundary conditions at the particle-solvent interface. The velocity $\mathbf{u}$ of a particle then equals the velocity of the solvent background, i.e., $\mathbf{u}^{\infty}$. According to the BD algorithm from Eq. (3.8) the particle displacement due to the external shear flow can be expressed as

$$\Delta\mathbf{r}^{\mathrm{shear}}(z) = \int_0^{\Delta t} \mathrm{d}t\, \mathbf{u}^{\infty}(z) \approx \mathbf{u}^{\infty}(z)\Delta t\,. \tag{8.5}$$

Inserting Eq. (8.2) with the new definition of the shear rate (Eq. (8.4)) into this equation yields

$$\Delta\mathbf{r}^{\mathrm{shear}}(z) = \mathbf{e}_{\mathrm{y}}(-u_{\max} + z\langle\dot{\gamma}\rangle)\Delta t\,. \tag{8.6}$$

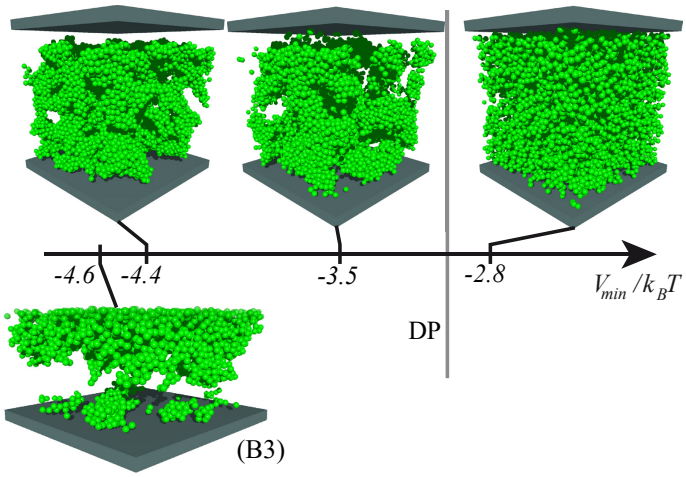

Figure 8.1: Rendered snapshots of samples in the vicinity of a wall obtained in (top) simulations with systems along path A and (bottom) an experiment with sample B3.

Since rearrangements in the vicinity of such a shear flow happen on a different (typically shorter) timescale, we introduce an adjusted *shear time-scale*

$$\tau_{\mathrm{s}} = \begin{cases} \tau_{\mathrm{B}}/Pe & , \quad Pe > 1 \\ \tau_{\mathrm{B}} & , \quad \text{else} \end{cases} , \tag{8.7}$$

which is more suitable to compare systems with different shear strengths.

8.3 Results

8.3.1 Confined gels

In Fig. 8.1 we illustrate qualitatively the effect of flat repulsive walls, that has been observed in simulations (*top panel*) and experiments (*bottom panel*). In continuous percolation, the particles occupy the whole volume, also in the vicinity of the wall. In directed percolated systems, in contrast, the vicinity of the wall is depleted of particles. This indicates that directed connections between particles tend to compact the network. This resembles syneresis, i.e. the macroscopic expulsion of fluid from a gel due to the shrinking of the network. This has been observed in a variety of materials, like gelatin [220], polysaccharide gels [221, 222], organogels [223], microgels [224] and also weakly attractive colloidal gels [225]. The link between network shrinkage and directed percolation might provide new aspects for the understanding of syneresis.

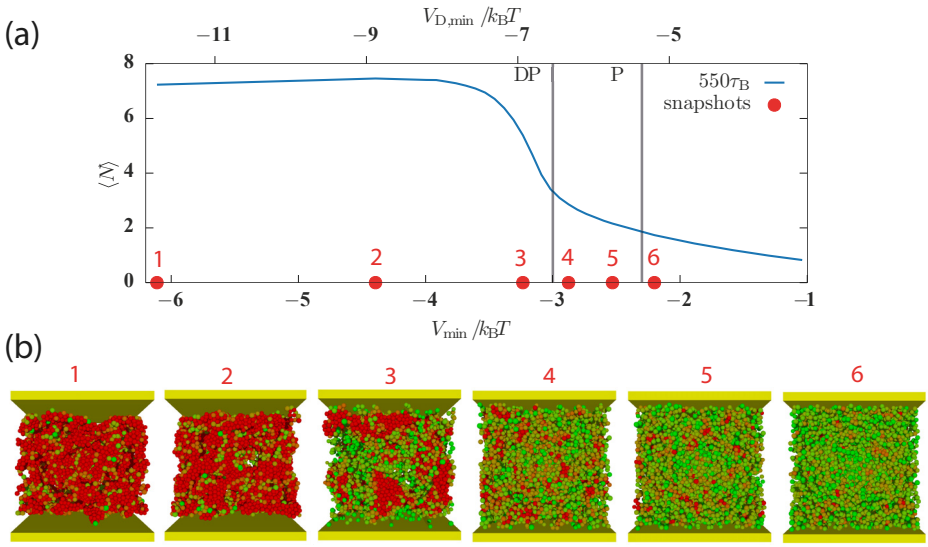

Figure 8.2: Confined gel without externally applied shear flow after an initial relaxation time of $550\tau_B$ for gels with different attraction strength and constant $\kappa\sigma = 40$ (along path A). (a) $\langle N_b \rangle$ as a function of V_{min} or $V_{D,min}$. (b) Snapshots of the final configurations of the different gels with attraction strengths according to the red points in plot (a): $V_{min,1} = -6.1k_BT$, $V_{min,2} = -4.4k_BT$, $V_{min,3} = -3.2k_BT$, $V_{min,4} = -2.8k_BT$, $V_{min,5} = -2.5k_BT$, $V_{min,6} = -2.2k_BT$. The particles are continuously colored with respect to the number of bonds, where *red* particles have 5 or more bonds and *green* particles have one or less bonds.

To further study the detachment, we focus on a number of six different gels (see Fig. 8.2) along path A (cf. Fig. 7.4). The samples are chosen in such a way, that three of them are beyond the DP transition (1-3), two are below the DP transition but beyond the P transition (4-5), and one is not percolated at all (6), in the non-shear case . In Fig. 8.2(a) the connection of the slight detachment from the wall with the directed percolation can easily be identified. Additionally, as the color code of the particles indicates, there are only few low-bonded particles deep in the DP phase (see Fig. 8.2(b)/1-2), whereas for the system close to the transition, large aggregates that are highly-bonded are surrounded by less-bonded and homogeneously distributed particles (see Fig. 8.2(b)/3). For the remaining systems (see Fig. 8.2(b)/4-6), one can see the formation of small clusters indicated by orange particles.

8.3.2 Confined and sheared gels

In this section the effect of the Couette shear flow on a confined gel is investigated. The protocol in order to obtain the final non-equilibrium steady-states reads as follows:
First, the systems are relaxed without shear for a time of $550\tau_B$ as described before.

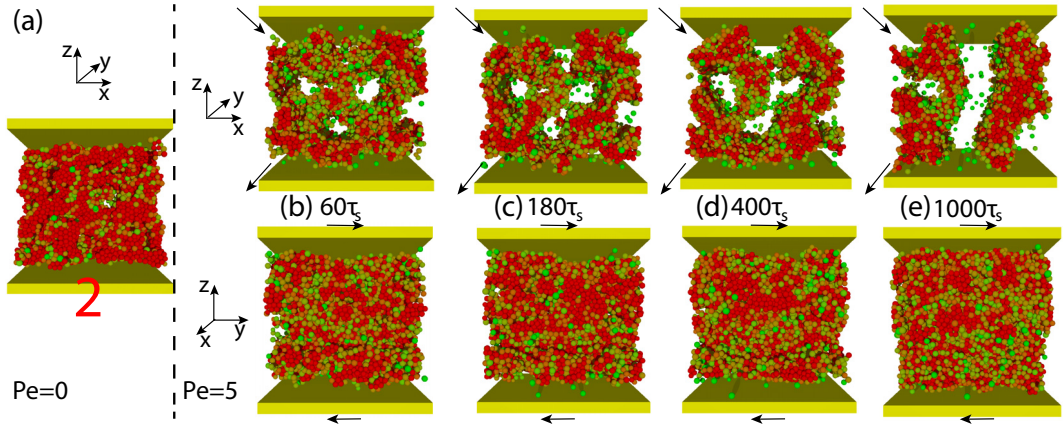

Figure 8.3: (a) xz-plane of the final configuration of the state point 2 ($\kappa\sigma = 40$ and $V_{\mathrm{min},2} = -4.4k_{\mathrm{B}}T$ after a relaxation time of $550\tau_{\mathrm{B}}$) from Fig. 8.2 which is used as a start configuration for the shear simulations (b-e): The shear force is linearly switched on within $30\tau_B$ from $Pe = 0$ to $Pe = 5$. Then the system is sheared continuously and the state is shown after (b) $60\tau_s$, (c) $180\tau_s$, (d) $400\tau_s$, (e) $1000\tau_s$. The upper panel shows the xz-plane perpendicular to the direction of the shear force, whereas the bottom panel shows the same snapshot from the side-face (the yz-plane).

Subsequently, the final states of the relaxed gels, which may already show the local detachment from the walls, are exerted to the additional external field. The shear flow is linearly switched on during a timespan of $30\tau_{\mathrm{B}}$. After that, the gels are being sheared for $1000\tau_{\mathrm{s}}$.

Switch-on of the Couette flow. The typical evolution in time of a sheared gel, that corresponds to point 2 (from Fig. 8.2) is illustrated in Fig. 8.3 for two point-of-views, i.e., looking on of the xz-plane (top) or on the yz-plane (bottom).

The gel in Fig. 8.3 represents the relaxed configuration after the initial $550\tau_{\mathrm{B}}$. Shortly after starting the shear, some of the strands inside the network break up. This is followed by a consecutive alignment of the open ends. This two-step process is the reason for the holes that become visible in the xz-view (see Fig. 8.3(b)). First only the thinner or longer strands break up, later thicker connections tear apart, as can be seen in the center of the simulation box at intermediate and long times (see Fig. 8.3(c-e)). The remaining large aggregations are elongated in the y- and z-direction and might be completely separate from other aggregations. They will be referred to as shear-induced *gel-slabs* in the following. Although they look rigid at first glance, particles inside such a slab rearrange locally by hopping from one neighbor to another rather than moving cooperatively as one large cluster.
On the other hand, the bottom panel of Fig. 8.3 displays the yz-planes of the same snapshots. First, no holes are visible from this point-of-view. Second, as indicated by a

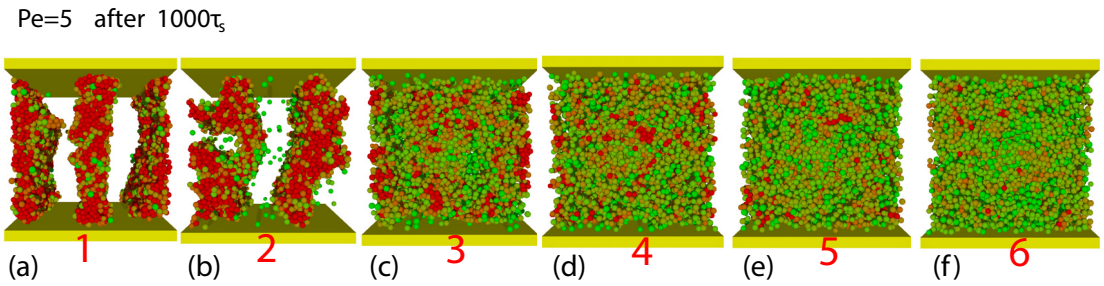

Figure 8.4: Final snapshots after shearing different gels for $1000\tau_s$ at the state points $\kappa\sigma = 40$ and (a) $V_{\mathrm{min},1} = -6.1k_BT$, (b) $V_{\mathrm{min},2} = -4.4k_BT$, (c) $V_{\mathrm{min},3} = -3.2k_BT$, (d) $V_{\mathrm{min},4} = -2.8k_BT$, (e) $V_{\mathrm{min},5} = -2.5k_BT$, (f) $V_{\mathrm{min},6} = -2.2k_BT$. In all figures the xz-plane is displayed at front.

larger number of green particles, the switch-on of the shear induces break-ups of some of the bonds, especially at the surfaces of the gel-slabs. This indicates, that the slabs are very compact inside, but contain rather loose particles at their surfaces.

Increasing V_{min}, constant Pe. In Fig. 8.4 snapshots of typical systems at the state points from Fig. 8.2 are shown for a shear rate according to $Pe = 5$ and after $1000\tau_s$ of shearing. For the systems that are below the DP threshold (4-6) the shearing has no apparent impact on the system. Despite some bond-fracturing, the systems remain in an overall homogeneous structure, in which most of the particles are still interconnected with each other in a similar way as in the unsheared system.

The gel, which was in the unperturbed case just beyond the DP transition (3), contained larger domains of clustered particles (cf. Fig. 8.2(b)). The size of the clusters has been reduced due to the shear forces. This becomes visible by a more homogeneous color distribution.

Finally, for the state points, that lay in the unperturbed case farther beyond the DP transition (Fig. 8.4(1-2)), the sheared networks tend to break up in gel-slabs. However, the stronger the attraction strength is the more highly bonded particles can be identified. For the gel of state point 1 nearly all particles exceed five bonds. The gel-slabs have high packing fraction inside, which compensates the large void volumes that arise between the gel-slabs. We expect that the large and compact structures remain stable for long times after stopping the Couette flow. Although this has not been investigated further, the stability of gel-slabs is expected in both cases (points 1 and 2), because the thermal energy is lower by a factor of at least 4 than the attraction strength and therefore cooperative rearrangements of very large clusters would be needed in order to split up one slab or merge two them.

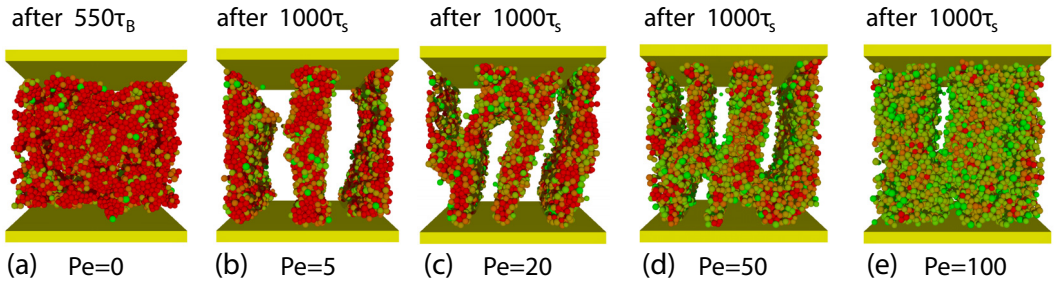

Figure 8.5: Final snapshots of the xz-plane of the final states after $1000\tau_s$ for the parameters $\kappa\sigma = 40$ and $V_{min} = -6.1k_BT$ (point 1) and the Peclét numbers (a) $Pe = 0$, (b) $Pe = 5$, (c) $Pe = 20$, (d) $Pe = 50$, (e) $Pe = 100$. The configuration in (a) has been used for the other simulations as an initial seed.

Constant V_{min}, increasing Pe. Now, we study the effect of shear strength at $V_{min,1} = -6.1k_BT$. The final configurations of the systems with different Peclét numbers are shown in Fig. 8.5. For the case of zero shear the system detaches from the wall as discussed before. Most of the particles are colored red, indicating a large number of bonds (≥ 5). Whereas for small shear rate (Fig. 8.5(b)) the number of highly bonded particles has barely changed, the overall structure undergoes a huge change, namely the formation of gel-slabs. This effect can clearly be observed up to $Pe = 50$, whilst the number of bonds per particle significantly decreases, as indicated by an increasing number of green particles. For $Pe = 100$ (Fig. 8.5(e)), much more loose and homogeneous structures are obtained. This is accounted to the large Pe and an additional (second) break-up of local cluster structures [226].

Interestingly, as the configuration at rest (Fig. 8.5(a)) has been used as a seed for the sheared systems, the accompanied lateral position of the major network-fracturing are located approximately at the same positions. This might be connected with a built-in weakness of the gel in the first place. However, this question will not be discussed within this work.

Void volumes and free paths We quantify the above described findings by introducing so-called *void volumes*, as employed in the study from N. Koumakis et al. [74]. For our purposes two distinct void volumes are defined. Their meanings are sketched in Fig. 8.6(a). For their calculation the simulation box is divided into a grid of $M_x \times M_y \times M_z$ points. Then for each point, the largest possible sphere that does not intersect with any particle of the gel is calculated. The radius of this sphere is denoted by Δs_R and is exemplarily sketched by the blue line in Fig. 8.6(a). The second measure is characterized by a (not necessarily finite) volume, which is elongated in the z-direction, as indicated by the yellow line in Fig. 8.6(a). It is defined for every grid point as the smallest free path in z-direction until a colloid is intersected and is denoted by Δs_z in the following.

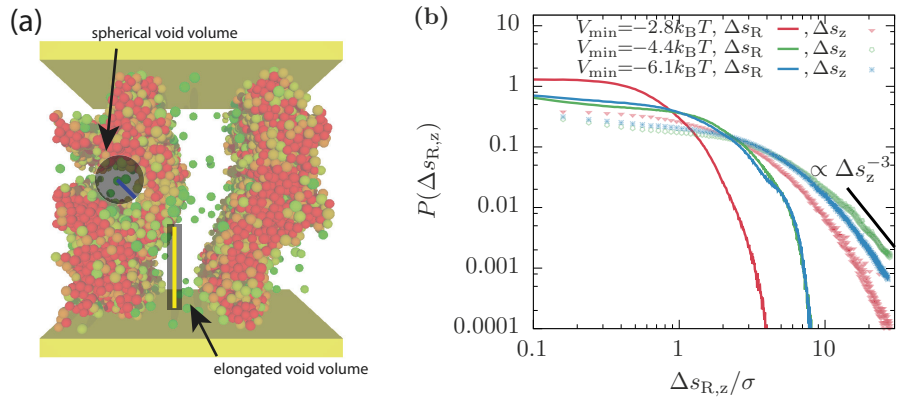

Figure 8.6: (a) Illustration of the definition of the two investigated void volumes, where the size is determined by the parameters Δs_R (blue line) and Δs_z (yellow line) as explained in the text. (b) Distribution of (lines) Δs_R and (symbols) Δs_z for the three state points 1,2, and 4 as given by Fig. 8.2. The black line is a guide to the eye and proportional to a power law Δs_z^{-3}.

We reduce our study on the three systems corresponding to the points 1,2, and 4. Then we plot the distributions $P(\Delta s_R)$ and $P(\Delta s_z)$ of the measures Δs_R and Δs_z in Fig 8.6(b) for the above-mentioned gels at rest. First, one can see the striking difference between the widths of the distributions of the void volumes for systems, which are not inside the DP phase (red) and those which are inside the DP phase (blue and green). Second, the elongated void volumes can be larger than the radial ones and seem to approach a Δs_z^{-3} power law for large Δs_z.

After the shear flow is switched on the distributions of void volumes change for both, the percolated and the directed percolated gels (see Fig. 8.7). In the percolated gel both void volume measures just become smaller with increasing Pe, indicated by a narrowing distribution (Fig. 8.7(a,b)). For the directed percolated gel, the distributions first become broader with increasing Pe and then contract again. Especially the case of the elongated measure Δs_z in Fig. 8.7(d) is interesting. Whilst the distribution is broadening with low Pe, it exhibits a power-law decay with an exponent -1 for intermediate lengths. For larger Pe the decay becomes approximately proportional to Δs_z^{-3} again. This goes along with the inner break-up of gel-slabs. A possible interpretation for the occurrence of the two exponents will be given in the following.

For the sheared system the elongated void measure along the z-direction becomes independent of the other spatial directions. As the plot suggests the remaining dependency is approximately proportional to the inverse of the length scale (in z-direction). Therefore, $P_{\text{shear}} = P_z \approx \Delta s_z^{-1}$ is the isolated (decoupled) probability for such a length along a single direction. In the case of no shear the structures are expected to be rather isotropic in all three spatial directions. Therefore the probability of finding a void length Δs_z in the z-direction should depend also on the other spatial directions. One can therefore conclude, that due to the isotropy the length of the elongated void volumes in one

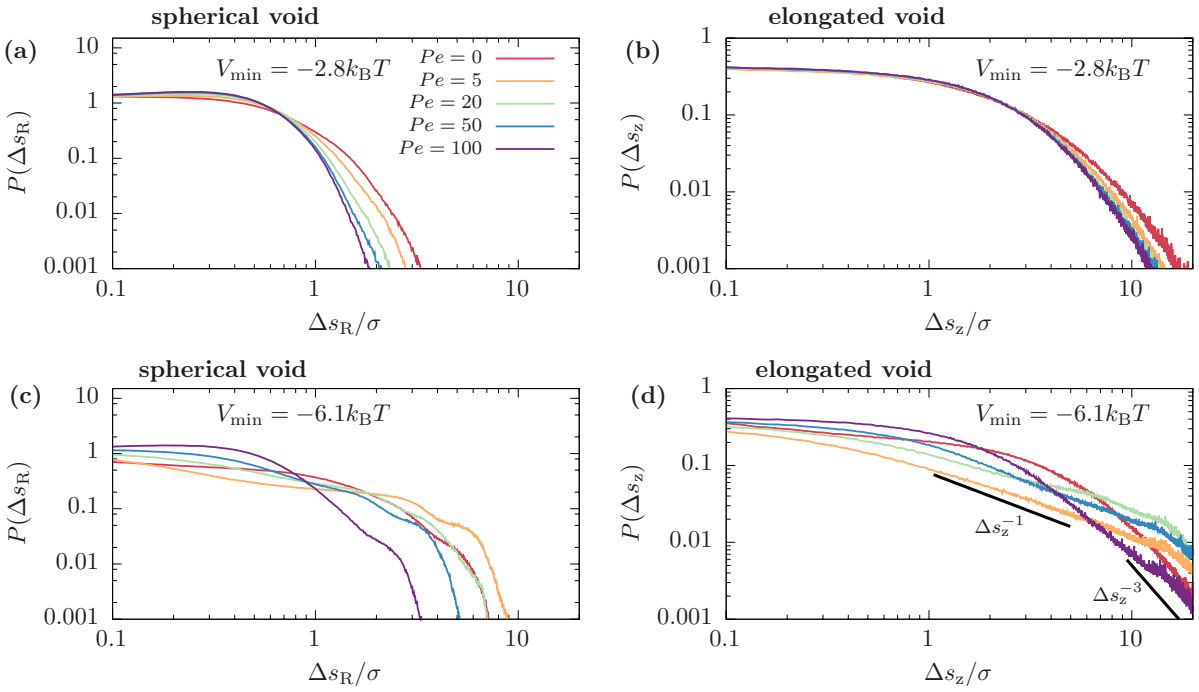

Figure 8.7: Double logarithmic plots of the distribution of (a,c) spherical and (b,d) elongated void volume measures Δs_R and Δs_z as described in the text. For a gel (a,b) below the DP transition (point 4, $V_{\min} = -2.8k_BT$) an (c,d) for a gel far beyond the DP transition (point 1, $V_{\min} = -6.1k_BT$). The black solid lines in (d) are guides to the eye and correspond to the power laws Δs_z^{-1} and Δs_z^{-3}.

direction is limited by a similar length (of free volume) in the other spatial directions, i.e. $P_{\mathrm{iso}} = P_{\mathrm{x}} P_{\mathrm{y}} P_{\mathrm{z}} \approx [\Delta s_{\mathrm{s}} \Delta s_{\mathrm{y}} \Delta s_{\mathrm{z}}]^{-1}$. Assuming, that all spatial directions are equal, we obtain the relation $P_{\mathrm{iso}} = P^3_{\mathrm{shear}}$. For extreme large Pe the constituents of the gel-slabs are teared apart. Therefore the whole slabs dissolve, the void volumes shrink again and a power-law decay with exponent -3 is regained.

8.4 Conclusion

We have shown, that gels beyond the DP transition possess a complex structural behavior if they are subjected to confinement and shear. This suggests that the observed effects are caused by the non-equilibrium properties of gels. Firstly, we have investigated the effect of confinement. Here, the gels were exerted to the external field of two parallel, flat, and completely repulsive walls. In the experiments as well as in the simulations we found local detachments of the network structures from the wall, but only for the samples that were directed percolated.
Secondly, in the simulations we have applied a Couette shear flow on the system. For low shear rates and increasing waiting times not only the thinner and longer network connections broke up, but also thicker strands were split. Here, in particular diagonally directed particle chains broke up and aligned parallel to the external shear field in a way that the re-aggregation of diagonally split strings became less probable. Whether the initial gel (at rest) was directed percolated or not had further influence on the final states during shear. For systems beyond the DP transition very compact gel-slabs formed, which were not rigid but rather exhibited an internal hopping motion of particles from one neighbor to the other. Although the fate of these slabs could not be fully determined, it is rather probable that they remain stable for long times. However, the expected long-time meta-stability of the gel-slabs will be explored in future simulations.

Additionally, we observed that the final location of the gel-slabs might be dependent on the location of previously built-in weaknesses of the network structure.
In the quantitative analysis of the gels we had a look at length-scales of two different types of void volumes, one being of a spherical shape and the other being elongated in z-direction. In the case of the formation of gel-slabs the appearance of different exponents in the distribution of the elongated void volume sizes indicated a decoupling of spatial directions in the network structures.

Chapter 9

List of publications

[1] **Particle segregation in a sedimenting bidisperse soft sphere system**

Matthias Kohl and Michael Schmiedeberg
Soft Matter, vol. 10, issue 24, p. 4340 (2014)
DOI: 10.1039/c4sm00140k

Abstract: We study the sedimentation process of a binary colloidal soft sphere system where significant overlaps of the particles are possible. We employ estimates of the equation of states in the small and large pressure limit in order to predict the final states of the sedimentation process. Furthermore, Brownian dynamics simulations were performed in order to confirm the predictions and to explore the dynamics of the sedimentation. We observe that the segregation process due to gravity usually consists of multiple steps. Instead of single particles moving upwards or downwards we usually observe that first local segregation occurs, then clusters consisting of particles of one species are formed that finally sink towards their equilibrium position within the final sedimentation profile. The possible final states include complex phases like a phase consisting of large particles on the top and the bottom of the system with small particles in between. We also observe metastable network-like structures.

Statement of the author: This paper has been written in cooperation with M. Schmiedeberg. Most of the work, including simulations, data analysis, and data presentation have been done by me. The text of the paper was written by both authors in an iterative process.

[2] **Anisotropic pair correlations in binary and multi-component hard-sphere mixtures in the vicinity of a hard wall: a combined density functional theory and simulation study**

Andreas Härtel, Matthias Kohl, and Michael Schmiedeberg
Submitted to: Physical Review E

Abstract: The fundamental measure approach to classical density functional theory has been shown to be a powerful tool to predict various thermodynamic properties of hard-sphere systems. We employ this approach to determine not only one-particle densities but also two-particle correlations in binary and six-component mixtures of hard spheres in the vicinity of a hard wall. The broken isotropy enables us to carefully test a large variety of theoretically predicted two-particle features by quantitatively comparing them to the results of Brownian dynamics simulations. Specifically, determine and compare the one-particle density, the total correlation functions, their contact values, and the force distributions acting on a particle. Furthermore, we theoretically calculate the direct correlation functions. We usually observe an excellent agreement between theory and simulations, except for small derivations in cases where local crystal-like order sets in. In addition, we demonstrate that due to the suppression of local crystallization, the predictions of six-component mixtures are better than those in bidisperse or monodisperse systems. Finally, we are confident that our results of the structural modulations induced by the wall lead to a deeper understanding of ordering in anisotropic systems in general, the onset of heterogeneous crystallization, caging effects and glassy dynamics close to a wall, as well as structural properties in systems with confinement.

Statement of the author: The idea of the paper has been developed by the authors on the International Soft Matter Conference, 2013 in Rome. I have dealt with the simulation part of the paper as well as with the graphical presentation of the data. The data analysis has been performed by AH and me, equally. AH carried out the DFT calculations. All authors wrote the manuscript.

[3] **Directed percolation identified as equilibrium pre-transition towards non-equilibrium arrested gel states**

Matthias Kohl, Ronja Capellmann, Marco Laurati,
Stefan U. Egelhaaf, and Michael Schmiedeberg

Submitted to: Nature Communications

Abstract: The macroscopic properties of gels arise from the presence of a load bearing network structure and slow dynamics. However, links between these structural and dynamical properties remain elusive. Different mechanisms have been proposed to cause the dramatic slowdown of the dynamics and the onset of aging at low temperatures or high densities, e.g., partial freezing, crowding, cluster aggregation, or continuous percolation of network structures. Here we present confocal microscopy experiments and simulations of gel-forming colloid-polymer mixtures with repulsive and attractive interactions. They reveal that directed percolation coincides with the slowdown of the dynamics and the onset of aging, and is a precursor of full dynamical arrest. The mean number of bonded neighbors is sufficient to define the onset of directed percolation, as well as its transitions to continuous percolation and dynamical arrest, i.e. gels, respectively. Directed percolation is also associated with a shrinking of the gel network which resembles syneresis.

Statement of the author: The paper has been written in cooperation with the Soft Condensed Matter Institute at the HHU Düsseldorf. The presented experiments have been carried out by Ronja Capellmann. The theoretical model, tho simulations, most of the numerical analysis of both simulation and experimental data, and the presentation of data have been elaborated by me. The text has been written cooperatively by all authors of the paper.

[4] ***In preparation:***
Anisotropy and memory during the single particle escape from a cage in the vicinity of a wall

Matthias Kohl, Andreas Härtel, and Michael Schmiedeberg

Plot: This paper will be mainly based on Chapter 6 of this thesis.

[5] ***In preparation:***
Shear-induced slab-like domains in a directed percolated colloidal gel

Matthias Kohl and Michael Schmiedeberg

Plot: This paper will be mainly based on Chapter 8 of this thesis.

Appendix A

Appendix

A.1 Fixed point iterations

In Sec. 2.6.4 the fixed point iterations have been shortly sketched for a general iteration scheme (Eq. (2.63)) and the *Picard-like* iteration scheme (Eq. (2.64)). The latter one is rather easy to implement, but unfortunately sometimes not sufficient to solve implicit equations within reasonable time. Sometimes it is even impossible to solve the equations due to the deficient convergence towards the fixpoint. Nevertheless, this algorithm has been applied to solve the DFT equation (Eq. (2.61)) transform the direct correlations via the OZ relation into total correlation functions.

A more sophisticated approach is given by the direct inversion in the iterative subspace (DIIS), which was proposed by K.-C. Ng [227] from necessity in order to solve the OZ relation within the HNC closure for very strong coupling parameters of charged particles. It can defined within a certain *linear* iteration scheme, where $\mathbf{a}_n$ define the series of iteration vectors and serve as *input vectors* vor the next iteration step. The *output vectors* are $\mathbf{b}_n$. Then we have the relationship

$$\mathbf{b}_n = \mathbf{T}(\mathbf{a}_n) \tag{A.1}$$

where the mapping function $\mathbf{T}$ is linear, for example a simple Picard iteration. The Ng-algorithm now requires the history of the last N vectors. For each member of this history, we can define the *error vector*

$$\mathbf{d}_n = \mathbf{b}_n - \mathbf{a}_n \tag{A.2}$$

The ansatz is, that the residuum of the next step shall be constructed via a linear combination of the previous error vectors, i.e.,

$$\mathbf{d}_{N+1} = \sum_{m=1}^{N} c_m \mathbf{d}_m \tag{A.3}$$

For the representation in the basis system of the error vectors, we want to minimize the norm of the next-step residuum vector, such that it should coincide with the zero vector. Therefore, we can define a Lagrangian

$$\mathcal{L} = \mathbf{c}^T \overset{\leftrightarrow}{D}\, \mathbf{c} - \lambda \left(\sum_{m=1}^{N} c_m - 1 \right) , \tag{A.4}$$

where λ is the undetermined Lagrangian parameter and the elements $D_{ij} = \langle \mathbf{d}_i, \mathbf{d}_j \rangle$ are defined by the standard vector space scalar product of the two error vectors $\mathbf{d}_i$ and $\mathbf{d}_j$. We can apply the Euler-Lagrange equations for the expression from Eq. (A.4), i.e.,

$$\frac{\partial \mathcal{L}}{\partial c_m} = 0 = \sum_{i=1}^{N} c_i \langle \mathbf{d}_i, \mathbf{d}_m \rangle + \sum_{j=1}^{N} c_j \langle \mathbf{d}_m, \mathbf{d}_j \rangle - \lambda \, . \tag{A.5}$$

The sums occuring on the right hand side are equal. Therefore, we can replace λ by 2λ and obtain a simple set of linear equations, from where the coefficients c_m can be determined

$$\begin{pmatrix} \langle \mathbf{d}_1, \mathbf{d}_1 \rangle & \langle \mathbf{d}_1, \mathbf{d}_2 \rangle & \cdots & \langle \mathbf{d}_1, \mathbf{d}_N \rangle & -1 \\ \langle \mathbf{d}_2, \mathbf{d}_1 \rangle & \langle \mathbf{d}_2, \mathbf{d}_2 \rangle & \cdots & \langle \mathbf{d}_2, \mathbf{d}_N \rangle & -1 \\ \vdots & \vdots & \ddots & \vdots & \vdots \\ \langle \mathbf{d}_N, \mathbf{d}_1 \rangle & \langle \mathbf{d}_N, \mathbf{d}_2 \rangle & \cdots & \langle \mathbf{d}_N, \mathbf{d}_N \rangle & -1 \\ -1 & -1 & -1 & -1 & 0 \end{pmatrix} \cdot \begin{pmatrix} c_1 \\ c_2 \\ \vdots \\ c_N \\ \lambda \end{pmatrix} = \begin{pmatrix} 0 \\ 0 \\ \vdots \\ 0 \\ -1 \end{pmatrix} , \tag{A.6}$$

where the last column of the matrix guarantees the normalization criterion $\sum_m c_m = 1$. After solving the set of equation, we can finally calculate the best approximation for the next iteration step according to the N-step-DIIS

$$\mathbf{a}_{N+1} = \sum_{m=1}^{N} c_m \mathbf{b}_m \, . \tag{A.7}$$

A.2 Bulk comparisons between DFT/FMT and BD simulations

In Chapter 5 we have presented two-particle direct correlations (Eq. (2.60)) and total correlations (Eq. (2.34)) in anisotropic situations for HS particles that reside in front of a wall. Access to former correlations ($c^{(2)}_{\nu\nu'}$) have been made possible by means of DFT calculations, whereas for the latter ones ($h^{(2)}_{\nu\nu'}$) we have transformed the direct correlation by making use of the general OZ relation (Eq. (2.93)). These total correlations were detailed studied for anisotropic, polydisperse, and dense systems. In this appendix, we visualized both kinds of correlation functions in Fig. A.1 for a monodisperse and a

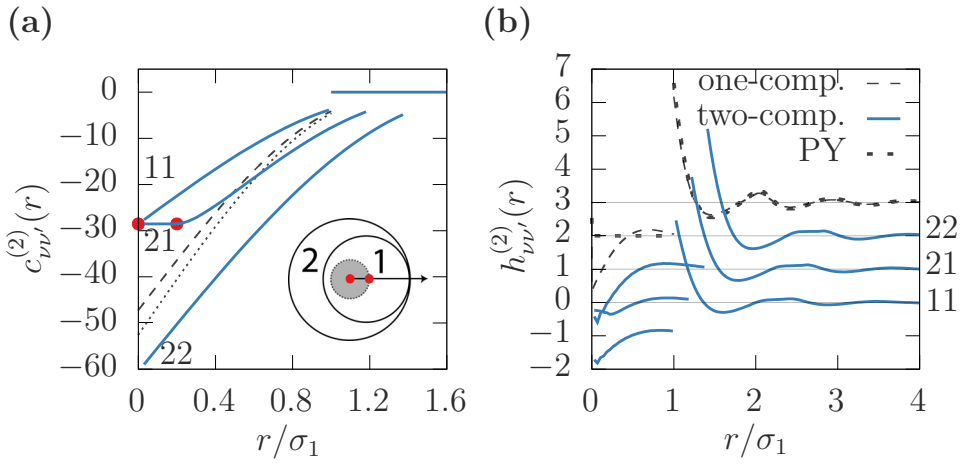

Figure A.1: (a) Direct and (b) total correlation functions in bulk for one- and two-component (50:50) hard-sphere systems with volume fraction $\phi = 0.5$. In the two-component case, the correlations between possible combinations of species are labeled by 11 (small/small), 21 (large/small), and 22 (large/large). All correlations are determined from our DFT calculations in combination with the OZ relation; for comparison we also show the analytically known Percus-Yevick (PY) result for the one-component system [122]. The inset in (a) sketches that if a small particle 1 is inside a larger particle 2 its center point can move within the gray (shaded) area without changing the intersection volume of the spheres. As a consequence, there is a plateau in the 21 curve between the two red (solid) dots.

binary system in bulk. In the binary system, four combinations between small and large particles exist, where the mixed combinations small/large and large/small are identical in bulk. The direct correlations are calculated using Picard iterations on DFT with FMT as described in Sections 2.6 and 2.7.

In the left plot (Fig. A.1(a)) one can nicely see the emergence of a plateau for $r < 0.2\sigma_1$, where $c^{(2)}$ is constant. This plateau stems from the fact, that the 3D-fundamental measures do not change the relevant integration volume V in the corresponding equation (Eq. (2.92)). In other words: the overlap volume of two unequally sized spheres remains constant as long as the smaller sphere is completely encapsulated by the larger one.

In the right plot (Fig. A.1(a)) the transforms of the direct correlation functions in bulk, i.e. $h^{(2)}_{\nu\nu'}$, are shown without a numerically cleared core as always done in the corresponding plots of the main chapter (Chap. 5). The calculated total correlations of our approach tend produce unphysical data in the core of the particles. The Percus-Yevick solution [122] is shown as a reference. Contrarily, it does not contain any values unequal to -1 inside the core (as it should). As stated in the main chapter, we deal with this fact by replacing the forbidden values with -1 in our plots.

A.3 Hankel transform of the anisotropic OZ relation

Starting with the direct correlation functions $c^{(2)}_{\nu\nu'}$ determined from FMT, we obtain the total pair correlation functions $h^{(2)}_{\nu\nu'}$ by solving the OZ relation as defined in Eq. (2.93) numerically. In a gedankenexperiment we rescale the involved correlation functions by a factor $\sqrt{\rho_\nu(\mathbf{r})\rho_{\nu'}(\mathbf{r}\,')}$ such that they are 0 in all locations that must not be reached by a particle. Therefore, it is sufficient to solve the OZ relation only outside of the wall, even if the original direct correlations might be nonzero inside the wall.

As shown in Eq. (5.5), we solve the OZ relation numerically in Fourier space, where convolutions become simple products. In our case, we consider functions with radial symmetry, i.e., functions $f(x, y)$ with $x = r\cos(\varphi)$ and $y = r\sin(\varphi)$ that do not depend on φ. Then, their Fourier transforms are

$$F(f)(k_x, k_y) = \frac{1}{2\pi}\int_{\mathcal{R}^2} \mathrm{d}x\mathrm{d}y\, f(x, y)e^{-\imath(xk_x+yk_y)}\,, \tag{A.8}$$

which in polar coordinates after the integration over φ leads to

$$F(f)\,(s) = \int_0^\infty \mathrm{d}r\, r f(r) J_0(sr)\,. \tag{A.9}$$

This result corresponds to a Hankel transform (or Bessel transform) as introduced in Eq. (5.4), which in general is defined by [228, 229]

$$F_\nu(u) = \mathrm{H}_\nu\left\{f(t)\right\} = \int_0^\infty \mathrm{d}t\, f(t) J_\nu(ut)t\,, \tag{A.10}$$

where $F_\nu(u)$ is called the Hankel transformed function of order ν of the function f if the integral exists. The function f can be a complex valued function and J_ν denote Bessel functions of the first kind that for integer ν are given by [154, 228, 229]

$$J_\nu(x) = \frac{1}{2\pi}\int_{-\pi}^{\pi} \mathrm{d}\tau\, e^{-\imath(\nu\tau - x\sin(\tau))}\,. \tag{A.11}$$

The inverse Hankel transform is given by

$$f(t) = \mathrm{H}_\nu^{-1}\left\{F_\nu(u)\right\} = \int_0^\infty \mathrm{d}u\, F_\nu(u) J_\nu(ut) u\,. \tag{A.12}$$

We employed the Hankel transform that for numerical calculations is available in the *Gnu Scientific Library* (GSL) and whose calculation scheme follows the work of H. F. Johnson [228] and D. Lemoine [229].

A.4 Explicit terms from the anisotropic FMT (White Bear II)

Preface. This part of the appendix supplies the derived terms that are used in the anisotropic FMT for a multi-component system in order to obtain the direct correlation functions (cf. Sec. 5.3). Major parts of this section have been written together with Andreas Härtel and Michael Schmiedeberg. Andreas Härtel implemented the necessary numerics.

From Eq. (5.2) we know that the direct correlation functions in FMT on a discrete numerical grid read

$$-c^{(2)}_{\nu\nu'}(\mathbf{r},\mathbf{r}') \approx \sum_{i=0}^{M-1}\sum_{\alpha}\sum_{\beta}\frac{\partial^2\Phi(z_i)}{\partial n_\alpha \partial n_\beta} W^{(\alpha\beta)}_{\nu\nu'}(\bar{I}_i, \boldsymbol{\Delta}), \tag{A.13}$$

where $\boldsymbol{\Delta} = \mathbf{r}' - \mathbf{r}$, z_i are the discrete and equidistant sample points along the z-axis separated by d_z, the weight-correlation functions $W^{(\alpha\beta)}_{\nu\nu'}(I,\mathbf{r})$ were defined in Eq. (5.3), and $\bar{I}_i$ is a corresponding interval $\bar{I}_i = [z_L, z_R]$, with $z_L = z_i - (\mathbf{r})_z - \frac{1}{2}d_\mathrm{z}$ and $z_R = z_i - (\mathbf{r})_z + \frac{1}{2}d_\mathrm{z}$ which contains z_i. Note that we employ $r_X \equiv (\mathbf{r})_X$ as a short writing for the X-component of the vector $\mathbf{r}$ in Cartesian coordinates spanned by $\{\hat{e}_x, \hat{e}_y, \hat{e}_z\}$.

The weight-correlation functions $W^{(\alpha\beta)}_{\nu\nu'}(I,\mathbf{r})$ are representations of convolutions of the translational invariant weight functions $w^{(\alpha)}_\nu$ and $w^{(\beta)}_{\nu'}$ from Eqs. (2.76)-(2.81) and (2.88) on the interval I. These weight functions have non-vanishing values solely on the volume S_ν or on the surface ∂S_ν of a sphere of species ν with radius R_ν. Thus, we consider two spheres A and B with centers in the origin and at $\boldsymbol{\Delta}$.

In order to calculate a function $W_{\nu\nu'}^{(\alpha\beta)}$ as given in Eq. (5.3), its integration interval I must have certain properties. To guarantee these properties, the interval I can be split into parts I_1 and I_2 with $I_1 \cap I_2 = \emptyset$ and $I = I_1 \cup I_2$, such that

$$W_{\nu\nu'}^{(\alpha\beta)}(I, \mathbf{\Delta}) := W_{\nu\nu'}^{(\alpha\beta)}(I_1, \mathbf{\Delta}) + W_{\nu\nu'}^{(\alpha\beta)}(I_2, \mathbf{\Delta}). \tag{A.14}$$

Subsequently splitting I in an appropriate way into intervals I_i guarantees the following necessary properties after splitting:

- Either the weight-correlation function vanishes on the interval I_i ($W_{AB}^{(\alpha\beta)}(I_i, \mathbf{\Delta}) = 0$) or both spheres S_A and S_B contain at least one point with z-component z for each point in the interval I_i ($\forall z \in I_i$, $\mathcal{V}_z := \mathcal{R}^2 \times \{z\}$: $\mathcal{V}_z \cap S_A \neq \emptyset$ and $\mathcal{V}_z \cap S_B \neq \emptyset$).
- The intersection $\partial S_A \cap \partial S_B$ of both spheres ∂S_A and ∂S_B either contains for all z in I_i at least one point $\mathbf{r}$ with z-component r_z or it contains for all z in the inner kernel $\mathring{I}_i$ no point $\mathbf{r}$ with z-component r_z.

Note that the whole intersection line $\partial S_A \cap \partial S_B$ can be contained in one slice $\mathcal{V}_z := \mathcal{R}^2 \times \{z\}$, when $\mathbf{\Delta} || \hat{e}_z$ (for visualization see Fig. A.2). We do not consider the special situation where the spheres touch in a single point which would contribute only to the point of the direct correlation function at particle contact whose value is not defined.

As can be seen from its definition in Eq. (5.3), the absolute value of the weight-correlation function $W_{AB}^{(\alpha\beta)}$ does not change if the spheres S_A and S_B exchange their positions and the interval I is adapted in an appropriate way, i.e., $I = [z_L, z_R]$ must been adapted to $I' = [(\mathbf{\Delta})_z - z_R, (\mathbf{\Delta})_z - z_L]$. However, the sign of the function changes when one of the involved weight functions is anti-symmetric and $\text{sign}(w_A)\text{sign}(w_B) < 0$; in our FMT approach, only the vectorial weight functions are anti-symmetric. Therefore, an exchange of the two spheres leads to

$$W_{AB}^{(\alpha\beta)}(I, \mathbf{\Delta}) = \text{sign}(w_A^{(\alpha)})\text{sign}(w_B^{(\beta)}) W_{BA}^{(\beta\alpha)}(I', \mathbf{\Delta}). \tag{A.15}$$

For this reason we only calculate combinations with $\alpha \geq \beta$, according to the order $3 > 2 > 1 > 0 > \mathbf{2} > \mathbf{1} > \overset{\leftrightarrow}{2}$. Furthermore, from the definition of the weight functions it follows

$$W_{AB}^{(\alpha 1)} = \tfrac{1}{4\pi R_B} W_{AB}^{(\alpha 2)}, \tag{A.16}$$

$$W_{AB}^{(\alpha 0)} = \tfrac{1}{4\pi R_B^2} W_{AB}^{(\alpha 2)}, \tag{A.17}$$

$$W_{AB}^{(\alpha \mathbf{1})} = \tfrac{1}{4\pi R_B} W_{AB}^{(\alpha \mathbf{2})}. \tag{A.18}$$

In summary, we have to calculate only the weight-correlation functions for the following combinations[1]:

$$\begin{aligned}(\alpha\beta) \in \big\{ &(33), (32), (3\mathbf{2}), (3\,\overset{\leftrightarrow}{2}),\\ &(22), (2\mathbf{2}), (2\,\overset{\leftrightarrow}{2}), (\mathbf{22}), (\mathbf{2}\,\overset{\leftrightarrow}{2}), (\overset{\leftrightarrow}{2}\,\overset{\leftrightarrow}{2}) \big\}. \end{aligned} \tag{A.19}$$

[1]Note, that vectorial weight functions are represented by bold numbers.

All other combinations can be obtained by the relations mentioned above.

If the support of $W_{AB}^{(\alpha\beta)}$ and the volume $\mathcal{V} = \mathcal{R}^2 \times I$ do overlap (have a non-vanishing intersection), three cases are left on this volume $\mathcal{V}$:

1. **sphere B inside sphere A**
   Sphere B is completely encapsulated by sphere A (or vice versa), i.e, without loss of generality:
   $S_A \cap S_B \cap \mathcal{V} = S_B \cap \mathcal{V}$ and $\partial S_A \cap S_B \cap \mathring{\mathcal{V}} = \emptyset$
2. **partial intersection**
   Different spheres with only partial intersection, i.e., without loss of generality:
   $\partial S_A \cap \partial S_B \cap \mathring{\mathcal{V}} \neq \emptyset$, but $S_A \neq S_B$
3. **two equal spheres**
   Equally sized spheres are at the same position
   $S_A = S_B$.

In the following sections we calculate the weight-correlation functions $W_{AB}^{(\alpha\beta)}$ in these three cases for all combinations mentioned in Eq. (A.19). During this calculation, we use the in-plane radii r_A and r_B of the spheres intersecting with a plane $\mathcal{V}_z$ perpendicular to the z-axis, i.e., of the circles $\mathcal{V}_z \cap S_A$ and $\mathcal{V}_z \cap S_B$ as shown in Fig. A.2(a). In our three cases, these radii are well-defined for all $z \in I$ with planes $\mathcal{V}_z$ within the volume $\mathcal{V} = \mathcal{R}^2 \times I$ of integration and read

$$r_A(z) = \sqrt{R_A^2 - z^2}, \tag{A.20}$$

$$r_B(z) = \sqrt{R_B^2 - \big((\boldsymbol{\Delta})_z - z\big)^2}. \tag{A.21}$$

Case 1 - sphere B inside sphere A

This case only occurs, when A is larger than B and when B is fully encapsulated. In such a situation the unit vectors pointing from the centers of sphere A or B towards their respective surfaces can be parametrized for $z \in I_i$ with cylindrical coordinates (γ, z) by

$$\frac{\mathbf{R}_A(\gamma, z)}{R_A} = \frac{1}{R_A} \begin{pmatrix} r_A(z)\cos(\gamma) \\ r_A(z)\sin(\gamma) \\ z \end{pmatrix}, \tag{A.22}$$

$$\frac{\mathbf{R}_B(\gamma, z)}{R_B} = \frac{1}{R_B} \begin{pmatrix} -r_B(z)\cos(\gamma) \\ r_B(z)\sin(\gamma) \\ z - (\boldsymbol{\Delta})_z \end{pmatrix}, \tag{A.23}$$

where $r_A(z)$ and $r_B(z)$ are given by Eqs. (A.20) and (A.21).

For all combinations, where the weight function of the larger encapsulating sphere is not $w_A^{(3)}$, both weight functions do not intersect and one trivially obtains $W_{AB}^{(\alpha\neq 3,\beta)} = 0$;

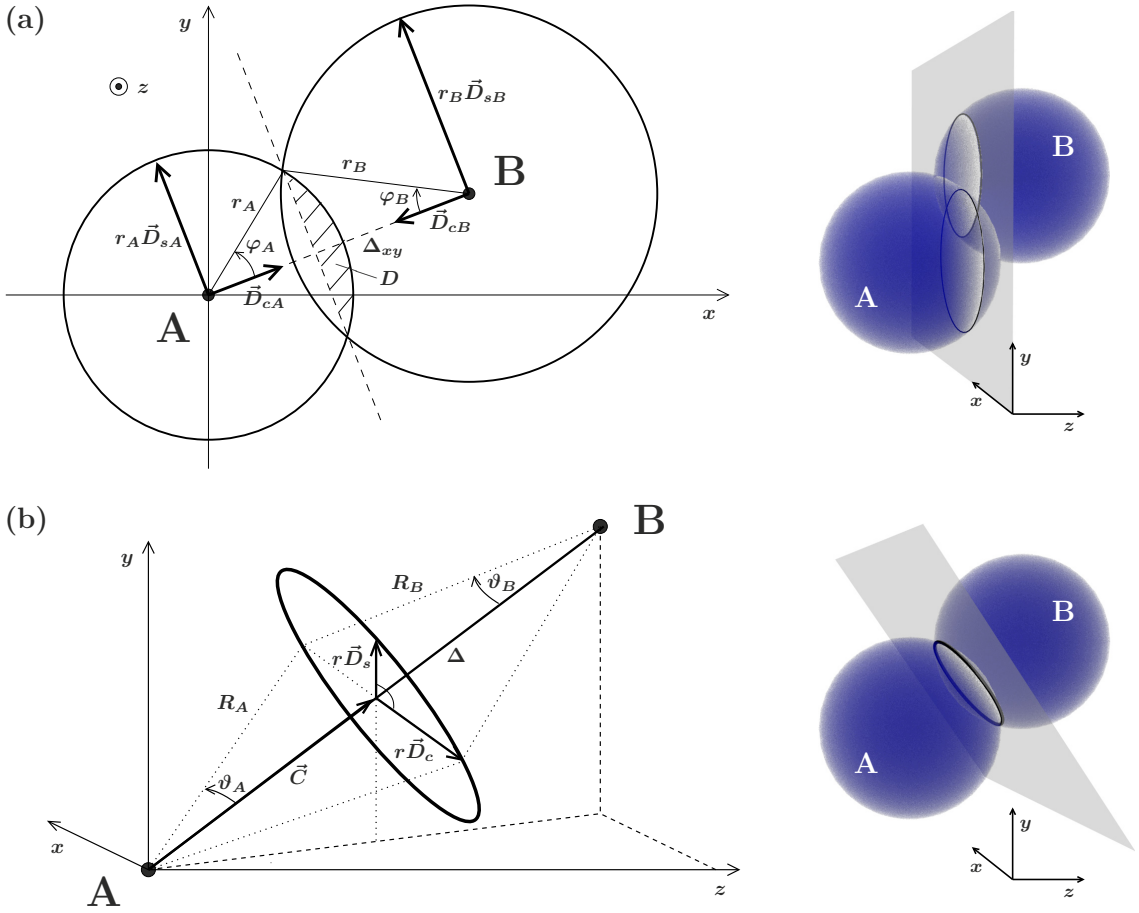

Figure A.2: Sketch of the intersection of two spheres A and B with radii R_A and R_B at a center-center distance of Δ. The sketch contains notations and parametrizations for (a) the intersection in the xy-plane and for (b) the intersection line, both illustrated on the right. Note that in (b) $|\mathbf{C}| = \Delta_A$ and $\Delta = \Delta_A + \Delta_B$.

we neglect the case where the encapsulated sphere touches the outer one in a single point. For the remaining combinations of weight functions the first two weight-correlation functions read

$$W_{AB}^{(33)} = \int_{z_L}^{z_R} \mathrm{d}z\, \pi r_B^2(z) = \left[\pi R_B^2 z + \frac{\pi}{3}\Big((\boldsymbol{\Delta})_z - z\Big)^3\right]_{z=z_L}^{z_R}, \tag{A.24}$$

$$W_{AB}^{(32)} = \int_{\mathcal{V}_i} \mathrm{d}\mathbf{r}\, \Theta\big(R_A - |\mathbf{r}|\big)\delta\big(R_B - |\mathbf{r} - \boldsymbol{\Delta}|\big)\,. \tag{A.25}$$

Since sphere B is encapsulated inside of sphere A, the Θ weight in Eq. (A.25) is equal to unity on the integration volume of interest. Furthermore, a linear parameter change for the xy-integration in this equation and a change to cylindrical coordinates $(r\cos(\gamma), r\sin(\gamma), z)$ lead to

$$W_{AB}^{(32)} = \int_{I_i} \mathrm{d}z \int_0^{2\pi} \mathrm{d}\gamma \int_0^{\infty} \mathrm{d}r\, r\delta\Big(R_B - \sqrt{r^2 + \big(z - (\boldsymbol{\Delta})_z\big)^2}\Big)\,. \tag{A.26}$$

In order to perform the integrals in Eq. (A.26), we use the equality

$$\delta\big(g(r)\big) = \sum_i \frac{\delta(r - r_i)}{|g'(r_i)|} \tag{A.27}$$

for a continuously differentiable function $g(r)$ with the finite set $\{r_i\}$ of simple zeros and the derivative $g'(r) = \partial g/\partial r$. In Eq. (A.26) the argument of the δ-distribution has the simple zero $r_1 = r_B(z)$ and $|g'(r_1)| = r/R_B$. Accordingly, the previous result of Eq. (A.26) becomes

$$W_{AB}^{(32)} = 2\pi R_B(z_R - z_L). \tag{A.28}$$

Similarly, it follows

$$W_{AB}^{(\mathbf{32})} = \int_{z_L}^{z_R} \mathrm{d}z \int_0^{2\pi} \mathrm{d}\gamma \int_0^{\infty} \mathrm{d}r\, R_B\delta\big(r - r_B(z)\big)\mathbf{R}_B(\gamma, z) = 2\pi\hat{e}_z \left[\frac{1}{2}z^2 - (\boldsymbol{\Delta})_z z\right]_{z=z_L}^{z_R}, \tag{A.29}$$

$$\begin{aligned} W_{AB}^{(3\overleftrightarrow{2})} =& \big(\hat{e}_\mathrm{x} \otimes \hat{e}_\mathrm{x} + \hat{e}_y \otimes \hat{e}_y\big) \\ &\times \frac{\pi}{R_B}\left[R_B^2 z + \frac{1}{3}\big((\boldsymbol{\Delta})_z - z\big)^3\right]_{z=z_L}^{z_R} \\ &+ \big(\hat{e}_z \otimes \hat{e}_z\big)\frac{2\pi}{R_B}\left[-\frac{1}{3}\big((\boldsymbol{\Delta})_z - z\big)^3\right]_{z=z_L}^{z_R} \\ &- \frac{\overleftrightarrow{\mathrm{I}}}{3} W_{AB}^{(32)}, \end{aligned} \tag{A.30}$$

where the outer product $\hat{e}_i \otimes \hat{e}_j$ between $\hat{e}_i$ and $\hat{e}_j$ is defined as the matrix product $\hat{e}_i \cdot \hat{e}_j^T$ with T indicating a transposed vector.

Case 2 - partial intersection

In this case, both spheres A and B intersect each other and the intersection occurs at z-positions with $z_L \leq z \leq z_R$. In order to calculate the weight-correlation functions $W_{AB}^{(\alpha\beta)}$ we distinguish two cases:

(2a) at least one of the corresponding weight functions incorporates a Θ weight:
$\Leftrightarrow \alpha = 3 \geq \beta$

(2b) no Θ-weight function is involved:
$\Leftrightarrow 3 > \alpha \geq \beta$

Case 2a - partial intersection, $\alpha = 3$

In this case, we employed numerical integration in order to determine $W_{AB}^{(\alpha\beta)}$ following some analytical calculations.

According to previous discussions, $\Delta_z := (\boldsymbol{\Delta})_z < |\boldsymbol{\Delta}|$ and $\Delta_{xy} := \sqrt{(\boldsymbol{\Delta})_x^2 + (\boldsymbol{\Delta})_y^2} > 0$. Thus, the vectors $\mathbf{R}_A$ and $\mathbf{R}_B$, which point from the center of the spheres S_A and S_B to their surface (at position z), can be parameterized by (see Fig. A.2)

$$\mathbf{R}_A(\varphi_A) = \mathbf{C}_A + r_A(z)\left(\mathbf{D}_{cA}\cos(\varphi_A) + \mathbf{D}_{sA}\sin(\varphi_A)\right) \tag{A.31}$$
$$\mathbf{R}_B(\varphi_B) = \mathbf{C}_B + r_B(z)\left(\mathbf{D}_{cB}\cos(\varphi_B) + \mathbf{D}_{sB}\sin(\varphi_B)\right), \tag{A.32}$$

where

$$\mathbf{C}_A = z\hat{e}_z \ , \ \mathbf{C}_B = (z - \Delta_z)\hat{e}_z, \tag{A.33}$$
$$\mathbf{D}_{cA} = \Delta_{xy}^{-1}(\Delta_x\hat{e}_x + \Delta_y\hat{e}_y) = -\mathbf{D}_{cB}, \tag{A.34}$$
$$\mathbf{D}_{sA} = \hat{e}_z \times \mathbf{D}_{cA} = -\hat{e}_z \times \mathbf{D}_{cB} = \mathbf{D}_{sB}. \tag{A.35}$$

The in-plane radii r_A and r_B are used as defined in Eqs. (A.20) and (A.21). From the law of Cosines it follows

$$r_A\cos(\varphi_A) = \frac{r_A^2 + \Delta_{xy}^2 - r_B^2}{2\Delta_{xy}} \ , \ \varphi_A \in (0,\pi) \tag{A.36}$$
$$r_B\cos(\varphi_B) = \frac{r_B^2 + \Delta_{xy}^2 - r_A^2}{2\Delta_{xy}} \ , \ \varphi_B \in (0,\pi), \tag{A.37}$$

where the correlated angles φ_A and φ_B become $\frac{\pi}{2}$ for vanishing radii r_A and r_B, respectively.

In the case of two Θ-weights, the intersection area of the kernel is given by two caps of the corresponding intersecting circles as illustrated in Fig. A.2(a). The area D of such a cap is given by the fraction $\frac{2\varphi}{2\pi}$ of the corresponding circle with a triangle subtracted

or added, depending on the opening angle of φ: if $\varphi \leq \frac{\pi}{2}$, the triangle is subtracted, otherwise added. With $h = |\sin(\varphi)|r$, the area follows with

$$D = \varphi r^2 - r^2 \cos(\varphi)\sin(\varphi). \tag{A.38}$$

Thus, the weight-correlation function for two Θ-weights follows with

$$\begin{aligned} W_{AB}^{(33)} = \int_{z_L}^{z_R} \mathrm{d}z \Big(& r_A^2(z)\big(\varphi_A - \sin(\varphi_A)\cos(\varphi_A)\big) \\ & + r_B^2(z)\big(\varphi_B - \sin(\varphi_B)\cos(\varphi_B)\big)\Big) . \end{aligned} \tag{A.39}$$

Referring to calculations from Eqs. (A.26) - (A.28) in case 1, we furthermore get

$$W_{AB}^{(32)} = \int_{z_L}^{z_R} \mathrm{d}z \int_{-\varphi_B}^{\varphi_B} \mathrm{d}\gamma \, R_B = 2\int_{z_L}^{z_R} \mathrm{d}z \, \varphi_B R_B \, . \tag{A.40}$$

Using the parameterization of $\mathbf{R}_B$ from Eq. (A.32), we obtain

$$\begin{aligned} W_{AB}^{(3\mathbf{2})} &= \int_{z_L}^{z_R} \mathrm{d}z \int_{-\varphi_B}^{\varphi_B} \mathrm{d}\varphi \, \mathbf{R}_B(\varphi) \\ &= 2\int_{z_L}^{z_R} \mathrm{d}z \, \left[\varphi_B \mathbf{C}_B + r_B(z)\mathbf{D}_{cB}\sin(\varphi_B)\right] . \end{aligned} \tag{A.41}$$

Using furthermore the equalities $\int \mathrm{d}x \, \sin^2(x) = \frac{x}{2} - \frac{1}{4}\sin(2x)$, $\int \mathrm{d}x \, \cos^2(x) = \frac{x}{2} + \frac{1}{4}\sin(2x)$, and $\int \mathrm{d}x \, \sin(x)\cos(x) = -\frac{1}{2}\cos^2(x)$, if follows

$$\left(W_{AB}^{(3\overset{\leftrightarrow}{2})}\right)_{ij} = \int_{z_L}^{z_R} \mathrm{d}z \int_{-\varphi_B}^{\varphi_B} \mathrm{d}\varphi \, \frac{R_B}{R_B^2} \left(\mathbf{R}_B(\varphi)\right)_i \left(\mathbf{R}_B(\varphi)\right)_j - \int_{z_L}^{z_R} \mathrm{d}z \int_{-\varphi_B}^{\varphi_B} \mathrm{d}\varphi \, R_B \frac{1}{3}\delta_{ij} \tag{A.42}$$

$$\begin{aligned} &= \int_{z_L}^{z_R} \mathrm{d}z \frac{2}{R_B} \Big[\varphi_B \left(\mathbf{C}_B\right)_i \left(\mathbf{C}_B\right)_j \\ &\quad + r_B(z)\sin(\varphi_B) \left(\mathbf{C}_B\right)_i \left(\mathbf{D}_{cB}\right)_j \\ &\quad + r_B(z)\sin(\varphi_B) \left(\mathbf{D}_{cB}\right)_i \left(\mathbf{C}_B\right)_j \\ &\quad + \left(r_B(z)\right)^2 \left(\frac{\varphi_B}{2} + \frac{1}{4}\sin(2\varphi_B)\right) \left(\mathbf{D}_{cB}\right)_i \left(\mathbf{D}_{cB}\right)_j \\ &\quad + \left(r_B(z)\right)^2 \left(\frac{\varphi_B}{2} - \frac{1}{4}\sin(2\varphi_B)\right) \left(\mathbf{D}_{sB}\right)_i \left(\mathbf{D}_{sB}\right)_j \Big] \\ &\quad - \frac{1}{3}\delta_{ij} W_{AB}^{(32)} \, . \end{aligned} \tag{A.43}$$

Finally, we calculated the remaining integral over the interval $I_i = [z_L, z_R]$ in Eqs. (A.39)-(A.43) numerically on a discrete grid of 16 points. Keep in mind that $z_R - z_L \leq d_z$ which is the numeric resolution of the grid of the direct correlation functions in Eq. (5.2).

Case 2b - partial intersection, $\alpha < 3$

On the interval $I_i = [z_L, z_R]$ of interest, an unique intersection circle between the surfaces ∂S_A and ∂S_B exists. Note, that the whole intersection circle might lay in one plane $\mathcal{R}^2 \times \{z_c\}$ if $\mathbf{\Delta} \parallel \hat{e}_z$. Otherwise, the distance $\mathbf{\Delta}$ must have non-vanishing contributions orthogonal to $\hat{e}_z$.

The intersection circle, as sketched in Fig. A.2(b), can be parameterized by the vector

$$\mathbf{r}_\mathrm{I}(t) = \mathbf{C} + \mathbf{D}_c r_\mathrm{I} \cos(t) + \mathbf{D}_s r_\mathrm{I} \sin(t), \tag{A.44}$$

where the radius $r_\mathrm{I} = \sqrt{R_A^2 - \Delta_A^2} = \sin(\vartheta_A) R_A$ follows from $R_B^2 = R_A^2 + \Delta^2 - 2R_A\Delta\cos(\vartheta_A)$ with $\Delta \equiv |\mathbf{\Delta}|$ and from $\Delta_A = \cos(\vartheta_A) R_A$.

For $\mathbf{\Delta} \nparallel \hat{e}_z$, the vectors in the parameterization read

$$\mathbf{C} = \Delta_A \frac{\mathbf{\Delta}}{|\mathbf{\Delta}|} = \frac{R_B^2 - R_A^2 - \Delta^2}{-2\Delta^2} \begin{pmatrix} \Delta_x \\ \Delta_y \\ \Delta_z \end{pmatrix}, \tag{A.45}$$

$$\mathbf{D}_s = \frac{\hat{e}_z \times \mathbf{\Delta}}{|\hat{e}_z \times \mathbf{\Delta}|} = \frac{1}{\Delta_{xy}} \begin{pmatrix} -\Delta_y \\ \Delta_x \\ 0 \end{pmatrix}, \tag{A.46}$$

$$\mathbf{D}_c = \frac{\mathbf{D}_s \times \mathbf{\Delta}}{|\mathbf{\Delta}|} = \frac{1}{\Delta_{xy}\Delta} \begin{pmatrix} -\Delta_x\Delta_z \\ \Delta_y\Delta_z \\ -\Delta_{xy}^2 \end{pmatrix}. \tag{A.47}$$

Moreover, $|\mathbf{D}_s \times \mathbf{\Delta}| = |\mathbf{\Delta}|$, because $\mathbf{D}_s \perp \mathbf{\Delta}$ and $|\mathbf{D}_s| = 1$. By definition it also follows $\mathbf{D}_s \perp \mathbf{D}_c$. To map the parameter t onto the given interval I_i we furthermore solve $z = (\mathbf{r}_\mathrm{I}(t))_z$ and find

$$\cos(t) = \frac{z - \frac{R_B^2 - R_A^2 - \Delta^2}{-2\Delta^2}\Delta_z}{-2\Delta_{xy}}\Delta. \tag{A.48}$$

Thus, the interval $I_i = [z_L, z_R]$ corresponds to the intervals $[t_1, t_2]$ and $[-t_2, -t_1]$, due to the symmetry properties of the Cosine.

In case $\mathbf{\Delta} \parallel \hat{e}_z$, when the whole intersection circle is located in one z-slice at $z = z_c$, we set the vectors in the parameterization to $\mathbf{C} = z_c\hat{e}_z$, $\mathbf{D}_s = \hat{e}_y$, and $\mathbf{D}_c = \hat{e}_x$. Then the whole circle is caught by the above defined intervals $[t_1, t_2]$ and $[-t_2, -t_1]$ with $t_1 = 0$ and $t_2 = \pi$.

Now, we consider the weight-correlation function

$$W_{AB}^{(22)} = \int_{z_L}^{z_R} \int\int \mathrm{d}\mathbf{r}\, \delta\big(R_A - |\mathbf{r}|\big)\delta\big(R_B - |\mathbf{r} - \mathbf{\Delta}|\big)\,. \tag{A.49}$$

Splitting the vector $\mathbf{r}$ into parallel and orthogonal components $\mathbf{r}_\parallel \parallel \mathbf{\Delta}$ and $\mathbf{r}_\perp \perp \mathbf{\Delta}$ and converting to cylindrical coordinates $(r\cos(\gamma), r\sin(\gamma), c \equiv |\mathbf{C}|)$ on the Euclidean base

$(\mathbf{D}_c, \mathbf{D}_s, \mathbf{C}/c)$, we find

$$W_{AB}^{(22)} = \int_{\mathcal{R}} \mathrm{d}c \int_{-t_2}^{-t_1} \mathrm{d}\gamma \int_0^{\infty} \mathrm{d}r\, r\delta\big(g_A(c)\big)\delta\big(g_B(r)\big) + \int_{\mathcal{R}} \mathrm{d}c \int_{t_1}^{t_2} \mathrm{d}\gamma \int_0^{\infty} \mathrm{d}r\, r\delta\big(g_A(c)\big)\delta\big(g_B(r)\big) \tag{A.50}$$

with the arguments $g_A(c) = R_A - \sqrt{r^2 + c^2}$ and $g_B(r) = R_B - \sqrt{r^2 + \big(c - |\mathbf{\Delta}|\big)^2}$, where the conditions concerning the z-integration from Eq. (A.49) have been transferred to conditions of the γ-integration.

In this tilted geometry, we first apply the identity from Eq. (A.27) to the second δ-distribution with argument $g_B(r)$ in Eq. (A.50) and achieve the simple zero $r_0 = \sqrt{R_B^2 - \big(c - |\mathbf{\Delta}|\big)^2}$ together with $|g_B'(c_0)| = r/R_B$. Second, we apply the same identity to the first δ-distribution with argument $g_A(c)$, where we already replaced the parameter r by the value which is set by the r-integration over the second δ-distribution, leading to $g_A(c) = R_A - \sqrt{c^2 + R_B^2 - \big(c - |\mathbf{\Delta}|\big)^2}$ with the simple zero $c_0 = \big(R_A^2 - R_B^2 + |\mathbf{\Delta}|^2\big)/(2|\mathbf{\Delta}|)$ and the corresponding $|g_A'(c_0))| = |\mathbf{\Delta}|/R_A$. Accordingly, we find

$$W_{AB}^{(22)} = \int_{\mathcal{R}} \mathrm{d}c \int_{-t_2}^{-t_1} \mathrm{d}\gamma \int_0^{\infty} \mathrm{d}r\, \frac{R_A R_B}{\Delta}\delta(c - c_0)\delta(r - r_\mathrm{I}) + \int_{\mathcal{R}} \mathrm{d}c \int_{t_1}^{t_2} \mathrm{d}\gamma \int_0^{\infty} \mathrm{d}r\, \frac{R_A R_B}{\Delta}\delta(c - c_0)\delta(r - r_\mathrm{I}), \tag{A.51}$$

which leads to the final result

$$W_{AB}^{(22)} = \frac{R_A R_B}{|\mathbf{\Delta}|} 2(t_2 - t_1). \tag{A.52}$$

The vectorial and tensorial weight-correlation functions are calculated in a similar manner. For this purpose, we define vectors

$$\mathbf{R}_A(t) = \mathbf{r}_\mathrm{I}(t) \text{ and } \mathbf{R}_B(t) = \mathbf{r}_\mathrm{I}(t) - \mathbf{\Delta} \tag{A.53}$$

which point from the centers of the spheres A and B to a point on the intersection line $\partial S_A \cap \partial S_B$, which is parameterized by t. In combination with Eq. (A.51) we obtain

$$\begin{aligned} W_{AB}^{(2\mathbf{2})} &= \frac{R_A R_B}{|\mathbf{\Delta}|} \int_{-t_2}^{-t_1} \mathrm{d}\gamma\, \frac{\mathbf{R}_B(\gamma)}{R_B} + \frac{R_A R_B}{|\mathbf{\Delta}|} \int_{t_1}^{t_2} \mathrm{d}\gamma\, \frac{\mathbf{R}_B(\gamma)}{R_B} \\ &= 2\frac{R_A}{|\mathbf{\Delta}|} \left[(\mathbf{C} - \mathbf{\Delta})\, t + r_0 \mathbf{D}_c \sin(t)\right]_{t=t_1}^{t_2}, \end{aligned} \tag{A.54}$$

$$\left(W_{AB}^{(2\overset{\leftrightarrow}{2})}\right)_{ij} = \frac{R_A R_B}{|\mathbf{\Delta}|}\int_{-t_2}^{-t_1} \mathrm{d}\gamma \left(\frac{(\mathbf{R}_B(\gamma))_i}{R_B}\frac{(\mathbf{R}_B(\gamma))_j}{R_B} - \frac{\delta_{ij}}{3}\right) + \frac{R_A R_B}{|\mathbf{\Delta}|}\int_{t_1}^{t_2} \mathrm{d}\gamma \left(\frac{(\mathbf{R}_B(\gamma))_i}{R_B}\frac{(\mathbf{R}_B(\gamma))_j}{R_B} - \frac{\delta_{ij}}{3}\right), \tag{A.55}$$

$$\left(W_{AB}^{(\mathbf{22})}\right)_{ij} = \frac{R_A R_B}{|\mathbf{\Delta}|}\int_{-t_2}^{-t_1} \mathrm{d}\gamma \frac{(\mathbf{R}_A(\gamma))_i}{R_A}\frac{(\mathbf{R}_B(\gamma))_j}{R_B} + \frac{R_A R_B}{|\mathbf{\Delta}|}\int_{t_1}^{t_2} \mathrm{d}\gamma \frac{(\mathbf{R}_A(\gamma))_i}{R_A}\frac{(\mathbf{R}_B(\gamma))_j}{R_B}, \tag{A.56}$$

$$\left(W_{AB}^{(\mathbf{2}\overset{\leftrightarrow}{2})}\right)_{ijk} = \frac{R_A R_B}{|\mathbf{\Delta}|}\int_{-t_2}^{-t_1} \mathrm{d}\gamma \frac{(\mathbf{R}_A(\gamma))_i}{R_A}\left(\frac{(\mathbf{R}_B(\gamma))_j}{R_B}\frac{(\mathbf{R}_B(\gamma))_k}{R_B} - \frac{\delta_{jk}}{3}\right) + \frac{R_A R_B}{|\mathbf{\Delta}|}\int_{t_1}^{t_2} \mathrm{d}\gamma \frac{(\mathbf{R}_A(\gamma))_i}{R_A}\left(\frac{(\mathbf{R}_B(\gamma))_j}{R_B}\frac{(\mathbf{R}_B(\gamma))_k}{R_B} - \frac{\delta_{jk}}{3}\right), \tag{A.57}$$

$$\left(W_{AB}^{(\overset{\leftrightarrow}{2}\overset{\leftrightarrow}{2})}\right)_{ijkl} = \frac{R_A R_B}{|\mathbf{\Delta}|}\int_{-t_2}^{-t_1} \mathrm{d}\gamma \left(\frac{\left(\overset{\leftrightarrow}{R}_A(\gamma)\right)_{ij}}{R_A^2} - \frac{\delta_{ij}}{3}\right)\left(\frac{\left(\overset{\leftrightarrow}{R}_B(\gamma)\right)_{kl}}{R_B^2} - \frac{\delta_{kl}}{3}\right) + \frac{R_A R_B}{|\mathbf{\Delta}|}\int_{t_1}^{t_2} \mathrm{d}\gamma \left(\frac{\left(\overset{\leftrightarrow}{R}_A(\gamma)\right)_{ij}}{R_A^2} - \frac{\delta_{ij}}{3}\right)\left(\frac{\left(\overset{\leftrightarrow}{R}_B(\gamma)\right)_{kl}}{R_B^2} - \frac{\delta_{kl}}{3}\right), \tag{A.58}$$

where $\overset{\leftrightarrow}{R}_A(\gamma) = \mathbf{R}_A(\gamma)\otimes\mathbf{R}_A(\gamma)$ with the tensor product $\otimes$, $\left(\overset{\leftrightarrow}{R}_A(\gamma)\right)_{ij} = (\mathbf{R}_A(\gamma))_i (\mathbf{R}_A(\gamma))_j$, and $\left(\overset{\leftrightarrow}{R}_B(\gamma)\right)_{ij} = (\mathbf{R}_B(\gamma))_i (\mathbf{R}_B(\gamma))_j$. The analytical form of Eqs. (A.55)-(A.58) follows from straight forward integration.

Case 3 - two equal spheres

In the last case, sphere B is equal to sphere A. This case of equal spheres corresponds to a limiting case of the first two cases such that we do not need additional calculations. For example, case 1 already covers all situations where $\alpha = 3$. These situations are addressed, when in the discussion in Sec. 5.4.2 the correlations between a small and a large particle are called similar to the self correlations of the small particles. In this discussion all cases with $\alpha \leq 2$ were neglected. In cases with $\alpha = 2$, we find

$$W_{AB}^{(22)} = \int_{z_L}^{z_R}\int\int \mathrm{d}\mathbf{r}\, \delta\left(R_A - \sqrt{r^2+z^2}|\right)\delta(R_B - R_A)\,. \tag{A.59}$$

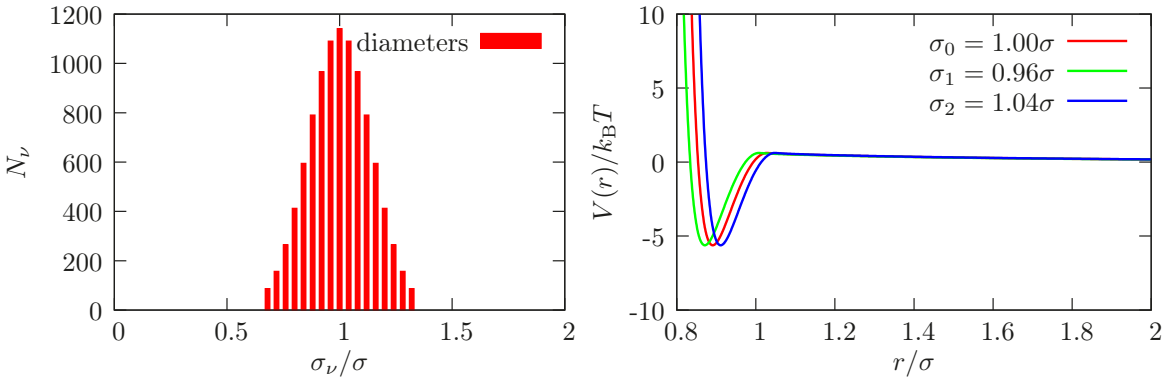

Figure A.3: (*Left*) Numbers N_ν of particles with diameters σ_ν. The total number of particles adds up to 9856 in order to fulfill the constraint of a normal distribution with approximate integer numbers. (*Right*) Typical potential shapes for particles with different model diameters σ_ν.

This result corresponds to Eq. (A.25) in case 1, where $\alpha = 3$ and $\beta = 2$, because the Θ-weight of sphere A completely contains the weight function of sphere B and as a consequence is irrelevant. Note, that here the naming of the spheres A and B was switched.

All remaining situations with $\alpha < 2$ can be reduced to already discussed cases with $\alpha = 2$, because all weights with $\alpha < 3$ are δ-weights and only differ in a prefactor. This applies even for the vectorial and tensorial weights

A.5 Polydispersity in gel simulations

In order to display the experimens better, which have been presented in Chap. 7, polydispersity was added to the simulation routine, as illustrated in Fig. A.3. As the two plots indicate, it was realized by splitting the total number of particles into species with different model diameters (Fig. A.3, left) and consecutively shifting the final curves of the potential or interaction forces by $\delta r = 0.04\sigma$ steps (Fig. A.3, right), such that 17 distinct diameters are obtained. These diameters have been chosen to be normal distributed with a polydispersity, i.e., the standard deviation, of $\approx 7\%$. Furthermore, a simple shift of the potentials conserves the depths and heights of the potential minima and maxima. Note, that the position of the total potential minimum (denoted by σ_eff in the main text) is not identical to the model parameter σ. It is rather smaller than the designated diameter and only coincides with it in the limit of infinite inverse screening lengths $\sigma\kappa$ or infinitely steep hard-core repulsions (cf. Eq. (7.4)).

A.6 Fitting experimental gels to the simulation

Calibration of C_0. The experiments have been carried out with charged particles. The charge of the particles is contained in the interaction parameter C_0 in the electrostatic part of the interaction potential (Eq. 7.5). Using simulations, C_0 is fitted. The fit is based on the pair correlation function $g(r)$ of a sample without added salt (C1, Tab. 7.1) and thus interactions that are dominated by the electrostatic interaction. In the fit, only the parameter C_0 is varied and, as suggested by the low salt concentration, $\kappa\sigma = 0.25$ is fixed. Best agreement with the data was obtained for $C_0 = 200\, k_\mathrm{B}T$. Consequently, this value was used for all samples. With C_0 fixed the attraction strength D_0 (Eq. 7.4) was successively increased, until a peak in $g(r)$ appeared at particle-particle contact.

Fitting via $\langle N_\mathrm{b}\rangle$. In order to map the experimental samples onto the $V_{\mathrm{D,min}}$– $\kappa\sigma$ plane, the positions of all samples have been fitted simultaneously based on their average number of bonds and taking into account the following two constraints: First, their relative distances along the $\kappa\sigma$ axis is given by their relative rather than their absolute screening lengths according to Tab. 7.1. Second, the attraction strengths D_0 corresponding to the three polymer concentrations $c_\mathrm{p}^\mathrm{free} = [c_\mathrm{p}^*, 2c_\mathrm{p}^*, 3c_\mathrm{p}^*]$ are assumed to differ by at least $4\, k_\mathrm{B}T$. Thus, only affine transformations of the sample positions in the $V_{\mathrm{D,min}}$– $\kappa\sigma$ plane are considered in a simultaneous fit of all sample positions. The abolute positions were determined by minimizing the difference between $\langle N_\mathrm{b}\rangle_\mathrm{sim}$ and $\langle N_\mathrm{b}\rangle_\mathrm{exp}$ as determined in simulations and experiments, respectively, i.e. the minimum $\mathrm{Min}\{\sum_{\mathrm{B}_i,\mathrm{C}_i,\mathrm{D}_i} |\langle N_{\mathrm{b},j}\rangle_\mathrm{sim} - \langle N_{\mathrm{b},j}\rangle_\mathrm{exp}|\}$, where the individual $\langle N_{\mathrm{b},j}\rangle_\mathrm{sim}$ are constrained by allowed affine transformation, as explained above. This fit determines the relative positions of all samples, such that the overall agreement between the average bond numbers from experiments and simulations is good. Note, that this fitting is enough for our purposes but that the absolute positions of the experimental samples are not necessarily determined exactly.

Unconstrained fit In order to determine the individual sample positions within the $V_{\mathrm{D,min}}$– $\kappa\sigma$ plane better, we additionally performed a free fit where the parameters are not constrained to any path. The results are represented by the light blue solid lines in Figs. 7.3 and 7.5. This fit relies on the minimization of the absolute error (vector) $\Delta g(r) = |g_\mathrm{sim}(r) - g_\mathrm{exp}(r)|$ between the pair correlations in simulations and experiments, respectively, over the interval $[\sigma, 3\sigma]$. Thus, the local pair correlations between experimental and simulation agree better, but the freely fitted positions cannot be mapped onto the affine grid of paths anymore.

Eidesstattliche Versicherung

Ich versichere an Eides Statt, dass die Dissertation von mir selbständig und ohne unzulässige fremde Hilfe unter Beachtung der „Grundsätze zur Sicherung guter wissenschaftlicher Praxis an der Heinrich-Heine-Universität Düsseldorf“ erstellt worden ist.

(Matthias Kohl)

Bibliography

[1] M. Kohl and M. Schmiedeberg, "Particle segregation in a sedimenting bidisperse soft sphere system," *Soft matter*, vol. 10, no. 24, pp. 4340–4347, 2014.

[2] A. Härtel, M. Kohl, and M. Schmiedeberg, "Anisotropic pair correlations in binary and multi-component hard-sphere mixtures in the vicinity of a hard wall: a combined density functional theory and simulation study," *submitted to: Phys. Rev. E*, 2015.

[3] M. Kohl, R. Capellmann, M. Laurati, S. U. Egelhaaf, and M. Schmiedeberg, "Directed percolation identified as equilibrium pre-transition towards non-equilibrium arrested gel states," *submitted to: Nature Communications*, 2015.

[4] M. Kohl, A. Härtel, and M. Schmiedeberg, "Anisotropy and memory during the single particle escape from a cage in the vicinity of a wall," *in preparation*, 2015.

[5] M. Kohl and M. Schmiedeberg, "Shear-induced slab-like domains in a directed percolated colloidal gel," *in preparation*, 2015.

[6] B. Berne and R. Pecora, *Dynamic light scattering: with applications to chemistry, biology, and physics*. Dover Publications, 2000.

[7] A. D. Dinsmore, E. R. Weeks, V. Prasad, A. C. Levitt, and D. A. Weitz, "Three-Dimensional Confocal Microscopy of Colloids," *Appl. Opt.*, vol. 40, no. 24, pp. 4152–4159, 2001.

[8] V. Prasad, D. Semwogerere, and E. R. Weeks, "Confocal microscopy of colloids," *Journal of Physics: Condensed Matter*, vol. 19, no. 11, p. 113102, 2007.

[9] H. Löwen, "Colloidal soft matter under external control," *Journal of Physics: Condensed Matter*, vol. 13, no. 24, p. R415, 2001.

[10] D. A. Huerta, V. Sosa, M. C. Vargas, and J. C. Ruiz-Suárez, "Archimedes' principle in fluidized granular systems," *Phys. Rev. E*, vol. 72, p. 031307, 2005.

[11] A. P. J. Breu, H.-M. Ensner, C. A. Kruelle, and I. Rehberg, "Reversing the Brazil-Nut Effect: Competition between Percolation and Condensation," *Phys. Rev. Lett.*, vol. 90, p. 014302, 2003.

[12] A. Rosato, K. J. Strandburg, F. Prinz, and R. H. Swendsen, "Why the Brazil nuts are on top: Size segregation of particulate matter by shaking," *Phys. Rev. Lett.*, vol. 58, pp. 1038–1040, 1987.

[13] D. C. Hong, P. V. Quinn, and S. Luding, "Reverse Brazil Nut Problem: Competition between Percolation and Condensation," *Phys. Rev. Lett.*, vol. 86, pp. 3423–3426, 2001.

[14] J. A. Both and D. C. Hong, "Variational Approach to Hard Sphere Segregation under Gravity," *Phys. Rev. Lett.*, vol. 88, p. 124301, 2002.

[15] P. M. Reis, T. Sykes, and T. Mullin, "Phases of granular segregation in a binary mixture," *Phys. Rev. E*, vol. 74, p. 051306, 2006.

[16] A. Saez, F. Vivanco, and F. Melo, "Size segregation, convection, and arching effect," *Phys. Rev. E*, vol. 72, p. 021307, 2005.

[17] N. J. Lorenz, H. J. Schöpe, and T. Palberg, "Phase behavior of a de-ionized binary mixture of charged spheres in the presence of gravity," *The Journal of Chemical Physics*, vol. 131, no. 13, 2009.

[18] M. Schmidt, C. P. Royall, A. van Blaaderen, and J. Dzubiella, "Non-equilibrium sedimentation of colloids: confocal microscopy and Brownian dynamics simulations," *Journal of Physics: Condensed Matter*, vol. 20, no. 49, p. 494222, 2008.

[19] C. G. Serrano, J. J. McDermott, and D. Velegol, "Sediments of soft spheres arranged by effectivedensity," *Nat Mater*, vol. 10, pp. 716–721, Sept. 2011.

[20] P. M. Biesheuvel and J. Lyklema, "Sedimentation-diffusion equilibrium of binary mixtures of charged colloids including volume effects," *Journal of Physics: Condensed Matter*, vol. 17, no. 41, p. 6337, 2005.

[21] A. Cuetos, A.-P. Hynninen, J. Zwanikken, R. van Roij, and M. Dijkstra, "Layering in sedimentation of suspensions of charged colloids: Simulation and theory," *Phys. Rev. E*, vol. 73, p. 061402, 2006.

[22] A. Torres, A. Cuetos, M. Dijkstra, and R. v. Roij, "Sedimentation of charged colloids: The primitive model and the effective one-component approach," *Phys. Rev. E*, vol. 75, p. 041405, 2007.

[23] R. van Roij, "Defying gravity with entropy and electrostatics: sedimentation of charged colloids," *Journal of Physics: Condensed Matter*, vol. 15, no. 48, p. S3569, 2003.

[24] J. Zwanikken and R. van Roij, "The sediment of mixtures of charged colloids:

Segregation and inhomogeneous electric fields," *EPL (Europhysics Letters)*, vol. 71, no. 3, p. 480, 2005.

[25] J.-P. Simonin, "Calculation of Equilibrium Sedimentation Profiles of Screened Charged Collloids," *The Journal of Physical Chemistry*, vol. 99, no. 5, pp. 1577–1581, 1995.

[26] A. Esztermann and H. Löwen, "Colloidal Brazil-nut effect in sediments of binary charged suspensions," *EPL (Europhysics Letters)*, vol. 68, no. 1, p. 120, 2004.

[27] T. Kruppa, T. Neuhaus, R. Messina, and H. Löwen, "Soft repulsive mixtures under gravity: Brazil-nut effect, depletion bubbles, boundary layering, nonequilibrium shaking," *The Journal of Chemical Physics*, vol. 136, no. 13, 2012.

[28] T. Biben and J.-P. Hansen, "Localized density profiles in binary colloidal suspensions," *Molecular Physics*, vol. 80, no. 4, pp. 853–859, 1993.

[29] T. Biben and J.-P. Hansen, "Sedimentation equilibrium in concentrated charge-stabilized colloidal suspensions," *Journal of Physics: Condensed Matter*, vol. 6, no. 23A, p. A345, 1994.

[30] M. Schmidt, M. Dijkstra, and J.-P. Hansen, "Floating Liquid Phase in Sedimenting Colloid-Polymer Mixtures," *Phys. Rev. Lett.*, vol. 93, p. 088303, 2004.

[31] L. Bellier-Castella and H. Xu, "Sedimentation profiles of polydisperse fluids," *Journal of Physics: Condensed Matter*, vol. 15, no. 32, p. 5417, 2003.

[32] C. S. O'Hern, L. E. Silbert, A. J. Liu, and S. R. Nagel, "Jamming at zero temperature and zero applied stress: The epitome of disorder," *Phys. Rev. E*, vol. 68, p. 011306, 2003.

[33] C. A. Angell, "Formation of Glasses from Liquids and Biopolymers," *Science*, vol. 267, no. 5206, pp. 1924–1935, 1995.

[34] A. J. Liu and S. R. Nagel, "Nonlinear dynamics: Jamming is not just cool any more," *Nature*, vol. 396, no. 6706, pp. 21–22, 1998.

[35] P. G. Debenedetti and F. H. Stillinger, "Supercooled liquids and the glass transition," *Nature*, vol. 410, no. 6825, pp. 259–267, 2001.

[36] G. B. McKenna, "Glass dynamics: Diverging views on glass transition," *Nat Phys*, vol. 4, no. 9, pp. 673–673, 2008.

[37] G. L. Hunter and E. R. Weeks, "The physics of the colloidal glass transition," *Reports on Progress in Physics*, vol. 75, no. 6, p. 066501, 2012.

[38] C. P. Royall, A. Malins, A. J. Dunleavy, and R. Pinney, "Strong geometric frustration in model glassformers ," *Journal of Non-Crystalline Solids*, vol. 407, no. 0, pp. 34 – 43, 2015.

[39] D. M. Sussman and K. S. Schweizer, "Theory of correlated two-particle activated glassy dynamics: General formulation and heterogeneous structural relaxation in hard sphere fluids," *The Journal of Chemical Physics*, vol. 134, no. 6, p. 064516, 2011.

[40] E. R. Weeks and D. A. Weitz, "Properties of Cage Rearrangements Observed near the Colloidal Glass Transition," *Phys. Rev. Lett.*, vol. 89, p. 095704, 2002.

[41] B. Doliwa and A. Heuer, "Cage Effect, Local Anisotropies, and Dynamic Heterogeneities at the Glass Transition: A Computer Study of Hard Spheres," *Phys. Rev. Lett.*, vol. 80, pp. 4915–4918, 1998.

[42] R. L. Jack, A. J. Dunleavy, and C. P. Royall, "Information-Theoretic Measurements of Coupling between Structure and Dynamics in Glass Formers," *Phys. Rev. Lett.*, vol. 113, p. 095703, 2014.

[43] C. P. Royall and S. R. Williams, "The role of local structure in dynamical arrest," *Physics Reports*, vol. 560, no. 0, pp. 1 – 75, 2015.

[44] P. Scheidler, W. Kob, and K. Binder, "Cooperative motion and growing length scales in supercooled confined liquids," *EPL (Europhysics Letters)*, vol. 59, no. 5, p. 701, 2002.

[45] J. Mittal, T. M. Truskett, J. R. Errington, and G. Hummer, "Layering and Position-Dependent Diffusive Dynamics of Confined Fluids," *Phys. Rev. Lett.*, vol. 100, p. 145901, 2008.

[46] M. Buzzacchi, I. Pagonabarraga, and N. B. Wilding, "Polydisperse hard spheres at a hard wall," *The Journal of Chemical Physics*, vol. 121, no. 22, pp. 11362–11373, 2004.

[47] B. Götzelmann, A. Haase, and S. Dietrich, "Structure factor of hard spheres near a wall," *53*, vol. 53, pp. 3456–3467, 1996.

[48] D. H. V. Winkle and C. A. Murray, "Layering in colloidal fluids near a smooth repulsive wall," *The Journal of Chemical Physics*, vol. 89, no. 6, pp. 3885–3891, 1988.

[49] R. Kjellander, "Inhomogeneous Coulomb fluids with image interactions between planar surfaces. II. On the anisotropic hypernetted chain approximation," *The Journal of Chemical Physics*, vol. 88, no. 11, pp. 7129–7137, 1988.

[50] K. Nygård, R. Kjellander, S. Sarman, S. Chodankar, E. Perret, J. Buitenhuis, and J. F. van der Veen, "Anisotropic Pair Correlations and Structure Factors of Confined Hard-Sphere Fluids: An Experimental and Theoretical Study," *Phys. Rev. Lett.*, vol. 108, p. 037802, 2012.

[51] K. Nygård, S. Sarman, and R. Kjellander, "Packing frustration in dense confined fluids," *The Journal of Chemical Physics*, vol. 141, no. 9, 2014.

[52] R. Kjellander and S. Sarman, "A study of anisotropic pair distribution theories for Lennard-Jones fluids in narrow slits. Part II. Pair correlations and solvation forces," *Molecular Physics*, vol. 74, no. 3, pp. 665–688, 1991.

[53] P. Gonzalez-Mozuelos, J. Alejandre, and M. Medina-Noyola, "Structure of a colloidal suspension confined in a planar slit," *The Journal of Chemical Physics*, vol. 95, no. 11, pp. 8337–8345, 1991.

[54] J. Carmer, A. Jain, J. A. Bollinger, F. van Swol, and T. M. Truskett, "Tuning structure and mobility of solvation shells surrounding tracer additives," *The Journal of Chemical Physics*, vol. 142, no. 12, 2015.

[55] G. Goel, W. P. Krekelberg, M. J. Pond, J. Mittal, V. K. Shen, J. R. Errington, and T. M. Truskett, "Available states and available space: static properties that predict self-diffusivity of confined fluids," *Journal of Statistical Mechanics: Theory and Experiment*, vol. 2009, no. 04, p. P04006, 2009.

[56] C. J. Dibble, M. Kogan, and M. J. Solomon, "Structure and dynamics of colloidal depletion gels: Coincidence of transitions and heterogeneity," *Phys. Rev. E*, vol. 74, p. 041403, Oct 2006.

[57] P. C. Royall, S. R. Williams, T. Ohtsuka, and H. Tanaka, "Direct observation of a local structural mechanism for dynamic arrest," *Nat Mater*, vol. 7, no. 7, pp. 556–561, 2008.

[58] A. de Candia, E. del Gado, A. Fierro, N. Sator, and A. Coniglio, "Colloidal gelation, percolation and structural arrest," *Physica A: Statistical Mechanics and its Applications*, vol. 358, no. 2-4, pp. 239–248, 2005.

[59] V. Trappe and P. Sandkühler, "Colloidal gels – low-density disordered solid-like states," *Current Opinion in Colloid & Interface Science*, vol. 8, no. 6, pp. 494 – 500, 2004.

[60] E. Zaccarelli, "Colloidal gels: equilibrium and non-equilibrium routes," *Journal of Physics: Condensed Matter*, vol. 19, no. 32, p. 323101, 2007.

[61] C. J. Dibble, M. Kogan, and M. J. Solomon, "Structural origins of dynamical heterogeneity in colloidal gels," *Phys. Rev. E*, vol. 77, p. 050401, 2008.

[62] K. N. Pham, A. M. Puertas, J. Bergenholtz, S. U. Egelhaaf, A. Moussaid, P. N. Pusey, A. B. Schofield, M. E. Cates, M. Fuchs, and W. C. K. Poon, "Multiple glassy states in a simple model system," *Science*, vol. 296, pp. 104–106, 2002.

[63] T. Eckert and E. Bartsch, "Re-entrant Glass Transition in a Colloid-Polymer Mixture with Depletion Attractions," *Phys. Rev. Lett.*, vol. 89, p. 125701, 2002.

[64] P. J. Lu, E. Zaccarelli, F. Ciulla, A. B. Schofield, F. Sciortino, and D. A. Weitz, "Gelation of particles with short-range attraction," *Nature*, vol. 453, no. 7194, pp. 499–503, 2008.

[65] S. Asakura and F. Oosawa, "On Interaction between Two Bodies Immersed in a Solution of Macromolecules," *The Journal of Chemical Physics*, vol. 22, no. 7, pp. 1255–1256, 1954.

[66] S. Asakura and F. Oosawa, "Interaction between particles suspended in solutions of macromolecules," *Journal of Polymer Science*, vol. 33, no. 126, pp. 183–192, 1958.

[67] L. Santen and W. Krauth, "Absence of thermodynamic phase transition in a model glass former," *Nature*, vol. 405, no. 6786, pp. 550–551, 2000.

[68] M. Y. Lin, H. M. Lindsay, D. A. Weitz, R. C. Ball, R. Klein, and P. Meakin, "Universality in colloid aggregation," *Nature*, vol. 339, no. 6223, pp. 360–362, 1989.

[69] H. Tanaka, J. Meunier, and D. Bonn, "Nonergodic states of charged colloidal suspensions: Repulsive and attractive glasses and gels," *Phys. Rev. E*, vol. 69, p. 031404, 2004.

[70] H. Sedgwick, S. U. Egelhaaf, and W. C. K. Poon, "Clusters and gels in systems of sticky particles," *Journal of Physics: Condensed Matter*, vol. 16, no. 42, p. S4913, 2004.

[71] N. Khalil, A. de Candia, A. Fierro, M. P. Ciamarra, and A. Coniglio, "Dynamical arrest: interplay of glass and gel transitions," *Soft Matter*, vol. 10, pp. 4800–4805, 2014.

[72] P. N. Segré, V. Prasad, A. B. Schofield, and D. A. Weitz, "Glasslike Kinetic Arrest at the Colloidal-Gelation Transition," *Phys. Rev. Lett.*, vol. 86, pp. 6042–6045, 2001.

[73] H. Sedgwick, K. Kroy, A. Salonen, M. B. Robertson, S. U. Egelhaaf, and W. C. K. Poon, "Non-equilibrium behavior of sticky colloidal particles: beads, clusters and gels," *Eur. Phys. J. E*, vol. 16, pp. 77–80, 2005.

[74] N. Koumakis, E. Moghimi, R. Besseling, W. C. K. Poon, J. F. Brady, and G. Petekidis, "Tuning colloidal gels by shear," *Soft matter*, vol. 11, no. 23, pp. 4640–4648, 2015.

[75] N. E. Valadez-Pérez, Y. Liu, A. P. R. Eberle, N. J. Wagner, and R. Castañeda Priego, "Dynamical arrest in adhesive hard-sphere dispersions driven by rigidity percolation," *Phys. Rev. E*, vol. 88, pp. 1–5, 2013.

[76] H. Hansen-Goos and R. Roth, "Density functional theory for hard-sphere mixtures: the White Bear version mark II," *Journal of Physics: Condensed Matter*, vol. 18, no. 37, p. 8413, 2006.

[77] R. Clausius, *On the Motive Power of Heat, and on the Laws which Can be Deduced from it for the Theory of Heat.* Annalen der Physik: Band 79, Dover, 1960.

[78] W. Thomson, "On the Dynamical Theory of Heat. Part V. Thermo-electric Currents," *Earth and Environmental Science: Transactions of the Royal Society of Edinburgh*, vol. 21, pp. 123–171, 1857.

[79] W. Nolting, *Grundkurs Theoretische Physik 6: Statistische Physik*. Grundkurs Theoretische Physik, Springer Berlin Heidelberg, 2007.

[80] E. Leutheusser, "Dynamical model of the liquid-glass transition," *Phys. Rev. A*, vol. 29, pp. 2765–2773, 1984.

[81] B. Lubachevsky, F. Stillinger, and E. Pinson, "Disks vs. spheres: Contrasting properties of random packings," *Journal of Statistical Physics*, vol. 64, no. 3-4, pp. 501–524, 1991.

[82] C. A. Angell, "Perspective on the glass transition," *Journal of Physics and Chemistry of Solids*, vol. 49, no. 8, pp. 863–871, 1988.

[83] C. A. Angell, "The old problems of glass and the glass transition, and the many new twists," *Proceedings of the National Academy of Sciences*, vol. 92, no. 15, pp. 6675–6682, 1995.

[84] H. Pelzer and E. P. Wigner, "Über die Geschwindigkeitskonstante von Austauschreaktionen," *Z Phys. Chem. B*, vol. 15, pp. 445–471, 1932.

[85] H. Eyring, "The Activated Complex in Chemical Reactions," *The Journal of Chemical Physics*, vol. 3, no. 2, pp. 107–115, 1935.

[86] H. Kramers, "Brownian motion in a field of force and the diffusion model of chemical reactions," *Physica*, vol. 7, no. 4, pp. 284 – 304, 1940.

[87] P. Hänggi, P. Talkner, and M. Borkovec, "Reaction-rate theory: fifty years after Kramers," *Rev. Mod. Phys.*, vol. 62, pp. 251–341, 1990.

[88] J. M. Lynch, G. C. Cianci, and E. R. Weeks, "Dynamics and structure of an aging binary colloidal glass," *Phys. Rev. E*, vol. 78, p. 031410, 2008.

[89] L. Cipelletti and L. Ramos, "Slow dynamics in glassy soft matter," *Journal of Physics: Condensed Matter*, vol. 17, no. 6, p. R253, 2005.

[90] A. V. Granato, "A derivation of the Vogel-Fulcher-Tammann relation for supercooled liquids," *Journal of Non-Crystalline Solids*, vol. 357, no. 2, pp. 334–338, 2011.

[91] N. Xu, T. K. Haxton, A. J. Liu, and S. R. Nagel, "Equivalence of Glass Transition and Colloidal Glass Transition in the Hard-Sphere Limit," *Phys. Rev. Lett.*, vol. 103, p. 245701, 2009.

[92] Y. S. Elmatad, D. Chandler, and J. P. Garrahan, "Corresponding States of Structural Glass Formers," *The Journal of Physical Chemistry B*, vol. 113, no. 16, pp. 5563–5567, 2009.

[93] V. Trappe, V. Prasad, L. Cipelletti, P. N. Segre, and D. A. Weitz, "Jamming phase diagram for attractive particles," *Nature*, vol. 411, no. 6839, pp. 772–775, 2001.

[94] G. Biroli, "Jamming: A new kind of phase transition?," *Nat Phys*, vol. 3, no. 4, pp. 222–223, 2007.

[95] L. Berthier, H. Jacquin, and F. Zamponi, "Can the jamming transition be described using equilibrium statistical mechanics?," *Journal of Statistical Mechanics: Theory and Experiment*, vol. 2011, no. 01, p. P01004, 2011.

[96] A. Ikeda, L. Berthier, and P. Sollich, "Unified study of glass and jamming rheology in soft particle systems," *Phys. Rev. Lett.*, vol. 109, p. 018301, 2012.

[97] L. Van Hove, "Correlations in Space and Time and Born Approximation Scattering in Systems of Interacting Particles," *Phys. Rev.*, vol. 95, pp. 249–262, 1954.

[98] J.-P. Hansen and I. R. McDonald, *Theory of Simple Liquids*. Academic Press, 3 ed., 2006.

[99] P. Attard, *Thermodynamics and Statistical Mechanics: Equilibrium by Entropy Maximisation*. Academic Press, 2002.

[100] W. Feller, *An Introduction to Probability Theory and Its Applications*. Wiley, 3 ed., 1968.

[101] D. Trzesniak, A.-P. E. Kunz, and W. F. van Gunsteren, "A Comparison of Methods to Compute the Potential of Mean Force," *ChemPhysChem*, vol. 8, no. 1, pp. 162–169, 2007.

[102] R. Evans, "The nature of the liquid-vapour interface and other topics in the statistical mechanics of non-uniform, classical fluids," *Advances in Physics*, vol. 28, no. 2, pp. 143–200, 1979.

[103] R. G. Parr, *Density-Functional Theory of Atoms and Molecules*. International Series of Monographs on Chemistry, Oxford University Press, USA, 1989.

[104] N. D. Mermin, "Thermal Properties of the Inhomogeneous Electron Gas," *Phys. Rev.*, vol. 137, pp. A1441–A1443, 1965.

[105] T. V. Ramakrishnan and M. Yussouff, "First-principles order-parameter theory of freezing," *Phys. Rev. B*, vol. 19, pp. 2775–2794, 1979.

[106] P. Tarazona, J. Cuesta, and Y. Martínez-Ratón, "Density Functional Theories of Hard Particle Systems," in *Theory and Simulation of Hard-Sphere Fluids and Related Systems* (A. Mulero, ed.), vol. 753 of *Lecture Notes in Physics*, pp. 247–341, Springer Berlin Heidelberg, 2008.

[107] V. Berinde, *Iterative approximation of fixed points*. Lecture Notes in Mathematics, Springer, 2007.

[108] V. I. Istratescu, *Fixed Point Theory an Introduction*. Mathematics and Its Applications, Springer, 2002.

[109] Y. Rosenfeld, "Free-energy model for the inhomogeneous hard-sphere fluid mixture and density-functional theory of freezing," *Phys. Rev. Lett.*, vol. 63, pp. 980–983, 1989.

[110] R. Roth, "Fundamental measure theory for hard-sphere mixtures: a review," *Journal of Physics: Condensed Matter*, vol. 22, no. 6, p. 063102, 2010.

[111] N. F. Carnahan and K. E. Starling, "Equation of State for Nonattracting Rigid Spheres," *The Journal of Chemical Physics*, vol. 51, no. 2, pp. 635–636, 1969.

[112] T. Boublík, "Hard-Sphere Equation of State," *The Journal of Chemical Physics*, vol. 53, no. 1, pp. 471–472, 1970.

[113] G. A. Mansoori, N. F. Carnahan, K. E. Starling, and J. T. W. Leland, "Equilibrium Thermodynamic Properties of the Mixture of Hard Spheres," *The Journal of Chemical Physics*, vol. 54, no. 4, pp. 1523–1525, 1971.

[114] A. Malijevsky and J. Veverka, "New equations of state for pure and binary hard-sphere fluids," *Phys. Chem. Chem. Phys.*, vol. 1, no. 18, pp. 4267–4270, 1999.

[115] J. E. Mayer and E. Montroll, "Molecular Distribution," *The Journal of Chemical Physics*, vol. 9, no. 1, pp. 2–16, 1941.

[116] J. E. Mayer and M. G. Mayer, *Statistical Mechanics*. Wiley, 1966.

[117] E. J. J. van Rensburg, "Virial coefficients for hard discs and hard spheres," *Journal of Physics A: Mathematical and General*, vol. 26, no. 19, p. 4805, 1993.

[118] Y. Rosenfeld, M. Schmidt, H. Löwen, and P. Tarazona, "Fundamental-measure free-energy density functional for hard spheres: Dimensional crossover and freezing," *Phys. Rev. E*, vol. 55, pp. 4245–4263, 1997.

[119] E. Kierlik and M. L. Rosinberg, "Free-energy density functional for the inhomogeneous hard-sphere fluid: Application to interfacial adsorption," *Phys. Rev. A*, vol. 42, pp. 3382–3387, 1990.

[120] J. K. Percus and G. J. Yevick, "Analysis of Classical Statistical Mechanics by Means of Collective Coordinates," *Phys. Rev.*, vol. 110, pp. 1–13, 1958.

[121] E. Thiele, "Equation of State for Hard Spheres," *The Journal of Chemical Physics*, vol. 39, no. 2, pp. 474–479, 1963.

[122] M. S. Wertheim, "Exact Solution of the Percus-Yevick Integral Equation for Hard Spheres," *Phys. Rev. Lett.*, vol. 10, pp. 321–323, 1963.

[123] P. Tarazona and Y. Rosenfeld, "From zero-dimension cavities to free-energy functionals for hard disks and hard spheres," *Phys. Rev. E*, vol. 55, pp. R4873–R4876, 1997.

[124] H. Hansen-Goos and K. Mecke, "Fundamental Measure Theory for Inhomogeneous Fluids of Nonspherical Hard Particles," *Phys. Rev. Lett.*, vol. 102, p. 018302, 2009.

[125] R. Roth, R. Evans, A. Lang, and G. Kahl, "Fundamental measure theory for hard-sphere mixtures revisited: the White Bear version," *Journal of Physics: Condensed Matter*, vol. 14, no. 46, p. 12063, 2002.

[126] M. Schmidt, H. Löwen, J. M. Brader, and R. Evans, "Density Functional for a Model Colloid-Polymer Mixture," *Phys. Rev. Lett.*, vol. 85, pp. 1934–1937, 2000.

[127] M. Oettel, S. Görig, A. Härtel, H. Löwen, M. Radu, and T. Schilling, "Free energies, vacancy concentrations, and density distribution anisotropies in hard-sphere crystals: A combined density functional and simulation study," *Physical Review E*, vol. 82, no. 5, p. 051404, 2010.

[128] A. Härtel, M. Oettel, R. E. Rozas, S. U. Egelhaaf, J. Horbach, and H. Löwen, "Tension and Stiffness of the Hard Sphere Crystal-Fluid Interface," *Phys. Rev. Lett.*, vol. 108, p. 226101, 2012.

[129] M. Oettel, S. Dorosz, M. Berghoff, B. Nestler, and T. Schilling, "Description of hard-sphere crystals and crystal-fluid interfaces: A comparison between density functional approaches and a phase-field crystal model," *Phys. Rev. E*, vol. 86, p. 021404, Aug 2012.

[130] F. Lado, "Static structure of polydisperse colloidal monolayers," *The Journal of Chemical Physics*, vol. 108, no. 15, pp. 6441–6446, 1998.

[131] H. H. H. Homeier, S. Rast, and H. Krienke, "Iterative Solution of the Ornstein-Zernike Equation with Various Closures Using Vector Extrapolation," *Computer Physics Communications*, vol. 92, pp. 188–202, 1995.

[132] R. Kjellander and S. MarCelja, "Inhomogeneous Coulomb fluids with image interactions between planar surfaces. I," *The Journal of Chemical Physics*, vol. 82, no. 4, pp. 2122–2135, 1985.

[133] R. Ishizuka and N. Yoshida, "Application of efficient algorithm for solving six-dimensional molecular Ornstein-Zernike equation," *The Journal of Chemical Physics*, vol. 136, no. 11, p. 114106, 2012.

[134] S. Jorge, E. Lomba, and J. L. F. Abascal, "An inhomogeneous integral equation for the triplet structure of binary liquids," *The Journal of Chemical Physics*, vol. 114, no. 8, pp. 3562–3569, 2001.

[135] J. M. Brader, "Structural precursor to freezing: An integral equation study," *The Journal of Chemical Physics*, vol. 128, no. 10, p. 104503, 2008.

[136] F. Lado, "Equation of State of the Hard-Disk Fluid from Approximate Integral Equations," *The Journal of Chemical Physics*, vol. 49, no. 7, pp. 3092–3096, 1968.

[137] J. M. J. van Leeuwen, J. Groeneveld, and J. de Boer, "New method for the calculation of the pair correlation function. I," *Physica*, vol. 25, no. 7-12, pp. 792–808, 1959.

[138] G. Zerah and J.-P. Hansen, "Self-consistent integral equations for fluid pair distribution functions: Another attempt," *The Journal of Chemical Physics*, vol. 84, no. 4, pp. 2336–2343, 1986.

[139] F. J. Rogers and D. A. Young, "New, thermodynamically consistent, integral equation for simple fluids," *Phys. Rev. A*, vol. 30, pp. 999–1007, 1984.

[140] E. Waisman, "The radial distribution function for a fluid of hard spheres at high densities," *Molecular Physics*, vol. 25, no. 1, pp. 45–48, 1973.

[141] M. P. Allen and D. J. Tildesley, *Computer Simulation of Liquids*. Oxford Science Publications, Oxford University Press, reprint ed., 1989.

[142] C. Holm and K. Kremer, eds., *Advanced Computer Simulation Approaches for Soft Matter Sciences III*. Advances in Polymer Science, Springer, 2009.

[143] S. Nosé, "A unified formulation of the constant temperature molecular dynamics methods," *The Journal of Chemical Physics*, vol. 81, no. 1, pp. 511–519, 1984.

[144] W. G. Hoover, "Canonical dynamics: Equilibrium phase-space distributions," *Phys. Rev. A*, vol. 31, pp. 1695–1697, 1985.

[145] A. Einstein, "Über die von der molekularkinetischen Theorie der Wärme geforderte Bewegung von in ruhenden Flüssigkeiten suspendierten Teilchen," *Annalen der Physik*, vol. 322, no. 8, pp. 549–560, 1905.

[146] D. S. Lemons and A. Gythiel, "Paul Langevin's 1908 paper "On the Theory of Brownian Motion" ["Sur la théorie du mouvement brownien", C. R. Acad. Sci. (Paris) 146, 530-533 (1908)]," *American Journal of Physics*, vol. 65, no. 11, pp. 1079–1081, 1997.

[147] M. Doi and S. F. Edwards, *The Theory of Polymer Dynamics*. Oxford University Press, USA, 1986.

[148] J. Rotne and S. Prager, "Variational Treatment of Hydrodynamic Interaction in Polymers," *The Journal of Chemical Physics*, vol. 50, no. 11, pp. 4831–4837, 1969.

[149] B. Dünweg and A. J. C. Ladd, "Lattice Boltzmann Simulations of Soft Matter Systems," Advances in Polymer Science, pp. 1–78, Springer Berlin Heidelberg, 2008.

[150] D. L. Ermak and Y. Yeh, "Equilibrium electrostatic effects on the behavior of polyions in solution: polyion-mobile ion interaction," *Chemical Physics Letters*, vol. 24, no. 2, pp. 243 – 248, 1974.

[151] J. Dzubiella, G. P. Hoffmann, and H. Löwen, "Lane formation in colloidal mixtures driven by an external field," *Phys. Rev. E*, vol. 65, p. 021402, 2002.

[152] H. Löwen and J. Dzubiella, "Nonequilibrium pattern formation in strongly interacting driven colloids," *Faraday Discussions*, vol. 123, pp. 99–105, 2003.

[153] A. Wysocki and H. Löwen, "Effects of hydrodynamic interactions in binary colloidal mixtures driven oppositely by oscillatory external fields," *J. Phys.: Condensed Matter*, vol. 23, no. 284117, 2011.

[154] W. H. Press, B. P. Flannery, S. A. Teukolsky, and W. T. Vetterling, *Numerical Recipes in C: The Art of Scientific Computing, Second Edition*. Cambridge University Press, 2 ed., 1992.

[155] G. E. P. Box and M. E. Muller, "A Note on the Generation of Random Normal Deviates," *Ann. Math. Statist.*, vol. 29, pp. 610–611, 06 1958.

[156] A. A. Louis, P. G. Bolhuis, and J. P. Hansen, "Mean-field fluid behavior of the Gaussian core model," *Phys. Rev. E*, vol. 62, pp. 7961–7972, 2000.

[157] B. M. Mladek, D. Gottwald, G. Kahl, M. Neumann, and C. N. Likos, "Formation of Polymorphic Cluster Phases for a Class of Models of Purely Repulsive Soft Spheres," *Phys. Rev. Lett.*, vol. 96, p. 045701, 2006.

[158] C. N. Likos, B. M. Mladek, D. Gottwald, and G. Kahl, "Why do ultrasoft repulsive particles cluster and crystallize? Analytical results from density-functional theory," *The Journal of Chemical Physics*, vol. 126, no. 22, 2007.

[159] S. D. Overduin and C. N. Likos, "Phase behaviour in binary mixtures of ultrasoft repulsive particles," *EPL (Europhysics Letters)*, vol. 85, no. 2, p. 26003, 2009.

[160] L. Berthier, A. J. Moreno, and G. Szamel, "Increasing the density melts ultrasoft colloidal glasses," *Phys. Rev. E*, vol. 82, p. 060501, 2010.

[161] M. Schmiedeberg, "Multiple reentrant glass transitions of soft spheres at high densities: Monotonicity of the curves of constant relaxation time in jamming phase diagrams depending on temperature over pressure and pressure," *Phys. Rev. E*, vol. 87, p. 052310, 2013.

[162] M. P. Ciamarra and P. Sollich, "High-order jamming crossovers and density anomalies," *Soft Matter*, vol. 9, pp. 9557–9561, 2013.

[163] T. Shinbrot and F. J. Muzzio, "Reverse Buoyancy in Shaken Granular Beds," *Phys. Rev. Lett.*, vol. 81, pp. 4365–4368, 1998.

[164] D. A. Huerta and J. C. Ruiz-Suárez, "Vibration-Induced Granular Segregation: A Phenomenon Driven by Three Mechanisms," *Phys. Rev. Lett.*, vol. 92, p. 114301, 2004.

[165] C. N. Likos, H. Löwen, M. Watzlawek, B. Abbas, O. Jucknischke, J. Allgaier, and D. Richter, "Star Polymers Viewed as Ultrasoft Colloidal Particles," *Phys. Rev. Lett.*, vol. 80, pp. 4450–4453, 1998.

[166] C. N. Likos, "Soft matter with soft particles," *Soft Matter*, vol. 2, pp. 478–498, 2006.

[167] C. Mayer, E. Zaccarelli, E. Stiakakis, C. N. Likos, F. Sciortino, A. Munam, M. Gauthier, N. Hadjichristidis, H. Iatrou, P. Tartaglia, H. Löwen, and D. Vlassopoulos, "Asymmetric caging in soft colloidal mixtures," *Nature Materials*, vol. 7, pp. 780–784, 2008.

[168] A. A. Louis, P. G. Bolhuis, J. P. Hansen, and E. J. Meijer, "Can Polymer Coils Be Modeled as "Soft Colloids"?," *Phys. Rev. Lett.*, vol. 85, pp. 2522–2525, 2000.

[169] A. Fernandez-Nieves, H. Wyss, J. Mattsson, and D. A. Weitz, *Microgel Suspensions: Fundamentals and Applications*. Wiley, 2011.

[170] M. Schmiedeberg, T. K. Haxton, S. R. Nagel, and A. J. Liu, "Mapping the glassy dynamics of soft spheres onto hard-sphere behavior," *Europhysics Letters*, vol. 96, no. 3, p. 36010, 2011.

[171] L. López-Flores, H. Ruíz-Estrada, M. Chávez-Páez, and M. Medina-Noyola, "Dynamic equivalences in the hard-sphere dynamic universality class," *Phys. Rev. E*, vol. 88, p. 042301, 2013.

[172] A. van Blaaderen, R. Ruel, and P. Wiltzius, "Template-directed colloidal crystallization," *Nature*, vol. 385, no. 6614, pp. 321–324, 1997.

[173] A. J. Dunleavy, K. Wiesner, R. Yamamoto, and C. P. Royall, "Mutual information reveals multiple structural relaxation mechanisms in a model glass former," *Nature Communications*, vol. 6, 2015.

[174] E. Grundke and D. Henderson, "Distribution functions of multi-component fluid mixtures of hard spheres," *Molecular Physics*, vol. 24, no. 2, pp. 269–281, 1972.

[175] R. D. Groot, J. P. van der Eerden, and N. M. Faber, "The direct correlation function in hard sphere fluids," *The Journal of Chemical Physics*, vol. 87, no. 4, pp. 2263–2270, 1987.

[176] Y.-X. Yu and J. Wu, "Structures of hard-sphere fluids from a modified fundamental-measure theory," *The Journal of Chemical Physics*, vol. 117, no. 22, pp. 10156–10164, 2002.

[177] Y.-X. Yu, J. Wu, Y.-X. Xin, and G.-H. Gao, "Structures and correlation functions of multicomponent and polydisperse hard-sphere mixtures from a density functional theory," *The Journal of Chemical Physics*, vol. 121, no. 3, pp. 1535–1541, 2004.

[178] T. Kawasaki, A. Ikeda, and L. Berthier, "Thinning or thickening? Multiple rheological regimes in dense suspensions of soft particles," *EPL (Europhysics Letters)*, vol. 107, no. 2, p. 28009, 2014.

[179] H. C. Andersen, J. D. Weeks, and D. Chandler, "Relationship between the Hard-Sphere Fluid and Fluids with Realistic Repulsive Forces," *Phys. Rev. A*, vol. 4, pp. 1597–1607, Oct 1971.

[180] P. Tarazona, R. Evans, and U. M. B. Marconi, "Pairwise correlations at a fluid-fluid interface: The influence of a wetting film," *Molecular Physics*, vol. 54, no. 6, pp. 1357–1392, 1985.

[181] R. Lovett, C. Y. Mou, and F. P. Buff, "The structure of the liquid–vapor interface," *The Journal of Chemical Physics*, vol. 65, no. 2, pp. 570–572, 1976.

[182] M. S. Wertheim, "Correlations in the liquid–vapor interface," *The Journal of Chemical Physics*, vol. 65, no. 6, pp. 2377–2381, 1976.

[183] H. B. Eral, D. van den Ende, F. Mugele, and M. H. G. Duits, "Influence of confinement by smooth and rough walls on particle dynamics in dense hard-sphere suspensions," *Phys. Rev. E*, vol. 80, p. 061403, 2009.

[184] V. N. Manoharan, M. T. Elsesser, and D. J. Pine, "Dense Packing and Symmetry in Small Clusters of Microspheres," *Science*, vol. 301, no. 5632, pp. 483–487, 2003.

[185] S. Mirigian and K. S. Schweizer, "Unified Theory of Activated Relaxation in Liquids over 14 Decades in Time," *The Journal of Physical Chemistry Letters*, vol. 4, no. 21, pp. 3648–3653, 2013.

[186] M. Fuchs and M. E. Cates, "Theory of Nonlinear Rheology and Yielding of Dense Colloidal Suspensions," *Phys. Rev. Lett.*, vol. 89, p. 248304, 2002.

[187] M. Fuchs and M. E. Cates, "A mode coupling theory for Brownian particles in homogeneous steady shear flow," *Journal of Rheology*, vol. 53, no. 4, pp. 957–1000, 2009.

[188] T. R. Kirkpatrick and P. G. Wolynes, "Connections between some kinetic and equilibrium theories of the glass transition," *Phys. Rev. A*, vol. 35, pp. 3072–3080, 1987.

[189] K. S. Schweizer, "Derivation of a microscopic theory of barriers and activated hopping transport in glassy liquids and suspensions," *The Journal of Chemical Physics*, vol. 123, no. 24, 2005.

[190] K. S. Schweizer and E. J. Saltzman, "Activated Hopping, Barrier Fluctuations, and Heterogeneity in Glassy Suspensions and Liquids," *The Journal of Physical Chemistry B*, vol. 108, no. 51, pp. 19729–19741, 2004.

[191] W. Götze and L. Sjögren, "Relaxation processes in supercooled liquids," *Reports on Progress in Physics*, vol. 55, no. 3, p. 241, 1992.

[192] T. R. Kirkpatrick, "Mode-coupling theory of the glass transition," *Phys. Rev. A*, vol. 31, pp. 939–944, 1985.

[193] W. Götze, *Complex Dynamics of Glass-Forming Liquids : A Mode-Coupling Theory: A Mode-Coupling Theory*. International Series of Monographs on Physics, OUP Oxford, 2008.

[194] G. Williams and D. C. Watts, "Non-symmetrical dielectric relaxation behaviour arising from a simple empirical decay function," *Trans. Faraday Soc.*, vol. 66, pp. 80–85, 1970.

[195] B. J. Alder and T. E. Wainwright, "Decay of the Velocity Autocorrelation Function," *Phys. Rev. A*, vol. 1, pp. 18–21, Jan 1970.

[196] Y. Pomeau and P. Résibois, "Time dependent correlation functions and mode-mode coupling theories," *Physics Reports*, vol. 19, no. 2, pp. 63 – 139, 1975.

[197] M. H. Ernst, J. Machta, J. R. Dorfman, and H. van Beijeren, "Long time tails in stationary random media. I. Theory," *Journal of Statistical Physics*, vol. 34, no. 3-4, pp. 477–495, 1984.

[198] H. M. Lindsay and P. M. Chaikin, "Elastic properties of colloidal crystals and glasses," *The Journal of Chemical Physics*, vol. 76, no. 7, pp. 3774–3781, 1982.

[199] A. M. Puertas, M. Fuchs, and M. E. Cates, "Simulation study of nonergodicity transitions: Gelation in colloidal systems with short-range attractions," *Phys. Rev. E*, vol. 67, p. 031406, 2003.

[200] W. van Megen, T. C. Mortensen, S. R. Williams, and J. Müller, "Measurement of the self-intermediate scattering function of suspensions of hard spherical particles near the glass transition," *Phys. Rev. E*, vol. 58, pp. 6073–6085, 1998.

[201] P. N. Segré, O. P. Behrend, and P. N. Pusey, "Short-time Brownian motion in colloidal suspensions: Experiment and simulation," *Phys. Rev. E*, vol. 52, pp. 5070–5083, 1995.

[202] G. C. Berry, "Thermodynamic and Conformational Properties of Polystyrene. I. Light-Scattering Studies on Dilute Solutions of Linear Polystyrenes," *The Journal of Chemical Physics*, vol. 44, no. 12, p. 4550, 1996.

[203] G. J. Fleer and R. Tuinier, "Analytical phase diagram for colloid-polymer mixtures," *Phys. Rev. E*, vol. 76, p. 041802, 2007.

[204] H. N. W. Lekkerkerker, W. C. K. Poon, P. N. Pusey, A. Stroobants, and P. B. Warren, "Phase Behaviour of Colloid + Polymer Mixtures," *EPL (Europhysics Letters)*, vol. 20, no. 6, p. 559, 1992.

[205] D. Aarts, R. Tuinier, and H. N. W. Lekkerkerker, "Phase behaviour of mixtures of colloidal spheres and excluded-volume polymer chains," *Journal of Physics: Condensed Matter*, vol. 14, pp. 7551–7561, 2002.

[206] M. E. Leunissen, *Manipulating colloids with charges and electric fields*. PhD, Utrecht University, 2007.

[207] A. Yethiraj and A. van Blaaderen, "A colloidal model system with an interaction tunable from hard sphere to soft and dipolar," *Nature*, vol. 421, no. 6922, pp. 513–517, 2003.

[208] C. P. Royall, W. C. K. Poon, and E. R. Weeks, "In search of colloidal hard spheres," *Soft Matter*, vol. 9, no. 1, p. 17, 2013.

[209] W. Schaertl and H. Sillescu, "Brownian dynamics of polydisperse colloidal hard spheres: Equilibrium structures and random close packings," *Journal of Statistical Physics*, vol. 77, no. 5-6, pp. 1007–1025, 1994.

[210] M. C. Jenkins and S. U. Egelhaaf, "Confocal microscopy of colloidal particles: towards reliable, optimum coordinates," *Advances in colloid and interface science*, vol. 136, no. 1-2, pp. 65–92, 2008.

[211] J. C. Crocker and D. G. Grier, "Methods of digital video microscopy for colloidal studies," *Journal of colloid and interface science*, vol. 179, pp. 298–310, 1996.

[212] T. H. Zhang, J. Klok, R. Hans Tromp, J. Groenewold, and W. K. Kegel, "Non-equilibrium cluster states in colloids with competing interactions," *Soft Matter*, vol. 8, pp. 667–672, 2012.

[213] A. Stradner, H. Sedgwick, F. Cardinaux, W. C. K. Poon, S. U. Egelhaaf, and P. Schurtenberger, "Equilibrium cluster formation in concentrated protein solutions and colloids," *Nature*, vol. 432, no. 7016, pp. 492–495, 2004.

[214] A. Stradner, F. Cardinaux, S. U. Egelhaaf, and P. Schurtenberger, "Do equilibrium clusters exist in concentrated lysozyme solutions?," *Proc. Natl. Acad. Sci. USA*, vol. 105, pp. E75–E75, 2008.

[215] C. S. O'Hern, S. A. Langer, A. J. Liu, and S. R. Nagel, "Random Packings of Frictionless Particles," *Phys. Rev. Lett.*, vol. 88, p. 075507, 2002.

[216] H. Hinrichsen, "Non-equilibrium critical phenomena and phase transitions into absorbing states," *Advances in Physics*, vol. 49, no. 7, pp. 815–958, 2000.

[217] H. E. Stanley, "Cluster shapes at the percolation threshold: and effective cluster dimensionality and its connection with critical-point exponents," *Journal of Physics A: Mathematical and General*, vol. 10, no. 11, p. L211, 1977.

[218] A. Bunde and S. Havlin, *Fractals and disordered systems*. Springer-Verlag, 1991.

[219] J. Vermant and M. J. Solomon, "Flow-induced structure in colloidal suspensions," *Journal of Physics: Condensed Matter*, vol. 17, no. 4, p. R187, 2005.

[220] M. Kunitz, "Syneresis and Swelling of Gelatin.," *J. Gen. Physiol.*, vol. 12, no. 2, pp. 289–312, 1928.

[221] T. Matsuhashi, "Agar," in *Food gels* (P. Harris, ed.), ch. 1, pp. 1–51, Elsevier Applied Science London, 1990.

[222] T. Divoux, B. Mao, and P. Snabre, "Syneresis and delayed detachment in agar plates," *Soft Matter*, vol. 11, pp. 3677–3685, 2015.

[223] J. Wu, T. Yi, Y. Zou, Q. Xia, T. Shu, F. Liu, Y. Yang, F. Li, Z. Chen, Z. Zhou, and C. Huang, "Gelation induced reversible syneresis via structural evolution," *J. Mater. Chem.*, vol. 19, no. 23, p. 3971, 2009.

[224] T. Gan, Y. Guan, and Y. Zhang, "Thermogelable PNIPAM microgel dispersion as 3D cell scaffold: effect of syneresis," *J. Mater. Chem.*, vol. 20, no. 28, p. 5937, 2010.

[225] L. Cipelletti, S. Manley, R. C. Ball, and D. A. Weitz, "Universal aging features in the restructuring of fractal colloidal gels.," *Phys. Rev. Lett.*, vol. 84, no. 10, pp. 2275–2278, 2000.

[226] N. Koumakis, A. B. Schofield, and G. Petekidis, "Effects of shear induced crystallization on the rheology and ageing of hard sphere glasses," *Soft Matter*, vol. 4, no. 10, 2008.

[227] K.-C. Ng, "Hypernetted chain solutions for the classical one-component plasma up to Γ=7000," *The Journal of Chemical Physics*, vol. 61, no. 7, pp. 2680–2689, 1974.

[228] H. Johnson, "An improved method for computing a discrete Hankel transform," *Comput. Phys. Commun.*, vol. 43, pp. 181–202, 1987.

[229] D. Lemoine, "The discrete Bessel transform algorithm," *J. Chem. Phys.*, vol. 101, no. 5, pp. 3936–3944, 1994.